nagra.

Arbeitsbericht NAB 22-34

Cement – Clay

Synthesis of Transport Across the Cement-Clay Interface

July 2022

National Cooperative
for the Disposal of
Radioactive Waste

Hardstrasse 73
P.O. Box 280
5430 Wettingen
Switzerland
Tel. +41 56 437 11 11

www.nagra.ch

nagra.

Arbeitsbericht NAB 22-34

Cement – Clay

Synthesis of Transport Across the Cement-Clay Interface

July 2022

N.I. Prasianakis, G. Kosakowski,
Th. Gimmi, P. Luraschi, G.D. Miron,
W. Pfingsten & S.V. Churakov

[1] Laboratory for Waste Management, PSI
[2] Institute of Geological Sciences, University of Bern

KEYWORDS

Cement-clay interaction, dissolution, precipitation, transport mechanisms, experiments, modelling

National Cooperative
for the Disposal of
Radioactive Waste

Hardstrasse 73
P.O. Box 280
5430 Wettingen
Switzerland
Tel. +41 56 437 11 11

www.nagra.ch

Nagra Arbeitsberichte ("Working Reports") present the results of work in progress that have not necessarily been subject to a comprehensive review. They are intended to provide rapid dissemination of current information.
This report was prepared on behalf of Nagra. The viewpoints presented and conclusions reached are those of the author(s) and do not necessarily represent those of Nagra.

Table of Contents

List of Tables

List of Figures

1 Introduction

The Swiss concept for long term disposal of radioactive waste foresees the construction of deep geological repositories for High Level Waste (HLW) and Long/Intermediate Level Waste (L/ILW) (Fig. 1-1). The placement of the repository within the stable low permeable rock formations in deep geological underground ensures long term passive radiological safety of the repository, including protection from human intrusion, erosion or even long term climatic and tectonic evolution.

In April 2008, the Federal Government approved the Sectoral Plan for Deep Geological Repositories (SGT, Sachplan geologische Tiefenlager) (SFOE 2008). The Sectoral Plan defines the site repository selection process, and generic repository design. The final, third stage of the Sectoral Plan has started in November 2018. In this stage, Nördlich Lägern has beenproposed as the siting region for the HLW and L/ILW combined repository, followed by the submission of documents for the general license application.

The post-closure safety of the underground repository relies upon a system of nested, passive engineered and geological barriers, with partially redundant and complementarity safety function. The major elements of the barrier systems are the waste matrices, the disposal canisters/ containers, the materials used for backfilling and sealing of the underground structures, and the host rock along with other geological formations that will provide an additional geological barrier (confining units).

Whereas the design of each barrier and its material selection (e.g. steel, cement, bentonite, etc.) is optimized to maintain its specific safety function, it is essential to ensure that chemical interaction between the different barrier materials does not lead to the degradation of their primary safety function and thus does not compromise the entire design of the multi-barrier system.

Cement is a widely used construction and waste binder material. Cement-based composites are the major components of the L/ILW storage systems (cf. Section 1.1). Cement paste is the primary material of the waste matrix for L/ILW radioactive waste. The containers are made of concrete and the void space within the container will be filled with a porous mortar. After the emplacement of the waste containers and filling of the void space with mortar, the caverns are closed with a sealing system, consisting of an initial seal made of a sand-bentonite mixture, a transition layer and, finally, closed with a concrete plug. The tunnel galleries are foreseen to be filled with clay-based material.

All possible geological siting regions, which are considered at the current stage of the site selection process, are located in Opalinus Clay formations (OPA clay). The pore water of cement-based materials is known to have a high pH and alkalinity, starting from initial pH = 12.6 – 13.0 and in the course of degradation slowly decreasing to pH = 11.0 –10.0. Contrary, the Opalinus Clay pore water has a close to neutral pH value of 7 – 8, a higher Mg concentration, and a higher inventory of silica, which can become available for mineral fluid interaction. This means essentially that there is a geochemically contrasting condition, with respect to the in situ environment in the currently considered host rocks (e.g., OPA clay), and cement and clay are not in thermodynamic equilibrium. It is expected that this geochemical contrast in the composition of cement and OPA clay pore water will eventually lead to material fluxes and dissolution-precipitation reactions at a thin zone around their respective interface. These chemical interactions will modify the mineralogical composition and local transport properties of the interfacial zone. The spatial and temporal extent of this interaction, even though it is not expected to be large, needs to be understood and quantified in order to evaluate the relevance of these changes for the safety function of the clay-based host rocks and buffer materials.

This report provides a state-of-the-art review of the current experimental and theoretical knowledge about cement/clay interaction. Chapter 2 provides the structural summary and overview of the cement/clay interaction processes and their relevance for the performance of the multi-barrier repository design and the repository in situ conditions. Chapter 3 provides a review of the experimental findings in the studies of cement/clay interactions, which are conducted at laboratory and field scales. Chapter 4 reviews the state of the art of numerical modelling techniques, and the concepts applied to model the experimental observations and to evaluate the expected long-term evolution of the interface zone, beyond the experimentally accessible timescale. Finally, the most important conclusions about the evolution of the cement-clay interface are summarized in Chapter 5.

1.1 Repository design

According to the current plans, two types of radioactive waste repositories are considered in Switzerland. One shall contain the high-level waste from the reprocessing and spent fuel elements (SF/HLW). Another one shall contain long and intermediate level waste (L/ILW) from the operation and decommissioning of nuclear power plants, as well as from non-nuclear energy related applications in research and medicine. The SF/HLW and L/ILW repositories can, in principle, be co-located in a combined repository concept, within Opalinus Clay (OPA) being the host rock (Fig. 1-1). Due to the differences in inventory, thermal output and the waste volumes, the repository design and the barrier materials for SF/HLW and L/ILW are very different. SF/HLW are stored in steel casks and enclosed by a bentonite barrier, which serves as the backfilling material (Fig. 1-2). The main role of the bentonite buffer is to provide sufficient swelling pressure in the repository, after the re-saturation of the emplacement tunnel, in order to sustain the lithostatic pressure of the host rocks and to ensure homogeneous and as isotropic as possible transmission of stresses caused by tunnel convergence onto the disposal casks. The swelling capacity of bentonite (i.e., the potential to build up the swelling pressure) and plasticity to ensure isotropic distribution of stresses is controlled by the properties of the Na-montmorillonite mineral, which is the main mineral phase of the bentonite. Complementary, the bentonite buffer contributes to the retention of radionuclides after the breaching of disposal casks.

The host rocks and confining units are responsible for the slow transport (e.g. by diffusion) and retention of radionuclides (adsorption and incorporation). These are the key barriers controlling the rate of radionuclide migration from the repository near field to the far field and the biosphere. The diffusive transport and retention processes contribute to the substantial retardation of the radionuclide release and, in combination with the decay processes, decrease the apparent radiological impact of the repository.

Opalinus Clay is considered as preferable host rock in all siting regions being under consideration in the Stage 3 SGT. The extremely low hydraulic conductivity of this OPA is attributed to the high content of clay minerals and small size of the pores. Furthermore, Opalinus Clay has been shown to possess self-sealing capacity ensuring the recovery of low hydraulic conductivity even after massive mechanical deformation (e.g. cracking). These properties of OPA are by far controlled by presence of swelling illite-smectite group of clay minerals. From the safety point of view, it is essential to ensure that swelling clay minerals are not transformed into non-swelling phases either by cation exchange or by mineral dissolution/precipitation reactions.

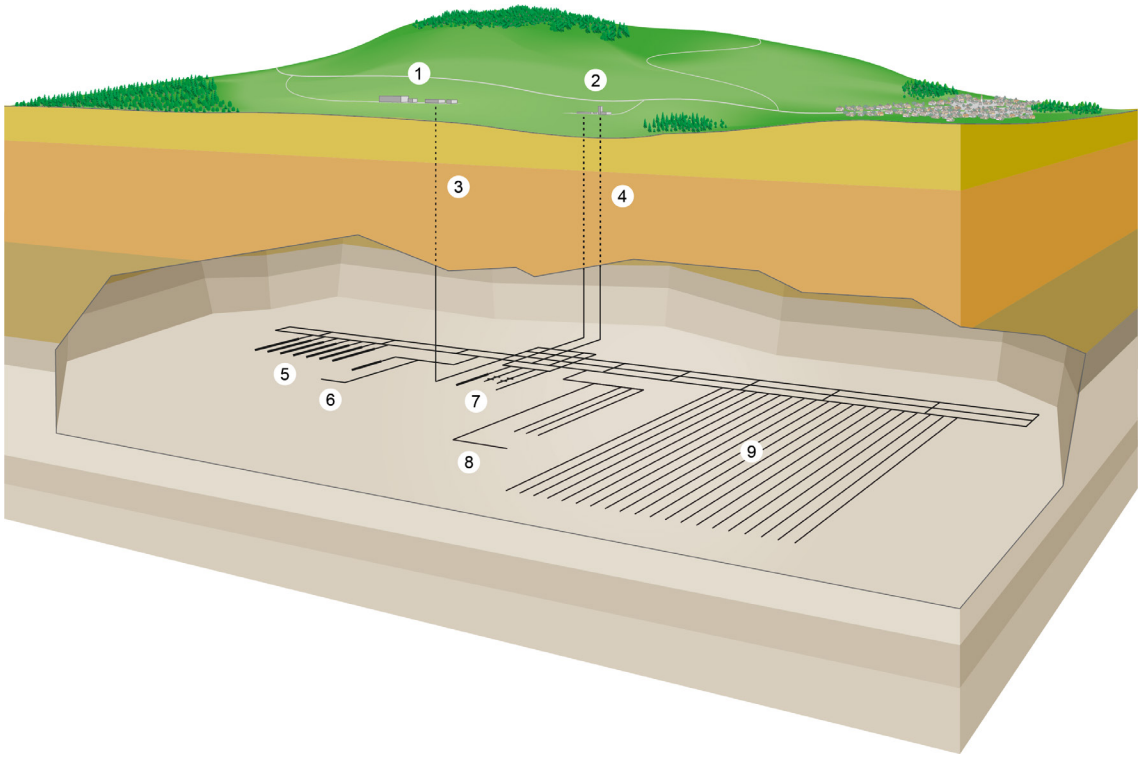

Fig. 1-1: Illustration of a combined repository for SF/HLW and for L/ILW

Legend: 1) Surface facility. 2) Auxiliary access facility. 3) Access shaft (main access). 4) Operations and ventilation shafts (auxiliary accesses). 5) Main repository L/ILW. 6) Pilot facility L/ILW. 7) Underground geological investigations/test areas. 8) Pilot facility HLW. 9) Main repository HLW.

Nagra (2022a)

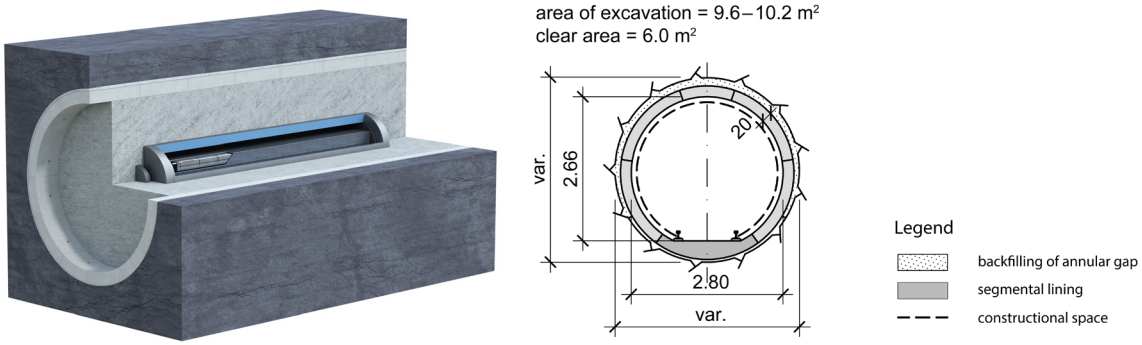

Fig. 1-2: Visualisation of the HLW emplacement drift

Towards the OPA, there is the tunnel support with pre-fabricated concrete elements (segmental lining) with the backfilled annular gap and the expected secondary porosity in the EDZ. The canister is emplaced on a pedestal made of compacted bentonite blocks and the tunnel back-filled with granular bentonite material (pellets). In the current SF/HLW repository design, the cementitious materials are applied in the tunnel support system. Their main (safety) function is to withstand the mechanical convergence of the tunnel during the construction and operational phases. After the emplacement of disposal casks, the backfilling with bentonite and re-saturation, the cement liner is expected to degrade with the surrounding host rocks and bentonite buffer (Nagra 2022b).

Cement is the main material used in L/ILW repository as seen in Fig. 1-3. Compared to the SF/HLW repository the cementitious contained waste has larger volume but much lower radionuclide inventory. Apart from hydrated cements, the repository construction materials contain aggregate materials and steel. Usually the wastes are solidified/embedded in a cement/mortar matrix, which itself is contained in steel drums. The main function of these drums is mainly needed for interim storage, handling and transport prior to the emplacement. Some wastes may also be embedded in bitumen.

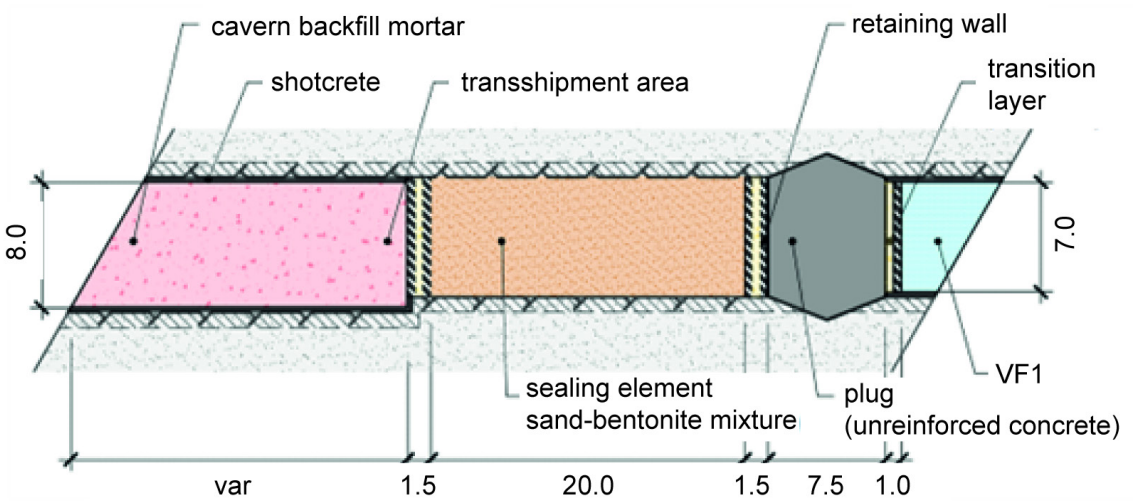

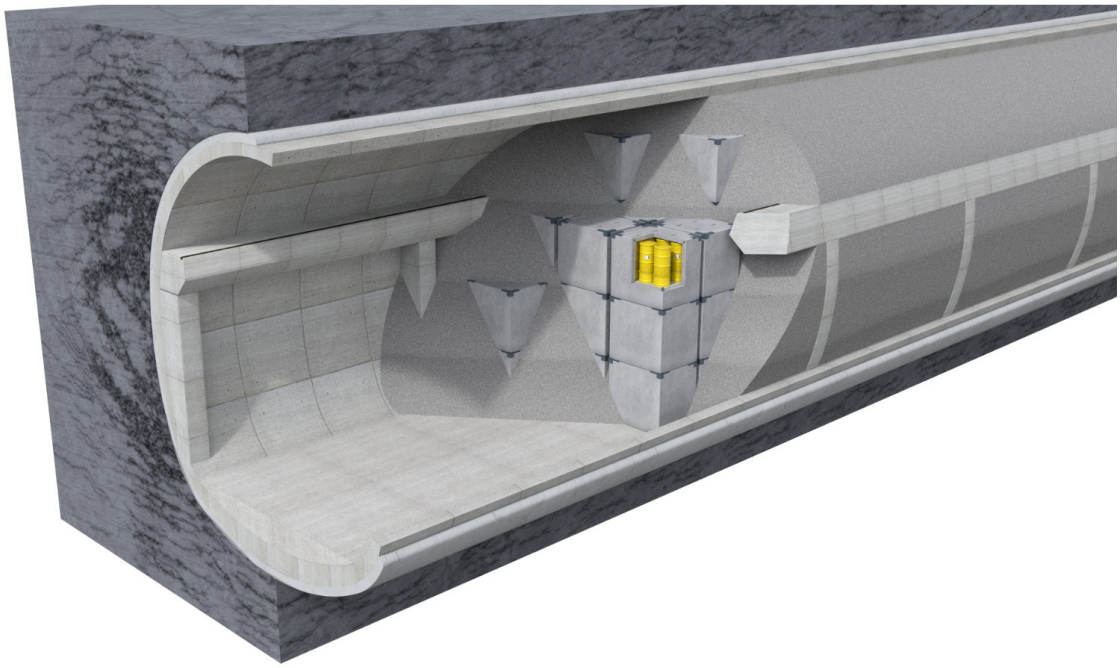

Fig. 1-3: Top: cross section of a seal V1-SMA of a L/ILW repository
Bottom: Emplacement tunnel of the foreseen L/ILW repository (Nagra 2022b)

The current repository design relies on generic descriptions of the material to be used, without explicit specification of the recipe for the cementitious material. The final specifications will be defined at the stage of the construction licence application. Ordinary Portland cement (OPC) is often considered as the reference cementitious binder in the L/ILW repository. Cement paste is the primary waste matrix for radionuclide. The containers are made of concrete and the void space within the container will be filled with a mortar. The disposal caverns for the L/ILW repository are reinforced by a tunnel support system made of reinforced shotcrete and concrete, which protect the walls from rock fall and take up the loads during the construction and emplacement phases. The space between the disposal containers and the cavern wall will be filled with a grain-supported mortar, which takes up the mechanical stresses by grain-to-grain contact while providing gas storage volume and space for gas escape between the aggregates. After the emplacement of the waste containers and filling the void space with specifically designed mortar (e.g. "monocorn" mortar), the caverns are closed with a sealing system, consisting of an initial seal made of a sand-bentonite mixture, a transition layer and, finally, closed with a concrete plug. The tunnel galleries will be filled with clay-based material. For the construction of the tunnels, a reinforced concrete or shotcrete liner support is used.

Cement/clay interfaces are encountered in:

SF/HLW-emplacement drift (e.g. No. 20 in Fig. 1-4):

- Opalinus Clay – cement tubbings where the annular gap (tubbing – OPA) is filled with some kind of mortar/grout – bentonite
- Bentonite – cement tubbings

ILW emplacement cavern (e.g. No. 13 in Fig. 1-4):

- Opalinus Clay – low pH cement fibre reinforced shotcrete

Tunnel systems (e.g. No. 3,9,10,15,16,17 in Fig. 1-4):

- Opalinus Clay – low pH cement fibre reinforced shotcrete – tunnel backfill (clay-based material)
- The sealing system contains among other components concrete plugs and seals made from bentonite or sand/bentonite mixtures. The clay and cement materials are separated **in tunnel direction** by gravel/sand layers. **Perpendicular to tunnel direction** there will be a direct contact of cement and clay materials with Opalinus Clay.

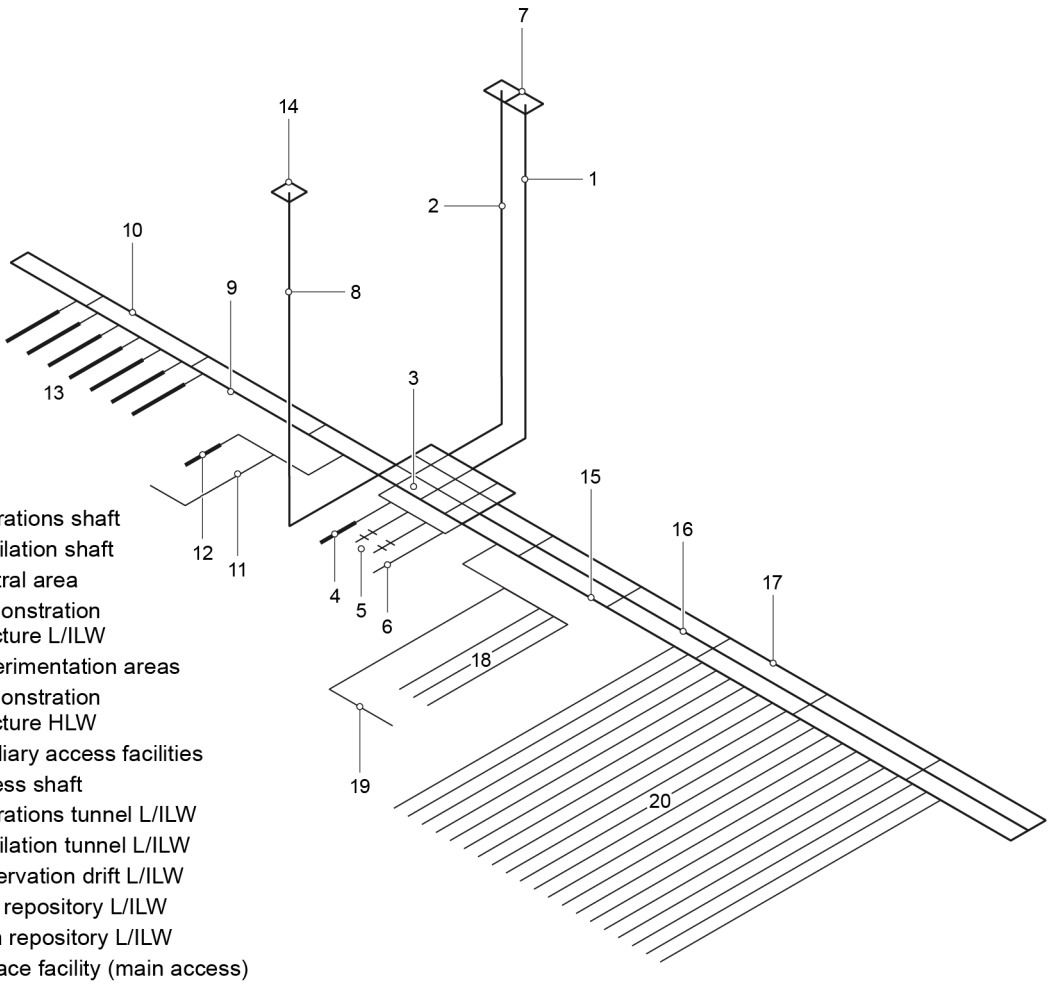

1 Operations shaft
2 Ventilation shaft
3 Central area
4 Demonstration structure L/ILW
5 Experimentation areas
6 Demonstration structure HLW
7 Auxiliary access facilities
8 Access shaft
9 Operations tunnel L/ILW
10 Ventilation tunnel L/ILW
11 Observation drift L/ILW
12 Pilot repository L/ILW
13 Main repository L/ILW
14 Surface facility (main access)
15 Operations tunnel HLW
16 Ventilation tunnel HLW
17 Construction tunnel HLW
18 Pilot repository HLW
19 Observation drift HLW
20 Main repository HLW

Fig. 1-4: System sketch of subsurface part of the Nagra's combined repository project
Nagra (2022a)

1.2 Repository near field evolution and governing processes

The HLW/SF and the L/ILW repository have distinct geochemical evolutionary scenarios, as the emplaced wastes, the dimensions of emplacement tunnels, the engineered buffers and the materials used for backfilling emplacement drifts and caverns are different between the two parts of the repository. The following summary describes the main processes controlling the evolution of chemical conditions and hydraulic regime which governs the changes at the cement/clay interfaces in the repository near-field. The detailed description of the processes in HLW/SF and L/ILW repositories are available in Leupin et al. (2016a) and Leupin et al. (2016b), respectively.

HLW/SF

The evolution of SF/HLW near field can be described with three main phases, an initial period where the repository components are built and operated, a transient hydraulic state after repository closure and a hydraulic steady state (Fig. 1-5). Major processes acting during each phase are the thermal output of waste canisters, the liquid re-saturation of the near field due to inflow water from host rock, and the generation of hydrogen gas due to anaerobic corrosion of the steel canisters that encapsulate the waste.

During repository operation and for some time after closure, geochemical processes in the repository will be dominated first by de-saturation in the vicinity of the tunnels. Shortly after repository closure, the re-saturation process will start. In the case of the SF/HLW emplacement drifts, the quasi fully saturated conditions are expected about one hundred years after closure; gas generation due to canister corrosion gives rise to very low gas saturation, in the order of 1%. During repository construction and before closure, tunnels and vaults are open to surface atmospheric conditions of pressure, humidity and redox, which lead to evaporation of water and mineral precipitation in the unsaturated zone of the excavation damaged zone (EDZ), and oxidation, especially of chemically-reduced minerals such as pyrite (FeS_2). The oxidising conditions prevailing during the operational phase and immediately thereafter change to reducing conditions, once the oxygen in the entrapped atmosphere is consumed by oxidation reactions in the near field.

Decay heat from SF and HLW will increase temperatures within and around the repository for long periods of time. The range of temperature within and around the SF/HLW near field depends on the thermal properties of the buffer which in principle depend on its saturation state and of the ambient (site-specific) rock temperature. The system should be designed in such a way, that temperatures in Opalinus Clay do not exceed 90 °C. It is expected that temperatures in the emplacement drifts are decreased close to ambient rock temperatures after about 10k years.

The initial temperature increase during the first decades after the emplacement of SF and HLW canisters nonetheless gives rise to a transient increase of pore pressure and rock stress, together with thermal expansion of the rock. The implications of these rock-mechanical effects are discussed in Section 3.2 of Leupin et al. (2016a).

The thermal pulse may also lead to further evaporation prior to eventual re-saturation. However, examples from underground rock laboratories show that, even after several years, the zone of partial de-saturation due to ventilation only extends to a depth of < 1 m from the tunnel walls, and it is unlikely that the additional heat from radioactive decay greatly increases the depth of the de-saturated zone (Bossart & Nussbaum 2007).

Gases are expected to be generated in a HLW repository as a result of anaerobic corrosion of metals (which produces H_2), and radiolysis of water (which principally produces H_2).

The amount of gas generated corresponds directly to the waste inventory (SF/HLW disposal canisters) and to structural materials associated with tunnel construction and repository operation. Correspondingly, gas production takes place predominantly on the surfaces of the canisters and waste materials and at the interface between backfilled tunnels and host rock. Gas production rates are largely determined by the nature of the canister materials and the tunnel support materials, as well as by the environmental conditions and the pore water chemistry.

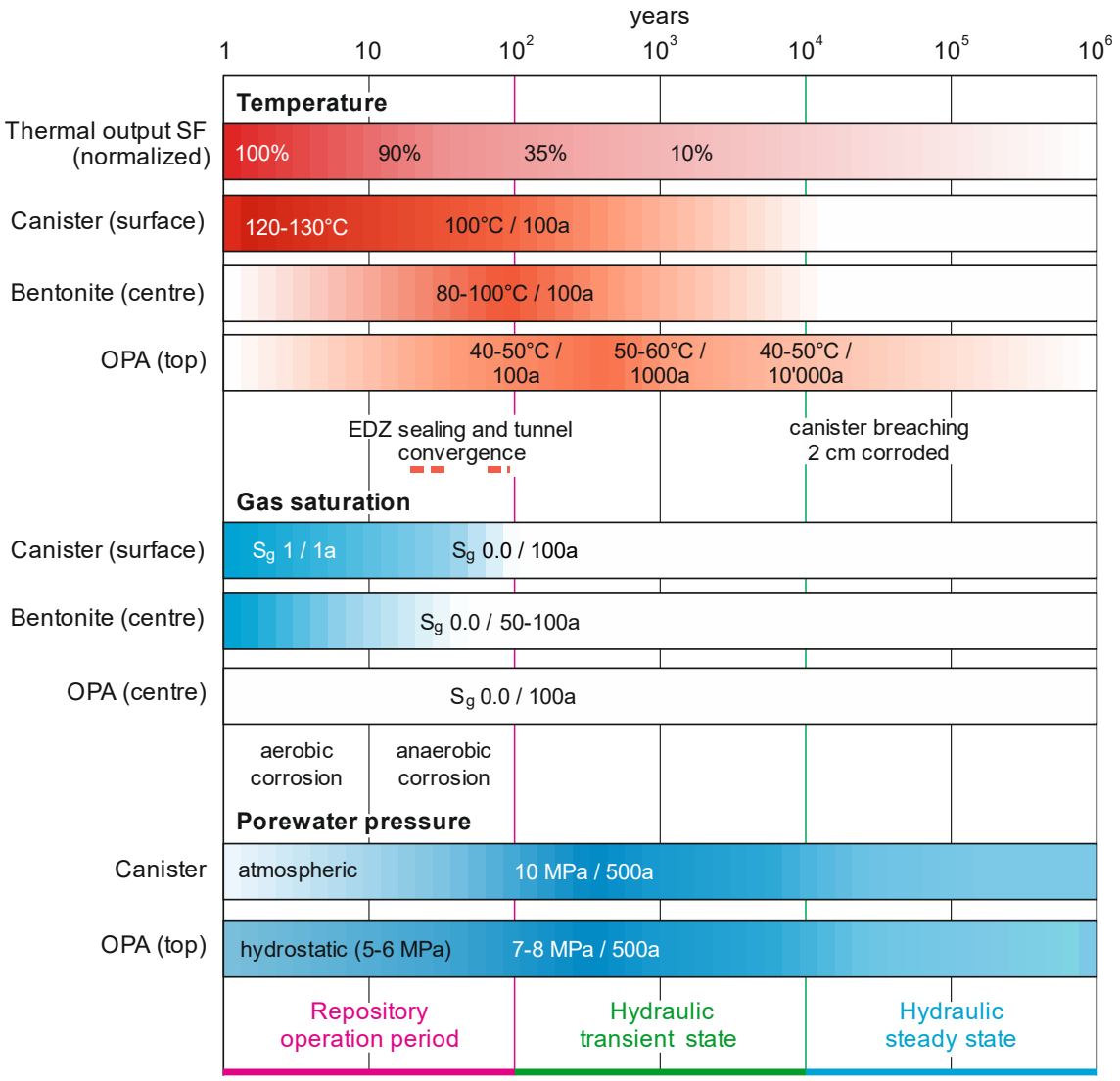

Fig. 1-5: Overview of the expected evolution of main processes in HLW repository based on a compilation of modelling reports and experimental data
Leupin et al. (2016a)

In the SF/HLW emplacement drifts, H_2 gas production under anaerobic conditions typically occurs under fully or partially saturated conditions (corrosion starts at relative humidity of about 60% depending on surface roughness and salt deliquescence (Landolt et al. 2009). A free gas phase develops when the local solubility limit of the gas is exceeded, which is associated with a distinct volume increase and a concomitant build-up of gas pressures.

In the SF/HLW emplacement drifts, gas generation processes at the canister surfaces may delay the saturation of the buffer. During the early post-closure period, a saturation front develops due to the steep pressure gradient for liquid flow into the low-permeability, high-suction bentonite material, resulting in early saturated conditions around the segmental liner with the embedded construction metals. At the same time, anaerobic conditions can be created locally due to oxygen consumption from aerobic corrosion. Hence, localised anaerobic conditions can co-exist temporarily with domains where oxidising conditions prevail.

Soon after waste emplacement, all flow and transport processes in the SF/HLW near field take place under non-isothermal conditions, with a significant temperature increase (> 100 °C) due to heat generation associated with radioactive decay of waste material (SF/HLW). This affects the saturation behaviour of the bentonite buffer, as pore water is evaporated and transported away by vapour diffusion into cooler regions, where the vapour condenses creating a counter flow of liquid water towards the canister. At late times, after failure of the SF/HLW canisters and when the buffer around the canisters is saturated, the gas pressure may exceed the hydrostatic pressure and gas bubbles may form locally in bentonite or at interfaces. In this case, the presence of trapped gas reduces the effective diffusion coefficient of the bentonite.

L/ILW

Similar to the evolution of a HLW/SF repository, the L/ILW repository evolution can be divided into a repository operation phase, a hydraulic transient state and a hydraulic steady state. The repository operation phase ends with repository closure 100 years after the waste emplacement (See Fig. 1-6). The successive hydraulic transient stage spans much longer as for the HLW/SF, while the hydraulic steady state might be only reached after more than 100k years.

Chemical conditions in the L/ILW repository, as well as their temporal changes, are driven by the interactions between hydrated cement, wastes (mainly organic matter and metals), steel, concrete aggregates and clays (Kosakowski et al. 2014). Considering the chemical nature of the major materials involved, two basic processes take place: an acid – base reaction (aggregate/clays – alkaline cement) and a redox reaction, the corrosion of iron. The chemical reactions only proceed if a sufficient amount of water is present, either as a (stagnant or mobile) aqueous phase or as a humid atmosphere. Timescales for some of these processes are illustrated in Fig. 1-6. Here, the following issues have been highlighted as being potentially-relevant:

- effects of construction
- effects of degradation of concrete and cement matrices (mineral precipitation/dissolution with porosity changes)
- degradation of organic materials
- metal corrosion
- effects of cement/clay interaction (mineral precipitation/dissolution with porosity changes)

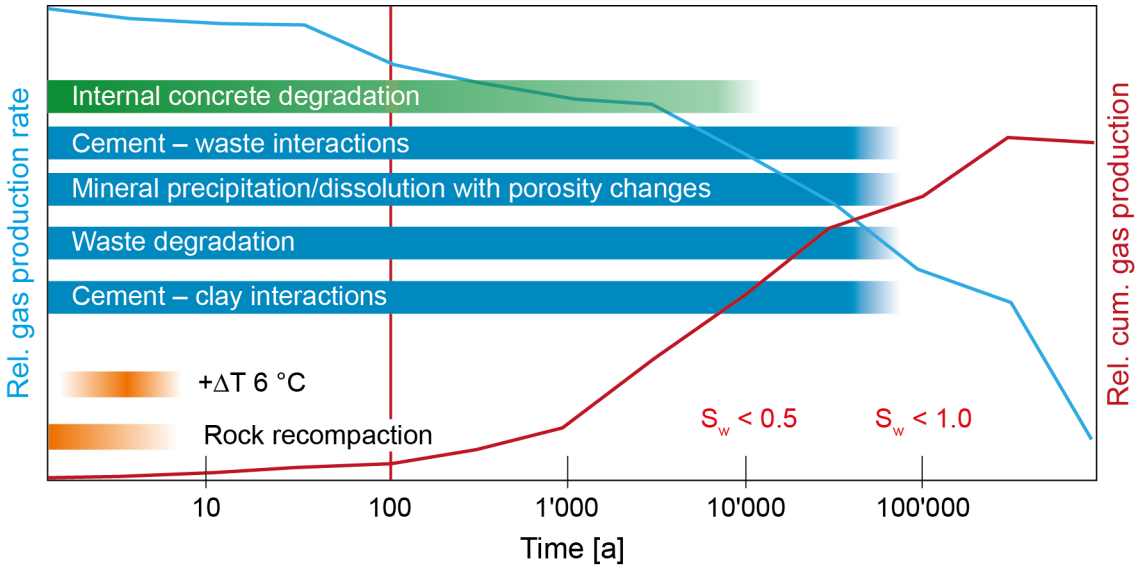

Fig. 1-6: Overview of the expected evolution of main processes in a L/ILW repository

The red vertical line indicates repository closure at 100 years and S_w indicates the degree of saturation of the emplacement cavern. (Fig. 3.1-1 from Leupin et al. 2016b).

During repository operation and the initial post-closure period, the geochemical processes in the repository will be dominated first by de-saturation of the rock in the vicinity of the tunnels. After repository closure, re-saturation will be affected by gas production due to the degradation of organic materials and the anaerobic corrosion of steel (Leupin et al. 2016c). The period of gas generation might be very long and a complete re-saturation of the near field might require more than hundred thousand years (Papafotiou & Senger 2016a).

During repository construction and before closure, tunnels and vaults will be connected to the surface atmosphere, which will influence the pressure, humidity and oxidation state of the tunnels and vaults. These conditions will lead to the evaporation of water, and oxidation, especially of chemically-reduced minerals such as pyrite (FeS_2) in the Opalinus Clay. The oxidising conditions prevailing during the operational phase and immediately thereafter will change to reducing conditions once the oxygen in the entrapped atmosphere is consumed.

Heat in the L/ILW emplacement caverns is produced by setting cement (hydration processes) (Poller et al. 2014) and by radioactive decay of the waste. By the time of repository closure, the cement will be close to fully hydrated. The release of hydration heat from mortar used in plugs to close the repository and/or shotcrete used to stabilise underground structures would occur within a few months, leading to a relatively short-term temperature increase within and around the repository.

The ambient temperature may range from about 45 – 50 °C at repository depth at Nördlich Lägern. A temperature rise in the host rock in the range of 5 to 10 °C due to hydration of cement materials is expected to have a negligible effect on chemical or physical processes.

Gases are generated in an L/ILW repository as a result of anaerobic corrosion of metals (which produces H_2), microbial and chemical degradation of organic matter (which may produce gaseous compounds CO_2, CH_4, which may incorporate ^{14}C) and radiolysis of water (which principally produces H_2). The sources of gas generation comprise the contributions directly related to the waste inventory, whereby gas generation from degradation of organic waste amounts to typically less than 20% of gas production from metal waste (Poller et al. 2016). In addition, structural materials used for tunnel construction and repository operation produce further volumes of H_2

that are small compared to gas production from the waste. Gas production takes place preferentially on the surface of the waste materials and at the interface between backfilled caverns and host rock. Gas production rates are largely determined by the nature of the structural materials and wastes to be disposed, as well as by the environmental conditions and the pore water chemistry at the loci of interaction.

Because the backfill material (mortar) is highly porous, the L/ILW emplacement caverns will saturate relatively slowly and water saturation will begin in the bottom part of the cavern (Papafotiou & Senger 2016a). The saturation distribution will be controlled by the capillarity of the different materials, as well as by gravity. That is, the construction concrete in the cavern base, which has small pores, will be saturated earlier than the mortar in the cavern roof and the cavern sides, which has large pores and therefore a low capillarity. H_2 generation due to the anaerobic corrosion of metals can potentially affect re-saturation. As the gas pressure increases in the cavern, the pore water in the backfill can be displaced. This will depend on the extent to which effective gas permeability of the cavern seal and adjacent EDZ allows the release of the accumulated gas from the repository caverns. Thus, depending on the assumed gas generation rate, host rock properties, and on the design of the sealing system, the de-saturation regime may last between a few thousand years and more than hundred thousand years.

Various transport mechanisms control the combined flow of gas and pore water in the backfill surrounding the L/ILW containers. These include advection and diffusion of dissolved gas, visco-capillary displacement of pore water and dilatancy-controlled gas flow at an elevated gas pressure (Senger et al. 2013). In contrast and independent of the actual gas transport mechanism, combined flow of gas and water through the sand/bentonite seal is associated with localisation phenomena such as capillary fingering and pathway dilation (Leupin et al. 2016a).

2 Cement/clay interaction and porosity change

2.1 Overview on clay and cement materials

Cement-based and clay-based materials have very different chemical compositions. Fresh cements are characterized by high alkalinity and pH of pore water (e.g. pH = 13.0 – 12.6) due to high initial concentrations of free alkali metal ions released during cement hydration. At the later stage of cement aging when in contact with clay, the pH is buffered at pH=12.6 by the dissolution of portlandite. Once the portlandite is consumed, the pore water chemistry is controlled by the reactivity of the C-S-H resulting in a gradual reduction of pH from 12.6 to 10.0. Therefore, at different stages of their degradation, the cementitious materials act as a sources of cationic calcium species and anionic hydroxides.

Opalinus clay pore water has close to neutral pH and an inventory of silica, carbonates and possibly sulfates aqueous species available for mineral fluid interactions. It is expected that the chemical contrast in the composition of cement and OPA clay pore water will lead to material fluxes and subsequent dissolution precipitation reactions at their interfaces. These chemical interactions will modify the mineralogical composition and transport properties of materials in the proximity of the interfacial zone. Dissolution/precipitation processes within the porous materials lead to microstructural changes and cause local decrease/increase of the porosity, affecting pores with sizes from nanometre to millimetre. The cation exchange reactions may affect the smectites' swelling capacity. At the same time the modification of the pore water composition can possibly affect the surface speciation mechanisms changing the sorption capacity of host rocks and engineered barriers. The spatial and temporal extent of this interaction needs to be quantified to evaluate the relevance of these changes for the safety function of the clay-based host rocks and buffer materials. A schematic of the relevant processes (example of cement-bentonite interaction) illustrates the interplay of different mechanisms in Fig. 2-1.

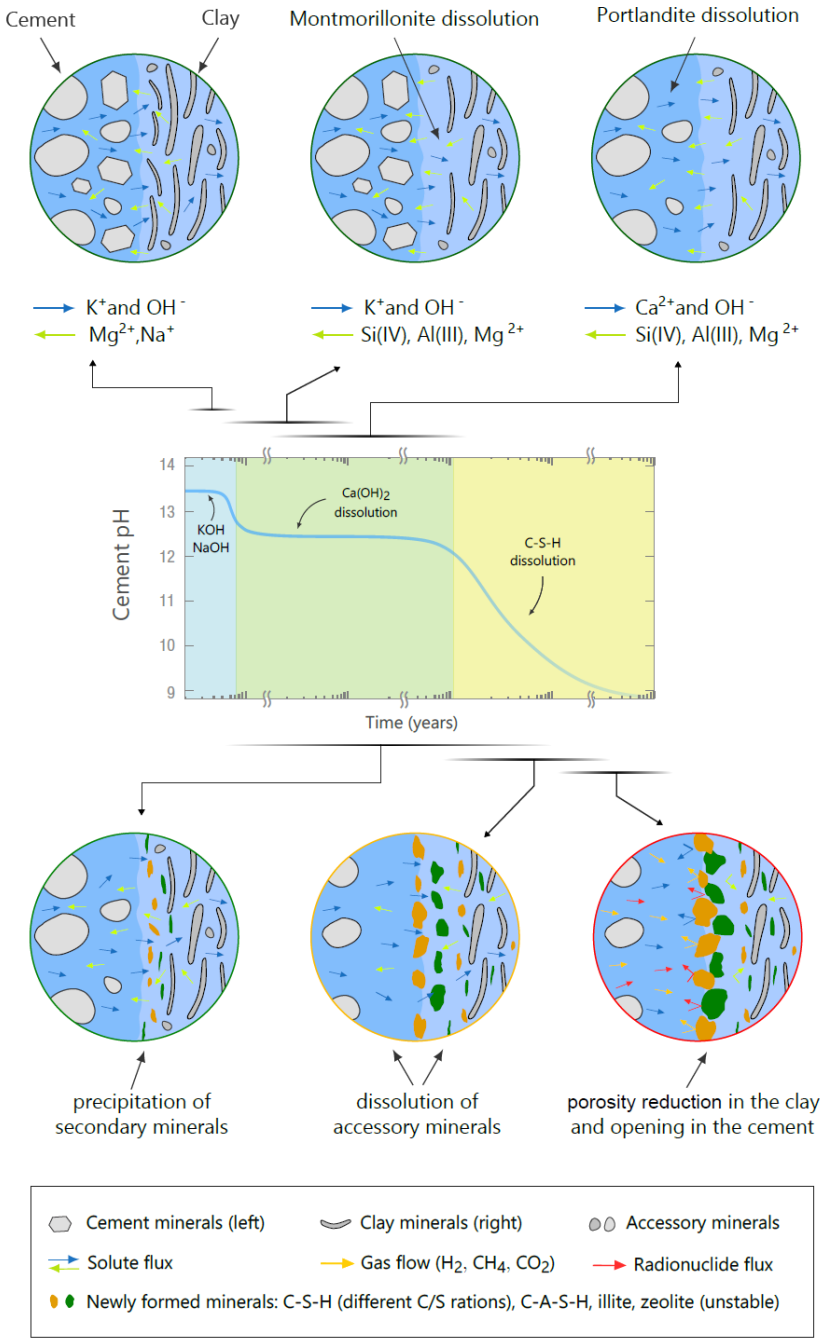

Fig. 2-1: Schematic of the major mechanisms and processes affecting the evolution of cement-bentonite interfaces, along with their subsequent effect on mass transport
The driving force is the geochemical contrast between cement and clay materials.
Shafizadeh (2019)

2.2 Microstructure properties of cementitious and clayey materials

Cementitious and clayey materials are hierarchical porous media with pore sizes ranging from few nanometers (interlayers of clay, cement gel pores) to few millimeters (macroscopic pores of cement) thus exhibiting a multiscale nature. The internal structure of these porous media is composed by a number of different minerals and phases resulting in complex geochemical fluid structure interactions. Moreover, most of the pore surfaces show permanent negative or positive charge with implications on the diffusive transport of ions. Both clay and concrete contain a variety of heterogeneities at different scales as depicted in Fig. 2-2 and Fig. 2-3.

Clay materials such as bentonites are mainly composed of smectites. Smectites form platy particles, sometimes clustered to aggregates, of radial size typically 0.001 to 1 µm (Fig. 2-2). The pore space between these particles is referred to as interparticle porosity. Each particle in turn is composed of 5 – 20 so called TOT layers (a sheet of octahedrally coordinated cations confined by two sheets of tetrahedrally coordinated cations) with, depending on density and/or chemical conditions, one to three or also more water layer spacing between them. The pore-space between the TOT layers is referred to as interlayer porosity. The TOT layers itself carries permanent negative charge and the interlayer pore space is occupied by hydrated cations which compensates for the negative structural charge of TOT layer. In addition to smectites, bentonites contain various accessory minerals such as quartz, calcite or gypsum. The microstructure of claystones such as Opalinus Clay is more complex (e.g., Nagra 2002) compared to that of bentonite, because it is composed of many different constituents, including fossils and various amounts of clay minerals, such as illite, kaolinite, chlorite or smectite. The content of the latter is much lower compared to bentonites. This gives rise to a very complex pore structure with heterogeneities at different scales.

In cementitious materials there are three main categories of pores: the gel pores associated with calcium silicate hydrates (C-S-H), the capillary pores and the macropores. At the smaller scales, the C-S-H has a layered structure with water filled interlayers and conceptualization of transport in these pores follows the concepts used for sheet silicates. The capillary and macro pores compose a well-connected network of pores which results in higher hydraulic conductivity and diffusivity values compared to clays. The respective pore-sizes with their characteristics along with the respective pore volume density are shown in Fig. 2-3 and Fig. 2-7.

The morphological heterogeneities of concrete can be conceptually divided into different material scales as shown in Fig. 2-3 (Patel et al. 2018): the macro-, meso-, micro-, sub-micro and nano-scales. At macro-scale concrete may be treated as continuum medium. The structure at the meso-scale is characterized by the aggregates, the interface transition zone (ITZ) and the cement paste. Both cement paste and ITZ may be treated as continuum, however the ITZ represents a more porous layer between aggregates and cement paste. The cement paste is composed by different hydrated phases such as calcium silicate hydrate (C-S-H), portlandite, AFm phases, etc. and unhydrated cement particles which are explicitly represented in the figure. The pore space between these hydrated phases is referred to as capillary porosity (> 1 µm). At this scale the C-S-H can be represented as a porous continuum phase. The sub-micron- and nano- scales further resolve the pore space within C-S-H gel. Sub-micron scale capillary pores (< 1 µm) consist of two types of C-S-H, represented as porous continuum, which are made up of the same C-S-H particles also known as elementary building block but differ in density. The low density C-S-H has lower density compared to high density C-S-H due to the presence of nitrogen accessible pores measureable during gas sorption experiments. The C-S-H particles themselves consist of sheets of tobermorite-like molecular structure with interlayer spacing between them which is resolved at nano-scale.

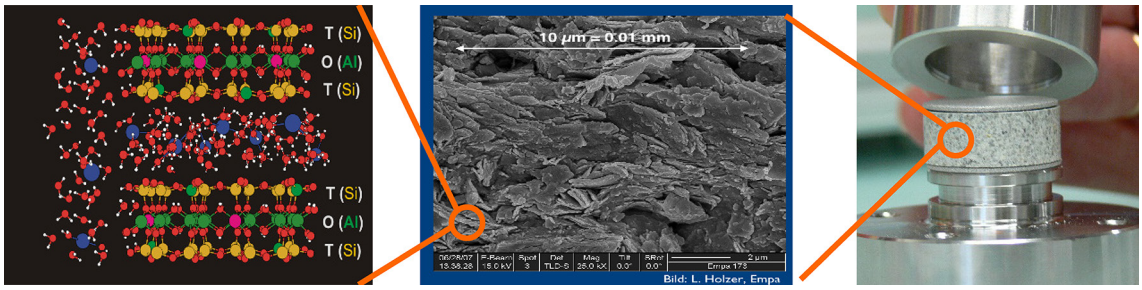

Fig. 2-2: Essential elements of clay structure at different scales. Left: atomistic representation of TOT-layers and interlayer porosity filled with water

Middle: SEM image of compacted Mt and a model based representation of Mt by particles with interlayer porosity and larger inter-particle pores. Right: compacted Mt used in a macroscopic diffusion experiment

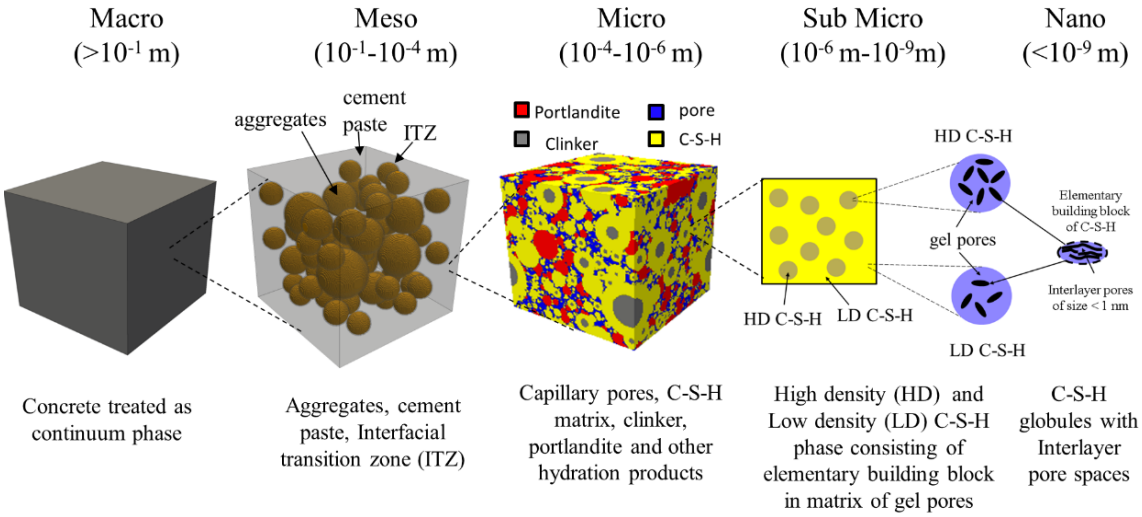

Fig. 2-3: Multiscale structural representation of cement

Pore-sizes cover a large number of spatial scales. Spatial and chemical heterogeneity is also shown. Reprinted from (Patel et al. 2018) with permission from Elsevier.

The distribution of pore sizes provides an insight into the internal structure of the material. The pore-size distribution can be to some extent measured with several techniques including, among others, mercury intrusion porosimetry, N_2 adsorption, nuclear magnetic resonance (NMR) or NMR-cryoporometry techniques. The different methods provide estimates for volume fractions of the corresponding pore sizes but cannot measure precisely an "absolute pore size distribution". The reason for that lies on the distinct procedure and fluid used for every technique. For Opalinus Clay (OPA), most of the pores excluding the interlayers pores are in the range ~ 3 – 30 nm, often with a peak at ~ 10 nm as shown in Fig. 2-4 (Wersin et al. 2013) for a sample from the Schlattingen borehole.

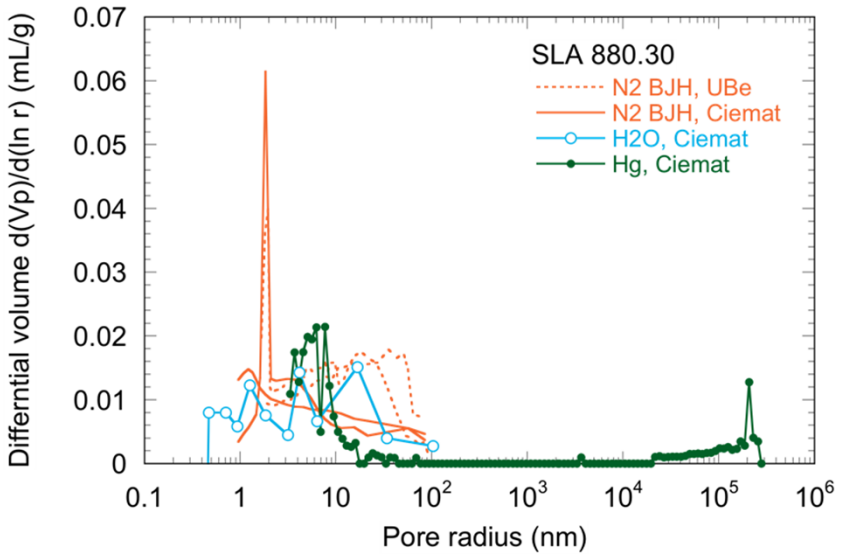

Fig. 2-4: Pore-size distributions (differential volume) for an Opalinus Clay sample from the Schlattingen Borehole

Three methodologies are used: the N_2 adsorption methodology, the H_2O isotherm and the Hg intrusion conducted at Uni Bern and Ciemat (from Wersin et al. 2013).

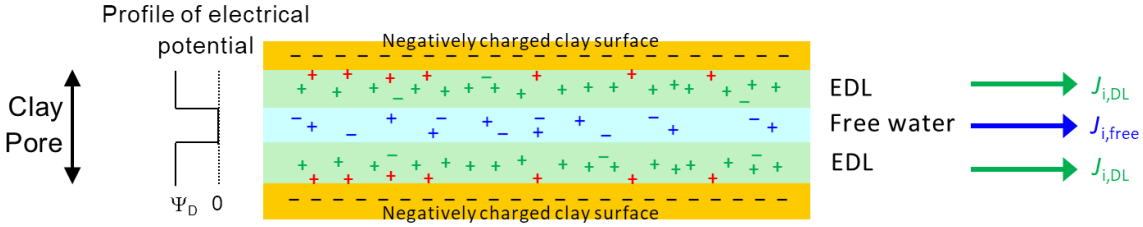

Fig. 2-5: Conceptual representation of the transport in clay nano-pores

The electrical double layer (EDL) is the place where cations neutralise the naturally occurring negative surface charge of the clay surface. Depending on the size of the pore, the EDLs might overlap or have a minimal effect on diffusive transport.

The hierarchical morphology of clays is characterized by the nano-scale interlayer porosity, the meso-scale porosity, and the pore space between grain boundaries. An electron microscope picture and the conceptualization of microscopic transport through the nano-pores of clays is shown in Fig. 2-5 and Fig. 2-6. Cationic and anionic species have different spatial distribution within the nano-pores. Depending on the model, the electrical double layer (EDL) can be described as a first layer (Stern layer) of cations which is attached to the clay surface, is immobile and partially neutralizes the naturally occurring negative surface charge of the clay surfaces. The second layer is also mostly composed by cations which however are mobile and are found in high concentration. This high concentration along the pore surface gives rise to an enhancement of the diffusive fluxes. Depending on the pore size, the EDLs may overlap (small nano-pores/ interlayers) or have very small contribution to the diffusive fluxes (larger pores). The relatively small size of the pores and the negative charge of the mineral surfaces that compose the clay, have a very strong influence on the transport of charged species. The neutral and positively charged chemical species, are in principle able to diffuse through entire pore space. Contrary, the negatively charged anions are repelled from the negatively charged mineral surfaces and cannot

enter the interlayer, narrow grain boundaries (interlayer equivalent pores). As a consequence, the anion accessible porosity due to anion exclusion, is smaller than the neutral and cation species accessible porosity of the clay (Plecis et al. 2005, Van Loon et al. 2007)

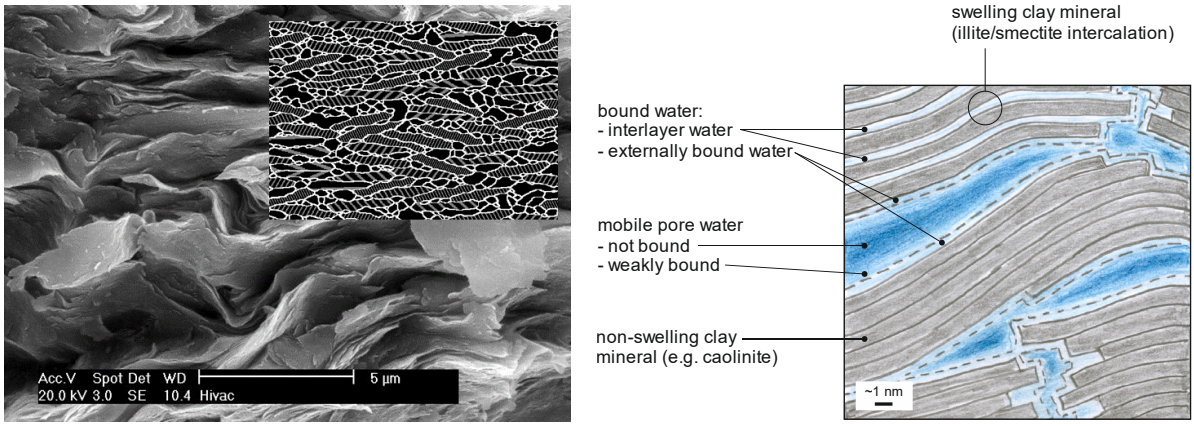

Fig. 2-6: Electron microscope image of a compacted clay and a 2D model for clay particle arrangement and interparticle and interlayer porosity distribution (left), schematic representations of clay rock texture, illustrating the various water properties and the heterogeneity of the different types of clay minerals at the nm scale (right)

Left: modified after Gimmi & Churakov (2019), right: Nagra (2002a)

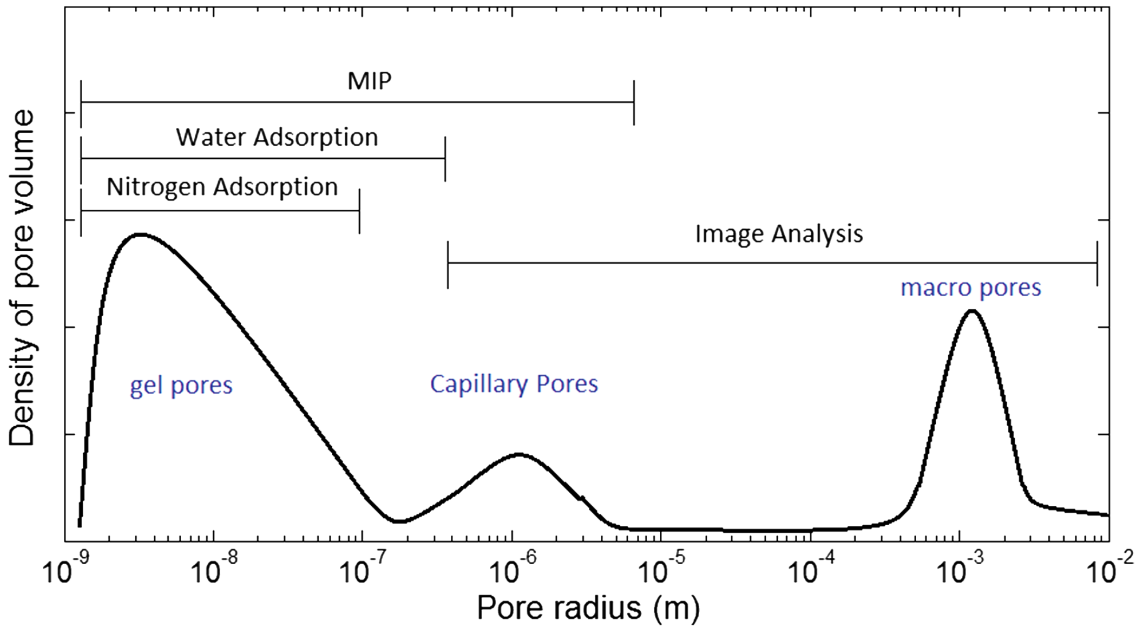

Fig. 2-7: Typical pore size volume density of cementitious materials along with the techniques which may be used for the respective measurements

The cement pores, where mass transport mainly occurs, may be classified in three categories: gel pores, capillary pores and macro pores.

Gong et al. (2013)

The transport properties within a porous medium depend not only on the distribution of the pore-sizes but also on their respective connectivity and topology as well as on the degree of saturation. In a fully saturated medium, mass transport in the liquid phase occurs via the continuous connected porosity (percolated phase). As the degree of saturation reduces, the connectivity of the pore network changes and the pores start to get disconnected. In partially saturated media, mass transport may occur both through the connected liquid or gas phases. The transport properties of a porous medium may also change because of the geochemical evolution of the medium. In subsurface disposal systems, several materials are brought together, as for example the cement in contact with clay. The alteration of the locally pre-existing geochemical conditions and the geochemical contrast between the different materials is the driving force of the geochemical evolution of these materials. Dissolution and precipitation processes may increase or reduce the porosity of the materials in a non-linear way.

2.3 State of the art on cement/clay interaction

2.3.1 Overview/general description

This section summarizes the information from most recent reviews and studies on cement/clay interaction in the framework of radioactive waste disposal (Bildstein et al. 2019, Gaucher & Blanc 2006, Savage et al. 2020, Seigneur et al. 2019, Wilson et al. 2021).

As detailed in Chapter 1 the cement- and clay-based materials are important components of the barrier system in deep geological disposal of radioactive waste. Cements and concrete are commonly used for waste immobilization (at waste package level), for disposal container, tunnel support, tunnel/cavern backfill and for sealing tunnels (Glasser 2013). Clay-based materials are mainly present as tunnel backfill and as tunnel sealing material. In addition, several countries plan to place deep geological repositories in clay rock formation, for example Switzerland, France or Belgium (Gautschi 2015).

Interfaces between both materials can be characterized by strong (geo-)chemical differences which drive the diffusive transport of solutes into both materials and induce formation of alteration fronts. Typically, dissolution of cement and clay phases are observed in combination with precipitation of secondary mineral phases at or near the material interface. Alteration distances depend on the transport regime (diffusion vs. advection) and the magnitude of solute flux, the inventory of materials that are participating in reactions, as well as changes of porosity affecting pores across all scales and transport properties of altered materials. In addition, the alteration fronts might be spatially smeared due to reaction kinetics. Some experimental studies and nearly all reactive transport calculations of cement/clay interactions show significant porosity changes due to precipitation/dissolution of minerals near the interface. Most of the modelling studies investigate the geochemical evolution of interfaces in low permeability media where diffusive transport dominates. They calculate a strong bulk porosity reduction in narrow zones. The reduction of the free connected pore space leads to a reduction of advective and diffusive mass fluxes across the interface slowing down the geochemical alteration processes. It is noted that under specific conditions complex transitions between re-equilibration and re-precipitation periods may exist resulting in an even stronger delay of further major geochemical alterations

Experimental validation of these processes in field experiments, under realistic transport conditions and with real materials is difficult. Advective and diffusive fluxes in clay media are very low and significant alterations of pore space due to cement/clay interactions are expected to occur only after relatively long times, possibly tens or hundreds of years. Some evidence for pore blocking (Wilson et al. 2021) from long-term observations on concrete/clay interfaces at the Tournemire industrial analogue (Gaboreau et al. 2011, Lalan et al. 2016, Soler 2013, Tinseau et al. 2006), from the Maqarin natural analogue (Martin et al. 2016, Pitty & Alexander 2014), the Mont Terri cement interaction (CI) experiment (Jenni et al. 2014, Mäder et al. 2017, Yokoyama et al. 2021) and the Grimsel FEBEX experiment (Gaboreau et al. 2020) exists (see Sections 3.1 and 3.2).

More recent laboratory studies conducted at Univ. Madrid (González-Santamaría et al. 2020a, 2020b) and at PSI (Luraschi et al. 2020, Shafizadeh et al. 2015) on small samples with cement and clay materials in contact show significant changes in water content and total porosity near the material interface, as well as a reduction of diffusive flux of tracers across the interface (see Sections 3.1 and 3.3).

In civil engineering, bored or screw piles made from reinforce concrete are commonly used for building foundations. They transfer the load of structures to soil or rock. For a bored pile a borehole is drilled in the soil and a reinforced concrete pile is poured in situ. Screw piles are directly driven or screwed into soil. For a pile in clay, the major contribution to working load capacity is from the shaft resistance, which might be affected by cement-clay interaction (Lee 2001). Most studies on pile/clay interaction deal with mechanical properties of the interface only. Lee (2001) investigated experimentally the interaction between concrete piles embedded in Oxford Clay, a silicate-mudstone. He found that pH in the mudstone was increased up to a distance of 25 mm from the pile interface after several month of interaction. For the porous sand-bentonite mixture, calcium concentrations in Oxford Clay are increased up to a distance of (less than) 80 mm. He could also observe a pronounced change of mechanical properties up to a distance of about 25 mm from the interface. He writes, that by dissolution of clay minerals at high pH aluminium and silica was released and pozzolanic reaction takes place whereby cementitious products such as calcium alumina hydrate and calcium silicate hydrate are formed. This could cause a 25 mm thick zone enriched with cementitious products that stabilized the clay.

Experimental studies on cement/clay interaction provide insight into mineral reactions, progress of reaction fronts and evolution of material parameters. Although long-term experiments like the Mont Terri CI-experiment run for more than one decade the time scale covered is much shorter than the time scale of interest for assessment of materials in a deep geological repository. For prediction of the spatial-temporal effects of cement/clay interaction after hundred thousands of years or more, computer models, calibrated with experimental evidence from long-term experiments and information from natural analogues, are commonly used.

When comparing early studies and reviews with the most recent ones, it is obvious, that different continuum scale reactive transport modelling studies give a consistent picture of evolution of cement/clay interfaces. Bildstein et al. (2019) specifically note that in the last 2 decades improvements in numerical codes and the accumulation of data acquired to feed thermodynamic and kinetic databases improved strongly the trust in reactive transport calculations. *"Overall, these simulations provide a better understanding of physical and chemical change and how materials interact: they give more confidence in the prediction of the durability of materials by converging on the alteration extent that can be expected at the interfaces between different materials over long periods of time…this is not to say that we fully understand all the physical and chemical phenomena or that modelling is fully representative of all the processes occurring in such complex systems."*

2.3.2 State-of-the-art knowledge on cement/clay interaction

Information on modelling studies for cement/clay interaction can be extracted from review papers on cement/clay interactions or similar topics (Bildstein et al. 2019, Gaucher & Blanc 2006, Kosakowski et al. 2014, MacQuarrie & Mayer 2005, Metcalfe & Walker 2004, Saripalli et al. 2001, Savage & Cloet 2018, Seigneur et al. 2019, Wilson et al. 2021), and from recent scientific publications (González-Santamaría et al. 2020a, 2020b, Idiart et al. 2020, Jenni & Mäder 2021, Marty et al. 2015a, Savage et al. 2020).

Savage & Cloet (2018) reviewed systematically modelling studies on evolution of cement/clay interaction with the aim to extract consequences for the safety requirements for the bentonite buffer and the Opalinus Clay. Wilson et al. (2021) reviewed experimental, analogue and modelling data for on the impact of cement on argillaceous rocks in radioactive waste.

Both studies agree largely in their findings, details on processes that govern evolution of cement and clay materials with the most important ones listed below:

- There is a reasonable good understanding of mineral changes that are observed and modelled at a contact between cement and clay materials.
- Migration of hydroxyl ions and associated increase of pore water pH in clays is the main driving mechanism for mineral alterations.
- High dissolution rates for primary minerals accelerate mineralogical transformations and porosity change, and limit the extent of alteration fronts due to reduction of mass transport. *Kinetic data appropriate for use in compacted clay systems and under near-equilibrium conditions remain uncertain* (Savage & Cloet 2018).
- The porosity is expected to be reduced at the cement/clay interface by precipitation, specifically at the clay side of the interface. It is not clear, if it is possible to completely reduce the porosity at the interface.
- Martin et al. (2016) investigated a sample from the Maqarin analogue and found that the alteration rim around a seemingly totally clogged vein still had a remaining porosity of about 19% according to MIP measurements with pores < 100 nm. Newer modelling and experimental studies indicate that anion and cation transport are differently affected by porosity change, an effect strongly correlated with the respective pore-sizes (Fukatsu et al. 2017, Jenni et al. 2017, Jenni & Mäder 2021). Typically, anion transport across interacting cement/clay interfaces is significantly more strongly reduced than cation transport. The effect is related to a "bottleneck effect" where diffusion of ions is limited by anion exclusion (Chagneau et al. 2015, Wigger et al. 2018). A diffusion pathway for cations might be blocked for anions by overlapping of electric double layers, which occurs typically in small pores or clay interlayers. Mineral precipitation is less probable in such small pores. Meldrum and O'Shaughnessy (Meldrum & O'Shaughnessy 2020) list several arguments for the inhibition of nucleation in smaller pores, which includes: 1) The limited availability of reactants/ions which are needed to form nucleation clusters of critical sizes in smaller pores. 2) Interaction of reactants/ions with charged/uncharged pore walls is more probable in small pores, which might influence crystallization. 3) Crystals with larger surface to volume ratio might have a higher solubility, which is called pore-size controlled solubility. This might favour crystal growth in larger pores. 4) The growth of crystals by accumulation of nano-crystals might be retarded in nano-pores.

- Based on mass balance considerations and numerical modelling it is expected that the zone of perturbed mineral and fluid chemistry in clays will be narrow. Significant changes in clay mineralogy that affect transport properties are expected, in the range of cm up to ten cm thick in 100'000 or more years (Savage & Cloet 2018, Wilson et al. 2021).

  The extent of the zone of perturbed mineral and fluid chemistry will be controlled mainly by mass transport across the cement/clay interface and the amount of cement material in contact with the clay. Inclusion of total porosity change feedback on mass transport in reactive transport models not only reduces the progress of alteration fronts, but also changes mineral evolution.

Benchmarking studies related to cement/clay interaction were conducted by Marty et al. (2015a) and Idiart et al. (2020). In general, the results obtained with different numerical codes agree well with each other. This shows that differences in predictions by numerical simulations are caused mainly by the modelling assumptions in terms of primary and secondary mineral phase selection, kinetic constraints and which type of coupling between transport and chemical processes is assumed. A benchmarking study specifically on the coupling between chemical and transport processes with respect to total porosity, tortuosity and permeability evolution was conducted by Xie et al. (2015). They conclude that, *"generally, good agreement is reached amongst the computer models despite significant differences in model formulations. Some differences are observed, in particular for the more complex scenarios involving clogging; however, these differences do not affect the interpretation of system behaviour and evolution".*

In a Philipine natural analogue study (e.g., Alexander et al. 2008, Reijonen & Alexander 2015) and the Cyprus natural analogue study (e.g., Alexander et al. 2013), the stability of bentonites under influence of alkaline natural groundwaters with the same pH- range as low-pH cements have been investigated. Both studies suggested that little reaction of the bentonite has occurred over millions of years. The authors concluded with respect to these analogue studies that:

- *the field conditions of this analogues are considered to realistically simulate those expected in a geological disposal facility*
- *the results indicate minimal mineralogical alteration of bentonite by alkaline groundwater over periods of 10^5 to 10^6 years with only very minor alteration and replacement of smectite by palygorskite along micro-fractures*
- *the main effect of the interaction of bentonite and alkaline groundwater is a replacement of exchangeable Na in the bentonite by Ca, which can impact the swelling behaviour and plasticity of the bentonite, and*
- *that the studies suggests that it will be feasible to use bentonite clay barriers together with low- alkali cement and concrete in a deep geological repository (DGR), without deleterious effects on the bentonite barrier due to reaction with leachates derived from the cementitious materials*

2.3.3 Uncertainties and limited processes understanding

Wilson et al. (2021) list in their review *the most important areas of uncertainty in terms of understanding the spatial and temporal evolution of cement-mudrock*. With regard to the topics discussed in this report these are the following:

- the effect of temperature
- the rate of precipitation/dissolution reactions in alkali-perturbed zone of the clay (rock)
- the nature and extent of pore-clogging at cement-argillite interfaces over relevant timescales

- change of radionuclide, gas and liquid transport across the cement/clay interface
- and the detailed effects of the alkali-perturbed zone on radionuclide/contaminant sorption

In addition, the effect of liquid saturation on evolution of cement/clay interfaces is largely unknown. Studies on the influence of water saturation on cement/clay interface processes are sparse. Bildstein et al. (2019) note that *"Another aspect of unsaturated porous media that is not yet widely treated in RTM relates to the dependence of chemical reactivity with regard to the water content, in particular looking at how the mineral and gas solubility and the aqueous speciation relate to capillary pressure at low water saturation."*

Wilson et al. (2021) remark that in most modelling studies of cementitious barriers, the effects of temperature variation are not considered. Many models assume standard conditions, usually a temperature of 25 °C and a pressure of 1 bar (100 kPa) which are the default conditions for most common thermodynamic databases. In general, kinetic control of dissolution and precipitation show a strong temperature dependence (Marty et al. 2015b). For Portland cement-based materials when temperatures rise above about 50 °C the stable phase assembly changes, i.e. ettringite is transformed into monocarbonate and monosulphate (Lothenbach et al. 2008b). Many zeolite and clay minerals are metastable with respect to similar minerals at higher temperatures (Wilson et al. 2021). One might note, that solubility data for most clay minerals at low temperatures are ambiguous (Jenni et al. 2019).

In accordance with Bildstein et al. (2019) and Savage & Cloet (2018) identified that the role of charged (clay) mineral surfaces, their effect on pore space partitioning and transport in different pore space compartments need to be included in future reactive transport modelling studies. *All modelling studies except one or two exceptions* (Berner et al. 2013, Jenni et al. 2017, Jenni & Mäder 2021) *have assumed that the total porosity in clay and bentonite is available for geochemical interactions. The nature of porosity in clays is the subject of much current debate so that alternative models should be considered in future to scope all possible outcomes of the cement-clay interaction process.*

The publication of Marty et al. (Marty et al. 2015b) includes an extended discussion on the sources of uncertainties for kinetic rate laws and parameters. Also in Section 3.2 of Jenni et al. (2019) uncertainties related to thermodynamic and kinetic modelling of bentonite and clay minerals in general (also under high pH conditions) are discussed extensively. Marty et al. (2015b) clearly state the following: *"Moreover, laboratory experimental rates and those measured in situ vary by up to several orders of magnitudes (Lüttge et al. 2013, Marty et al. 2009, Velbel 1990, White & Brantley 2003, Zhu 2005). Significant differences are also observed in similar experiments dealing with the same material. For Lüttge et al. (2013), these discrepancies cannot be attributed to experimental artifacts (analytical uncertainties, data acquisition methods, etc.). Authors identify extrinsic and intrinsic sources of rate variations (depending on the observation scale). Extrinsic sources come from heterogeneities (porosity, mineralogical and chemical compositions, etc.) inside the media that should be represented. From this point of view, their consideration is the responsibility of the modeler. Intrinsic sources of rate variations are also attributed to heterogeneities at the crystal scale (crystal-defect distributions, impurities, etc.). Only kinetic Monte-Carlo models are able to show a large variation in total rate over time (Lüttge et al. 2013). However, this method is limited at the crystal scale. Therefore, the use of TST[1] kinetic models appears to be currently unavoidable for large-scale simulation, even if the use of a mean or rate-limiting value describing the reaction rate appears to be questionable."* In addition, e.g. disconnected pores or partial water saturation might compartment the pore space and slow down or interrupt microscopic transport of solutes. In such a compartmented pores the water

[1] According to IUPAC (IUPAC, 2019) the Transition State Theory (TST) describes rates *of elementary reactions by assuming a special type of equilibrium, having an equilibrium constant, to exist between reactants and activated complexes.*

composition might vary considerably. All these conditions make it very difficult to assign a single effective surface area for reaction kinetics. In addition, the pore space geometry, the mineral grain size and surface roughness of mineral grains might change significantly during dissolution (and precipitation of other reaction products). Frequently, this effect is lumped into a "chemical reactivity" function which links liquid water saturation with a reduction of kinetic rates (Huang et al. 2021, Thouvenot et al. 2013).

The kinetics of the transformation from montmorillonite to illite was investigated by Savage et al. (2020) for a marine sediment profile penetrated by the Ocean Drilling Program (ODP) offshore Japan. They found that full thermodynamic and kinetic modelling of this process might give significantly higher rates for illitization than observed. They concluded that *models involving full kinetic and thermodynamic treatment of mineral dissolution-precipitation reactions must be carefully applied to simulate other transformation reactions of montmorillonite relevant to the geological disposal of HLW, such as those arising from the interaction of montmorillonite with iron/steel, cement and/or groundwater.*

2.4 Mechanisms/processes related to cement/clay interaction

Cement and clay materials are essential parts of the barrier system. Due to the existence of strong geochemical contrasts, which imply large solute concentration gradients across cement/clay interfaces, the transport of solutes drives the geochemical alteration of the original materials. Depending on solute composition and transport regime, the induced effects can be complex and induce changes in the materials involved.

Generally, in cement materials, the following changes are observed:

- Calcium and OH^- leaching (by diffusion or advection) cause sequential dissolution of cement phases according to degradation model by Berner (1992), Wieland & Kosakowski (2020).
- Ingress (by diffusion or advection) of dissolved CO_2 from clay can cause cement carbonation, i.e. the transformation of hydrated cement phases to carbonate.
- Silica and Alkali ions from dissolution of reactive alumina-silicate aggregates at elevated pH in cements can promote formation of C-S-H in cements. For the pozzolanic reaction, calcium from dissolution of portlandite and C-S-H is used to form C-S-H with low(er) C/S ration until equilibria with dissolved silica is achieved. As reaction products have typically a higher volume than the dissolved cement phases, the capillary porosity is decreasing. Additionally influx of silica from clay might promote C-S-H formation near the cement/clay interface.
- Ingress of sulphate might cause formation of ettringite, gypsum or thaumasite. Typically, the local capillary porosity is decreased and macroscopic cracking of concrete is observed, if ettringite is precipitated in confined spaces (Whittaker & Black 2015).
- The ingress of chloride in high concentrations might enhance corrosion of steel embedded in concrete.
- The ingress of magnesium sulphate or magnesium chloride are specific forms of sulphate or chloride attack. The magnesium can exchange with calcium in the hydrated cement paste and causes enhanced degradation of cement material. Calcium bearing phases are dissolved and replaced by M-S-H, brucite or other magnesium bearing phases.

In the clay materials the following changes are observed:

- Ingression of OH^- causes an increase of pH, which affects the stability of the mineral assembly in clay materials. Dissolution of clay minerals is controlled by (slow) dissolution kinetics. Increase of pH in clays also changes sorption of radionuclides. Progress of pH front is retarded by pH buffering through mineral reactions and (only small capacity) amphoteric clay edge sites.
- Ingress of calcium from the cement may first lead to some calcium carbonate precipitation, but later in combination with silica due to dissolution of silicates and clay minerals at elevated pH it might cause precipitation for C-S-H. Porosity near the cement/clay interface is decreased and mass fluxes are reduced.
- Transport (by diffusion or advection) of alkalis from cement into clay materials will change cation exchanger population, which in turn affects swelling (for swelling clays) and also affects sorption by cation exchange for radionuclides.

2.4.1 Cement degradation

Previous models of cement degradation have focussed on the temporal evolution of the cement matrix and pore water composition by leaching due to groundwater ingress from the host rock or rain and soil-type water (Atkinson et al. 1985, Berner 1992, Hoch et al. 2012, Jacques et al. 2010, Kosakowski et al. 2014, Neall, 1994). Note that the chemical composition of the infiltrating waters is very different form the composition of cement-type pore waters. The cement degradation models have been considered in earlier safety assessments performed by Nagra (Nagra 2002a, 1994) and more recently, in modelling studies on the geochemical evolution of the L/ILW near field (Kosakowski et al. 2014) and the interface between clay rock and cementitious materials (Kosakowski & Berner 2013). In SGT-E2 the chemical degradation of cement was modelled in terms of groundwater ingress from the host rock (Kosakowski & Berner 2013, Kosakowski & Smith 2014). In this approach, diffusion-controlled transport of pore water constituents from the cementitious near field into the host rock is the driving force for the temporal evolution of the composition of the pore water in the cementitious near field. In accordance with thermodynamic equilibrium, the latter process reproduces the sequential dissolution of cement phases from the hydrate assemblage of hydrated cement paste, thus giving rise to sequential changes in the solid phase composition with time.

The three main stages with progressively lower pH of the pore water with the course of time compose the main features of the diffusion-controlled models of cement degradation (see Fig. 2-8). In a simplified manner, these stages of cement degradation can be described as follows:

Stage I: The first stage accounts for fresh hydrated cement with pH of the pore water between 12.5 and 13.5 at 25 °C. The solution composition is dominated by high concentrations of free alkali metal ions, which are released from the clinker minerals during cement hydration. Equivalent OH^- concentrations are generated to fulfil charge balance.

Stage II: The pH of the pore water is controlled by portlandite solubility. The large inventory of the mobile alkalis has significantly been reduced due to uptake by alkali-binding minerals or exchange with the solutes of the pore water of the surrounding host rock. Solubility of portlandite fixes the total Ca concentration $[Ca]_{tot}$ at $\sim 2 \cdot 10^{-2}$ M and the pH at ~ 12.5. This stage is characterized by the presence of portlandite and C-S-H phases with a high Ca/Si ratio in hydrated cement.

Stage III: This stage follows once portlandite is dissolved due to uptake of Ca by secondary precipitates (e.g. $CaCO_3$ in the case of CO_2 formation) or exchange of Ca with the solutes of the pore water of the surrounding host rock. The pH drops continuously to lower values. The pH

ranges between 10 and 12.5 and is controlled mainly by incongruent dissolution of C-S-H phases. The Ca/Si (C/S) ratios of C-S-H phases changes from initially ~ 1.65 at pH ~ 12.5 to ~ 0.8 at pH ~ 10 as a consequence of the incongruent dissolution of C-S-H phases (Atkins & Glasser 1992, Tits et al. 2014). Congruent dissolution of the C-S-H phases occurs at the end of stage III, buffering the pH at ~ 10 (Ochs et al. 2016).

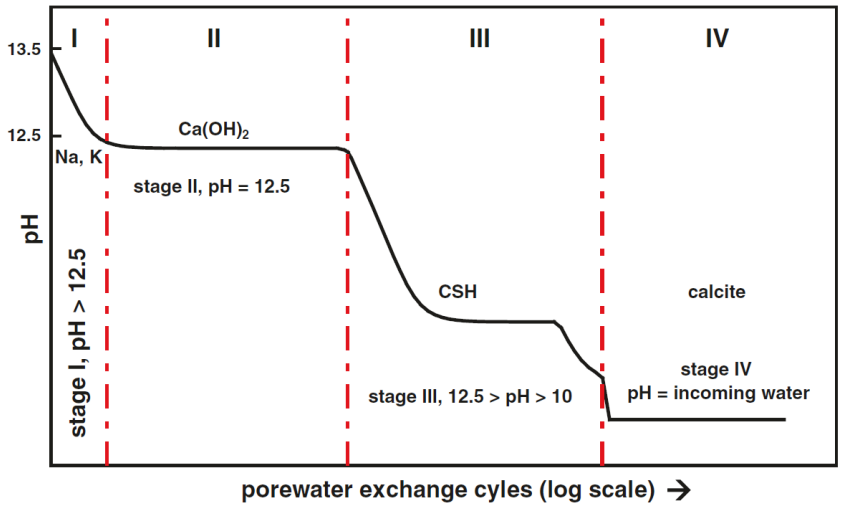

Fig. 2-8: Schematic presentation of the degradation stages of cement as function of the pore water exchange cycles by groundwater ingress

Reprinted from Ochs et al. (2016) with permission from Springer Nature.

Stage IV: The final stage of cement degradation is reached, once all Ca bearing cement phases (portlandite, C-S-H, AFt, AFm) are dissolved. The pH is controlled by incoming water and by equilibrium with carbonates (calcite) (Ochs et al. 2016). This final stage can only be reached if the cement is carbonated with considerable amounts of CO_2, or if Ca is leached by high fluxes of incoming formation water. The latter can be excluded as possible degradation mechanism for a repository placed in a low permeability clay formation (Kosakowski et al. 2014).

Hence, the first three stages are characterised by specific compositions of the phase assemblage of hydrated cement and the corresponding pore water in equilibrium with the solid. The latter information, essentially the changes in the pore water and solid phase compositions in the first three stages, has been used as input to the development of previous cement sorption data bases (Bradbury & Van Loon 1996, Wieland 2014, Wieland & Van Loon 2003).

In a deep geological repository, concrete degradation will not be homogeneous in space and in time. Several degradation mechanisms will act concurrently on different time scales. In addition, other processes e.g. water saturation in specific concrete materials and parts of the repository might delay locally chemical processes in general, and the concrete degradation specifically.

Externally driven processes are the ingress of formation water and the diffusion-driven equilibration of formation and concrete pore water.

- As formation water inflow is very small, complete concrete degradation is limited to very small zones at places with elevated water flux (Kosakowski & Smith 2014). In addition, degradation is limited, as a high number of pore water exchange cycles is needed (corresponds to high inflow of formation water) to reach stages III or IV.

- The diffusion-driven equilibration of pore water composition at the contact of Opalinus Clay host rock and concrete exhibits the first three concrete degradation stages as outlined in Kosakowski et al. (2014). Stage IV relevant to the complete dissolution of C-S-H, was not observed in those calculations. The progress of reaction/degradation fronts slows down with time, which is typical for a diffusion-controlled process. Under fully water saturated conditions stage I will only exist for a relatively short time period, as high alkali concentrations are reduced due to diffusive equilibration with host rock pore water. Portlandite could be dissolved up to 2 meter distance from clay/concrete interface after 100'000 years (Kosakowski et al. 2014), such that stage III will be reached only "behind" the portlandite dissolution front. Eventually, porosity reduction at clay/concrete interface might reduce the progress of reaction fronts considerably. Most importantly, in a partially liquid saturated repository near field diffusive fluxes are reduced by orders of magnitude, which will delay the progress of the reaction fronts and the evolution of the materials also by orders of magnitude.

2.4.2 Carbonation

Carbonation of cementitious materials is a chemical process where dissolved carbon dioxide (CO_2) is reacting with calcium from hydrated cement phases to form calcium carbonates and other minerals. One should note that these reactions release the water structurally bound in cement hydrates. After complete carbonation, i.e. after hydrated cement phases are completely consumed, the originally high pH of the cement pore water drops to neutral values and the cement is in degradation stage IV (Fig. 2-8). The reactions are quite fast and carbonation progress depends mainly on the transport of carbon species towards unreacted cement phases. Carbonation is commonly observed in cement materials that are in contact with atmosphere under humid conditions. Progress of carbonation fronts is known to depend on gas diffusion and relative humidity (Ashraf 2016, Leemann & Moro 2017, Russell et al. 2001, Steiner et al. 2020, Winter 2009) and is fastest for relative humidity between 60 – 80%. Under such conditions, the concrete is de-saturated to such a degree that relatively fast diffusion of atmospheric CO_2 is possible and still enough water in contact with the cement phases exist to allow dissolution of reactants. Atmospheric carbonation of Ordinary Portland cement (paste) decreases the capillary porosity and transport parameters, while carbonated blended cements show increase in transport parameters. Dutzer et al. (2019) could show that this observations are related to the competition between porosity reduction and (micro-) cracking induced by carbonation.

Experimental investigations show that carbonation fronts are not sharp (Parrott & Killoh 1989, Thiery et al. 2007) which is in part attributed to the influence of chemical reaction kinetics (Morandeau et al. 2014, Thiery et al. 2007). The role of the ratio between the characteristic time of carbonation reaction to a characteristic diffusion time was discussed for example by Muntean et al. (2011). In general, if the characteristic time for reaction is much smaller than the time for diffusion of CO_2 then the zone of reaction is small as compared to the progress of the reaction front.

In the context of radioactive waste disposal atmospheric carbonation of cement-based materials during operation of a repository was investigated by Trotignon et al. (2011, 2009). They predicted a minimal carbonation of materials. Savage & Cloet (2018) state that in systems involving natural clay formations, the high partial pressure of carbon dioxide (P_{CO2}) plays a key role in the alteration process, and leads to an abbreviated zone of alteration of aluminosilicate minerals due to the rapid reduction of porosity at the cement-clay interface, as a result of Ca^{2+} and OH^- ions leached from the cement/concrete, reacting with CO_2(aq) diffusing from the clay formation to form solid calcium carbonate (calcite/aragonite). These conclusions are somewhat contradicted by the results of the Mont Terri CI project, where precipitation of carbonate was observed, but not to a degree that the overall porosity was significantly affected (Jenni et al. 2014, Mäder et al. 2017,

Yokoyama et al. 2021). In their modelling study for the CI experiment Jenni et al. (2017) could reproduce the absence of a carbonation layer on the cement side. Kosakowski (2018) could show with his modelling study of the CI experiment that carbonate formation is parallel to the movement of a high pH front in the clay. In that case, dissolved calcium fluxes towards clay exceeded dissolved carbon fluxes towards cement.

Furthermore, Nakarei et al. (2021a, 2021b) used dedicated experimental setup to enforce porosity clogging at cement/bentonite interfaces by adding sodium carbonate to the bentonite. They were only able to enforce capillary porosity clogging by adding sodium carbonate in very high amounts (pore water concentration close to solubility limit), which created quickly a few micro-meter thick carbonate layer between cement and bentonite. If sodium carbonate admixture were below a certain threshold, formation of a carbonate layer at early times resulted in an incomplete carbonate layer and solute fluxes across the interface were reduced. On the long-term, no further reduction of the overall porosity at the interface due to carbonate precipitation was observed.

2.4.3 Reaction of cement phases with silica

The reaction of cement phases with silica is one of the most common reactions in hardened concrete. For the reaction of cement hydrates with silica two kind of reactions may co-exist, the so-called Alkali-Silica Reaction (ASR) and the pozzolanic reaction. While in the pozzolanic reaction calcium hydroxide reacts with silicic acid and forms C-S-H, for ASR alkali hydroxides (NaOH/KOH) at high pH form an ASR product that is composed of silica and alkali hydroxide plus some calcium. The ASR is often accompanied by a degradation of the matrix and thus a failure of the infrastructure, while the pozzolanic reaction is often promoted as it enhances the strength of concrete.

The pozzolanic reaction is the chemical reaction that occurs in Portland cement upon the addition of pozzolans. A pozzolan is defined according to ACI Committee 116 (Farzam 2000) as "a siliceous or siliceous and aluminous material that in itself possesses little or no cementitious value but that will, in finely divided form and in the presence of moisture, chemically react with calcium hydroxide (a hydration product of portland cement) at ordinary temperatures to form compounds having cementitious properties". A very broad overview on "pozzolana and pozzolanic cements" is given by Massazza (1998) in Chapter 10 of "Lea's Chemistry of Cement and Concrete" (Hewlett 1998).

In chemical terms, the pozzolanic reaction occurs between portlandite ($Ca(OH)_2$), and silicic acid (H_4SiO_4) and produces calcium-silicate-hydrate C-S-H:

$$Ca(OH)_2 + H_4SiO_4 \rightarrow CaH_2SiO_4 \cdot 2\ H_2O$$

According to Thomas (Thomas 2013) *"typically, the C/S ratio … of the C-S-H that forms from this reaction will be lower than the C/S ratio measured for C-S-H in hydrated portland cement without pozzolan, and the difference will vary depending on the age, type, and amount of pozzolan*".

A potential internal source of silica is the kinetically controlled dissolution of silica bearing aggregates. For the service lifetime of common engineered concrete structures aggregate-cement reaction can be minimized by choice of aggregates and is normally not an issue. For the very long service lifetime of concrete in deep geological repositories, reactions of cement phases with silica released by very slowly reacting alumina-silicate minerals might be relevant (Glasser 2013). In case of cement/clay interaction, dissolved silica originates from the dissolution of clay, silicate and other alumina-silicate minerals at elevated pH (see Fig. 2-9).

2.4.4 Ingress of sulphate

The ingress of sulphate might give rise to the formation of ettringite. If ettringite precipitates in confined space and becomes damaging, this is called (external) sulphate attack. Typical sulphate concentration in Opalinus Clay are around 2.5×10^{-2} mol kg^{-1} H_2O (Savage & Cloet 2018). Concentrations can be increased for case of pyrite oxidation. Ingress of sulphate into cement materials causes formation of ettringite $Ca_6Al_2[(OH)_{12}(SO_4)_3]\cdot 26\,H_2O$ and, in later stages, gypsum. Specifically the monosulphate phase is converted into ettringite. The additional needed calcium is provided by portlandite and C-S-H dissolution. The formation of ettringite by itself is a positive effect, as this is an important phase for radionuclide sorption in cements (Wieland & Van Loon 2003). In the framework of cement/clay interaction, formation of ettringite was observed for a contact of OPC with Opalinus Clay. For the contact of ESDRED, a low pH cement, with Opalinus Clay the Ca-Al-sulphates (monosulphate, ettringite) become unstable at pH lower than 12 (Mäder et al.2017).

Both, ettringite and gypsum are minerals that contain high amounts of water. Therefore their formation is highly expansive and might cause mechanical damage (crack formation) of cement materials (Winter 2009). In sulphate resistant cements, the amount of tricalcium aluminate is reduced which limits the amount of AFm (e.g. monosulphate) and AFt (e.g. ettringite) phases and avoids mechanical damage, without losing too much sorption capacity. For the case of cement/ clay interfaces, use of sulphate resistant cements does not necessarily prevent formation of calcium-aluminium-sulphates, as additional aluminium might be provided by dissolution of silicium-aluminium minerals due to elevated pH on the clay side.

The thaumasite $[Ca_3Si(OH)_6\cdot 12H_2O]\,(SO_4)(CO_3)$ form of sulphate attack (TSA) is a process which occurs only in the later or last stages of the sulphate attack. After the initial sulphate-induced deterioration, which leads to the precipitation of ettringite and partly gypsum, sulphate concentrations may be enriched, which can lead to the reaction of finely ground limestone with sulphates in solution, which in turn leads to the formation of thaumasite. A prerequisite for this reaction is that high sulphate contents of more than 10 wt.-% by weight cement paste ($SO_3/Al_2O_3 > 3$) are present as derived from experimental observations (Schmidt 2007, Schmidt et al. 2009). The formation of thaumasite leads to the expansion, cracking and degradation of cementitious materials (Schmidt 2007, Schmidt et al. 2009). This process occurs mainly but not only at low temperatures (approx. < 10 °C) over several months. The thaumasite form of sulfate attack requires a source of sulphate and also of carbonate (Abubaker et al. 2014, Winter 2009). Other than ettringite, thaumasite does not require a source for aluminium to form. The calcium needed for thaumasite formation is provided by dissolution of cement phases, mainly portlandite and C-S-H. In the context of soil-structure interaction the thaumasite form of sulfate attack at concrete/clay interfaces was investigated by Brueckner et al. (2012). They brought a concrete sample in contact with a sulphate-containing Lower Lias Clay, with a sulphate content of 2.03 – 2.45 g/l. After 27 month up to 24 mm thaumasite attack reaction products formed while the thickness mainly depended on the interface pH and interface pressure.

2.4.5 Ingress of chloride

Ingress of high amounts of chloride is a major concern for reinforced concrete, as high chloride concentrations strongly increase corrosion of rebar and generate cracks (Phung et al. 2018). The interaction of chloride itself with cement phases does not lead to the formation of detrimental expansive phases (Glasser et al. 2008). At elevated chloride concentrations Friedel's salt, a layered double hydroxide (LDH), is formed by chloride interaction with AFm phases. As other AFm phases, Friedel's salt is an anion exchanger mineral which might act as a sorbent for anionic radionuclides.

2.4.6 Ingress of magnesium

The pore water of Opalinus Clay contains some amount of dissolved magnesium, for the Opalinus Clay at the Mont Terri Underground Research Laboratory in Switzerland about 20 mmol/l (Pearson et al. 2011). Due to diffusion of dissolved magnesium towards cements the formation of magnesium rich phase (M-S-H or hydrotalcite like) was observed in the Mont Terri CI experiment for interfaces between low-pH cements (ESDRED, LAC) and Opalinus Clay in the cement (Mäder et al. 2017). Similar observation of magnesium enrichment at the cement side of a cement/clay interface was reported by Yokoyama et al. (2021) for interfaces of bentonite with LAC and OPC.

Influence of magnesium influx on concrete is described normally as a specific form of (magnesium) sulphate attack or (magnesium) chloride attack (Bonen 1992, Kunther et al. 2013, Rasheeduzzafar et al. 1994, Whittaker & Black 2015). In case of magnesium sulphate attack, the magnesium can exchange with calcium in the hydrated cement paste and causes formation of brucite in combination with gypsum (Whittaker & Black 2015). Due to the very low solubility of brucite, a solution saturated with brucite will have a pH at about 10.5, which is too low to stabilize C-S-H or ettringite. This might promote decalcification of the cement (Whittaker & Black 2015). Formation of magnesium-silicate-hydrate (M-S-H) in cements exposed to magnesium sulphate was also reported (Al-Amoudi 2002, Gollop & Taylor 1996).

2.4.7 Clay degradation

Clay materials in contact with cement materials are altered due to influx of hydroxyl and alkali (potassium, sodium) ions which induce mineral alteration fronts (Gaucher & Blanc 2006, Savage 2013, Savage et al. 2007, Savage & Cloet 2018, Wilson et al. 2021). Commonly, close to the cement/clay interface, mineral alteration fronts are observed that are advanced by a fluid alteration front (Wilson et al. 2021). The extent of alteration zones, the mineralogical changes and the changes in material properties strongly depend on the type of cement and clay materials, as well as the transport regime (c.f. 2.5.2).

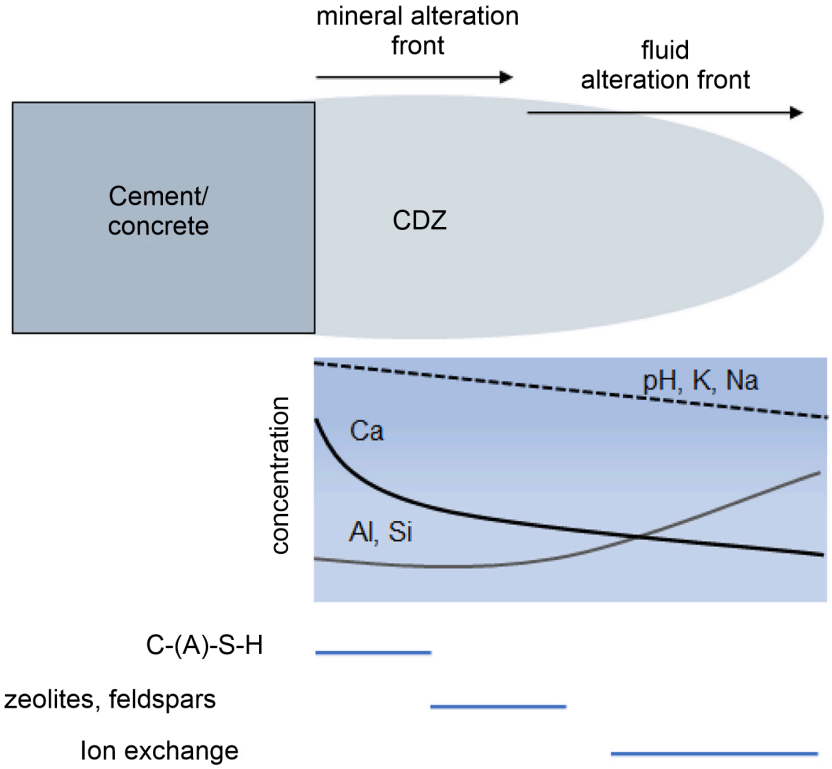

Fig. 2-9: Properties of a chemically disturbed zone (CDZ) in clay rock due to interaction with cement

Reprinted from Savage (2011), Wilson et al. (2021) with permission from Elsevier.

2.4.8 pH plume in clays

Pore water pH in clay materials is normally close to neutral values. Influx of OH^- ions (advection or diffusion) from the cement side will increase the pore water pH. It is difficult to directly measure pore water pH in dense clay materials, therefore progress of pH front can be only traced by induced mineral transformations. However, mineral transformations may considerably lag behind pH alterations due to slow reaction kinetics. Generally the progress of a pH front depends on the transport regime and is believed to be diffusion dominated for a repository in Opalinus Clay (Kosakowski 2013).

In small scale experiments like those of Luraschi et al. (2020) pH breakthrough into the "small" clay water reservoir behind the clay plug was observed, although mineral alterations were only observed near the interface to the cement. This shows that pH in the clay part of the sample is not completely buffered by mineral reactions (for the given small time and space scales of months and cm).

An important, but relatively slow process that reduces high pH, is the dissolution of rock forming minerals, mainly alumino-silicates. In numerical models that use equilibrium control of mineral solubility, pH is largely buffered by dissolution of primary minerals in combination with precipitation of secondary phases. This limits the extent of the pH plume (Kosakowski & Berner 2013) in a diffusive transport regime. In numerical models that utilize kinetic control on dissolution/precipitation of minerals, the progress of pH front strongly depends on the mass flux

across the cement/clay interface in combination with the rate with which the hydroxyl ions are consumed by the reactions. The uncertainty related to kinetic parameters is directly reflected in the calculated pH of a fluid alteration zone.

Another important process for the retardation of hydroxyl ions (and radionuclides) is that of clay edge site sorption (Savage & Cloet 2018). The buffering of the ≡ SOH sites is based upon their amphoteric nature, that is, they can protonate ($\equiv SOH_2^+$) or deprotonate ($\equiv SO^-$), depending on the solution pH. The capacity of these sites, which has been determined in short-term titration experiments, is about 10% of the cation exchange capacity of the clay (i.e. ~ 0.1 moles per kg of clay) (Berner et al. 2013).

2.4.9 Mineralogical changes and porosity evolution

Influx of OH^- ions and associated increase of pore water pH in clays is the main driving mechanism for mineral alterations. Under alkaline conditions dissolution of clays, silicates and other (accessory) minerals is accelerated (Marty et al. 2015b, Palandri & Kharaka 2004). Kinetic parameters are highly uncertain (Marty et al. 2015b). Upon dissolution of primary minerals and influx of alkalis from cement side, secondary cement phases (e.g. C-S-H, M-S-H), aluminosilicates (zeolites, feldspars, feldspathoids) and potentially secondary clays will form (Wilson et al. 2021). The overall system evolution is governed by a complex interplay between (original) cement and clay compositions, transport regime and geochemical gradients, presence of charged mineral surfaces, (cat)ion exchange, surface complexation, and kinetically controlled mineral dissolution/precipitation (Savage & Cloet 2018, Wilson et al. 2021). The precipitation of secondary minerals in clays is associated with an interaggregate decrease in porosity (Bartier et al. 2013, Gaboreau et al. 2011, Read et al. 2001, Shafizadeh et al. 2020) that decreases mass flux fluxes across such altered zones (Fukatsu et al. 2017, Luraschi et al. 2020).

Commonly reactive transport models are employed at continuum scale, i.e. transport properties (bulk porosity, diffusivity, permeability) and geochemical properties (mineralogy, water composition) are representative averaged properties of each sub-volume of the model. Such models normally predict porosity clogging at cement/clay interfaces (Savage & Cloet 2018). The clogging time depends on the rate of kinetic control of mineral precipitation/dissolution and is often dependent on the grid resolution of the utilized model (Marty et al. 2009) and choice of secondary minerals that are allowed to precipitate (Savage & Cloet 2018). High dissolution rates for primary minerals accelerates mineralogical transformations and porosity change, which limits the extent of alteration fronts due to reduction of mass transport (Wilson et al. 2021). More recently, Jenni et al. (Jenni et al. 2017, Jenni & Mäder, 2021) used a dual-porosity approach to model different cement/clay interfaces from the Mont Terri CI experiment. They demonstrated that it is possible to clog part of the pore space and still allow mass transport of neutral and cationic species along interlayers and outer surfaces of clay minerals. Anion fluxes are orders of magnitudes lower. This is in-line with recent experimental diffusion measurements across clay zones with reduced interaggregate porosity caused by precipitates (Chagneau et al. 2015, Fukatsu et al. 2017, Luraschi et al. 2020).

2.4.10 Cation exchange

Cation exchange initiated by high fluxes of alkali ions from cement towards clay dominate initial evolution of clays. Cation exchange is linked with clay swelling properties since smectite clays can absorb water into interlayers and swell in volume. Exchange of Ca^{2+} from concrete for Na^{+} in clay interlayers may reduce swelling pressure (Savage & Cloet 2018). On the long-term, i.e. for a HLW bentonite buffer within several thousands of years (Kosakowski & Berner 2018), it can be expected that the cation exchanger composition will be equilibrated with the largest available (accessible) reservoir for cations, which is normally the host rock. Equilibration times depend on cation transport between the different materials. For the CI experiment alkali metal ion concentrations between an altered zone around cement filled boreholes were levelled in a few years (Kosakowski 2018), although the cation exchanger population was changed. For a typical HLW near field levelling out ion concentrations relevant for cation exchanger might take significantly longer, possible several thousands of years or more (Kosakowski & Berner 2013).

2.5 Porosity evolution at reacting interfaces

2.5.1 Porosity

Porosity or void fraction is a measure of empty volume within a material (i.e. "non-solid"). It is expressed as fraction of total volume and varies between 0 and 1. Alternatively it can be expressed as a percentage and varies between 0% and 100%". Specifically in various geoscientific and engineering disciplines, "*the porosity of a porous medium describes the void space in the material, where the void may contain, for example, air or water.*"

For most applications, the porosity is defined at a continuum scale, i.e. porosity is a representative property of the medium without explicit differentiation of the pore-sizes. In order to establish a representative porosity of a porous medium the representative elementary volume (REV) needs to be defined. The REV is the smallest volume over which the property can be defined and yield a value representative of the whole (Bear 1972, Hill 1963).

Porosity is an important property that relates continuum-scale transport description to pore scale transport (Tartakovsky & Dentz 2019). This includes advective and diffusive transport of liquids, gases and dissolved species. The most recent review paper on reactive transport in evolving porous media by Seigneur et al. (2019) summarizes changes induced in a porous medium by reactions and feedback mechanisms that influence transport of fluid and gases trough porous media. For an extended discussion on porosity change due to fluid-mineral reaction in "tight rock" from a mineralogical viewpoint see the review paper of Putnis (2015).

The porosity itself does not provide a full geometric description of the pore space necessary to relate transport on pore scale to continuum scale transport. Other important properties on continuum scale are the tortuosity and the constrictivity. The tortuosity is the lengthening of the transport pathway in relation to the shortest distance between two points, while the constrictivity accounts for the variation of cross-section of a transport pathway (van Brakel & Heertjes 1974).

Porosity definitions dependent on physical characteristics

Porosity can become an ill-defined parameter, specifically in complex porous media with complicated pore structure, wide distribution of pore sizes or electrically charged pore surfaces. Distinct physical and chemical processes might take place within different parts of the water or gas filled pore space. This includes the concepts related to "connected pore space", "dead end pores" or "open pores" and "closed pores".

Specifically for transport of solutes, it is known, that the "transport porosity", i.e. the accessible water saturated pore space, might be different for various solutes and (colloidal) particles (Kosakowski 2004). For clay media Pearson (1998) introduced the concept of "geochemical" porosity for clay-rich media, which is the water available for water-rock interaction and solute transport. He states: "*It is to be distinguished conceptually from total and water-content porosity, and from advective and diffusive transport porosity. In coarse-strained rock, all types of porosity may have nearly the same value, so it is not necessary to distinguish among them. In fine clay-rich materials where transport is by diffusion, geochemical and diffusion porosities for water molecules are the same as the water-content porosities. For solutes, which do not have access to interlayer water of clay minerals or surface-sorbed water, these porosities are only one-third to one-half the water-content porosities.*" A very detailed summary on porosity, structure and state of water in pore space in Opalinus Clay is provided in Section 5.4 of Nagra NTB 02-03 (Nagra 2002b).

There are multiple methods to measure porosity, and most methods give different results because the different physical/chemical/geometrical methods which are used, do not sample the total porosity or other parts of the water or gas filled pore space in a porous medium (Nagra 2002b). Common methods are the drying of samples at 105 °C to measure the "water-loss porosity, helium or nitrogen (gas) pycnometry, image analysis, mercury intrusion porosimetry, water absorption (Andreola et al. 2000, Münch et al. 2015, Nagra 2002b), NMR (Bowers et al. 1995), neutron scattering (Shafizadeh et al. 2020, 2015) or lab and field tracer tests (Gimmi et al. 2014, Van Loon & Jakob 2005).

The concept of different ‘types of porosity' and different results of porosity measurements is related to the wide distribution of pore sizes in clays and cements, which have a multi-scale porosity (Fig. 2-3, 2-4 and 2-7). Beside macropores (capillary pores with diameter greater than 50 nm) those materials contain considerable amounts of micropores (pores with less than 2 nm diameter) and mesopores (with pores between 2 and 50 nm diameter). Please note that different fields use different definitions, so the pore sizes associated with macro-, meso- and micropores are typically much bigger for highly water conducting materials typically investigated in e.g. groundwater hydrology or vadose zone hydrology (Dippenaar 2014).

For clay materials, the pore space is typically divided into inter-granular pores (micropores) and intra-granular pores (mesopores) (Kuila & Prasad 2013, Nagra 2002b, Yuan & Rezaee 2019). Compacted clays and hard clay rocks contain a large fraction of inter-granular pores smaller than 10 nm. Water in those pores is largely affected by the presence of charged clay surfaces. The existence of small pore throats causes a considerable effect on transport of solutes and on the possibility to drain the material. For many clay minerals, the intra-granular porosity is related to hydrated interlayers with widths of less than 2 nm.

A similar concept for the partitioning of pore space into different domains exists for hydrated cement paste (Feldman & Sereda 1968, Jennings et al. 2008, 2002, Pinson et al. 2015). Capillary pores with a diameter above 10 nm are assumed comparable to the macropores in clay materials. The so-called gel porosity is composed of small mesopores, which are associated with the size and arrangement of C-S-H crystals. Similar to clay minerals, C-S-H crystals contain micropores in form of hydrated interlayers.

Porosity reduction and porosity clogging

The term "porosity clogging" is commonly used to describe a complete or partial reduction of void space that causes a significant reduction of transport in porous media, with loosely defined limits (Torkzaban et al. 2015b). For the time scale of the waste repository, because of the hierarchical nature and heterogeneity of the involved materials and precipitates, a significant reduction of the porosity will most likely not result in a halt of mass transport processes (c.f. Chapter 5). The effect of chemo-mechanical processes as described in Jenni and Mäder (2018) is not considered here.

Changes of the multiscale porosity can be caused by different mechanisms:

- Biogeochemical processes due to dissolution/precipitation of mineral phases driven by transport processes (Seigneur et al. 2019), microbial activities (Brovelli et al. 2009), diagenesis (Pape et al. 2000) or temperature/pressure changes (Scott & Driesner 2018). Such changes are observed u. a. for reactive barriers (Claveau-Mallet & Comeau, 2020, Indraratna et al. 2020, Mayer et al. 2001, Wantanaphong et al. 2006), chemical reactors (Botes et al. 2018), or in relation to extraction/injection of waters in oil/gas wells, geothermal wells and groundwater wells (Torkzaban et al. 2015b). In Section 2.5.2 we present different clogging scenarios Type I – IV associated with precipitation of mineral phases.
- "Physical clogging" caused by particle or colloid transport and filtration/sedimentation processes at pore walls and pore throats (Torkzaban et al. 2015a). Physical clogging is often observed in granular media (Tang et al. 2020), but also in concrete (Kia et al. 2017). Clogging of media due to particle transport is nearly always related to a change of constrictivity due to clogging of pore throats by particles with diameters bigger than the pore diameter (Kia et al. 2017). It is commonly observed, that chemical changes and particle/colloid transport are interrelated (Liu et al. 2020, Torkzaban et al. 2015a).

2.5.2 Control of porosity change at cement/clay interfaces by transport

Precipitation and dissolution processes are nearly always associated with volume changes (capillary porosity change and mineral volumes). The extent of these volume changes is well known, but the impact on the geometry of the pore space is not well known. The geometry of the pore space is a key factor for various relevant material properties such as the pore size distribution, the connectivity, and the reactive surfaces. It affects not only the transport and the mechanical properties but also subsequently the chemical parameters such as the chemical reactivity or kinetic rates (Hommel et al. 2018).

Most recently available chemical, mechanical and transport models at continuum scale describe macroscopic (continuum-scale) changes of porosity, but do not account for microscopic (subgrid) changes, or for the competition between different processes. It is conceivable that the inappropriate consideration of microscopic processes may give rise to a significant uncertainty in formulation and parameterization of kinetic control on mineral dissolution and precipitation at the macroscopic scale (Kurganskaya & Rohlfs 2020, Noiriel & Daval 2017).

A common modelling scenario related to clogging in porous media and at material interfaces, specifically cement/clay, is described in Kosakowski and Smith (2014) and shown in Fig. 2-10. We classify this scenario as "**Type I**" throughout the text. Two geochemically different materials, e.g. quartz sand and cement material, are in contact. Due to diffusive mixing of pore waters at the interface, a mineral phase is precipitated, in this case calcium-silicate-hydrate (C-S-H). It is noted that in reality the C-S-H precipitates are characterised by gel and interlayer porosity essentially allowing mass diffusion, however at a reduced rate. Due to the consumption of the reaction products, the corresponding concentrations at the interface are decreased. The supply of reactants

is provided by leaching of calcium from cement phases and dissolution of silica grains. In order to be able to clog the porosity, the zone of mixing for reactants has to be stationary in order to allow accumulation of precipitates.

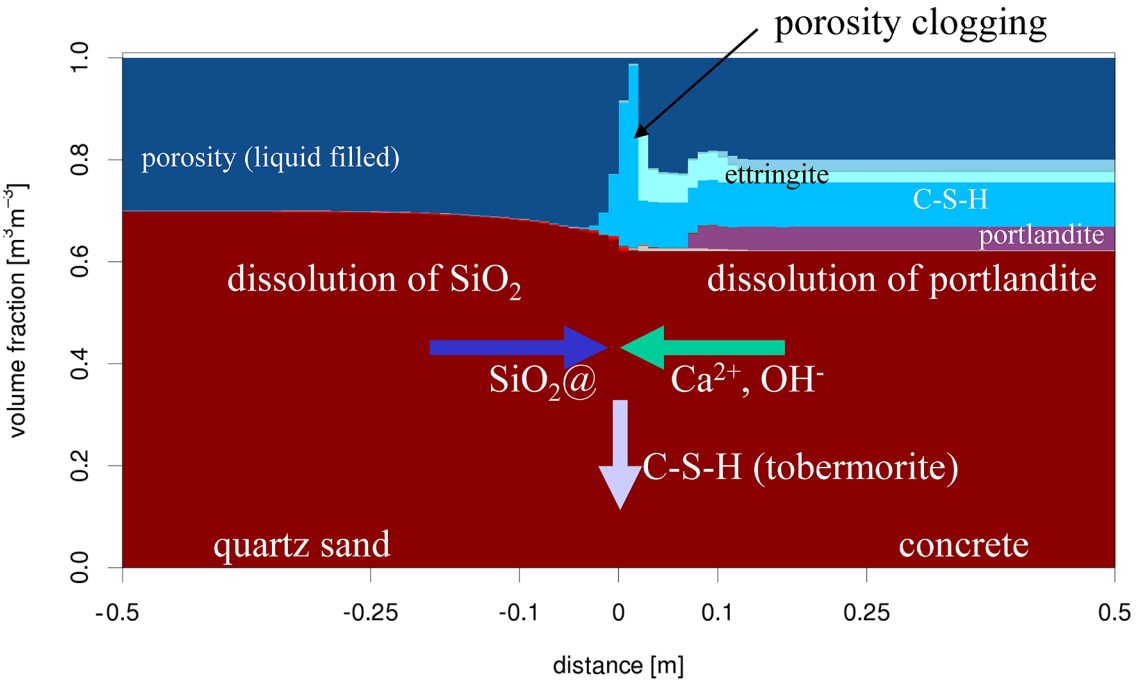

Fig. 2-10: Concept of a clogging interface between reactive quartz sand (left) and concrete (right) in a diffusive transport regime

C-S-H microstructure is not taken into account as possible mass transport pathway.

Kosakowski & Smith (2014)

This scenario **Type I** is also provided in Fig. 2-11 a). The fronts of dissolving mineral phases fix an equilibrium concentration for the reactants, while in the mixing zone, at the locations where precipitation occurs, the lower equilibrium concentrations of the reactants are controlled by the precipitated phase. Typically for such scenarios, the diffusive fluxes decrease with time due to the increasing distance of reaction fronts to the mixing zone. It might well be, that the dissolution fronts on both sides from the interface move with different speed. The mixing front respectively the region for precipitation does not move, as long as the reactant fluxes are the same. In other words, the region of precipitation will be located at the region, where reactant fluxes are the same. This scenario is typical for cement/clay interaction (Berner et al. 2013, Gaucher & Blanc 2006, Kosakowski & Berner 2013, Marty et al. 2015a). The diffusive fluxes decrease with reaction front distance from the mixing zone. Therefore, the progress of reaction fronts x in such a system typically shows a square root dependence on time t and an apparent diffusion coefficient D_a:

$$x \propto \sqrt{D_a t} \tag{2.1}$$

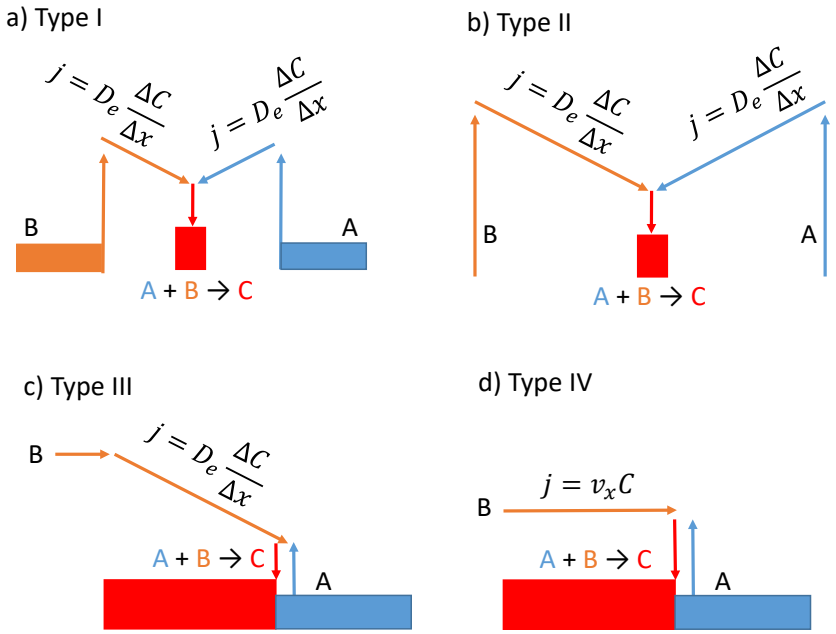

Fig. 2-11: Conceptual scenarios for interaction between dissolution/precipitation reactions and transport of reactants

Type I: Dissolution of phases which provides reactants A and B, then diffusive transport towards a mixing zone where phase C is precipitated. b) Type II: Diffusive transport of reactants A and B towards a mixing zone where phase C is precipitated. Reactants A and B are kept at constant concentration at a certain distance from the mixing zone. c) Type III: Reactant B is present at the boundary of a porous medium with a constant concentration and diffuses into the porous medium where A is dissolved and C is precipitated. d) Type IV: Reactant B is transported by advection into the medium, where A is dissolved and C is precipitated.

Fig. 2-11 b) shows a **Type II** scenario, which is a variation of the Type I scenario in a). The reactants are not provided by dissolution reaction, but they are kept constant at certain distances from the mixing zone. This is a situation typically encountered in precipitation experiments (Chagneau et al. 2015, Fukatsu et al. 2017). In this case, the region of precipitation will be stationary, as long as concentrations at the boundary are fixed.

A case where the mixing region is systematically moving is shown in Fig. 2-11 c) as **Type III**. The concentration for one reactant B is fixed, by a large well mixed reservoir, or by a very slowly moving dissolution front (large amount to dissolve). The dissolution front that provides the other reactant A is moving much faster. In this case, the zone of precipitation follows the movement of the dissolution front for reactant A. This type of situation is typically encountered for atmospheric carbonation of concrete (Despotou et al. 2016, Muntean et al. 2011, Muntean & Böhm 2009, Ta et al. 2016, Thiery et al. 2007). Progress of reaction fronts in such a diffusive system is often characterized by the square root dependence on time as defined in Eq. 2.1.

Finally yet important, Fig. 2-11 d) shows a **Type IV** scenario, the most common scenario related to advective transport of one reactant. This type of scenario is commonly encountered in flow-through or injection experiments (Poonoosamy et al. 2020, 2015). In this case, similar to c), reactant B enters a porous medium where reactant A is provided by dissolution of a mineral phase. The region of precipitation for C is at the place where A is dissolved. If advective transport of B is constant in time, the zone of precipitation is moving with a constant velocity. This scenario has

a strong interplay with mechanical (non-chemical) transport mechanisms, as colloids and particles are mainly transported by advection and chemical processes often control formation and (im)mobilization of colloids and particles.

2.6 Effect of partial saturation conditions on transport mechanisms

In specific locations within the foreseen nuclear waste repository, the partial saturation conditions are expected to hold for an extended period of time. During the construction and emplacement phase, the L/ILW repository will be de-saturated from water, and the tunnels and emplacement rooms will be ventilated, according to present regulations at an atmosphere of 50% – 60% relative humidity (RH%) (p. 43 in Diomidis et al. 2016). After closure, water will be transported from the surrounding host rock and the repository will eventually re-saturate in a process that is delayed for more than 100'000 years due to gas generated by several geochemical/biological mechanisms. Due to the presence of water, corroding metals will produce hydrogen, and the degradation of organic materials will result in the generation of several other gaseous species like carbon dioxide and methane (Diomidis et al. 2016). Microbes are expected to play a role in consuming gas. At partially saturated conditions, both the diffusivity and permeability of the materials depend on the degree of saturation and can be expressed in terms of relative- or effective- diffusivity and permeability.

Among other mechanisms of material de-saturation (multiphase flow), the exposure of the materials to air with constant relative humidity, or with gas volumes of variable relative humidity, also results in removal of water from the inner structure. At such conditions several processes are in competition: a) evaporation/condensation phase changes, b) the diffusion of water vapour through the percolated gas phase and c) absorption/desorption processes. A typical water moisture-content versus relative humidity graph for concrete is shown in Fig. 2-12. Fully saturated concrete which is exposed to low relative humidity de-saturates up to a degree, which is described by the desorption isotherms. Similarly, partially saturated concrete will increase its saturation when exposed to high relative humidity conditions. Note that the isotherms show the water degree at equilibrium and do not provide information about the time needed for the transition of the system.

The de-saturation of concrete starts from the surface that is exposed to air and gradually advances to the internal concrete volume. For cementitious materials, the macroscopic pores (larger pore-volumes) are more susceptible in losing the water content and are followed by the capillary and gel pores. At extremely low values of relative humidity, the capillary pores will also start to de-saturate, which may be followed by local structural changes. Moisture transport within the internal concrete volume depends on the microstructure features such as the pore size distribution, the water to cement (w/c) ratio and the cement type (Fahim et al. 2019). Similar, for clay materials (and especially for clay rocks), water in the macropores is depleted first, followed by water in mesopores around grain boundaries, while water in the interlayers drains only at comparably low relative humidities (which is then also related to structural changes). At a relative humidity RH ~ 50%, the connectivity of the water phase in the macro-pores is expected to start de-percolating, thus reducing the effective diffusivity of solutes. However, a percolated water phase (also in form of water film) will still exist connecting most of the macro-pores, the capillary pores and the gel pores, through which the solute transport will continue, but at a slower pace. The hydraulic properties of cementitious materials are typically more favourable to mass transport compared to clay materials, which are characterized by ultra-low permeability values. In other words, the liquid and gas transport is limited by the presence of clay materials. Due to the smaller pore-sizes and lower hydraulic transport properties at a RH~ 50% the small pores in clay material will be water filled and sufficient connectivity due to abundance of interlayer pores will continue to exist.

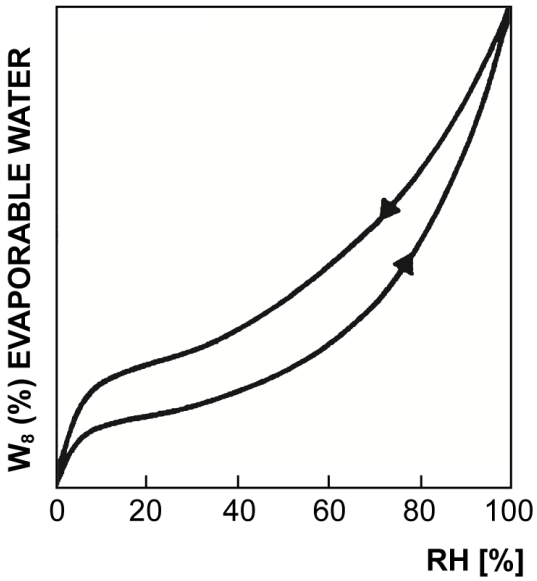

Fig. 2-12: Typical adsorption/desorption water isotherms in concrete correlating the moisture content (% of evaporable water) with the relative humidity conditions (RH%)

Reprinted from Andrade et al. (1999) with permission from Elsevier. These curves show the saturation degree at equilibrium.

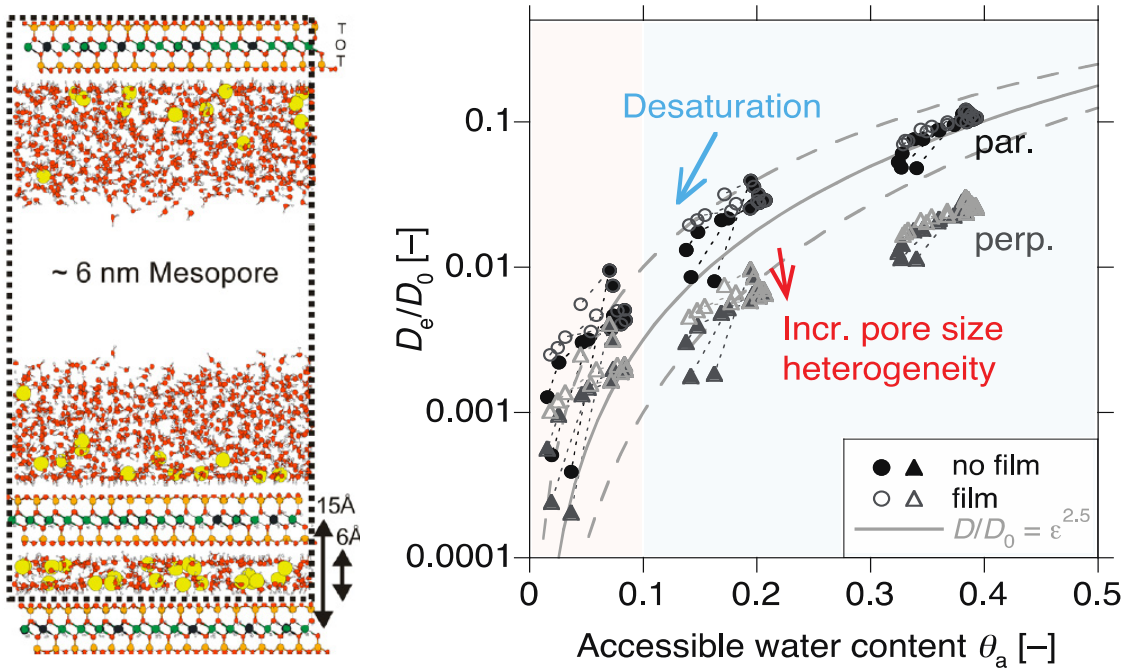

Fig. 2-13: Left: a snapshot from MD simulations of Cs montmorillonite at RH 85%, right: numerical predictions of the drop of the effective diffusion coefficient D_e due to partial saturation conditions, for several clay geometry realisations

Left: Oxygen atoms are red, hydrogen atoms white, silica atoms light brown, aluminum atoms green. magnesium atoms black, and Cs atoms yellow. Water film layers are partially occupying the mesopore volume (Churakov 2013). Right: θ_a <0.1 corresponds to anion diffusion (Gimmi & Churakov 2019).

Cationic and anionic species are transported essentially in aqueous phase, and the de-saturated pore space does not contribute to their transport. Experimental studies and modelling suggest that partial saturation strongly reduces the diffusive flux of the ions (Savoye et al. 2012, 2010). The main contribution to this effect is the decrease of the solute accessible porosity. Especially for clays, the effect is very different for the cationic and anionic species. In the argillaceous rocks dominated by illite-smectite minerals the interlayer porosity remains saturated even at extremely low relative humidity the charged mineral surface remains covered with a water film. Cations can diffuse through the interlayers and an interconnected aqueous phase will persist even at very low saturation levels. However, the diffusion proceeds at a much slower pace and the tortuosity of the relevant aqueous phase increases dramatically. On the contrary, the anions are mostly excluded from the transport through the interlayers and to a large extent from the proximity to the negatively charged surfaces which are covered with water films. At low saturation levels, the anion accessible porosity becomes disconnected, leading to very limited transport. In Fig. 2-13 (left), a 6 nm mesopore of a Cs montmorillonite at relative humidity RH = 85% is shown with its corresponding water films (Churakov 2013). In Fig. 2-13 (right; Gimmi & Churakov 2019), the effective diffusion coefficient D_e, over the diffusion coefficient in the bulk D_0 for anions and water tracer versus the accessible water content is plotted, for several clay realisations. The water content is altered due to de-saturation caused by changes in RH. Anion mobility is severely restricted as seen in the region of (0 – 0.1) accessible water content θ_a for a claystone. Archie curves are also plotted following a regression process for upscaling of the results to macroscopic codes.

In the case of OPA, the air and the produced gases due to the degradation of materials, will be slowly transported away by various two-phase mechanisms. Corresponding processes are depicted in Fig. 2-14 and include transport because of water ingress or gas pressure build up, dissolution of gases in the liquid phase and subsequent advection and diffusion through the percolated liquid phase, or by dilatant gas pathways in the presence of large pressure differences. The advective and diffusive transport of gases depend on the local hydraulic gradients, the gas concentration gradient and the solubility of gas in the clay pore-water. The low hydraulic conductivity of OPA significantly reduces the efficiency of this transport mechanism. The second mechanism, the two-phase flow transport mechanism, occurs when the pores are filled with gas which replaces the pre-existing pore water. For that, the visco-capillary forces provide a measure of the resistance to flow. For OPA, very high gas pressure gradients of the order p_{ep} = 1 – 10 MPa (gas entry pressure) are needed to overcome these forces. This mechanism applies only to the freely mobile water within the OPA, which is less than 50% of the existing water. The third mechanism which allows gases to be transported is the pathway dilation mechanism, which occurs in the presence of long-term gas pressures and is related to microfractures that may be generated much before the tensile strength of the formation is exceeded (Senger et al. 2013). This process results in local increase of porosity and permeability.

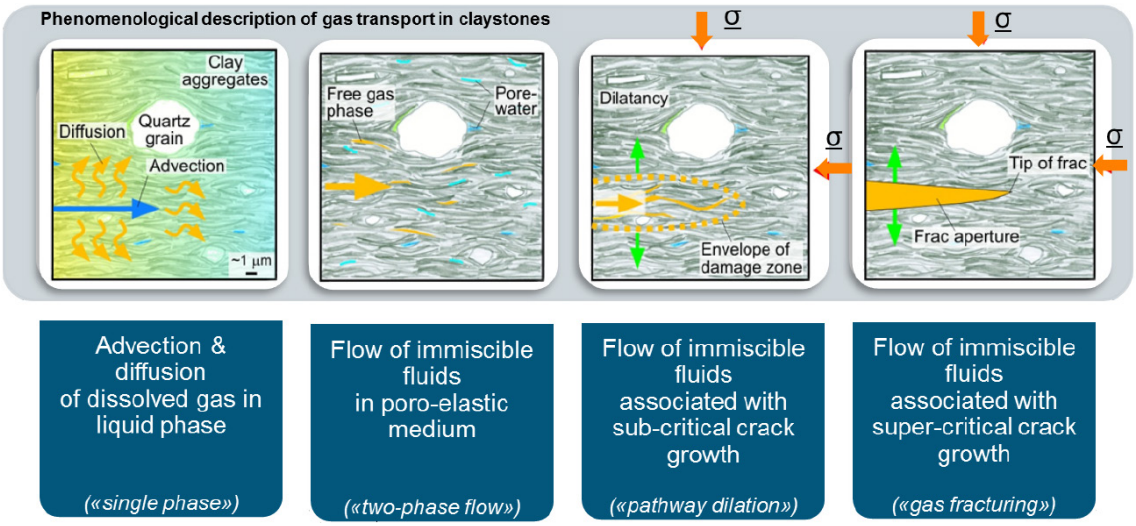

Fig. 2-14: Classification and analysis of gas transport processes in ultra low permeability rock such as the Opalinus Clay
Senger et al. (2013)

Partial saturated conditions will also have a strong influence on the local geochemical evolution of the materials. Due to geochemical reactions of dissolution and precipitation, the transport properties of the materials are changing in a non-linear way. At partially saturated conditions diffusion will advance at a slower pace, and at very low saturation states, the geochemical reactions will be halted. Subsequently, it is expected that at partially saturated conditions the geochemical evolution of the cement/clay interfaces within the waste repository will be evolving much slower.

It should be noted that this is not a universal monotonic trend. For example, the carbonation of cement, which is one of the major cement altering mechanisms proceeds at a different pace depending on the RH, having a maximum influence at 50% RH < 80% (Papadakis et al. 1991). The underlying mechanisms of this behaviour have been only recently understood and investigated in depth and is attributed in a complex interplay of water availability and transport of reactants in gas and liquid phase, as well as the effect on kinetics of precipitation (Steiner et al. 2020).

2.7 Desaturation and water availability as limiting mechanisms for porosity change

It is well known that iron corrosion rates (Stefanoni et al. 2018) and more generally (bio)chemical reactions are strongly inhibited in a dry environment where water availability is limited. As soon as the relative humidity is lower than a threshold value, the reaction almost stops. In fact, threshold values might be different for different reactions. For example, corrosion of an iron surface exposed to atmosphere was found to slow down strongly below a first threshold relative humidity of 55% and was reduced even more below a second threshold value of 20% (Watkinson et al. 2004)

For reactions in porous media, the threshold value depends specifically on the pore size distribution, which connects the (partial) water saturation of the medium with the relative humidity of the gas phase. This might cause speedup of processes, if reactants can be transported in the gas phase. For example, as discussed, the carbonation fronts move fastest at about 50 – 70% relative humidity in most concrete materials (Russell et al. 2001, Winter 2009). At higher humidity, the CO_2 fluxes slow down as increasingly more pores are water-filled and fast diffusion in gas-filled pores is replaced by slow diffusion in water-filled pores. At lower humidity, however, there is insufficient water in larger pores to drive carbonation reactions.

In Seigneur et al. (2019) the reactive surface (in kinetic models) is used as surrogate for reactivity. However, they did not account for a change of reactive surface area upon liquid saturation changes and thus they cannot consider reactivity changes due to dry-out processes.

To account for the slowing down of chemical reactions at dry conditions (Trotignon et al. 2011) multiplied the various mineral dissolution/precipitation rates with a function $R(t,x)$ to scale chemical reactivity with relative humidity RH of the gas phase. This chemical reactivity R was calculated for each time step and each discretized volume. R varies between zero, if no reactions take place due to lack of water, and one, if the reactions are not limited by the availability of water. R was calculated with a phenomenological approach proposed by Bazant and Najjar (1972) for the hydration of cement paste under partially liquid saturated conditions:

$$R = (1 + (7.5 - 7.5RH)^4)^{-1} \tag{2.2}$$

Which indicates that the reactivity decreases progressively from one to zero as the water saturation approaches the residual saturation.

Another function was implemented by Suckling et al. (2011), where the reactivity varies linearly between a minimum value for relative humidity RH_{min} and an upper value RH_{max}.

$$R = \begin{cases} 1 & 1 < X \\ X & 0 < X < 1 \\ 0 & X < 0 \end{cases} \text{ where } X = \frac{RH - RH_{min}}{RH_{max} - RH_{min}} \tag{2.3}$$

These definitions of the reactivity functions are defined in terms of RH, but they are connected to the saturation of the medium via Kelvins equation, which relates the relative humidity with the radius of the largest water filled pore in a porous medium (Evans et al. 1986).

2.8 Transport through partially saturated bentonite structures

Bentonite is a material considered as a buffer/filling material and as an engineered barrier for the geological disposal of radioactive waste. Some of the characteristic properties of bentonite, which make this material an ideal candidate is a) the low hydraulic conductivity which minimises ion transport, b) the swelling pressure, which provides mechanical support to the repository, c) the capacity to transport gases, and d) the chemical retention of radionuclides. The emplacement of bentonite may happen in the form of compacted bentonite bricks, in a pellet form or in granular form. A typical pore size density for a grain of bentonite, for poured bentonite and for compacted bentonite (all dried) is depicted in Fig. 2-15 (Seiphoori 2015).

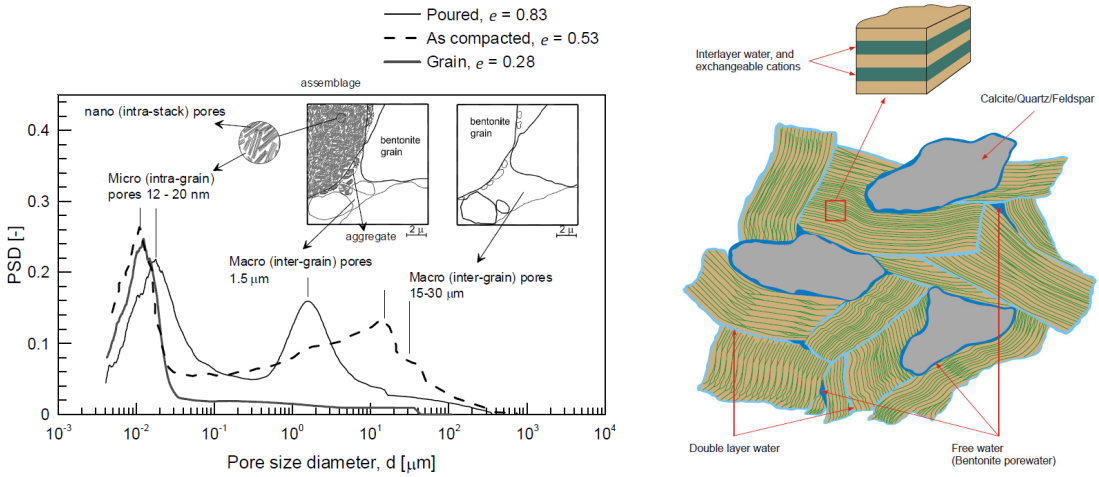

Fig. 2-15: Bentonite pore-size density of a bentonite grain, of poured bentonite and of compacted bentonite, with *e* being the total void ratio and a conceptual picture of a Bentonite grain

Left: Seiphoori (2015), right: Bradbury & Baeyens (2002)

The three different forms of bentonite filling material, result in a medium that has different pore size density distribution. For the pellet form, relatively large pores of the order of tens of micrometers will exist during compaction, because of the size of the pellets compared to the size of small grains. However, at a fully saturated state, the hydromechanical properties of pellet based or granular based evolved bentonite are indistinguishable as is verified by laboratory and large scale experiments (Mont Terri EB experiment).

After emplacement, ingress of water from the surrounding host rock, will saturate the bentonite material resulting in its swelling, in a process that is expected to last around 100 years (Jenni et al. 2019). The gypsum that is contained in bentonite will dissolve and Ca ions will be released. The exact geochemical reactions depend on the material with which the bentonite is in contact. When in contact with cement, and due to portlandite dissolution, Ca and OH^- ions will be transported into the bentonite causing mineral precipitation and local decrease of porosity. In the next 10'000 years the geochemical contrast will be smoothed out and transport will occur mainly via diffusion. Dissolution and precipitation reactions will slightly change the transport properties exactly at the interfaces, by forming the so-called skins. Between 10^4 and 10^6 years, a quasi-steady state will be established, where the material evolution will be on-going at a much slower pace. At certain locations the porosity reduction due to mineral precipitation will also proceed in a way to reduce the hydraulic diffusivity of the material.

3 Experiments of cement/clay interaction

3.1 Short literature review, international results

Within the EURAD ACED project (Deissmann et al. 2021) summarized all the existing knowledge available on the relevant processes and transients occurring at the interfaces between materials, focusing on materials combinations relevant for the chemical evolution of ILW and HLW disposal cells in European repository concepts. They addressed glass-steel, cement/mortar-granite, cement/concrete-clay, steel/iron-bentonite, steel/iron-cement/concrete, and steel/iron-granite interfaces, where especially the experiments on cement/concrete-clay interfaces are of interest here. In their structured overview, they looked at, among others, existing (experimental) data on relevant processes occurring at the interfaces, and identified comprehensive reviews on various aspects of cement/clay interactions (e.g., Bildstein et al. 2019, Gaucher & Blanc 2006, Lalan et al. 2016, Marty et al. 2015a, Metcalfe & Walker 2004, Savage 2011, Savage & Cloet 2018), and short-term laboratory (e.g., Adler et al. 1999, Dauzeres et al. 2010, Raúl Fernández et al. 2016) and longer-term in situ experiments (up to about 20 years) at different underground research laboratories like HADES, Mol, Belgium (Phung et al. 2018, Read et al. 2001), Mont Terri, Switzerland (e.g. Dauzeres et al. 2016a, Jenni et al. 2014, Lerouge et al. 2017, Mäder et al. 2017), Bure, Department Meuse/Haute Marne, or at the Tournemire site in France (e.g., Bartier et al. 2013, Gaboreau et al. 2011, Tinseau et al. 2006), as well as the FEBEX experiment in the Grimsel test site in Switzerland (e.g. Fernández et al. 2017, Turrero & Cloet 2017). More recently performed studies on low-pH cement/clay interaction have been investigated within the CEBAMA project (e.g. Duro et al. 2020) studying the low-pH concrete formulations (rich in fly ash and slag, respectively) in contact with Callovo Oxfordian clay in the Bure underground research laboratory. In addition, the influence of temperature on the behaviour of high pH OPC based cement paste (CEM I) and different low-pH concrete formulations in contact with argillite from Tournemire has been studied by Lalan et al. (2016). Experiments performed at 70 °C showed a more pronounced degradation of the clay rock and an alteration of the cementitious material that was more pronounced in the low-pH cementitious material compared to the CEM I based material. Dolder et al. (2017, 2014) studied the influence of alkaline solutions on MX-80 bentonite. Similarly, González-Santamaría et al. (2020a) studied the morphological and compositional changes of bentonite after contact with three different alkaline solutions. Recently, Gaboreau et al. (2020) investigated perturbations in concrete after 13 years of contact with FEBEX bentonite. Wilson et al. (2021) present also an overview on many of these experimental results. In summary for the laboratory and in situ experiments mentioned above, which address cement/clay interactions for temperature ranges from 20 to 120 °C and interaction times from 1 month to 100 years, precipitation-dissolution-degradation fronts and related capillary porosity changes have been observed in a range of less than a millimeter to a few centimeter on both sides of the interface (Deissmann et al. 2021, Tab. 4-1), i.e. limited spatial interaction zones.

3.2 Experimental work at the Mont Terri rock laboratory

In the framework of the cement/clay Interaction **(CI) experiment at the Mont Terri** URL interactions between various types of cement and Opalinus clay or bentonite have intensely been studied (Mäder et al. 2017). Six main studies (Bernard et al. 2020a, Dauzeres et al. 2016b, Jenni et al. 2014, Lerouge et al. 2017, Mäder et al. 2017, Yokoyama et al. 2021) provided a detailed analysis of mineralogical changes taking place under realistic boundary conditions over periods of several years. Interfaces of Opalinus Clay with three different types of cementitious materials (based on OPC and two low-pH binders, namely ESDRED (60% CEM I + 40% silica fume) and low alkali cement (LAC, 90% CEMIII/B + 10% nanosilica) were investigated in these studies after 2.2, 4.9 and 10.2 years (Bernard et al. 2020a, Dauzeres et al. 2016a, Jenni et al. 2014, Lerouge et al. 2017, Mäder et al. 2017). Samples where OPC paste and ESDRED paste were in

contact with Opalinus Clay were studied by Bernard et al. (2020a). Interfaces of bentontite (MX-80 pellets) emplaced and saturated in boreholes and then in contact with OPC or LAC over 4.9 and 10 years were analysed by Yokoyama et al. (2021). Other materials such as high fly ash/silica fume OPC (developed in Japan) and "Supercontainer Cement" (CEM I 42.5N HSR with calcite aggregates, developed in Belgium) were also used to backfill boreholes, but these materials were not yet analysed so far.

Experiments such as the CI field experiment, or any other field and laboratory experiment, where two geochemically different materials are brought into contact, give in principle rise to Type I reactions as defined in Section 2.5.2. The dissolution of solids originally present is the source of solutes that will start to interdiffuse across the material interface. The exact location of precipitations will depend on the respective solute fluxes. Depending on the capacity (total amount) of a dissolving solid phase and the time, the type of solutes that interdiffuse may change with time, which may in principle also lead to a re-dissolution of newly precipitated phases, and thus possibly to a movement of precipitation fronts. Furthermore, depending on the total amounts of solid phases, the reactions could also appear as Type III reactions.

In samples where concrete materials were in contact with Opalinus Clay for 2.2 years, Jenni et al. (2014) observed a complex zonation with a partly strong Mg enrichment adjacent to the interface in both low-pH conscrete materials studied but not (or less) in OPC concrete, and a decrease of the calcium content linked to a decalcification of the initial low-pH cements (Fig. 3-1, Tab. 3-1). It was mentioned that the aggregates in the concrete or cracks partly affected the delineation of the zones, and accordingly also the determination of distances from the interface. In addition, a decrease in S close to the interface in the cementitious material occurred, and an enrichment of S ion in higher pH regions (away from the interface) was observed, possibly leading to formation of additional ettringite, AFm of AFt there. Consistently, the carbonated zones showed a reduced porosity, as determined from autoradiography measurements following the impregnation of dried samples with a ^{14}C labelled resin. However, the nature of the carbonate phases in low pH cementitious material remained unclear.

Dauzeres et al. (2016) confirmed the earlier work of Jenni et al. (2014) based on the analysis of samples where concrete and clay were in contact for 5 years. In this case, the degraded region in both studied low-pH cementitious materials extended over ~ 2–4 mm, with a Mg enrichment and decalcification close to the interface. The mineralogical phase associated with the Mg enrichment was identified as a gel-like Mg-Si phase (M-S-H). Lerouge et al. (2017) described the results obtained after 5 years of interaction between LAC concrete and OPA, with the interactions limited to a roughly 1 mm thick highly porous white crust developed on the concrete side. Quantitative mineralogical mapping provided evidence of a Mg-rich phase imbedded in the matrix of calcite, C-S-H and other cement phases. The Mg-rich phase was shown to be a tri-octahedral 2:1 phyllosilicate.

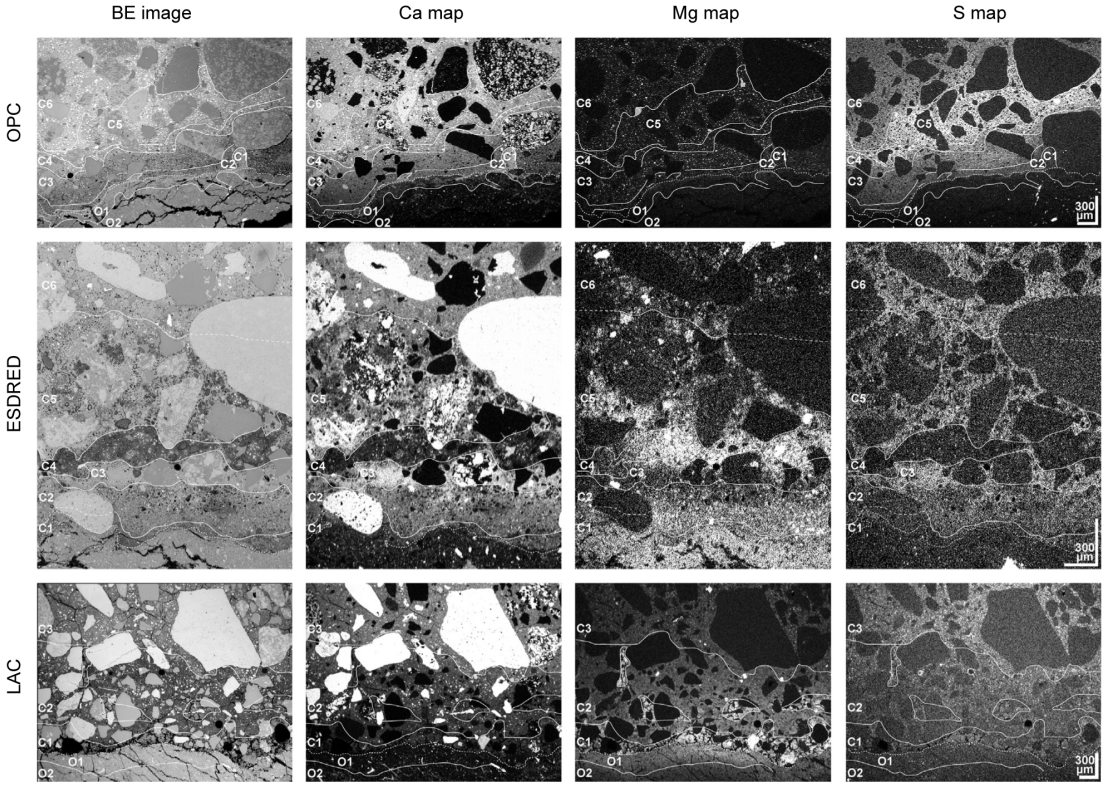

Fig. 3-1: SEM BE images and Ca, Mg, and S EDX maps of sections across the interfaces of Opalinus Clay with OPC concrete (top row), with ESDRED concrete (middle row), and with LAC concrete (bottom row) in samples from the Mont Terri CI experiment after two 2.2 years of interaction

Different zones identified in cement (C1-C6) and in OPA (O1-O2) are numbered and indicated by solid lines (dotted across aggregates); the cement/claystone interface is marked with a dotted line (reprinted from Jenni et al. 2014 with permission from Elsevier).

The results obtained in samples from the CI experiment with OPC concrete or ESDRED mortar contacting Opalinus Clay for 2.2 and 4.9 years are summarized by Mäder et al. (2017). While Ca enrichment and a weak increase of Mg and S was seen in Opalinus Clay near the interface contacting OPC after 2.2 years, this was no longer the case for samples that reacted 4.9 years (Tab. 3-2). It is unclear if the faint Mg enrichment observed in OPA at the very interface moved with time away from the interface. However, it was found in OPC mortar at 7 – 8 mm from the interface after 3.2 years, and in several older OPC concretes approximately at the same location (ages up to 10.2 years). Ca depletion on the OPC side was observed after 2.2 and 4.9 years. Also, the increase in S propagated further into the OPC after 4.9 years compared to 2.2 years. It must be mentioned that the very low water cement ratio of the 2.2 years OPC (w/c = 0.35) complicates a comparison with the 4.9 years sample (w/c = 0.8). The complex zonation shown in the OPC in Fig. 3-1 might be attributed to a delayed cement hydration, caused by the very low water content and an initial water flux into the slightly dried borehole surface layer. For Opalinus Clay in contact with ESDRED mortar (Tab. 3-3), alterations remained very similar after 4.9 years compared to 2.2 years, with mainly an enrichment in Mg near the interface. In the ESDRED mortar, the zonations became simpler after 4.9 years. While there were alternating zones with increasing and decreasing concentrations after 2.2 years, after 4.9 years a general depletion in Ca and enrichment in Mg up to a distance of about 1.4 mm, and a slight depletion in S in the same region were observed. The interpretation in terms of solute fluxes and processes by Mäder et al. (2017) is presented in Fig. 3-2.

Tab. 3-1: Main observations reported by Jenni et al. (2014) for various samples of cement-clay interfaces from the Mont Terri CI Experiment after an interaction time of 2.2 years

Sample	**Alterations in clay**	**Alterations in concrete/cement**
OPA/OPC	Ca enrichment in first ~ 250 µm Elevated calcite content in first 1 mm High Ca content in veins connected to cement Weak Mg and S enrichment near the interface Cation exchanger near interface is depleted in Mg, and enriched in Na, K; Ca not affected Partial degradation of sulfides (pyrite) to sulfates, hematite coating on pyrite	Carbonation near interface Decrease of Ca towards interface Slight Mg enrichment away from the interface S enrichment about 300 – 1'000 µm away from interface
OPA/ESDRED	Increased Ca and Mg in first 100 µm Weak increase of S in thin layer Cation exchanger depleted in Mg, enriched in Na near interface No porosity change (within detection limits)	Carbonation towards interface Decrease of Ca towards interface, but Ca maximum at ~ 300 – 600 ~ µm distance to interface Mg and S enrichment in zone behind Ca maximum
OPA/LAC	Clearly increased Mg in first 250 µm Weak increase of S in thin layer	Carbonation of interface area up to 1.5 mm or more Ca depletion near interface Mg enrichment in first 200 – 400 µm S increase away from interface (> ~ 1 mm)
General interpretation		
• Dissolution of portlandite in OPC due to lowering of pH. Temporarily Ca diffusion towards OPA. At the same time, diffusion of carbonate species from OPA into OPC, which react with Ca hydrates and may form calcite. Larger extent of zone(s) of carbonation in ESDRED, LAC compared to OPC because of increased diffusion (higher w/b ratio of cement material resulting in higher porosity). • Large gradient of Mg from OPA to cement material; leads to depletion of Mg on the exchanger of OPA, as well as with alite to formation of Mg hydrate (possibly hydrotalcite) in OPC and ESDRED. Further away from interface, Mg hydrate forms without alite (possibly M-S-H). In LAC, strong uptake of Mg near interface leads probably to M-S-H (intergrown with other hydrates). Thin Mg layer in OPA cannot be explained. • No clear evidence of zone of reduced porosity in OPA next to OPC, nor for mineralogical changes of smectites.		

Tab. 3-2: Characteristics of OPC-Opalinus Clay interface samples after 2.2 (2) and 4.9 (5) years of interaction as summarized by Mäder et al. (2017)

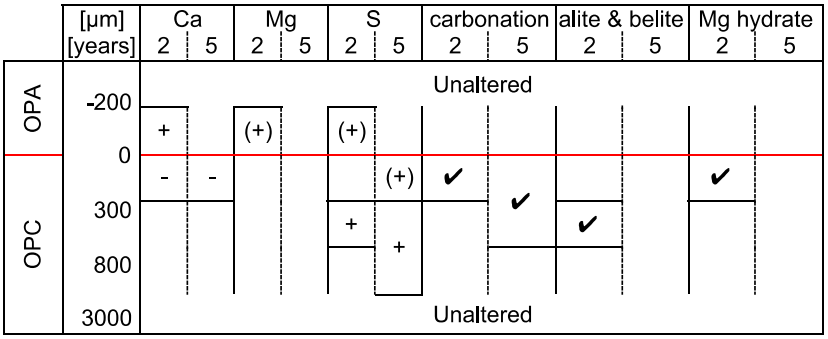

Empty cells: same characteristics as unaltered material. Approximate thickness of layers in µm is indicated

+, −, ✔ represent "enriched", "depleted", and "present", relative to the unaltered OPA or cement far from interface. (+): Small enrichment

Tab. 3-3: Characteristics of ESDRD-Opalinus Clay interface samples after 2.2 (2) and 4.9 (5) years of interaction as summarized by Mäder et al. (2017)

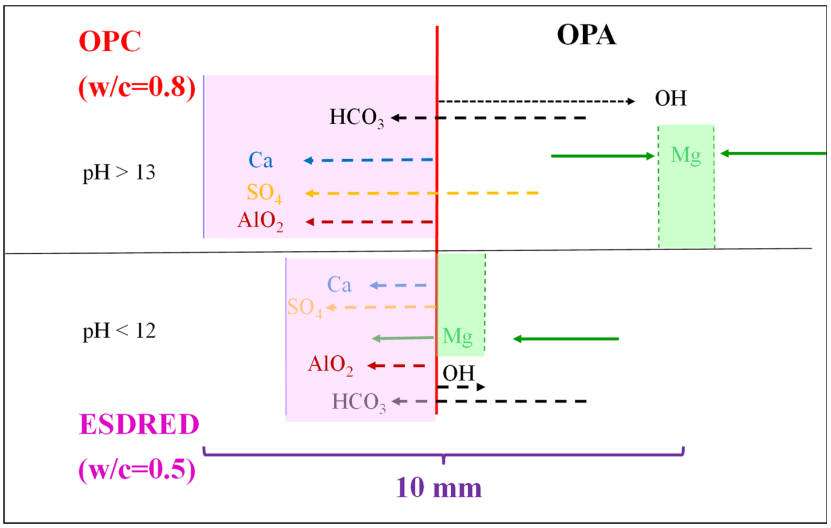

Fig. 3-2: Interpretation of the observations for samples from the CI experiment with OPC concrete or ESDRED mortar and Opalinus Clay (OPA) in terms of solute fluxes resulting in the observed element enrichments

Mäder et al. (2017)

Bernard et al. (2020a) performed SEM/EDS analysis as well as µ-XRD mapping to locate and identify the mineral phases on each side of interfaces between OPC paste or ESDRED paste and Opalinus Clay. These measurements were done on samples that reacted for 3.2 years. The more advanced technique of µ-XRD mapping compared to SEM/EDS measurements, and the use of cement pastes instead of concretes, were important in order to derive additional insights into the processes. In addition, they also investigated some OPC mortar-OPA samples. They reported that the hydrates portlandite, ettringite and C-S-H present in the Portland cement (PC) paste were dissolved in contact with the Opalinus Clay (OPA) up to different depths after 3.2 years (cf. Tab. 3-4; ~ 1 mm for ettringite; ~ 0.2 mm for portlandite; complete dissolution of C-S-H up to 0.1 mm and less complete/less visible dissolution up to ~ 1-mm), and that the ettringite from ESDRED seemed to be destabilized to a larger distance (≥ 3 mm). In contrast to former studies, calcite could not be clearly observed at the interface OPC paste-OPA with µ-XRD, but was well developed at the interface ESDRED paste-OPA. Calcite was, however, seen in more conventional bulk XRD measurements of OPC mortar that contacted OPA (at a distance of ~ 3 mm, but not at 9 mm). Dissolution of clay minerals remained below the detection limit.

From their SEM/EDS measurements, Bernard et al. (2020a) could confirm a Mg enrichment within the OPA that contacted OPC paste, detached from the interface (~ 2 – 3 mm, only at an edge of the sample), similarly as reported previously by Mäder et al. (2017). These latter authors observed a Mg enrichment in OPA ~ 6 – 8 mm behind the interface of OPA-OPC cement samples that reacted for 4.9 years and mentioned that the enrichment is likely due to a precipitation of a new phase, as the enrichment is clearly above Mg contents of a fully Mg-exchanged clay matrix. The µ-XRD measurements of Bernard et al. (2020) within the Mg enriched zone did, however, not reveal any changes with respect to the mineral proportions of chlorite, illite, quartz, brucite and kaolinite. It could be hypothesized only that the enrichment may be related to a nano-crystalline M–S–H phase or a poorly crystalline hydrotalcite. The source of Mg is very likely the original clay exchanger, where Mg has been replaced by Ca from the cement.

Tab. 3-4: Observations from SEM/EDS and µ-XRD measurements reported by Bernard et al. (2020) for Opalinus Clay (OPA)-OPC paste and for Opalinus Clay-ESDRED paste interface samples from the Mont Terri CI Experiment after an interaction time of 3.2 years

Sample	**Alterations in OPA**	**Alterations in cement paste**
OPA/OPC paste	SEM/EDS: • Slight Ca enrichment near interface • Decrease of S (up to ~ 3 mm, sample limit) • Mg enrichment at ~ 2 – 3 mm (edge of sample) µ-XRD: • No detection of calcite near interface • No changes of mineral proportions of crystalline chlorite, illite, quartz, brucite and kaolinite within Mg enriched zone	SEM/EDS: • Ca decrease near interface • Slight increase of Si, Na, Al, S near interface µ-XRD: • No detection of calcite near interface • Disappearance of portlandite up to ~ 0.2 mm • Disappearance of ettringite up to ~ 1 mm • Disappearance of C-S-H up to ~ 0.1 mm, reduction of C-S-H up to ~ 1 mm
OPA/ESDRED paste	SEM/EDS: • Slight increase of Ca near interface • Increase of Mg up to ~ 1 mm µ-XRD: • No detection of calcite near interface	SEM/EDS: • Decrease of Ca up to ~ 1 mm • Decrease of Cl up to ~ 1.5 mm • Increase of Na and Mg up to ~ 0.5 mm • Slight increase of S near interface µ-XRD: • Destabilization of ettringite up to ~ 3 mm or more • Detection of calcite near interface

Yokoyama et al. (2021) divided the bentonite part of core samples from the Mont Terri CI experiment into slices of 3 – 5 mm thickness in order to obtain a profile of its mineralogical composition towards the interface with OPC or LAC after 4.9 and 10 years of interaction. In addition, elemental distributions were measured (Fig. 3-3). Regarding the mineral composition of bentonite, they reported that cristobalite was dissolved within a range of 10 mm from the interface in both LAC/MX-80 and OPC/MX-80 samples after 4.9 years, while calcite precipitated near the interface in OPC/MX-80 samples (Tab. 3-5). The range where cristobalite was dissolved did advance only slightly in LAC-MX and remained about identical after 10 years of interaction compared to 4.9 years of interaction. Gypsum, initially present in MX-80, did also dissolve near the interface. An increase of Ca was observed in MX-80 near the interface, while a decrease was detected towards the interface in the cement material in both sample types. Furthermore, secondary products containing Mg (e.g., M-S-H) precipitated in the first 20 mm of the bentonite. No changes in the mineralogical nature of montmorillonite (i.e., the formation of illite or beidellite, increase in layer charge) were detected, however, for samples that reacted 4.9 or 10 years.

All alterations observed by Yokoyama et al. (2021) in bentonite developed within the first 4.9 years, and very limited progress was observed for the subsequent 5 years. It was hypothesized that this change in reaction rate could be related either to a reduction of porosity in the bentonite by newly formed products that slows down further mass transfer, or to a comparably rapid initial transfer of hydration water from the cement material towards the initially unsaturated bentonite. No discrimination between the two hypotheses was possible from the available data.

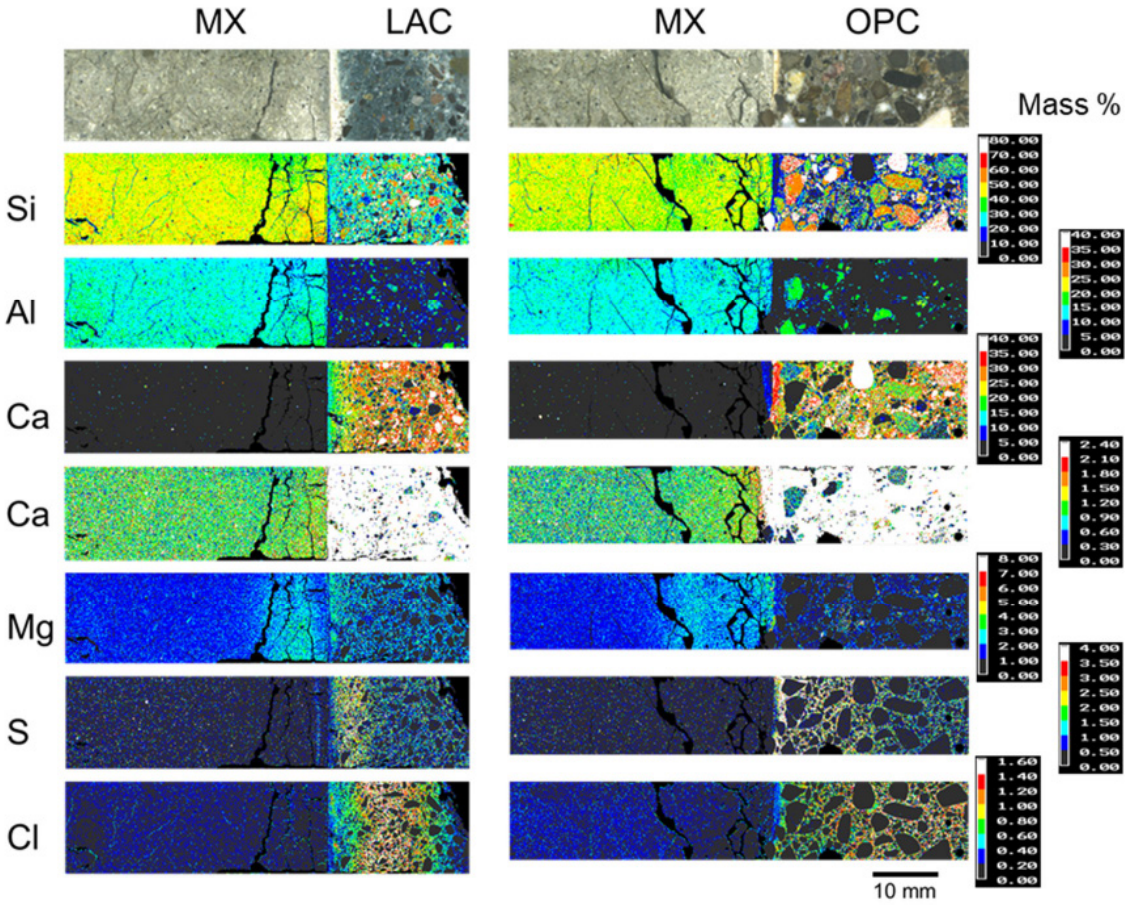

Fig. 3-3: Elemental distributions in samples from the Mont Terri CI experiment including MX-80 in contact with LAC or OPC for 10 years
Taken from Yokoyama et al. (2021)

Tab. 3-5: Main observations reported by Yokoyama et al. (2021) for various interface samples from the Mont Terri CI Experiment after an interaction time of 4.9 and 10 years

Sample	**Alterations in OPA**	**Alterations in cement paste**
OPA/OPC paste	SEM/EDS: • Slight Ca enrichment near interface • Decrease of S (up to ~ 3 mm, sample limit) • Mg enrichment at ~ 2 – 3 mm (edge of sample) µ-XRD: • No detection of calcite near interface • No changes of mineral proportions of crystalline chlorite, illite, quartz, brucite and kaolinite within Mg enriched zone	SEM/EDS: • Ca decrease near interface • Slight increase of Si, Na, Al, S near interface µ-XRD: • No detection of calcite near interface • Disappearance of portlandite up to ~ 0.2 mm • Disappearance of ettringite up to ~ 1 mm • Disappearance of C-S-H up to ~ 0.1 mm, reduction of C-S-H up to ~ 1 mm

Sample	**Alterations in bentonite**	**Alterations in concrete/cement**
MX-80/OPC	Increase of Ca near the interface Increase of Mg in first 20 mm Dissolution of cristobalite within first 10 mm Precipitation of calcite near the interface Dissolution of gypsum near the interface No change of mineralogical nature of montmorillonite	Decrease of Ca towards the interface Increase of S in first ~ 15 mm after 10 a Increase of Cl in comparably wide zone near the interface No significant change of montmorillonite content observed (only very weak tendency of decrease towards the interface)
MX-80/LAC	Increase of Ca near the interface Increase of Mg in first 20 mm, precipitation of Mg phase (e.g., M-S-H) Dissolution of cristobalite within first 10 mm after 4.9 a, slightly more exten§ded after 10 a Dissolution of gypsum near the interface No change of mineralogical nature of montmorillonite	Decrease of Ca towards the interface Increase of S in first ~ 5 mm the interface after 10 a Increase of Cl in first ~ 15 mm No significant change of montmorillonite content observed
General interpretation		
• Probably precipitation of newly formed Mg phase in first 20 mm of MX-80 (e.g., M-S-H, hydrotalcite-like phase) • Precipitation of secondary phases containing Ca and Mg • Diffusion of S and Cl from MX-80 pore water into cement material; possibly precipitation of new phase (e.g., monosulfate, ettringite, Friedel's salt)		

3.3 Laboratory experimental work at PSI

This section summarizes the laboratory work on cement-clay samples performed at the LES, PSI. The work was done within the framework of two PhD theses (Luraschi 2022, Shafizadeh 2019), and the data are partly published (Luraschi et al. 2020, Shafizadeh et al. 2020, 2015).

3.3.1 Motivation for experimental work at the laboratory scale

Field scale experiments (see Section 3.2) have shown that alterations at cement-clay interfaces strongly depend on the specific material properties of the involved components such as their chemical composition, their capillary porosity and their diffusion coefficient. Model simulations help to determine relevant reaction pathways, but they need to be supported by independent experimental observations. Data from field sites provide information on intermediate to large space and time scales, but heterogeneities at these scales, the complexity of involved natural materials, as well as not exactly known boundary and initial conditions makes the interpretation of observations partly difficult. Accordingly, there is a need for small-scale, well-controlled laboratory experiments with comparably simple materials. Such experiments on model interface samples help to address questions such as i) which reaction pathways are followed or dominating in a given system, ii) which phases are responsible for alteration of the porosity (if it occurs), and iii) how do the diffusion properties across such interfaces evolve with time. While many research works address the questions of dominating reactions and observed mineral changes at interfaces, few and mostly indirect experimental data exists on the evolution of the transport properties, and notably on the evolution of the solute diffusion coefficients on both sides of the material interfaces. Accordingly, an experimental setup was developed (Luraschi 2022, Luraschi et al. 2020, Shafizadeh 2019, Shafizadeh et al. 2020, 2015) that allowed both, to collect data on the temporal variation of the diffusion coefficient for samples consisting of various interface materials, as well as on the mineralogical alterations that are responsible for the variation.

3.3.2 Overview on investigated samples and methods

Several small samples that represent a material interface and consist of a plug of 5 mm diameter and 5 mm length of each material (clay and cement, Fig. 3-4) were prepared in the laboratory and let react for several years. The samples, confined in a Teflon sleeve and an aluminium sample holder, were saturated with a clay or cement pore water, respectively, and kept under nitrogen atmosphere to reduce carbonation. The samples were generally (but with interruptions) in contact with larger reservoirs filled with the corresponding clay and cement pore waters.

In a first phase, this setup with two material interfaces corresponds to a reaction setup of Type I according to the classification in 2.5.2. As the total amount of solids is limited by the small size of the samples, it is possible that a certain solid component (e.g., portlandite) may be completely dissolved during the experiment. The reaction setup may then change to Type II, where solute concentrations are defined through the external solution reservoirs.

All used interface samples represent simplified model systems of materials and conditions which are expected in real disposal sites. Laboratory tests were conducted starting with relatively simple mineralogical composition setups, and then with setups with gradually increasing complexity. Simplified model systems provide an insight to the main underlying mechanisms and results can be interpreted more easily compared to complex natural systems.

A first series of interface samples (samples C, D, cf Tab. 3-6) was prepared from high porosity hardened OPC paste and Na montmorillonite. The OPC had a porosity of ~ 0.63 as measured by mercury injection (cf. Tab. 3-7); it is considered that this value represents the total, water-filled porosity of the material, even though it is unclear to which degree it also represents any gel porosity. The clay had a bulk dry density of 1.31 to 1.67 g cm^{-3} and a porosity between 0.40 and

0.53 as calculated from the bulk and grain densities. These values include all types of pores, including interlayer and external (interparticle) pores. These samples were monitored over a time of 6 years at ambient temperatures. In a second series (E), samples consisting of two different cement types (OPC paste and ESDRED mortar) were brought in contact with Opalinus Clay and MX-80 bentonite, respectively. These samples were investigated over a period of 2 years at ambient temperatures. Finally, a third series with additional samples of OPC paste in contact with Na-montmorillonite, bentonite and Opalinus Clay was prepared (samples H). These samples were let react at an elevated temperature of 70 °C and were monitored for a period of 8 months.

Several samples were analysed in a non-destructive way by neutron imaging at the ICON beamline (Paul Scherrer Institut, Switzerland), in order to infer localized changes in water content, which is a proxy for total porosity. The derivation of porosities from the neutron images is not trivial. It requires separate calibrations for the cement and the clay part, which limits the application to reacting systems. Nevertheless, total porosity changes have been successfully quantified following the methodology described in Shafizadeh et al. (2020).

Through-diffusion experiments with HTO and ^{36}Cl as tracers were performed for many of the samples at various times to detect potential changes in transport properties. The setup is described in Shafizadeh (2019) and Luraschi et al. (2020). Effective diffusion coefficients for the whole sample are obtained in this way. Assuming that the samples are characterized by regions of different properties in series, it is possible to back calculate diffusion coefficients of a specific region, provided all other diffusion coefficients are known (cf. Luraschi et al. 2020). Diffusion properties of clearly altered zones were calculated in this way, assuming that the rest of the samples did not experience major changes.

Mineralogical investigations (SEM/EDX, TGA, XRD) were performed after termination of the experiments. At later stages, non-destructive X-ray tomography was also performed for some samples to delineate regions with mineralogical/structural changes.

Tab. 3-6 below contains an overview on the investigated samples and on the measurements that were performed. Tab. 3-7 presents geometrical parameters, bulk dry densities and porosities of samples on which diffusion coefficients were measured, and Tab. 3-7 gives the pore waters used in the experiments. Further details on the applied methods and on results can be found elsewhere (Luraschi 2022, Luraschi et al. 2020, Shafizadeh 2019, Shafizadeh et al. 2020, 2015).

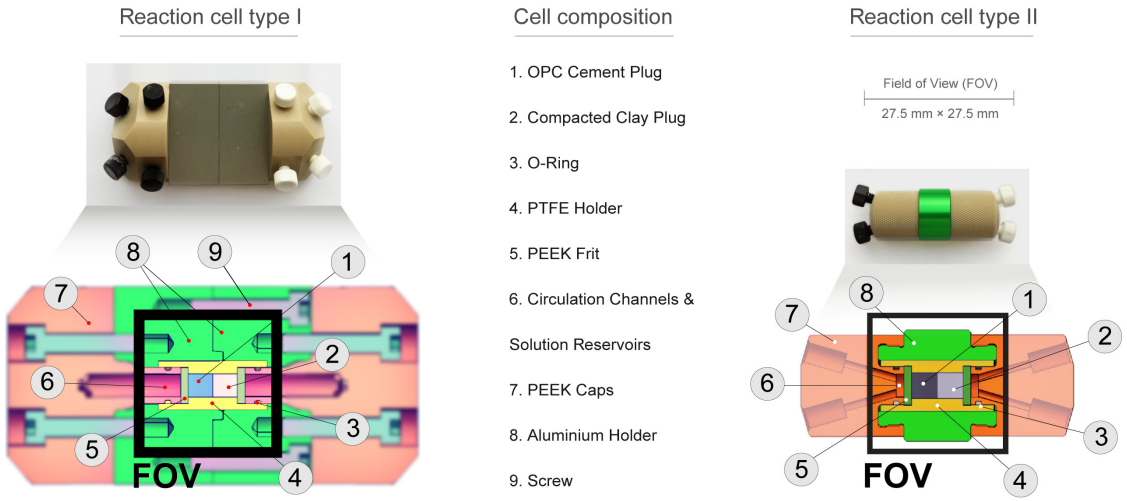

Fig. 3-4: Two generations of diffusion cells developed to investigate interactions between clay and cement

The cell Type II was developed after test measurements with cell Type I. Most of the samples were kept in Type II cells. The clay sample (bright grey area) and the cement sample (dark gray area) have a diameter of 5 mm and a length of 5 mm each. The black squares define the Field of View for neutron imaging.

Shafizadeh (2019), Shafizadeh et al. (2020)

Tab. 3-6: Samples prepared to investigate cement-clay interactions at the laboratory scale at the LES (PSI) and overview on the performed measurements

Details can be found in Luraschi (2022), Luraschi et al. (2020), Shafizadeh (2019), Shafizadeh et al. (2020, 2015). OPC is hardened ordinary Portland cement paste, OPA Opalinus Clay, ESDRED a low pH cement paste. IC stands for ion chromatography.

Sample	**Interface type**	**Performed experiments**	**Comment**
C1	Na Montmorillonite-OPC	Diffusion exp., Neutron imaging	HTO + ^{36}Cl as tracers
C3	Na Montmorillonite-OPC	Diffusion exp., Neutron imaging, X-ray tomography, XRD	HTO + ^{36}Cl as tracers
C4	Na Montmorillonite-OPC	Diffusion exp., Neutron imaging	HTO + ^{36}Cl as tracers
C5	Na Montmorillonite-OPC	Diffusion exp., Neutron imaging	HTO + ^{36}Cl as tracers
C8	Na Montmorillonite-OPC	Diffusion exp., Neutron imaging	HTO + ^{36}Cl as tracers
C11	Na Montmorillonite-OPC	Diffusion exp., Neutron imaging	HTO + ^{36}Cl as tracers
C15	Na Montmorillonite-OPC	Diffusion exp., Neutron imaging	HTO + ^{36}Cl as tracers
C20	Na Montmorillonite-OPC	Diffusion exp., Neutron imaging	HTO
C25	Na Montmorillonite-OPC	Neutron imaging, SEM/EDX	
C29	Na Montmorillonite-OPC	Neutron imaging, SEM/EDX	
D5	Na Montmorillonite-OPC	SEM/EDX	
D6	Na Montmorillonite-OPC	SEM/EDX Diffusion exp., Neutron imaging	HTO + ^{36}Cl as tracers

Tab. 3-6: Cont.

Sample	Interface type	Performed experiments	Comment
D11	Na Montmorillonite-OPC	Diffusion exp.	HTO + ^{36}Cl as tracers
E4	OPA-OPC	Diffusion exp., Neutron imaging	HTO
E13	OPA-ESDRED	Diffusion exp., Neutron imaging	HTO
E16	OPA-ESDRED	Diffusion exp., Neutron imaging	HTO
E17	OPA-ESDRED	Diffusion exp., Neutron imaging	HTO
E20	OPA-OPC	Diffusion exp., Neutron imaging, X-ray tomography	HTO
E21	OPA-OPC	Diffusion exp., Neutron imaging, X-ray tomography	HTO
E22	Bentonite-OPC	Diffusion exp., Neutron imaging	HTO + ^{36}Cl as tracers
E23	Bentonite-OPC	Diffusion exp., Neutron imaging, X-ray tomography	HTO + ^{36}Cl as tracers
E24	Bentonite-ESDRED	Diffusion exp., Neutron imaging, X-ray tomography	HTO + ^{36}Cl as tracers
E25	Bentonite-ESDRED	Diffusion exp., Neutron imaging	HTO + ^{36}Cl as tracers
E26	Bentonite-OPC	Diffusion exp., Neutron imaging	HTO + ^{36}Cl as tracers
P_Na	Na-montmorillonite	Diffusion exp., IC measurements: evolution of the reservoir pore water	HTO + ^{36}Cl as tracers
P_Ca	Ca-montmorillonite	Diffusion exp., IC measurements: evolution of the reservoir pore water	HTO + ^{36}Cl as tracers
P_K	K-montmorillonite	Diffusion exp., IC measurements: evolution of the reservoir pore water	HTO + ^{36}Cl as tracers
P_Be	Benonite	IC measurements: evolution of the reservoir pore water	
HT_1/2	Na Montmorillonite-OPC	pH + IC measurements: evolution of the reservoir pore water	Exp. under nitrogen atmosphere at 70 °C
HT_3/4	Bentonite-OPC	pH + IC measurements: evolution of the reservoir pore water	Exp. under nitrogen atmosphere at 70 °C
HT_5/6	OPA-OPC	pH + IC measurements: evolution of the reservoir pore water	Exp. under nitrogen atmosphere at 70 °C

Tab. 3-7: Characteristics of the OPC paste and the Na montmorillonite in samples used for diffusion experiments

Sample	**Interface contact**	**Clay**			**Cement**		
		Length [mm]	**Dry density** [kg/m^3]	**Porosity**[1] [-]	**Length** [mm]	**Dry density** [kg/m^3]	**Porosity**[2] [-]
C1	14.03.2013	5.5	1'670	0.40	4.5	700	0.63
C3	25.09.2013	5.0	1'500	0.46	5.0	700	0.63
C4	25.06.2013	5.5	1'310	0.53	4.5	700	0.63
C5	25.09.2013	5.1	1'440	0.49	4.9	700	0.63
C8	02.06.2014	4.7	1'540	0.45	5.3	700	0.63
C11	13.06.2014	5.0	1'490	0.47	5.0	700	0.63
C15	13.06.2014	5.0	1'450	0.48	5.0	700	0.63
C20	18.07.2014	4.9	1'520	0.46	5.1	700	0.63
D6	25.09.2017	5.0	1'560	0.44	5.0	700	0.63
D11	06.10.2017	5.0	1'530	0.45	5.0	700	0.63

[1] Calculated from the dry density using a grain density of 2'800 kg m^{-3}
[2] Determined by MIP (Sarott et al. 1992)

Tab. 3-8: Composition of the used synthetic pore water (total concentrations) for OPC (Wieland et al. 1998), Na-montmorillonite (Shafizadeh et al. 2020), ESDRED mortar (Dolder et al. 2014), MX-80 Benonite (Bradbury & Baeyens 2002; adapted for 1'500 kg m^{-3} dry density) and Opalinus Clay (Mäder et al. 2017)

	OPC [mM]	**ESDRED**[1] [mM]	**Na-montmorillonite** [mM]	**Bentonite, MX-80** [mM]	**Opalinus Clay** [mM]
Na	114	24	300	243	241
K	180	12	-	1.2	1.6
Ca	1.6	26	-	9.5	2.5
Mg	-	-	-	7.1	17
Cl	-	-	300	67.5	300
S^{VI}	3	2	-	104	14
Al	0.05	-	-	-	-
Sr	-	-	-	0.08	0.51
$C_{org.}$	-	-	-	0.88	0.476
Formate	-	66	-	-	-
pH	13.3	11.3	8.7	8	7.6

[1] For ESDRED pore water Na, Ca and K are present as formate, according to Dolder et al. (2014).

3.3.3 Results for Ordinary Portland Cement (OPC) – Na montmorillonite samples

3.3.3.1 Evolution of the porosity

Several OPC-Na montmorillonite samples were repetitively investigated using neutron imaging to derive the porosity evolution. Data for up to 5.3 years of interaction are available. In most samples, clear changes of the volumetric water content, which can be derived from the neutron images and serves as a proxy for porosity for the saturated samples, were detected. The porosity was, however, never reduced to zero, as discussed in detail below.

Figs. 3-5 and Fig. 3-6 illustrate typical changes for two samples (C1 and C5). In these samples, the total porosity on the cement side of the interface tended to increase with increasing reaction time, accompanied by a porosity reduction on the clay side of the interface. Fig. 3-7 shows a closer view of the interface for these two samples at select reaction times. The porosity in the cement and clay regions near the interface changed differently over time, very likely due to dissolution and precipitation reactions. For sample C1, the region of increased porosity in the cement extended up to ~ 2 – 3 mm or more within the 5.3 years, whereas the region of decreased porosity in the clay extended up to ~ 2 mm. For sample C5, the extents were smaller, in the order of ~ 1 mm in the cement and ~ 1 – 2 mm in the clay within ~ 300 d. The shorter extents are related to the shorter interaction time, but the low-porosity zone in the clay of sample C5 was generally narrower compared to that in sample C1. Interestingly, the extent of the low-porosity zone in the clay remained about constant at times > 600 d, or at least only minor changes were visible even after 1950 d: the black and light blue curves in Fig. 3-6 (bottom right) for 4.6 and 5.3 years, respectively, show only a small further reduction of the porosity in this region compared to the situation at 599 d. It can be hypothesized that the decrease of total porosity reduced the further exchange of solutes across the interface slowing down all underlying processes, and thus also lowered further reactions in this area. The results of these samples are discussed more in detail in the following paragraphs.

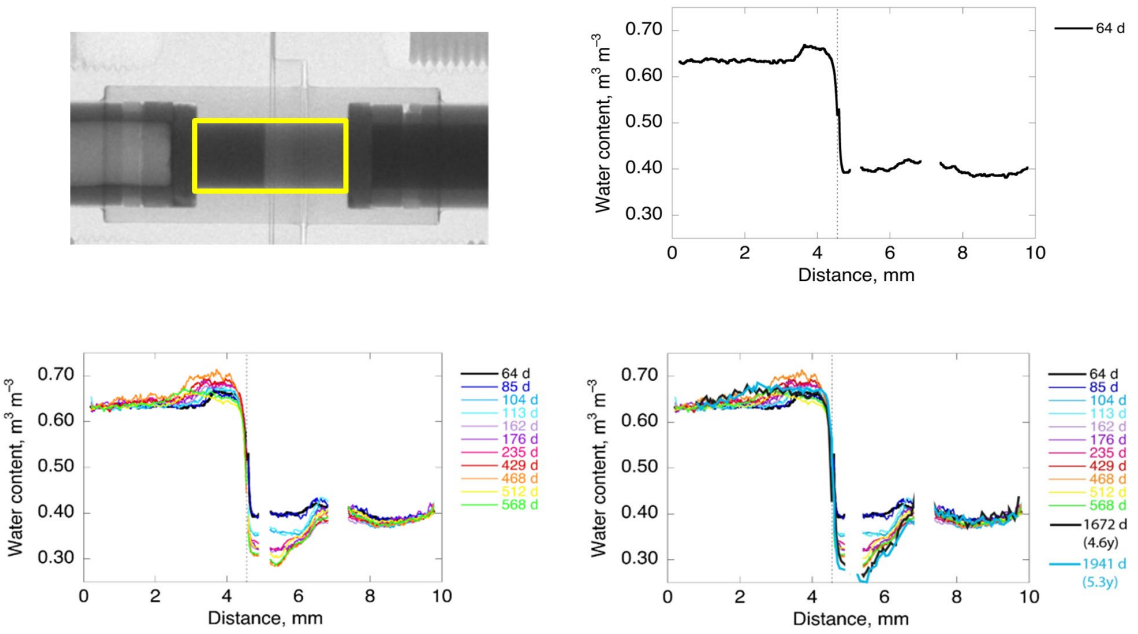

Fig. 3-5: Evolution of the water content (a proxy for total porosity) in the OPC (left) – Na montmorillonite (right) sample C1 over a time of 5.3 years

Top left: 2D neutron radiography from which the water content profiles was derived; the yellow rectangle represents the zone of interest, with the cement on the left and the clay on the right. Top right: Water content profile after 64 d of interaction. Bottom left and right: Water content profiles up to 586 d and up to 5.3 years, respectively. Regions blanked out were artefacts created by the joints of the aluminium sample holder of cell Type I.

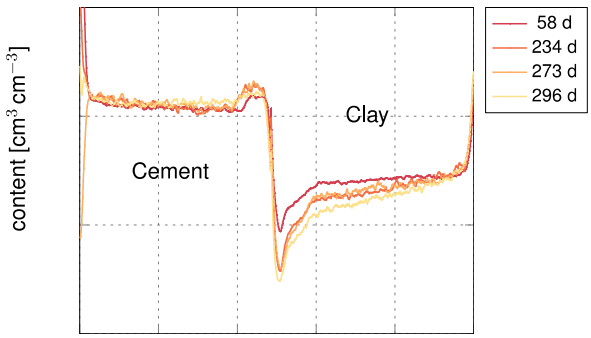

Fig. 3-6: Time evolution of the water content in the OPC-Na montmorillonite sample C5 over a time of ~ 300 days

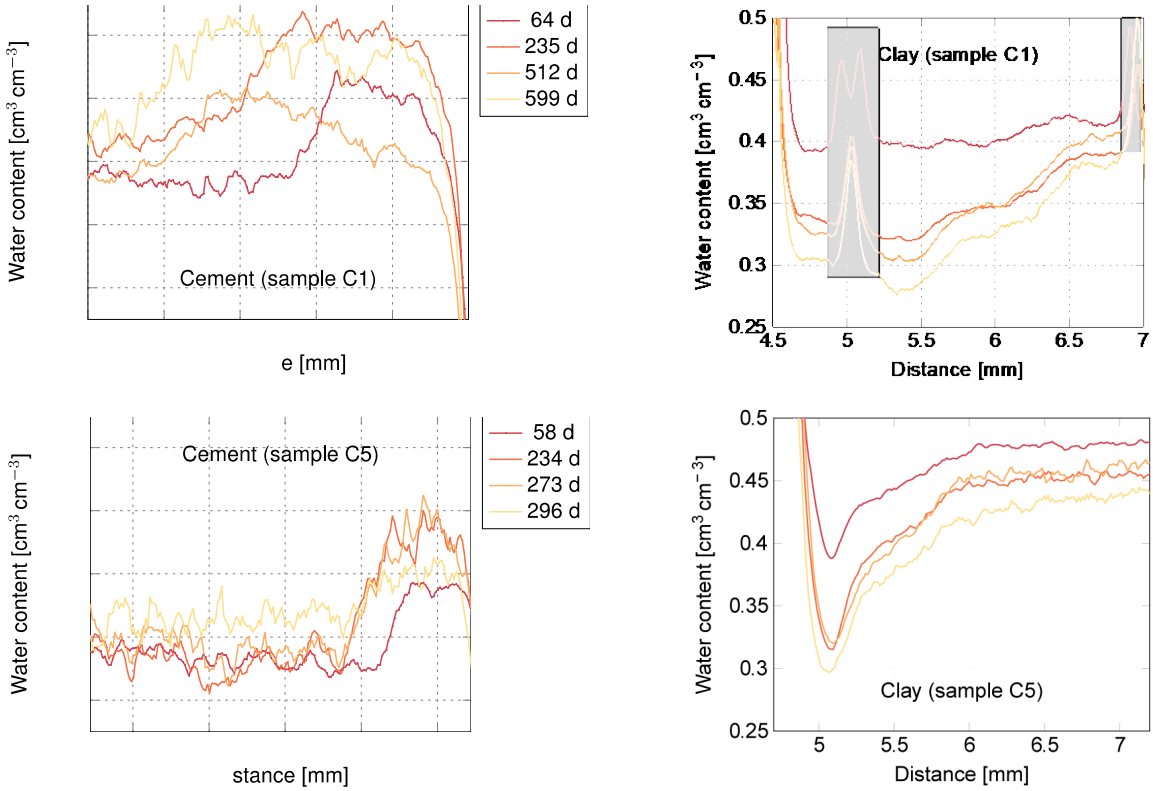

Fig. 3-7: Details of the time evolution of the water content in the OPC-Na montmorillonite samples C1 and C5

Top left and right: Cement and clay part of sample C1, respectively. Bottom left and right: Cement and clay part of sample C5, respectively. Two regions (near 5 mm and 7 mm) with artefacts originating from joints of the sample holders are grayed out in the top right plot; these joints were eliminated in the later used modified sample holders (Shafizadeh 2019).

The evolution of the extent of the alteration zone with time is illustrated in Fig. 3-8. It shows the locations of the porosity fronts as a function of time in cement and clay for samples C1 and C5. The location of the front was defined as midpoint of the steep increase or decrease in porosity, and the error bars capture the approximate width of this front. The front position on the cement side in sample C1 advanced steadily with time up to the last plotted point after about 600 days, where it reached a distance of 2 mm. At the last measurement times of ~ 4.6 years and ~ 5.3 years (positions not shown), the front has clearly further advanced to a distance of about 2.5–3 mm from the interface, but has become relatively diffuse and shows again a somewhat lower porosity compared to earlier maximum values. For sample C5, the front propagates somewhat slower compared to sample C1. Sample C1 had the highest initial montmorillonite density (and corresponding lowest initial montmorillonite porosity). This may affect the rate of dissolution reactions on the cement side, but there are various feedback mechanisms that could play a role and affect the different extents of this (net) dissolution zone in the cement.

The relation between the position of the porosity front in the cement and the reaction time can be approximately described here by the square root of time law:

$$x \approx \sqrt{D_a t}\,,$$

where x is the distance between the diffusive front and the interface, D_a is an apparent diffusion coefficient, and t is the reaction time since interface contact. An apparent diffusion coefficient D_a is generally defined as effective diffusion coefficient divided by the rock capacity (which includes the sorption capacity) and thus generally characterizes the transient diffusive transport of a reacting, retarded solute. The D_a as used here, however cannot be related to a retardation coefficient, as in the case of transport of a linearly sorbing tracer; it just very broadly characterizes the approximate transient behaviour of the reaction front. Cement-clay interactions involve strongly non-linear, time-dependent reactions, so using a constant D_a for the front evolution on the cement side over 600 d (solid blue line in Fig. 3-8) is a strong oversimplification. Looking at the front propagation within the cement more in detail, it appears that there are two major transport regimes during the 600 d of this experiment (Fig. 3-8 – dashed blue line). The reactive transport front advances up to a distance of about 1.5 mm during the first 200 d, then remains unchanged for the next 200 d, starts to propagate up to 2 mm in the following 200 d and slows down again.

The evolution of the interface is different on the clay side. There, the position of the front of reduced porosity appears to be more or less stagnant during the entire period of observations. Already at the first measurement after two months (64 days), the front was located at about 2 mm from the interface. It seems that the zone with perturbed porosity had been early formed as a result of the interface contact, but this zone did then not expand further during a reaction time of up to about 600 days, even though reactions within this zone (e.g., porosity reduction) further proceeded. So, the front remained rather sharply delimited on the clay side, and it did not advance any further from the last point shown at 600 d even after ~ 5.3 years (points not shown).

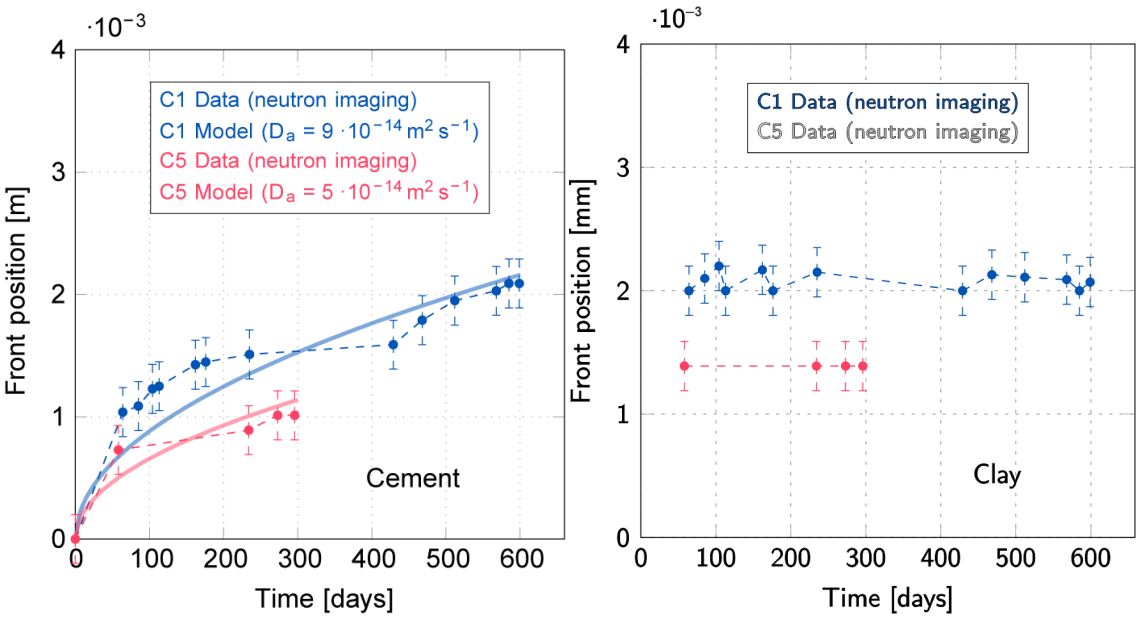

Fig. 3-8: Advancement of the porosity fronts away from the interface as a function of time in samples C1 and C5

Left: Front position in cement, Right: Front position in clay, both estimated as distance of midpoint of steep porosity change to the interface. The model curves in the left figure are a strong oversimplification (see text for discussion).

The changes of porosity values with time at three different locations within the cement and the clay, respectively, derived from the neutron radiographs are presented in Fig. 3-9. The porosity tended to alter more in the areas near the interface compared to the areas far away from it for both cement and clay. The amount of net porosity change is higher for the clay side compared to the cement side.

The porosity trends in sample C1 seem to be more or less monotonic in both, cement (increasing) and clay (decreasing), up to about 450 days. Then, the trend appears to reverse on both sides, with a porosity decrease in cement and a porosity increase in clay, up to about day 512. These temporary inversions of the trends may be real (e.g., caused by precipitation of newly formed phases in the cement and redissolution of phases in the clay), but they could also represent a measurement artefact (e.g., calibration problem). The inversions are strongest on the cement side close to the interface, and weaker further away from the interface and on the clay side, which could indicate that they are indeed related to local transport and reaction processes. Such changes of trends suggest that different reactions start to dominate at different times. While dissolution and precipitation reactions may occur in parallel, the observation in terms of the porosity, i.e., the sum parameter, just indicates that on the cement side, dissolution mostly – with the exception around day 500 – outweighs precipitation during the experiment, whereas on the clay side, precipitation mostly outweighs dissolution.

Interestingly, not all investigated samples did show the same reaction pattern. For some samples, nearly no changes in porosity were observed, or changes were only visible on the clay side, or appeared to be less strong in the local magnitude but more extended in space (Fig. 3-10). The reasons that led to the different patterns of reaction are not clear. It is possible that small variations of material parameters between samples (e.g. clay density and porosity, carbon content in the cement), or small variations of parameters within a given sample (microstructural heterogeneities) may favour the development of one or the other type of pattern. The different patterns may thus be related to the variability of the process, which is related to the variability of the parameters. As an example, the comparably weak, but extended reactions seen in sample C8 on both sides of the interface (Fig. 3-10 top) could be related to comparably large diffusion coefficients in the clay, which lead to less localized reactions compared to sample D6 (Fig. 3-10 bottom). The same may be true for sample C29 (Fig. 3-10 bottom), but there, additional measurement times would be required to arrive to a clear conclusion with regard to the reaction pattern.

In any case, the different patterns may, at least to some degree, also be related to technical limitations of the experiments. For instance, radiographs smooth and average out possible 3D heterogeneities in a 2D domain. If the contact surface is not at an angle of 90° with respect to the cylinder axis, the projection of the interface may, depending on the rotational position of the sample during the neutron measurement, the measured signal is superposition of signals from clay and cement domains.

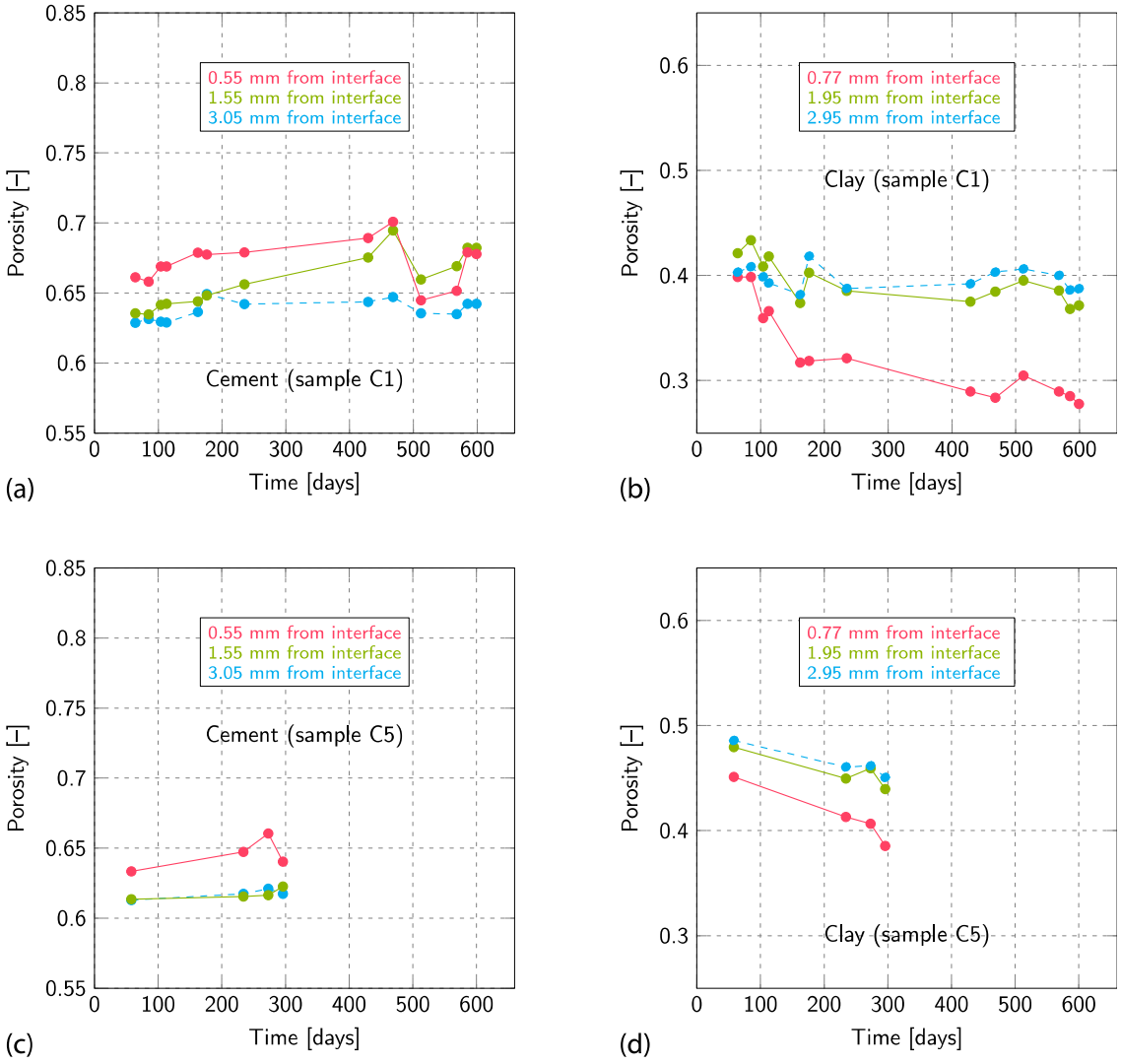

Fig. 3-9: Changes of total porosity as a function of reaction time at different positions in cement (left plots) and clay (right plots) for samples C1 (top row) and C5 (bottom row)

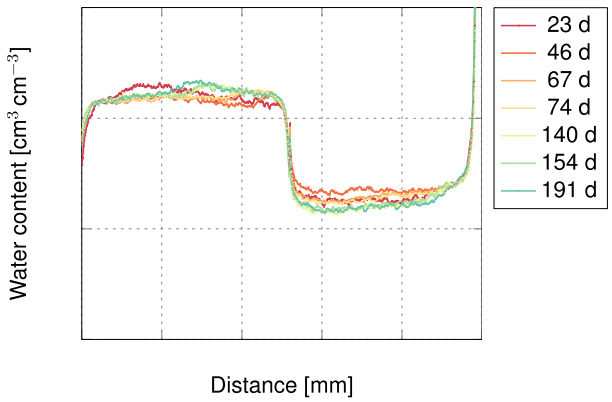

Fig. 3-10: Profiles of the water content in the OPC-Na montmorillonite sample C8 after various interaction times

3.3.3.2 Visualization of reaction fronts by X-ray micro-tomography

Several cement-clay samples were investigated at EMPA Dübendorf by means of X-ray micro-tomography in order to obtain 3D information on the evolution of the different interface samples in a non-destructive way. Depending on the sample, the exposure time was between 45 and 120 minutes. During this time the samples were exposed to air. Tab. 3-9 provides an overview of the samples investigated with X-ray tomography, as well as a short summary of the main observations (please note that results for samples consisting of other materials than OPC and Na-montmorillonite will be discussed in a following section).

The OPC-Na montmorillonite sample C3 was previously investigated by means of neutron imaging: a low-porosity region was observed forming on the clay side at the interface and a high-porosity region was visible on the cement side (extending with time). After about six years of interaction, the same sample was investigated by X-ray tomography. A special program allowed segmenting the different intensities retrieved by the X-ray measurement and to estimate regions of reduced or increased mineral density (possibly higher or lower porosity) or regions with newly precipitated minerals in a qualitative way (Fig. 3-11).

In the OPC, right at the interface a thin region (300 – 500 µm) containing new minerals is observed. This precipitation is likely to influence the porosity, but no quantitative estimate can be provided. Between ~ 0.5 and 1 mm from the interface, mineral dissolution results in a higher porosity region. From 1 to 2 mm from the interface porosity decreases again. The region from 2 to 3.5 mm appears to be devoid of portlandite and no precipitation is observable, while from 4 to 5 mm portlandite is still visible.

In the Na-montmorillonite, the X-ray tomography confirmed clearly the zone of low porosity already observed by means of neutron imaging. A very dense zone appears at the interface with a dimension of ~ 1 mm. To be noted is a peak of intensity after 300 – 500 um (corresponding to higher density). This region matches with the zone where the highest sodium concentration is present (see below). This fact suggests that a Na phase is responsible for the low porosity region that formed.

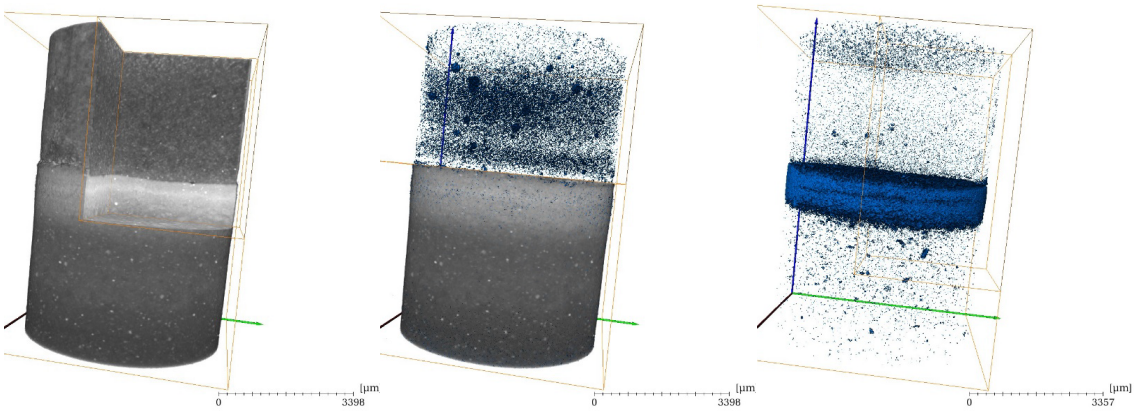

Fig. 3-11: Tomogram of OPC-Na montmorillonite sample C3

Left; clay at bottom, cement at top) after about six years of interaction, from which a (qualitative) porosity distribution on the cement side was derived (middle, with dark blue areas representing pores), as well as a (qualitative) visualization of the high density region mainly in the Na montmorillonite part (right, dark blue and blue areas). Manuscript available and in preparation for publication by Luraschi et al.

Tab. 3-9: Overview on main findings from X-ray tomography for various samples (OPC-Na montmorillonite, OPC-Opalinus Clay, ESDRED mortar-Opalinus Clay, OPC-bentonite, and ESDRED mortar-bentonite

In preparation for publication by Luraschi et al.

	Interface type	**Interaction time**	**Short summary of observations**
C3	Na montmorillonite-OPC	6 years	High density (thus possibly low porosity) region in clay is well visible. Different porosity zones in cement are observed
C4	Na montmorillonite-OPC	6 years	
E20	Opalinus Clay-OPC	1.5 years	No clear mineralogical changes in clay are detectable. Different dissolution-precipitation reactions in the cement at the interface
E21	Opalinus Clay-OPC	1.5 years	
E17	Opalinus Clay-ESDRED	1.5 years	No visible mineralogical changes in clay. A region with higher porosity in cement close to the interface is detected
E23	Bentonite (MX-80)-OPC	1.5 years	Higher density (thus possibly lower porosity) region in clay is detected. Dissolution-precipitation-reactions at the interface on the cement side is detected.
E24	Bentonite (MX-80)-ESDRED	1.5 years	No visible mineralogical change in clay. Higher porosity region close to the interface in cement.

3.3.3.3 Evolution of the diffusive properties

The changes in the porosity of porous media, as reported in the previous subsection, affect the transport properties of the media and diffusive solute fluxes the material interfaces. To quantify these effects, diffusion coefficients were measured in the cement-clay samples after different interaction times by through-diffusion experiments (cf. Tab. 3-6). The diffusion measurements provided first the so-called raw effective diffusion coefficients $D_{e,raw}$, which represent the diffusion coefficient for the entire sample including the filters (Fig. 3-12). Knowing the filter diffusion coefficients, values $D_{e,sample}$ for the entire sample were derived. Furthermore, neglecting the comparably small increase in porosity on the cement side and assigning measured diffusion coefficients of unaltered OPC to the entire cement part, effective diffusion coefficients $D_{e,clay}$ can be calculated based on the geometric parameters of the different components in the sample. Finally, using the diffusion coefficient measured for unaltered montmorillonite, the value of the diffusion coefficient of the zone with strongly reduced porosity (which is sometimes denoted as skin) can be derived. Details about the procedure and experimental setup are given in (Luraschi et al. 2020).

Results of diffusion experiments through reacting OPC-Na montmorillonite samples with HTO as tracer are shown in Fig. 3-13, while those with ^{36}Cl as tracer are shown in Fig. 3-14. Data up to an interaction time of six years are available (Tab. 3-10 and 3-11). For both tracers, the diffusive fluxes across the interface samples clearly decreased with interaction time for those samples, in which a zone with clearly reduced porosity was detected by neutron imaging. As stated in the previous subsection, in some samples such a zone with reduced porosity was not clearly visible. In such samples, the diffusive flux (i.e., $D_{e,raw}$ or $D_{e,sample}$) or also the clay diffusion coefficient $D_{e,clay}$ decreased only slightly with respect to the initial value. The data on diffusion and on porosity changes appear thus to be fully consistent. The reasons leading to the different behaviour

(with or without a clear porosity reduction zone) are currently not clear, but they may be related to specific characteristics of the samples (e.g., porosity, local heterogeneities with respect pore size distributions or minor accessory mineral components), or experimental artefacts. The role of larger scale heterogeneities in the clay and cement materials could affect the formation of reaction fronts and of continuous zones with increased and reduced porosity. Ideally, the effect of such heterogeneities should be tested by running experiments at larger scales, as for instance done in the Mont Terri CI experiment.

In the samples older than 2 years of reaction time, the diffusive flux of HTO did not reduce any further during following ~4 years of subsequent observations, indicating that there was no complete reduction of the porosity that could hinder the HTO transport at any point in time. In contrast, in some samples no anion flux could be measured any more, and the decrease of $D_{e,clay}$ in samples where a flux could still be measured was much more pronounced compared to that of HTO (note the logarithmic *y*-axis in Fig. 3-12, while a linear *y*-axis is used in Fig. 3-11). Thus, the anion accessible porosity (often called free porosity) was much stronger affected than the total (water accessible) porosity of the sample (Luraschi et al. 2020).

The combination of neutron imaging (Shafizadeh et al. 2020) with data from the through-diffusion experiments allowed estimating the diffusive properties of the different regions that are formed when OPC and montmorillonite came in contact (Luraschi et al. 2020). According to the neutron imaging data, the montmorillonite part of the sample was strongly affected by reactions with the cement pore water and can be subdivided in different regions, while the cement part, having a large porosity already initially, was affected less, as schematically displayed in Fig. 3-12. By considering the OPC diffusive properties as constant for the entire OPC part, i.e., neglecting the region of slightly increased porosity, the diffusion coefficient of different domains was calculated, notably that of the entire 5-mm clay plug (model 2) or that of the clay skin (model 3). Results are displayed in Figs. 3-13 to 3-15. For model 3, the properties of the clay region not affected by porosity changes were set either to those of Na-montmorillonite, or to those of K- or Ca-montmorillonite, because changes of the exchanger composition may have occurred beyond regions were the porosity was clearly reduced. All evaluated diffusion coefficients are given in Tab. 3-8 and 3-9.

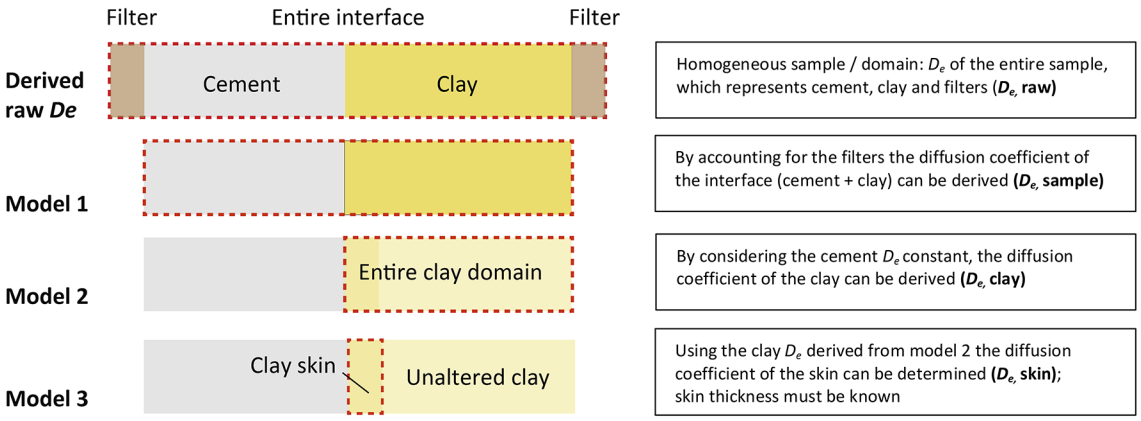

Fig. 3-12: Schematic representation of the different regions or components for which D_e was obtained

The red dashed line represents the region taken into consideration for D_e derivation in each model.

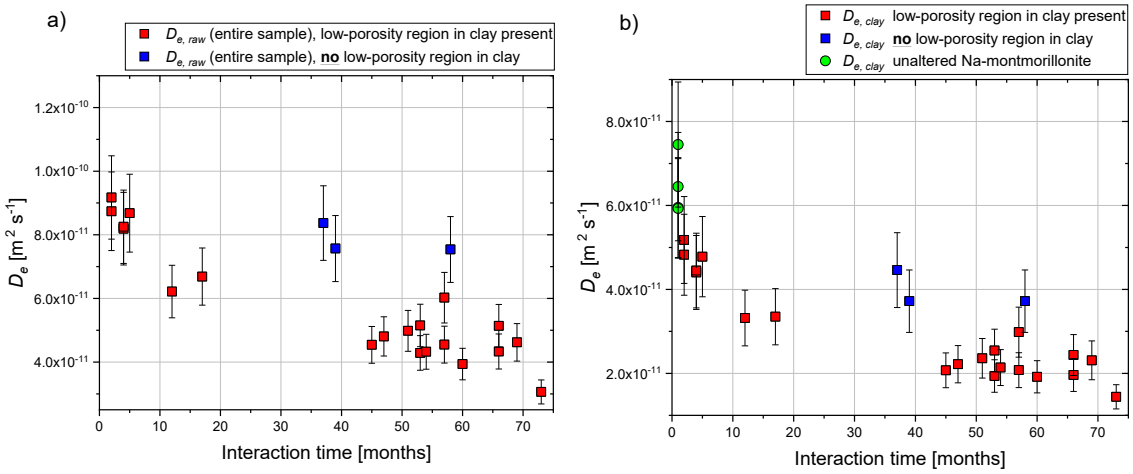

Fig. 3-13: Evolution of the average effective diffusion coefficient D_e of HTO in OPC-Na montmorillonite samples for (a) the entire system ($D_{e,\ raw}$) composed of filters, cement and clay), and (b) for the clay part only ($D_{e,\ clay}$)

In (b), measured D_e in unaltered montmorillonites are also shown for comparison.

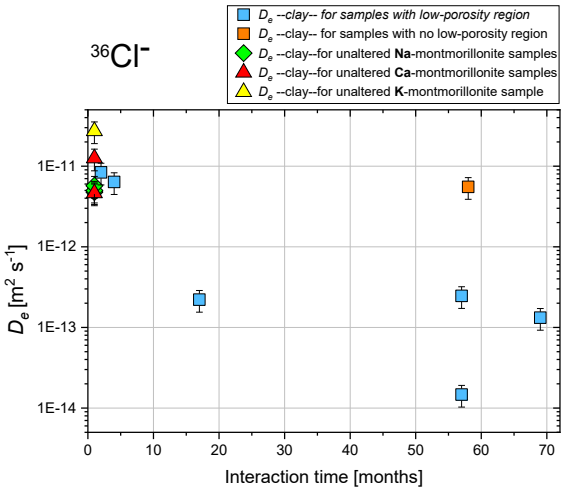

Fig. 3-14: Evolution of the average diffusion coefficient D_e of ^{36}Cl in OPC-Na montmorillonite samples for the clay part only ($D_{e,\ clay}$)

For comparison, measured D_e in unaltered montmorillonites are also shown.

The evolution of the diffusion coefficients derived for the region with reduced porosity in the clay-based on different assumptions are presented in Fig. 3-13. While absolute values depend on the model assumptions, the general behaviour is similar in samples studied. It is observed that the HTO diffusion coefficient in this zone dropped significantly, by one order of magnitude or more, within a time of about 6 years. The drop happened mainly within the first about 2 years, which is consistent with the time scale of the development of the low porosity zone. Later, it remained constant when considering the uncertainties of the values. For Cl, the zone becomes nearly impermeable: The drop in the Cl diffusion coefficient is about three to four (or more) orders of magnitude larger compared to that in HTO diffusion, as in many cases no anion flux could be measured anymore. Blocking the transfer of anions may reduce the further reactivity of the system, as it is also relevant with respect to pH changes (OH transport), but no data for the time-dependence of OH transport was obtained. Furthermore, except for equimolar counter-diffusion of cations, such blocking may affect reactive transport in general through charge balance coupling.

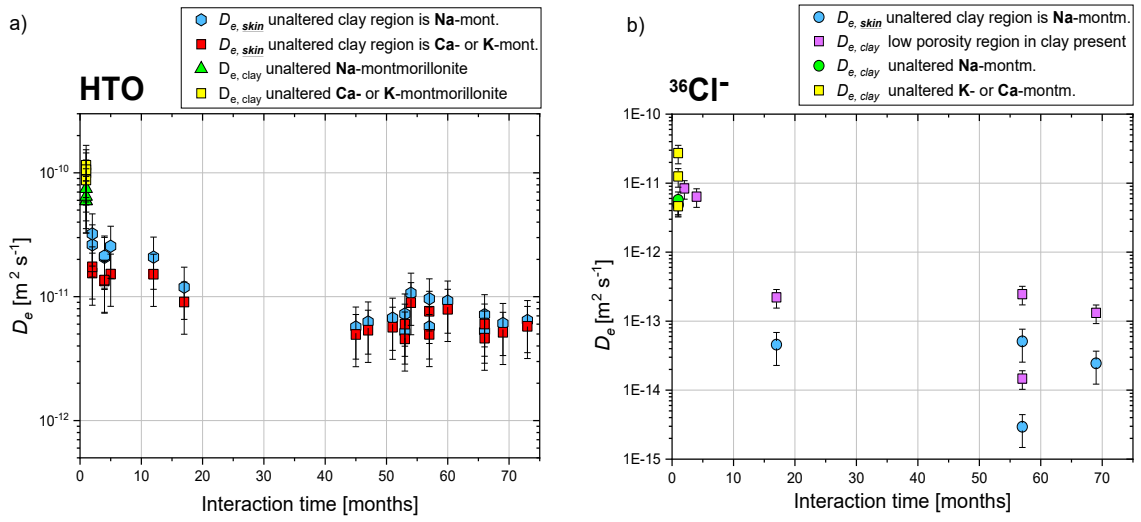

Fig. 3-15: Evolution of the effective diffusion coefficient $D_{e,skin}$ of HTO (left) or ^{36}Cl (right) of the zone with reduced porosity in the Na-montmorillonite

The diffusion coefficient is calculated considering the unreacted part of the clay as Na-montmorillonite (blue) or K/Ca-montmorillonite (red). In the right plot, effective diffusion coefficients for ^{36}Cl of the entire clay domain are also shown (pink), in addition to the values for the low-porosity zone (light blue). $D_{e,skin}$ was calculated considering the unreacted part of the clay as Na-montmorillonite in this case. The values of unaltered montmorillonites are shown at very short interaction time.

Tab. 3-10: Effective diffusion coefficients for HTO for the various regions of the clay domain

See Fig. 3-12

$D_{e,raw}$: effective diffusion coefficient for sample and filters. $D_{e,sample}$ (model 1): for interface sample (cement, clay) without filters. $D_{e,clay}$ (model 2): for clay region. $D_{e,skin}$ (model 3): for skin region of reduced porosity, evaluated assuming an average diffusion coefficient of Na-montmorillonite (model 3a) or of K- or Ca-montmorillonite (model 3b) for the unaltered clay part. A skin thickness of 1 mm according to Shafizadeh et al. (2020) was used. Data from Luraschi et al. (2020).

Sample	**interaction time** [months]	$D_{e,raw}$	$D_{e,sample}$ **(model 1)**	$D_{e,clay}$ **(model 2)**	$D_{e,skin}$ **(model 3a, Na-mont.)**	$D_{e,skin}$ **(model 3b, K-, Ca-mont.)**
C1	12	6.2×10^{-11}	5.5×10^{-11}	3.3×10^{-11}	2.1×10^{-11}	1.5×10^{-11}
	54	4.3×10^{-11}	3.7×10^{-11}	2.1×10^{-11}	1.1×10^{-11}	9.0×10^{-12}
	60	3.9×10^{-11}	3.3×10^{-11}	1.9×10^{-11}	9.2×10^{-12}	7.9×10^{-12}
	73	3.1×10^{-11}	2.5×10^{-11}	1.4×10^{-11}	6.4×10^{-12}	5.8×10^{-12}
C3	5	8.7×10^{-11}	8.2×10^{-11}	4.8×10^{-11}	2.6×10^{-11}	1.5×10^{-11}
	47	4.8×10^{-11}	4.1×10^{-11}	2.2×10^{-11}	6.3×10^{-12}	5.4×10^{-12}
	53	4.3×10^{-11}	3.6×10^{-11}	1.9×10^{-11}	5.2×10^{-12}	4.6×10^{-12}
	66	4.3×10^{-11}	3.7×10^{-11}	2.0×10^{-11}	5.3×10^{-12}	4.6×10^{-12}
D6	2	8.7×10^{-11}	8.2×10^{-11}	4.8×10^{-11}	2.6×10^{-11}	1.6×10^{-11}
	4	8.2×10^{-11}	7.6×10^{-11}	4.4×10^{-11}	2.1×10^{-11}	1.3×10^{-11}
	17	6.7×10^{-11}	6.0×10^{-11}	3.3×10^{-11}	1.2×10^{-11}	9.1×10^{-12}
D11	2	9.2×10^{-11}	8.7×10^{-11}	5.2×10^{-11}	3.2×10^{-11}	1.7×10^{-11}
	4	8.3×10^{-11}	7.7×10^{-11}	4.4×10^{-11}	2.1×10^{-11}	1.4×10^{-11}
C5	51	5.0×10^{-11}	4.3×10^{-11}	2.4×10^{-11}	6.7×10^{-12}	5.7×10^{-12}
	53	5.2×10^{-11}	4.4×10^{-11}	2.5×10^{-11}	7.3×10^{-12}	6.0×10^{-12}
	66	5.1×10^{-11}	4.5×10^{-11}	2.4×10^{-11}	7.2×10^{-12}	6.0×10^{-12}
C15	45	4.5×10^{-11}	3.9×10^{-11}	2.1×10^{-11}	5.7×10^{-12}	5.0×10^{-12}
	57	6.0×10^{-11}	5.3×10^{-11}	3.0×10^{-11}	9.6×10^{-12}	7.6×10^{-12}
C8	39	7.6×10^{-11}	6.9×10^{-11}	3.7×10^{-11}	-	-
	58	7.5×10^{-11}	6.9×10^{-11}	3.7×10^{-11}	-	-
C20	37	8.4×10^{-11}	7.8×10^{-11}	4.5×10^{-11}	-	-
C11	57	4.5×10^{-11}	3.9×10^{-11}	2.1×10^{-11}	5.7×10^{-12}	5.0×10^{-12}
C4	69	4.6×10^{-11}	3.9×10^{-11}	2.3×10^{-11}	6.1×10^{-12}	5.2×10^{-12}

Tab. 3-11: Effective diffusion coefficients for $^{36}Cl^-$ for the various regions of the clay domain
See Fig. 3-12
$D_{e,raw}$: effective diffusion coefficient for sample and filters. $D_{e,sample}$ (model 1): for interface sample (cement, clay) without filters. $D_{e,clay}$ (model 2): for clay region. $D_{e,skin}$ (model 3): for skin region of reduced porosity, evaluated assuming an average diffusion coefficient of Na-montmorillonite for the unaltered clay part and a skin thickness of 1 mm according to Shafizadeh et al. (2020). Data from Luraschi et al. (2020).

Sample	**interaction time** [months]	$D_{e,raw}$	$D_{e,sample}$ **(model 1)**	$D_{e,clay}$ **(model 2)**	$D_{e,skin}$ **(model 3, Na-mont.)**
D11	2	2.0×10^{-11}	1.6×10^{-11}	8.4×10^{-12}	-
	4	1.5×10^{-11}	1.2×10^{-11}	6.4×10^{-12}	-
D6	17	5.7×10^{-13}	4.4×10^{-13}	2.2×10^{-13}	4.6×10^{-14}
C11	57	3.8×10^{-14}	2.9×10^{-14}	1.5×10^{-14}	3.0×10^{-15}
C15	57	6.4×10^{-13}	4.9×10^{-13}	2.5×10^{-13}	5.1×10^{-14}
C8	58	1.4×10^{-11}	1.1×10^{-11}	5.5×10^{-12}	-
C4	69	3.1×10^{-13}	2.4×10^{-13}	1.3×10^{-13}	2.5×10^{-14}

The effective diffusion coefficient of a porous medium is strongly related to the medium's porosity. Various empirical relations exist, such as Archie's relationship, according to which D_e and the porosity ε are related through a power law,

$$D_e = \varepsilon^m \tag{3.1}$$

with m, the so-called cementation exponent, typically being a fitting parameter. It is interesting to check whether the derived diffusion coefficients for the various clay parts follow a similar relation as reported for other montmorillonites. Such a comparison is presented in Fig. 3-16 including the data listed above and data from the literature. For HTO, the data for the altered clay as well as for the zone with reduced porosity match approximately the Archie's relationship (dashed line) obtained for unmodified Na-montmorillonites or bentonites with different porosities, with m=4.4. It is to note that the exact definition of the zone of reduced porosity, with regard to extension and porosity, is not straightforward, which leads to the comparably large error bars. The same plot for chloride is more difficult to interpret. This is mostly related to a very large uncertainty of the anion (chloride) accessible porosity, which cannot be estimated reliably for the altered clay plug or the skin region from the presented data. The dashed line represents Archie's relationship with m=2. Note that the alteration in porosity of the investigated samples is due to the cement/clay interaction, and subsequent formation of a low porosity region, while the rest of the data refer to unreacted samples of different porosity. Even though there are considerable uncertainties in the derived Archie's relations, they may be used as first estimates when implementing a feedback of total porosity changes on changes of diffusion coefficients in reactive transport models.

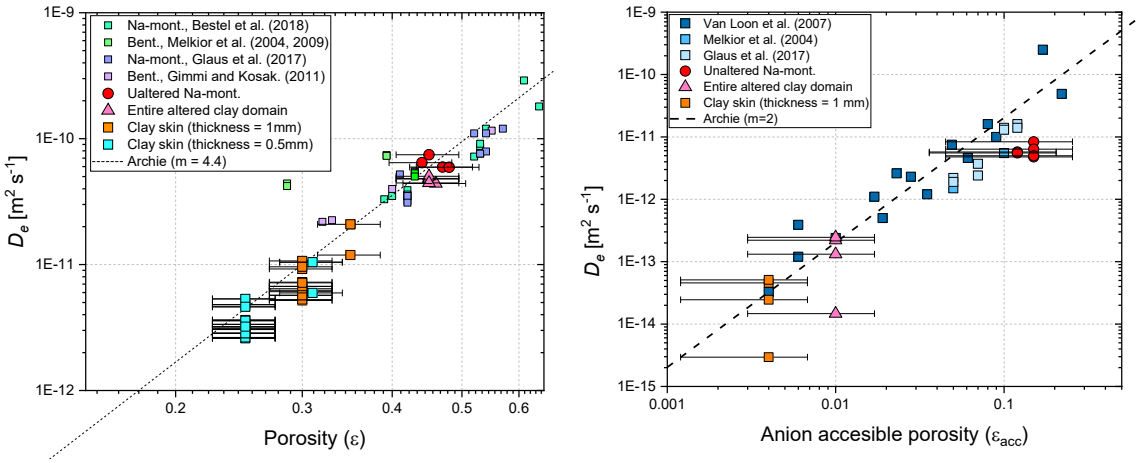

Fig. 3-16: Relationship between the effective diffusion coefficient of HTO (left) or of ^{36}Cl (right) and the diffusion accessible porosity for Na-montmorillonite and bentonite

Besides the data listed in the previous subsection for the entire clay part and for the zone with reduced porosity, data from the literature are shown as well. The dashed line represents the classical Archie's relation with $m = 4.4$ for HTO and $m = 2$ for ^{36}Cl. HTO accessible porosities for the skin regions (left) were derived from the data of Shafizadeh et al. (2020); the error on these porosities is estimated to be ± 10%. Cl accessible porosities (right) for the entire clay domain (pink symbols) and the skin region (orange symbols) are only rough estimates with very large uncertainties. Figures from Luraschi et al. (2020).

3.3.3.4 Mineralogical alterations

XRD intensity diagrams for the cement side of two OPC-Na-montmorillonite samples showing different reaction patterns are displayed in Fig. 3-17, while the intensity diagrams for the clay side of the same samples are presented in Fig. 3-18. The distribution of the Ca/Si ratio within different samples OPC-Na-montmorillonite samples is shown in Fig. 3-19.

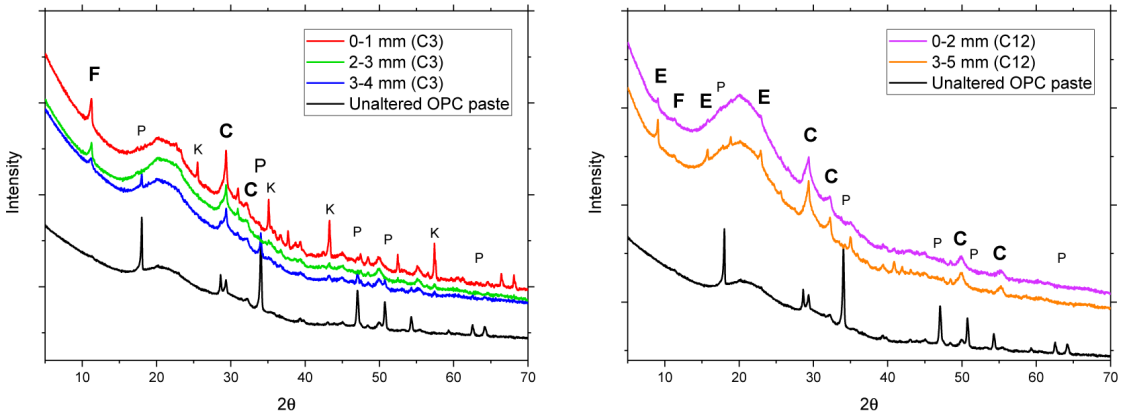

Fig. 3-17: XRD intensity diagrams for cement samples located at different distance from the interface and for unaltered OPC paste

(a) Sample C3: low porosity region formed on the clay side leading to specific alteration within the cement part. (b) Sample C12: no clear low porosity region seen on the clay side; the cement sample reacted completely. Reflection identification, F: Friedel's salt, P: portlandite, C: C-S-H (in addition to the broad unlabeled reflection), K: korundum (polishing paper), E: ettringite.

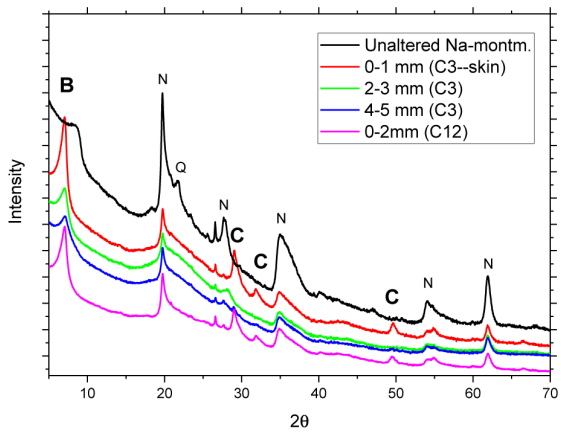

Fig. 3-18: XRD intensity diagrams of clay parts of sample C3 after > 5 years interaction time (for samples taken at different distances to the interface), of sample C12 after > 4.5 years interaction time, and of an unaltered Na-montmorillonite sample

Reflection identification, B: Ca-Na montmorillonite, N: Na-montmorillonite, C: C-S-H, Q: SiO_2 (cristobalite).

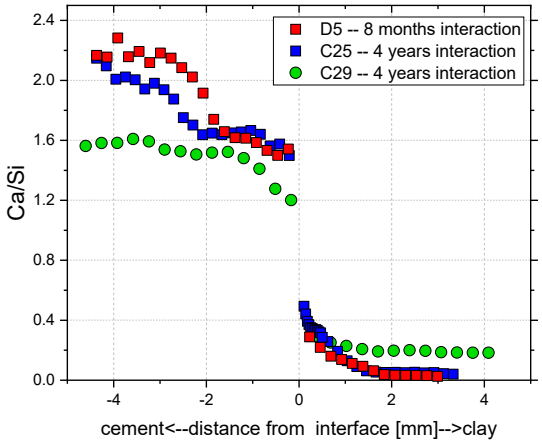

Fig. 3-19: Profiles of Ca/Si ratio from SEM/EDX maps of three different OPC-Na-montmorillonite samples

In sample C29, no clear low porosity region formed on the clay side, while in the samples D5 and C25 such low porosity zones were clearly identified.

- Ettringite is very sensitive to pH and is expected to decompose at pH below 11.5 – 12. It is therefore not present anymore close to the interface. Also, the clay pore water does not include any sulphate, which will also lead to diffusion of sulphate away from the OPC, rendering ettringite unstable.
- The formation of AFm phases is detected especially close to the interface. The observed XRD reflexes together with the geochemical environment suggest that Friedel's salt is forming (chloride AFm). The closer to the interface the greater the presence. The formation of those phases is caused by the in-diffusion of chloride from the clay side.
- On one hand the strong drop in Ca/Si ratio and the low pH condition at the interface suggest that C-S-H phases as well start to be unstable. On the other hand XRD results indicate an increased presence of C-S-H at the interface on the cement side (first 500 µm). The formation of additional C-S-H could be connected to the in-diffusion of silica from the clay side (likely to originate from dissolution of clay minerals or any traces of other minerals such as cristobalite, quartz, if present). The observed increase of C-S-H at the interface could partially be related to the storing conditions of the samples (not always connected to reservoirs) and is not completely understood.
- The new formation of Friedel's salt indicates an increased amount of aluminum in solution (likely to originate from dissolution of ettringite and/or clay minerals). It is therefore likely that aluminum substitution inside the C-S-H structure took at least partially place. Part of the C-S-H are therefore C-(A)-S-H, as often indicated in the literature (Fernández et al. 2016), although no clear evidence was found in our samples. If pH is low enough, zeolites may also form, but no evidence was found either.

The Na-montmorillonite in contact with the OPC strongly reacted after some months of contact, and significant mineralogical alteration became visible. In most samples the majority of mineralogical changes that could be tracked took place close to the interface, that is, within the first mm (or the first few mm) of the clay, which showed a strong porosity decrease. In a few samples, no strong porosity decrease was observed. The main features *in the altered clay region* of OPC-Na-montmorillonite samples, as evidenced by the above figures and additional data, are the following.

- Dissolution of cristobalite and partial dissolution of quartz was observed in XRD. This releases silica in solution, which is then available for other reactions.
- Montmorillonite partially dissolves (decrease of the major reflection at 19 °2θ). Its dissolution results in silica and alumina release into solution (and likely magnesium, although it could not be shown).
- A strong enrichment of calcium was observed within the first mm of the interface after up to 4 years interaction, and increased Ca contents continued within the first ~ 2 mm. XRD and TGA revealed that C-S-H phases precipitate, leading to a capillary porosity decrease by more than 0.1, that is, from ~ 0.4 (or more) to ~ 0.3 (or less) (Shafizadeh et al. 2020). Precipitation of C-S-H phases is thus the main process responsible for the decrease of the diffusion coefficient observed by means of through-diffusion experiments. The high alumina content in solution suggests that at least part of the C-S-H may incorporate Al^{3+}, becoming, at least partially, C-(A)-S-H (but it could not be directly confirmed).
- Due to the higher affinity of Ca with respect to Na for the exchanger site, Na-montmorillonite turns into Ca-montmorillonite by cation exchange reaction.

- Nevertheless, Na enrichment within the low porosity zone was observed for most of the samples. Na could be partially incorporated within the C-(A)-S-H structure or could be related to local formation of sodic beidellite, as already described by other authors (Gaucher et al. 2004).

3.3.4 Studies on the systems composed of OPC or ESDRED mortar and bentonite or Opalinus Clay

Opalinus Clay samples used for these experiments are originating from the Mont Terri rock Laboratory (from the CI experiment). Samples were drilled parallel to bedding, which can be partly recognized from the structures of the fossil shells. They were put in contact with the hardened high-porosity OPC paste that was also used for the montmorillonite-OPC experiments, as well as with ESDRED samples. The latter were also drilled from samples of the CI experiment in Mont Terri (far from any material interface). ESDRED is a low pH (11.7) mortar. It does not contain portlandite; the first pH-buffering minerals are therefore C-S-H phases. Furthermore, MX-80 bentonite was used, compacted to a bulk dry density of 1'500 kg m^{-3}. It is largely composed of Na-montmorillonite, but contains also accessory minerals (e.g., pyrite, feldspars, quartz, cristobalite) which may play a role as well.

3.3.4.1 Visualization by X-ray micro-tomography

An overview on the different samples investigated and the main, but preliminary conclusions from the X-ray investigations are given in Tab. 3-7.

Fig. 3-20 shows results for an OPC sample in contact with Opalinus Clay. In the OPC, a visible alteration due to contact with Opalinus Clay extends up to ~ 1 mm into the cement paste after 1.5 years of interaction. Portlandite dissolution is well observable in the 2D slice obtained from the tomography. Interestingly, at the interface, in the first ~ 100 µm a new mineral phase or new mineral phases have precipitated. These phases are partially filling the porosity formed by the dissolution of primary minerals. According to Mäder et al. (2017), newly formed precipitates are calcite grains forming in alkaline condition due to the supply of Ca^{2+} from the cement pore water and the carbonate from OPA. However, it is not clear which mineral is forming at the interface. The enlargement in the bottom of Fig. 3-20 illustrates the formation of the mineral precipitates at the interface and the empty pores (dark spots) left after Portlandite dissolution. A plot of the X-ray tomogram intensity profile across the interface illustrates the different zones clearly. One also sees that the cement has several cracks, mostly perpendicular to the cylinder axis, which were probably formed during insertion in the Teflon holder. It does, however, not appear that these cracks played an important role with regard to transport and reactions between cement and clay.

In the Opalinus Clay there is only little alteration recognizable; the most interesting feature is a dark zone close to the interface. The intensity profile across the interface clearly evidences this zone (label 1). It is likely related to a slight increase in the porosity of the Opalinus Clay close to the interface following some mineral dissolution.

A slice of a tomogram of the ESDRED-Opalinus Clay sample is presented in Fig. 3-21. The ESDRED mortar is composed of sand grains (<0.5 mm) and a matrix consisting mainly of C-S-H. Quartz sand and C-S-H have a similar intensity in the X-ray image; therefore they are partly difficult to distinguish. It is to be noted that close to the interface (1-1.5 mm) the ESDRED matrix appears slightly darker. This may be related to C-S-H destabilization by contact with the about neutral pH Opalinus Clay pore water. Beyond this small altered region close to the interface, no relevant (mineralogical) changes are observable on the cement side.

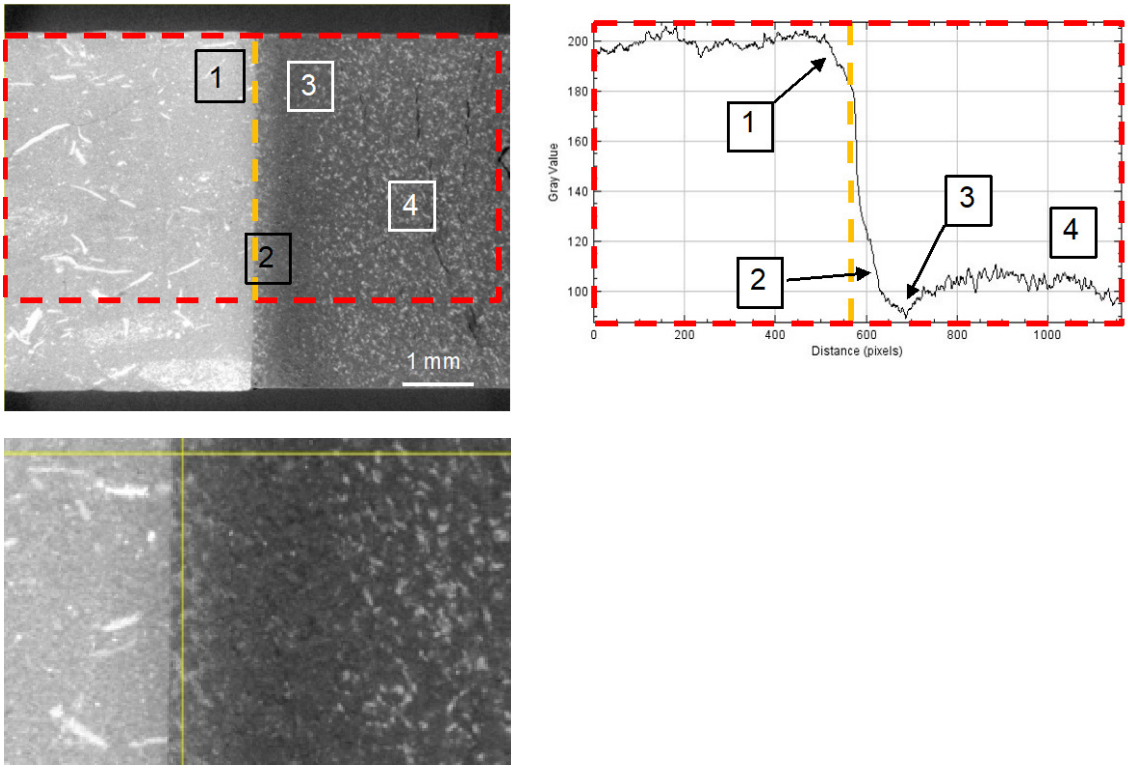

Fig. 3-20: Top left: Cross section of an OPC-Opalinus Clay sample after 1.5 years of interaction derived from X-ray tomography (OPC on right side, Opalinus Clay on left)

Brighter color corresponds to lower (electron) density of the material. Top right: Corresponding intensity profile, with (1) region in Opalinus Clay with lower intensity (likely due to mineral dissolution), (2) mineral precipitation at interface, (3) region in OPC without portlandite, (4) region in OPC with portlandite. Bottom: Zoom of a part of the cross section.

The same applies also for the Opalinus Clay part of this sample. A slightly darker zone (which could hint to increased porosity) seems to exist within narrow region in the first 1 mm from the interface, similarly as in the OPC-Opalinus Clay sample. But it is difficult to recognize, and accordingly, its significance is rather uncertain. The properties and origin of this zone should be confirmed by other measurements before making any interpretation.

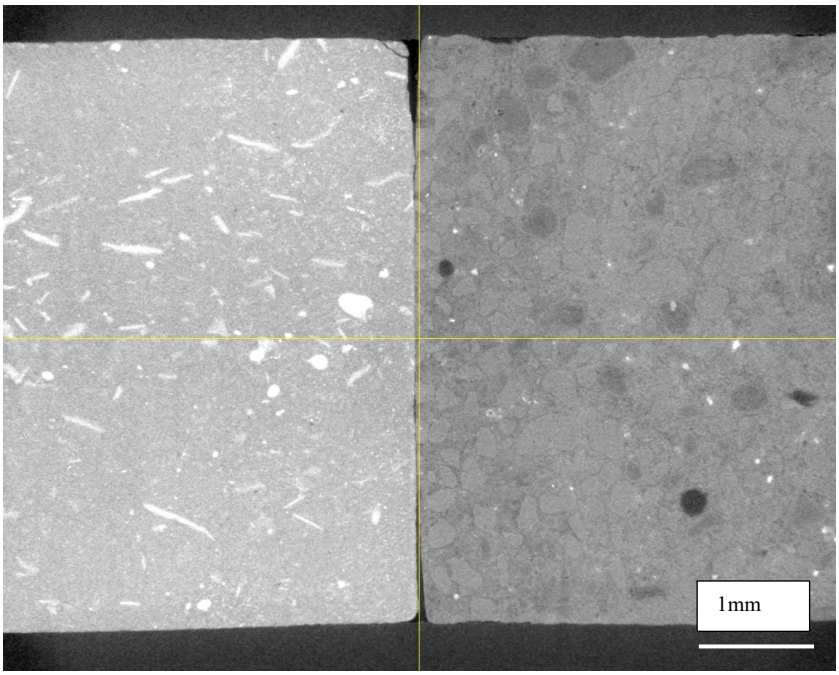

Fig. 3-21: Cross section of an ESDRED-Opalinus Clay sample after 1.5 years of interaction derived from X-ray tomography
ESDRED on right side, Opalinus Clay on left side

The OPC-bentonite sample (Fig. 3-22) appears to behave very similar to the OPC-Na-montmorillonite sample, which is related to the fact that bentonite MX-80 is largely composed of Na-montmorillonite. However, it contains also accessory minerals such as pyrite and feldspars, which could affect the reaction patterns. As previously observed for the OPC Na-montmorillonite samples, portlandite dissolution is visible in the OPC near the interface. For this specific sample, which reacted for approximately 1.5 years, the extent of the region without portlandite is approximately 1.5 mm. Similarly, as for the OPC-Na-montmorillonite sample C3, very close to the interface precipitation of a new phase within the OPC is visible. The OPC sample is internally cracked at several places (perpendicular to cylinder axis), possibly due to pressure during insertion in the sample holder. On the bentonite side, a higher density region is observed in the first ~ 0.5 mm. Especially remarkable is a thin (<50 µm) region with very high intensity, slightly behind the original material interface. Furthermore, some very high density (i.e., heavy) mineral spots are visible within the bentonite matrix. This is very likely pyrite.

In general, the observed alterations are very similar to those in the OPC-Na-montmorillonite samples, but show a smaller spatial extension explained by the shorter reaction time of 1.5 y compared to the 6 y in the former experiments. The specific sample was also investigated by means of neutron imaging. A low porosity region was detected there on the bentonite side and a high porosity region on the OPC side. X-ray tomography confirms these observations and gives supplementary information regarding the mineralogical evolution of the interface.

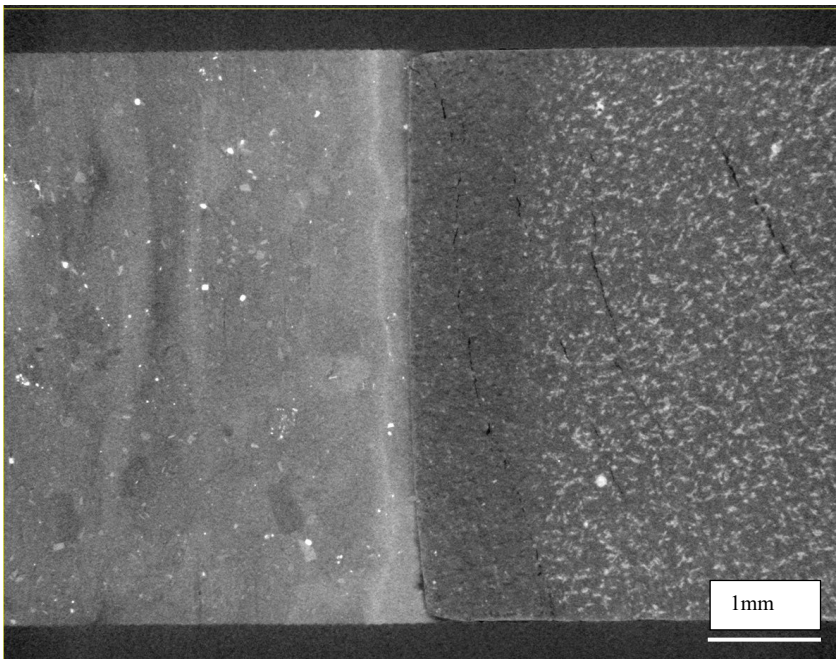

Fig. 3-22: Cross section of an OPC-bentonite (MX-80) sample after 1.5 years of interaction derived from X-ray tomography
OPC on right side, bentonite on left side

Results for the ESDRED-bentonite sample are shown in Fig. 3-23. Similarly, as for the tomography slice of the ESDRED-Opalinus Clay sample, no strong alterations can be observed. Close to the interface, the matrix of the ESDRED mortar seems to be a little darker, which could hint to C-S-H dissolution. A high intensity mineral present in the ESDRED matrix appears to be less stable near the interface (fewer bright spots). In the ESDRED-Opalinus Clay sample, rather few of these bright spots were visible anyway, so it is not clear whether these observations are transferable to the other samples. No relevant mineralogical or intensity changes can be noted on the bentonite side, except for a very slight (but uncertain) darkening in the first ~ 0.5 mm, similarly as for the ESDRED-Opalinus Clay sample. The absence of clear mineralogical alterations after a reaction time of 1.5 y when compared to samples including OPC is likely related to the lower pH of the ESDRED cement, but it may also be related to the lower porosity of the ESDRED mortar compared to the OPC cement. A lower porosity (and thus lower diffusion coefficient) will tend to slow down the movement of any fronts, but, at the same time, alterations could be more pronounced due to the larger masses that can react.

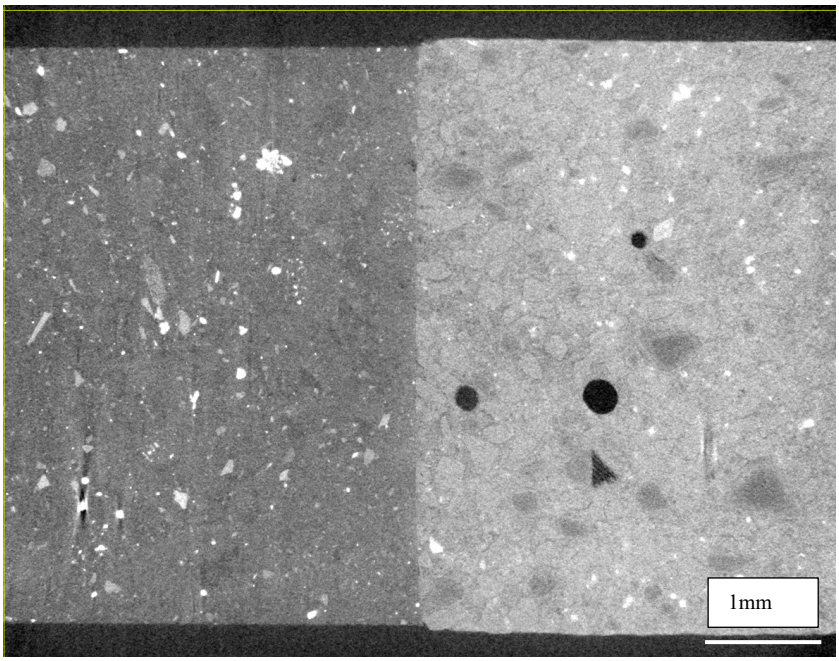

Fig. 3-23: Cross section of an ESDRED-bentonite (MX-80) sample after 1.5 years of interaction derived from X-ray tomography
ESDRED on right side, bentonite on left side

3.3.4.2 Evolution of the diffusive properties

Through-diffusion experiments were performed on some of the samples consisting of various cement and clay components after two years of interaction, in order to monitor the evolution of the diffusivity of the samples with interfaces prepared from different components. Results are displayed in Fig. 3-24.

For all measured samples a clear decrease of the diffusion coefficient of HTO was observed after 2 years interaction between cement and clay. In general, bentonite samples display higher reactivity (faster decrease of diffusivity) compared to Opalinus Clay samples. For bentonite-OPC samples, after 8 months of interaction a decrease of the diffusion coefficient to ~ 61% of its original value was observed. The subsequent measurement after 2 years indicates that the $D_{e,\,HTO}$ decreased to ~ 40% with respect to the unaltered interface. For Opalinus Clay-OPC samples, the diffusivity was measured only after 2 years of interaction; a decrease to ~ 60% compared to the initial value was observed, with slightly higher final values than bentonite-OPC samples. The ESDRED cement mortar has a lower porosity and diffusion coefficient. Therefore, the unaltered ESDRED-clay interface samples have a significantly lower initial (unaltered) $D_{e,\,HTO}$. In this case as well, bentonite samples are more reactive and display a diffusivity decrease to ~ 52% of the initial value after 8 months interaction and a slight further decrease in the following year, reaching a $D_{e,\,HTO}$ representing 44% of the initial value after ~ 2 years. ESDRED-Opalinus Clay samples were also measured only after 2 years interaction. The measurements indicate a $D_{e,\,HTO}$ value that dropped to 64% of its initial value of the unaltered interface.

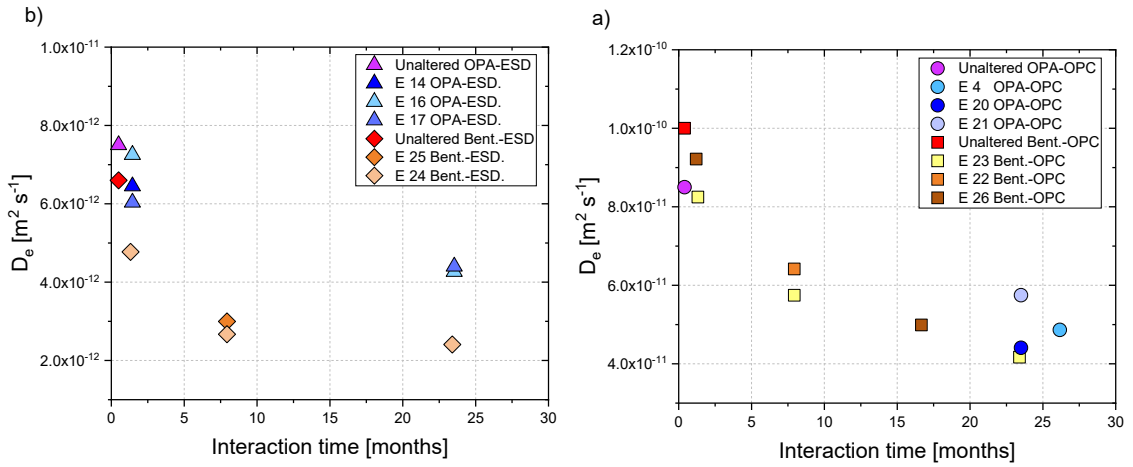

Fig. 3-24: Evolution of the diffusion coefficient D_e of HTO for (a) OPC paste in contact with bentonite and Opalinus Clay, and (b) ESDRED mortar in contact with bentonite and Opalinus Clay

All displayed values of unaltered samples represent theoretical (calculated) values. For these calculations the following values where used: Opalinus Clay: $D_{e,\,HTO} = 5 \cdot 10^{-11}$ (Bossart et al. 2017), bentonite $D_{e,\,HTO} = 6.1 \cdot 10^{-11}$ (Na-montmorillonite value from Luraschi et al. 2020), OPC paste $D_{e,\,HTO} = 2.8 \cdot 10^{-10}$ (Tits et al. 2003), ESDRED mortar $D_{e,\,HTO} = 4 \cdot 10^{-12}$ (estimate).

3.3.4.3 Mineralogical alterations

The mineralogy of the investigated samples after a reaction time of 2 years was analysed by various analytical techniques. Some of the results are shown in Fig. 3-25 and 3-26. The following conclusions can be drawn on the basis of the measurements:

- Ordinary Portland cement (OPC) samples in contact with clay are all characterized by portlandite dissolution (with consequent porosity increase, as inferred from neutron imaging on other samples). The extension of the OPC region without portlandite depends on i) the diffusive properties of the interface components, which affect the overall reactivity of the interface, ii) the formation of a low porosity region in the clay, which leads to a reduction of the diffusive transport of solutes across the interface and slows down the overall evolution and extent of the interface alteration. As the bentonite had a larger porosity and larger diffusion coefficients than Opalinus Clay, mass transfer tended to be faster in systems with bentonite, leading to a more extended region of portlandite dissolution.
- Ca, released into solution by portlandite dissolution, diffuses across the interface and leads to increase of Ca/Si ratio in the clay. This is more prominent in bentonite-OPC samples compared to Opalinus Clay-OPC samples. The diffused calcium is retained in clay due to cation exchange exchanger and also precipitates as C-S-H on the bentonite side. The extension of the Ca enrichment zone is 1.5 mm for OPA and up to 2 – 3 mm for bentonite after 2 years. The latter is similar as in OPC-Na-montmorillonite samples after the same time.
- On the cement side an enrichment in aluminum is observed in all samples except in the ESDRED-OPA sample, but to a different degree. The closer to the clay the higher the enrichment.
- Sodium is also slightly enriched close to the interface in both Opalinus Clay and bentonite samples in contact with OPC paste.

- No calcium enrichment in the clay near the interface is observed in samples in contact with ESDRED mortar, which is characterized by the absence of portlandite.
- The matrix of the ESDRED mortar is mainly composed of C-S-H; it appears to be, at least partially, dissolving.
- The ion ratios of the ESDRED mortar in Fig. 3-26 include the quartz and feldspar aggregates, which explains their low values. Measurements on the matrix only revealed a decrease of the Ca/Si ratio and a decrease of the sulfur content (possibly related to ettringite dissolution) towards the interface.
- The main feature of Opalinus Clay in contact with the ESDRED cement is the strong enrichment in magnesium observed within the first mm (Fig. 3-26b). A similar enrichment (but of lower intensity) was observed in samples with bentonite. In general, the clays seem to be less affected by ESDRED mortar than by OPC, which can be attributed to the absence of portlandite and the milder geochemical contrast (pH difference) between the two materials.

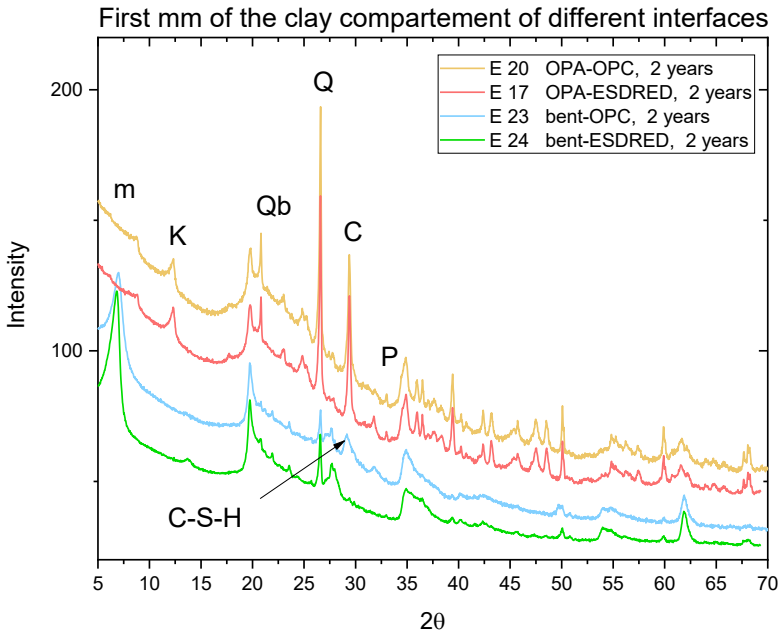

Fig. 3-25: Powder XRD pattern of the first mm of the clay for samples composed of various cement and clay components and reacted for ~ 2 years

m = montmorillonite, K =kaolinite, Qb = cristobalite, Q = quartz, C = calcite, P = pyrite. OPA = Opalinus Clay, bent = bentonite (MX-80)

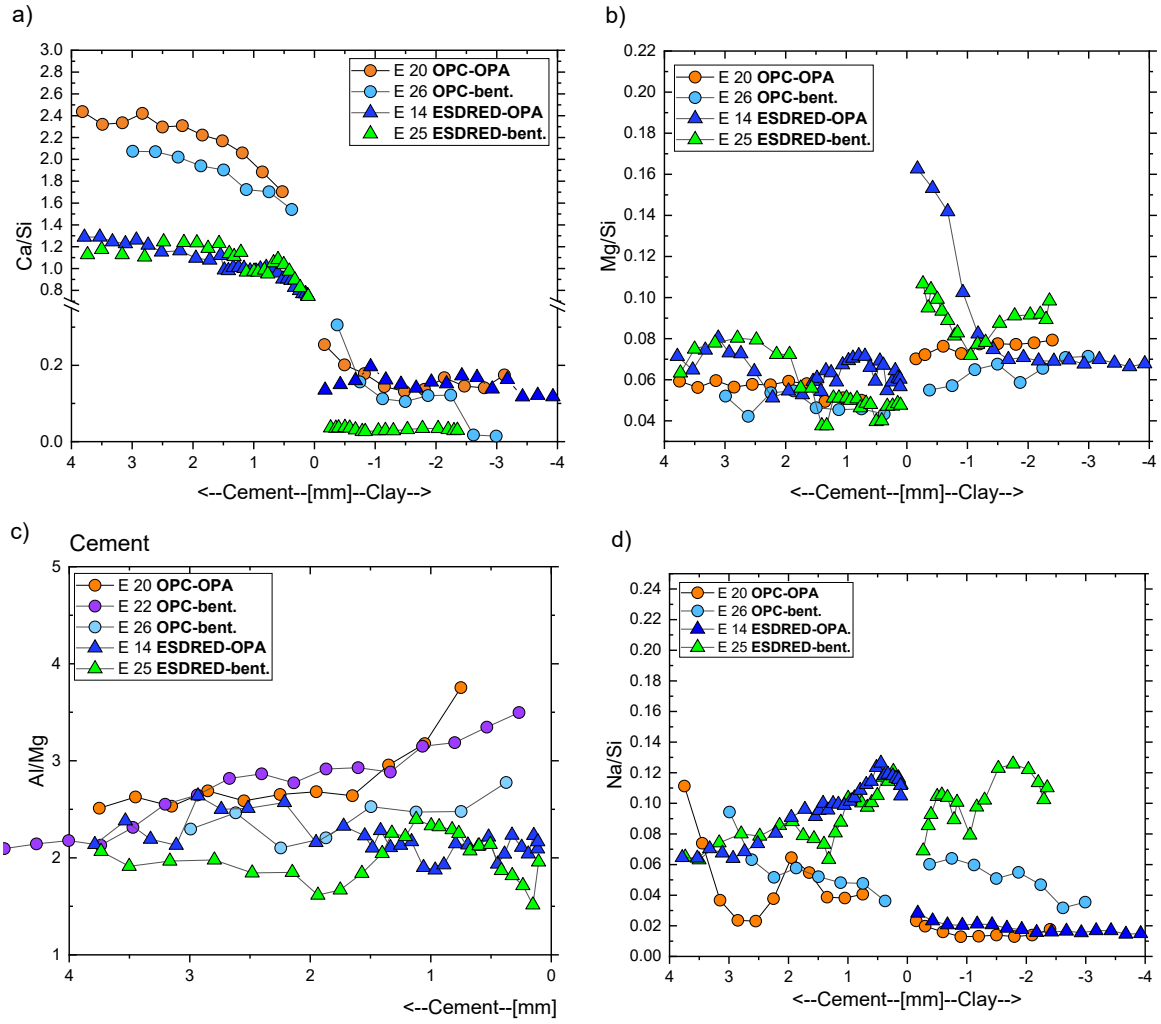

Fig. 3-26: SEM/EDX profiles (including aggregates for ESDRED mortar, averages of a series of maps; moving average for ESDRED mortar parts) across the investigated samples consisting of various cement-clay combinations

(a) Ca/Si ratio for cement and clay compartments; (b) Mg/Si ratio for cement and clay compartments, (c) Al/Mg ratio of the cement compartment only; (d) Na/Si ratio of the cement and clay compartment. OPA = Opalinus Clay, bent = bentonite (MX-80). The investigated samples reacted for ~ 2 years.

3.3.5 Results for systems composed of OPC and montmorillonite, bentonite or Opalinus Clay investigated at 70 °C

The evolution of cement-clay interfaces at elevated temperatures allows to assess the influence of temperature on the microstructural evolution. Interface samples were prepared from hardened OPC paste in contact with Opalinus Clay, bentonite and Na-montmorillonite, respectively. They were saturated with the corresponding pore waters and were kept under nitrogen atmosphere at an elevated temperature of 70 °C for 8 months. The samples were constantly connected to the corresponding pore water reservoirs during the entire experiment. After 8 months, HTO diffusion experiments were performed at room temperature. The samples were investigated *post mortem* by means of different analytical techniques, to correlate the variations seen in the diffusivity with mineralogical alterations.

3.3.5.1 Evolution of the diffusive properties

The samples of bentonite and montmorillonite in contact with OPC show a very similar behaviour to the experiment at the ambient conditions. The decrease of the diffusion coefficient is detected already after 8 months of interaction. The D_e decreased to about 35 – 45% with respect to the initial value. The measured diffusivity in the clay compartment after 8 months at 70 °C is very similar to that of a sample reacted for ~ 24 months at room temperature (~ 25 °C, decrease to about 40% of initial value, Fig. 3-27). This can be explained as follows: the elevated temperatures in the experiment result in increase of solute diffusion coefficients and correspondingly increase of solute fluxes, and thus to an increased reactivity of the interface in general. According to the Arrhenius law and applying an activation energy of 21 kJ mol^{-1} K^{-1} as is typical for water diffusion in clays, the temperature change from 25 °C to 70 °C leads to an increase of the diffusion coefficients by a factor of about 3. Although there are some differences between the different samples (e.g. density, total porosity, tortuosity, detailed chemical composition), it appears that by increase of the temperature from 25 °C to 70 °C and thus the increase of transport rates by a factor of about 3, the overall rate of geochemical alterations at the interface is increased by a similar ratio. This suggest that the extent of reaction fronts is controlled by ion fluxes in solution. The samples with Opalinus Clay in contact with OPC for 8 months still show a similar diffusion coefficient as at the beginning of the experiment. At ambient temperature, the reduction of D_e was also less pronounced than in samples with montmorillonite or bentonite, but it was clearly evident (reduction to ~ 60% after two years, compared to ~ 40% for montmorillonite and bentonite). This may have several reasons: i) the materials at the interface were not perfectly in contact, with some air captured in between, reducing solute transfer and the interface reactivity, ii) fractures in the cement or inside the OPA led to a high diffusivity, such that the conditions necessary for the formation of a zone of reduced porosity are not met, iii) the slower diffusion coefficient of Opalinus Clay generally slows down the development of such zones, or iv) reaction kinetics are more important, even at 70 °C, for Opalinus Clay as compared to montmorillonite, making overall reactivity slow. The last hypothesis appears less likely, but from the diffusion data alone, it is not possible to judge which hypothesis is most likely.

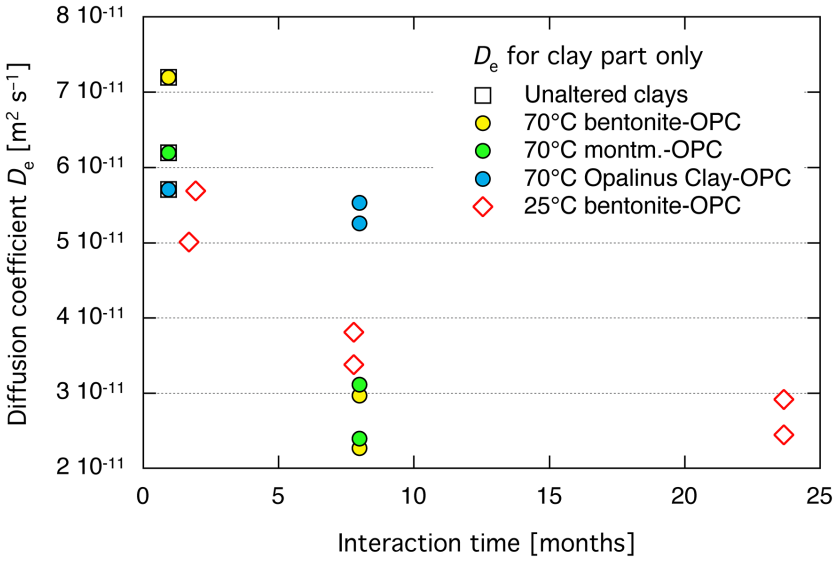

Fig. 3-27: Evolution of the diffusion coefficient (D_e) of the clay part with increasing interaction time for different clays and at different temperatures

Unaltered clays represent the value for unaltered OPA (light blue), bentonite (yellow) and montmorillonite (green), respectively.

3.3.5.2 Mineralogical alterations

SEM/EDX investigations of the montmorillonite and bentonite samples indicate, similarly as observed for samples reacted at room temperature, dissolution of portlandite on the cement side and subsequent enrichment of calcium on the clay side (Fig. 3-28). Ettringite is also expected to be unstable at 70 °C. On the clay side, formation of C-S-H phases within the first mm was detected by XRD (Fig. 3-28). Both samples reveal quartz and montmorillonite dissolution, resulting in increased contents of silica and aluminum in solution available for other reactions. The XRD patterns suggest that OPC - montmorillonite and OPC - bentonite samples react very similarly and show almost the same mineralogical modifications. SEM/EDX investigations reveal a region of ~ 1.5 mm inside the cement where portlandite is dissolved, and a region of 1.0-1.5 mm in clay compartment with higher Ca inventory.

XRD investigations of the samples composed of OPC – Opalinus Clay did not show any significant mineralogical alteration on the clay side. X-ray tomography performed on this sample indicated that the interface was not fully in contact with the clay (a gap of 200 µm was present between the two components). This explains the weaker interaction, even though it is likely that this gap was fluid saturated pore water.

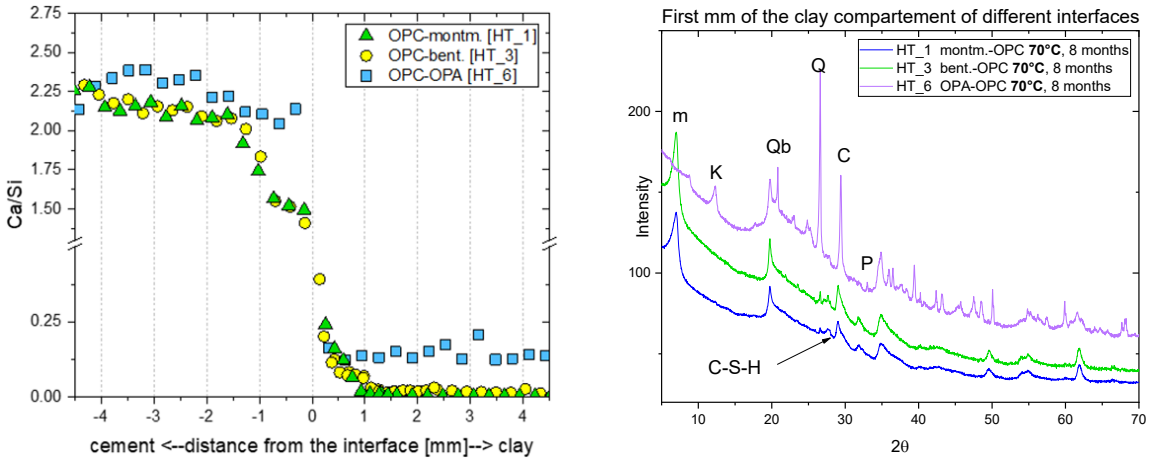

Fig. 3-28: Left: Ca/Si ratios obtained by SEM/EDX analysis for the samples investigated at 70 °C. Right: Powder XRD patterns of material from the first mm of the clay parts of these samples

m = montmorillonite, K = kaolinite, Qb = cristobalite, Q = qtz, C = calcite, P = pyrite

3.3.6 Summary of key findings and process understanding derived from the small-scale laboratory experiments at LES, PSI

3.3.6.1 OPC-Na-montmorillonite samples at ambient temperature

- The investigated OPC-Na montmorillonite samples reacted relatively quickly, which is also related to the high porosity of the OPC and the corresponding large diffusivity. Already after some months, a decrease in the diffusivity and variations in the mineralogy were observed.
- The decrease in diffusivity of the entire interface sample was related to the appearance of a low-porosity zone in the montmorillonite, as derived from neutron imaging. This zone extended up to ~ 2 mm into the clay within 6 years, with a pronounced minimum mostly somewhere near 1 mm. It mainly developed within the first year. Porosity within this zone continued to decrease slightly, but the zone did hardly further expand.
- The capillary porosity on the OPC side adjacent to the interface generally increased slightly, as was derived from neutron imaging. The increase was obviously related to the dissolution of portlandite. While the extent of this zone of larger porosity steadily increased with interaction time (up to ~ 2 mm in two years, and larger distances within 6 years), the capillary porosity did not monotonically increase. Depending on position, it did later also decrease and partly increase again. This is likely related to dynamic precipitation and possibly re-dissolution of newly formed phases in zones where portlandite has dissolved.
- Not all samples contain narrow low-porosity regions. In a few samples, the decrease of porosity is spread nearly over the entire 5 mm of the sample, while in a few other samples no clear patterns are detected. The reasons for the different behaviour are not clear, but it could be related to small variabilities of properties between samples and especially at their interface. This would suggest that natural heterogeneities present at the repository scale may lead to non-uniform development of a low-porosity zone.
- The main reactions (Fig 3-29) on the OPC side were the dissolution of portlandite and ettringite, leading to the increase of porosity. Precipitation of Friedel's salt was observed; it is related to the high chloride content of the montmorillonite pore water and to the aluminum and silica availability in solution.
- On the clay side, the alkaline pore water of the cement partially dissolved quartz and clay. The pH front very likely advances further than the zones with altered ion ratios, as an increase in pH was observed in the clay water reservoir at the end of the clay plug. The available silica and aluminum, together with the calcium diffusing from the cement, led to the precipitation of C-(A)-S-H phases and consequent porosity reduction. The zone of reduced porosity is not only enriched in Ca, but also in Na.
- Especially the C-(A)-S-H precipitation on the clay side led to a strong decrease in diffusivity of reactants, which slows down further mineralogical modification at the interface. During the monitoring period from 1.5 to 6 years, the alteration proceeds much slower compared to the reactivity in the first experimental year.
- Apart from C-(A)-S-H precipitation, a series of minor alterations occurred on both sides of the interface (Friedel's salt precipitation, Ca–Na cation exchange in montmorillonite).
- The reduction of the diffusion coefficient for the anion Cl was much stronger than for the neutral tracer HTO. Anions can only access the so-called free porosity (mainly larger pores, cf. subdivision of pore space of a clay in Fig. 3-30), whereas water tracers can access all pores, including interlayer and interlayer equivalent pores.

- It can thus be speculated that precipitations in the clay compartment took place preferentially in the free porosity, i.e., in larger pores. This strongly reduces or even prohibits the diffusion of anions, while HTO can circumvent blocked larger pores via interlayers such that HTO diffusion through the Na-montmorillonite still takes place.
- The strong reduction of the anionic diffusion coefficient is anticipated, even if the zones responsible for this reduction are relatively thin, unless the partly reduced pore space is re-opened by other (e.g., mechanical cracking, dissolution) processes.

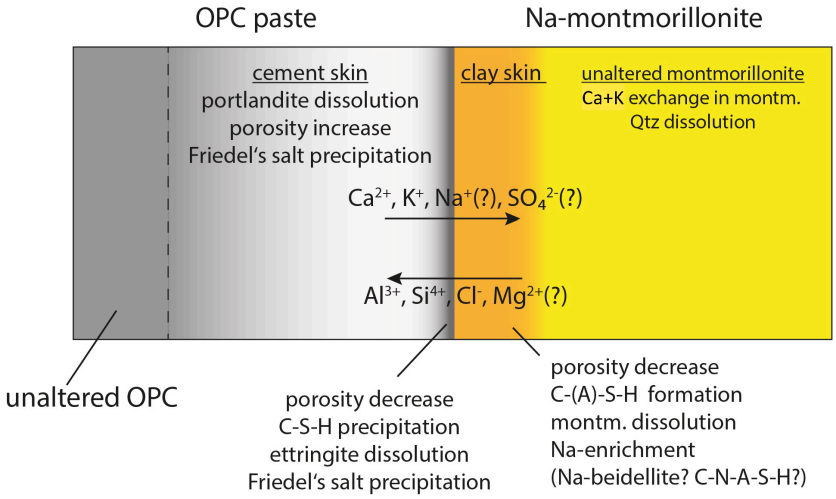

Fig. 3-29: Schematic summary of the main reactions observed in small samples consisting of OPC paste and Na montmorillonite
Luraschi et al. (nd)

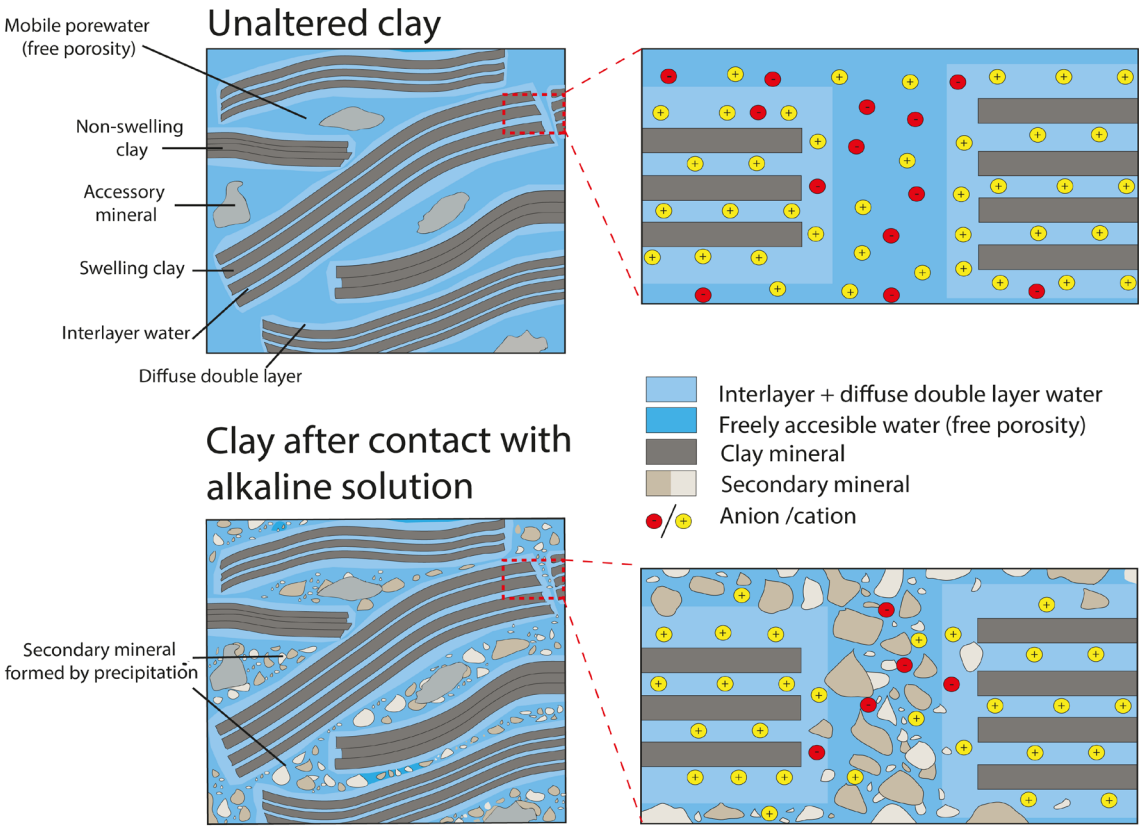

Fig. 3-30: Schematic illustration of a porous medium composed of clay minerals and pore environments for unaltered clay, and for clay after contact with alkaline solution (e.g. cement pore water)

The exact locations where precipitations take place (free porosity only or interlayer/diffuse double layer) and precipitation type (homogeneous vs heterogeneous) are not clear. Figure from Luraschi et al. (2020).

3.3.6.2 Samples with different cement and clay types at ambient temperatures

- All samples prepared from combinations of OPC or ESDRED mortar and Na-montmorillonite or MX-80 bentonite showed a decrease in diffusivity after 2 years interaction time, as did the previously investigated OPC-Na-montmorillonite samples. Samples with bentonite displayed a stronger and faster decrease of the diffusive properties compared to those with Opalinus Clay, likely because of higher porosity and higher D_e of ions in the bentonite than in OPA.
- The OPC-bentonite samples showed a behaviour very similar to that of OPC-Na-montmorillonite samples, while the patterns were different in various respects for OPC-Opalinus Clay samples.
- C-S-H formation has been observed inside the first mm of the bentonite in OPC-bentonite samples (Fig. 3-31). ESDRED-bentonite samples showed a region with increased magnesium content in the bentonite close to the interface. The Mg originates very likely from the exchanger sites (Fernández et al. 2009, González-Santamaría et al. 2020b). The Mg bearing phase has not been identified; M-S-H is a possible candidate.

- Opalinus Clay-OPC interfaces showed an increase of calcium content on the clay side towards the interface. Although no clear phase identification was possible so far, possibly also for these samples a small amount of C-S-H has precipitated. Nevertheless, the main reason for decrease of the diffusivity at the interface is probably the precipitation of a new phase (possibly calcite) at the interface just within the cement side, as observed in tomographic images.
- The Opalinus Clay-ESDRED mortar interface samples showed a remarkable enrichment of Mg on the Opalinus Clay side within the first mm at the interface. The Mg originates very likely from the exchanger sites e.g. (Fernández et al. 2009), possibly also from some dolomite dissolution. The XRD investigation did not detect a significant mineralogical change.

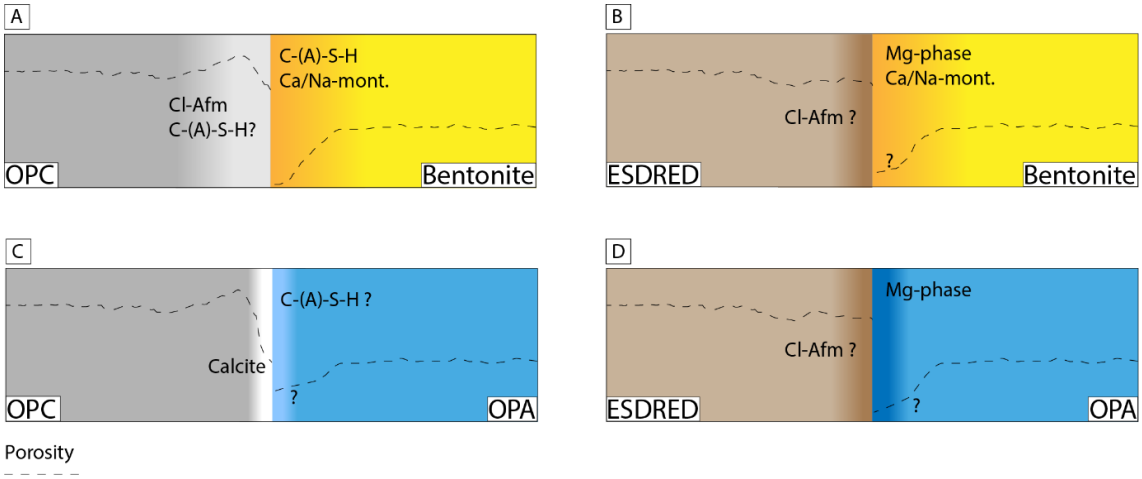

Fig. 3-31: Schematic illustration of the extent of alteration zones and of reactions (only precipitates shown) as observed in samples prepared from various materials after an interaction time of two years

Expected total porosity profiles are also shown qualitatively as dashed line. (a) OPC paste-bentonite (MX-80), (b) ESDRED mortar-bentonite (MX-80), (c) OPC paste-Opalinus Clay, (d) ESDRED mortar-Opalinus Clay. Figure prepared for publication by Luraschi (in preparation).

3.3.6.3 Samples with different cement and clay types at temperature 70 °C

- At temperature 70 °C, the decrease of the diffusion coefficient in montmorillonite or bentonite in contact with OPC occurred ~ 3-times faster than at room temperature (similar diffusion coefficients after 8 months at 70 °C as after ~ 24 months at 25 °C).
- The observed mineralogical evolution after 8 months at 70 °C in these samples is very similar to that of samples reacted at room temperature for 24 months. Thus, similar reactions appear to occur, but at a clearly faster rate. However, at 70 °C ettringite and possibly also AFm will no longer be stable, so some differences in mineral transformations will be present.
- No clear reduction of the diffusion coefficient was observed for Opalinus Clay-OPC samples after 8 months at 70 °C, and only weak indications of precipitations at or near the interface. It is currently unclear why the acceleration of the processes seen in samples with montmorillonite or bentonite is not equally seen in samples with Opalinus Clay.

3.3.6.4 Strengths and limitations of investigations on the small samples

The investigations on small samples in the laboratory have many advantages compared to field experiments or natural analogues. For instance, it is possible to work with simplified systems, their boundary and initial conditions can be better controlled, it is possible to change a single parameter only between two experiments, various non-destructive measurements as well as transport experiments can be performed repeatedly, and the samples can be kept for variable durations. But it is clear that the chosen setup has also some limitations when trying to extrapolate the observations to the field scale. The main limitation is obviously a comparably small dimension of the samples, which is an asset for handling in the lab, but also limits the scale of observations (<5 mm). Also the contact with the reservoir solutions at comparably small distance to the interface possibly leads to comparably large buffering and/or mass transfer, thus accelerating the evolution of interface reactions. This is an advantage from the experimental point of view, but can also be seen as a conservative upper limit for the reactivity of the interface at field scale. Finally, for various investigations the samples had to be detached from the solution reservoirs for certain measurements, which may have created slightly different boundary conditions that vary between samples.

3.3.7 Comparison of results from the small laboratory samples with results from the Mont Terri CI experiment

It is interesting to compare the results obtained on small samples with those from the Mont Terri CI field experiment, in order to find similarities and differences, the latter possibly related to the different boundary conditions. However, various combinations of material components were investigated and over different times, which limits the possibilities of direct comparisons. Also, no diffusion coefficients could be measured in the field experiment so far (currently, such an experiment is running), and only limited porosity data are available from the CI samples.

In many respects, the observations obtained at the two scales are similar in those cases where comparisons were possible. For instance, both types of experiments with **OPC** (a concrete in the field experiment and a highly porous paste in the lab experiment) and **bentonite** (or **montmorillonite**) revealed that:

- Reactions happen relatively fast (relevant already within 1 to 2 years and continue at a slower rate over the next 5 to 10 years).
- Ca becomes depleted on the cement side and enriched on the clay side.
- Portlandite and ettringite dissolve on the cement side, in a zone increasing with interaction time.
- Cristobalite dissolved on the clay side; in contrast, a partial dissolution of quartz was found in the laboratory experiments, but not in the field experiment
- New phases precipitate on the cement side, probably at a later stage, as well as on the clay side; the exact identification of these phases is often difficult.

Some differences were, however, also noted. While a zone with clearly enriched Mg was encountered in the clay compartment in samples from the CI field experiment, no such clear Mg enrichment was found in the clay from the small OPC-bentonite or -montmorillonite laboratory samples. On the other hand, an enrichment in Na was seen in the clay in these laboratory samples at the location of the low porosity zone, but no Na enrichment was reported for the field samples (there, Na enrichment was found in ESDRED or OPC in contact with Opalinus Clay (Bernard et al. 2020a).

The comparison of results for field and laboratory samples composed of **various cement materials** and **Opalinus Clay** is challenging due to the limited number of observations. It appears that:

- Alterations on the clay side proceed slower when compared to those in bentonite.
- Ca becomes depleted on the cement side and enriched on the clay side, as for the samples with bentonite or montmorillonite.
- Alterations on the clay side are less pronounced in the samples with ESDRED as compared to the samples with OPC.
- A clear enrichment of Mg was seen in Opalinus Clay contacting ESDRED mortar in both, the samples from the CI field experiment and in the small laboratory samples.
- A Na enrichment was seen within ESDRED or OPC near the interface to Opalinus Clay in field samples from the CI experiment (Bernard et al. 2020a) but not yet in small laboratory samples.

4 Reactive transport modelling and simulations

4.1 Introduction to RT, description of models and methods

Reactive transport modelling is the computational methodology which allows to model the observations of the experiments and is used to predict the geochemical evolution of the materials relevant to the repository. Typical processes that are modelled are the diffusive and advective multiphase heat and mass transport, along with the geochemical reactions which result in sorption, mineral dissolution and mineral precipitation. The involved processes are of multiscale nature and therefore there exist several numerical approaches suited for the spatial scale of interest, e.g. molecular dynamics and finite volume repository scale solvers.

4.1.1 Rate laws for precipitation/dissolution

Out-of-equilibrium geochemical processes are often described with help of reaction rates. This makes it possible to include a timeline in the process description. Many kinetic models exist, often specialized for certain applications. For reactive continuum scale transport the so-called "Lasaga"-type kinetic models are popular. They are based on transition state theory (TST) as detailed in Lasaga (1981a, 1981b). Several databases for rate laws exist, e.g. the collection of Palandri & Kharaka (2004) and the data from (Marty et al. 2015a) which are part of the Thermoddem TDB.

Both databases use a typical "Lasaga" type rate law for the dissolution/precipitation of minerals in the following formulation from Palandri & Kharaka (2004):

$$\frac{dm}{dt} = -SA \begin{bmatrix} k_{acid}^{298.15K} e^{\frac{E_{acid}}{R}\left(\frac{1}{T}-\frac{1}{298.15K}\right)} a_{H^+}^{n_1} (1-\Omega^{p_1})^{q_1} \\ + k_{neutral}^{298.15K} e^{\frac{E_{neutral}}{R}\left(\frac{1}{T}-\frac{1}{298.15K}\right)} (1-\Omega^{p_2})^{q_2} \\ + k_{base}^{298.15K} e^{\frac{E_{base}}{R}\left(\frac{1}{T}-\frac{1}{298.15K}\right)} a_{OH^-}^{n_3} (1-\Omega^{p_3})^{q_3} \end{bmatrix} \quad (4.1)$$

The reaction rate dm/dt [mol/s] depends on a (reactive) surface area SA [m^2] and on three terms that describe three different reaction mechanisms; a standard "neutral", an H^+-catalysed "acid" and an OH^--catalysed "base" mechanism. Each mechanism is parameterized with help of a kinetic reaction constant k [mol m^{-2} s^{-1}] at a temperature of 298.15 K and an exponential term (Arrhenius law) for the temperature T [K] dependence with a mechanism specific activation energy E [J mol^1] and the gas constant R.

The last term for each mechanism includes the mineral saturation index Ω=Q/K where Q is the activity product of the dissolved mineral constituents and K the equilibrium constant (solubility product). This term describes the distance to the equilibrium state. The parameters p and q are empirical and dimensionless and describe the influence of the reaction rate on mineral saturation index. Typically they can be obtained by fitting experimental data (Marty et al. 2015b, Palandri & Kharaka 2004).

Additionally, the "acid" and "base" mechanism includes a dependence on the activity of H^+ and OH^-. The power exponents n_i are typically obtained by fitting experimental values measured at different pH. Please note, that in Palandri & Kharaka (2004) the "base" mechanism (third term) in Eq. 4.1 uses the activity of H^+ raised to a reaction order with negative sign instead of the activity of OH^-.

4.1.2 Uncertainties related to reaction rates

The publication of Marty et al. (2015b) includes an extended discussion on the sources of uncertainties for rate laws and parameters. Also in Section 3.2 of Jenni et al. (2019) uncertainties related to thermodynamic and kinetic modelling of bentonite (also under high pH conditions) are discussed in details.

In the following we summarize some important conclusions provided in Marty et al. (2015b) and Jenni et al. (2019).

Marty et al. (2015b) clearly state the following:

"Moreover, laboratory experimental rates and those measured in situ vary by up to several orders of magnitudes (Lüttge et al. 2013, Marty et al. 2009, Velbel 1990, White & Brantley 2003, Zhu 2005)*. Significant differences are also observed in similar experiments dealing with the same material. For Lüttge et al.* (2013)*, these discrepancies cannot be attributed to experimental artifacts (analytical uncertainties, data acquisition methods, etc.). Authors identify extrinsic and intrinsic sources of rate variations (depending on the observation scale). Extrinsic sources come from heterogeneities (porosity, mineralogical and chemical compositions, etc.) inside the media that should be represented. From this point of view, their consideration is the responsibility of the modeller. Intrinsic sources of rate variations are also attributed to heterogeneities at the crystal scale (crystal-defect distributions, impurities, etc.). Only kinetic Monte-Carlo models are able to show a large variation in total rate over time* (Lüttge et al. 2013)*. However, this method is limited at the crystal scale. Therefore, the use of TST kinetic models appears to be currently unavoidable for large-scale simulation, even if the use of a mean or rate-limiting value describing the reaction rate appears to be questionable."*

One important, if not the most important, source of uncertainty is the value of the surface area *SA* in Eq. 4.1. Kinetic rates are frequently measured with dissolution experiments of small mineral particles suspended in a relatively high amount of solution (which is constantly stirred/mixed). Firstly, it is straightforward to measure the BET surface area for mineral powder and secondly during the experiment the whole grain surface is in contact with the solution, although possibly not all surfaces dissolve with the same rate (Fischer et al. 2014).

It has been recognized, that the reaction rates estimated from field observations are often significantly lower than those measured in lab experiments (Brantley 2008; see discussion in White & Brantley 2003). In rocks and artificial media like concrete, the liquid to solid ratio is much lower and the surface of mineral grains is not evenly in contact with the pore fluid. Recent experimental studies demonstrate that the pore-scale reactivity of minerals in combination with microscopic and macroscopic transport controls the evolution of the corresponding material at macroscopic scale (Kurganskaya & Rohlfs 2020, Noiriel & Daval 2017, Poonoosamy et al. 2020, Prasianakis et al. 2017).

In addition, e.g. disconnected pores or partial water saturation might de-percolate the pore space and might slow down or interrupt microscopic transport of solutes. The pore water composition in different compartment might vary considerably. All these conditions make it very difficult to assign a single variable for the effective surface area. In addition, the pore space geometry, the mineral grain size and surface roughness of mineral grains might change significantly during dissolution (and precipitation of other reaction products). Frequently this effect is lumped into a "chemical reactivity" function (see Section 3.1.3) which links liquid water saturation with a reduction of kinetic rates (Huang et al. 2021, Trotignon et al. 2011).

It should be noted that the reactive surface area is normally used as a lumping parameter in reactive transport calculations (Beckingham et al. 2017). As all other variables in Eq. 4.1 are fixed by either database entries or thermodynamic calculations, the only "free" variable is the surface

area that is used to scale the rates to desired values, if necessary. In this sense, Seigneur et al. (2019) defined the reactive surface area as surrogate for reactivity in their description of reactive transport.

As noted before by Marty et al. (2015b) similar experiments for the "same" material might give significantly different experimental results. In addition, experiments do not necessarily cover all chemical conditions of interest. Specifically, data on very high or very low pH might be missing. For such a case, it is unknown if rates can be reliably extrapolated to other chemical conditions. This is a problem for some minerals as described in Palandri & Kharaka (2004), where the authors specifically limit the applicability of their fits due to lack of data for alkaline chemical conditions.

The choice of datasets for fitting kinetic rates in general and specifically the pH dependence might be very different between kinetic databases. In addition, Palandri & Kharaka (2004) and Marty et al. (2015b) show that the use of different regression methods might give significant order-of-magnitude differences in rate constants.

4.1.3 Numerical aspects in reactive transport codes

On continuum scale, modelling the temporal evolution of strong total porosity changes is challenging, if porosity change is controlled by several intertwined chemical, kinetic and transport processes. Marty et al. (2009) conducted a numerical study on evolution of cement/clay interface under diffusive transport conditions. They demonstrated that the time estimate for porosity clogging is not well defined in reactive transport models with equilibrium reactions and depends on the spatial discretization. In a diffusive transport regime (Fig. 2-11 a), b) or c)) clogging times, in terms of numerical decrease of total porosity to a defined value close to zero, change with the square of the discretization, i.e. if the discretization representative element (mesh step size, length in transport direction) increases with a factor of 10, clogging times increase with a factor of 100. Only in cases where the reaction kinetics control the availability of at least one reactant, it is possible to find an upper limit for mesh size, i.e. calculated clogging times will not change if mesh size is smaller (Fig. 4-1; see also Hayek et al. 2012, 2011). If the controlling kinetic process is fast, the corresponding mesh size might become very small and the volume of a single mesh element may result being smaller than the representative element volume (REV) of the numerical solver. We also note that per definition a representative element volume on continuum scale does not contain any explicit description of the porespace topology, and that all properties within the same volume are homogenized.

Xie et al. (2015) conducted a benchmarking study on reactive transport problems that involve total porosity and permeability changes due to kinetically controlled mineral dissolution and precipitation. They conclude *"that, generally, good agreement is reached amongst the computer models despite significant differences in model formulations. Some differences are observed, in particular for the more complex scenarios involving clogging; however, these differences do not affect the interpretation of system behaviour and evolution."*

This study demonstrates, that differences between numerical models in terms of system evolution (strong total porosity reduction) are mostly not caused by numerical implementation. Instead, the modeller's choice of assumptions, concepts, processes and parameters influence the modelling results.

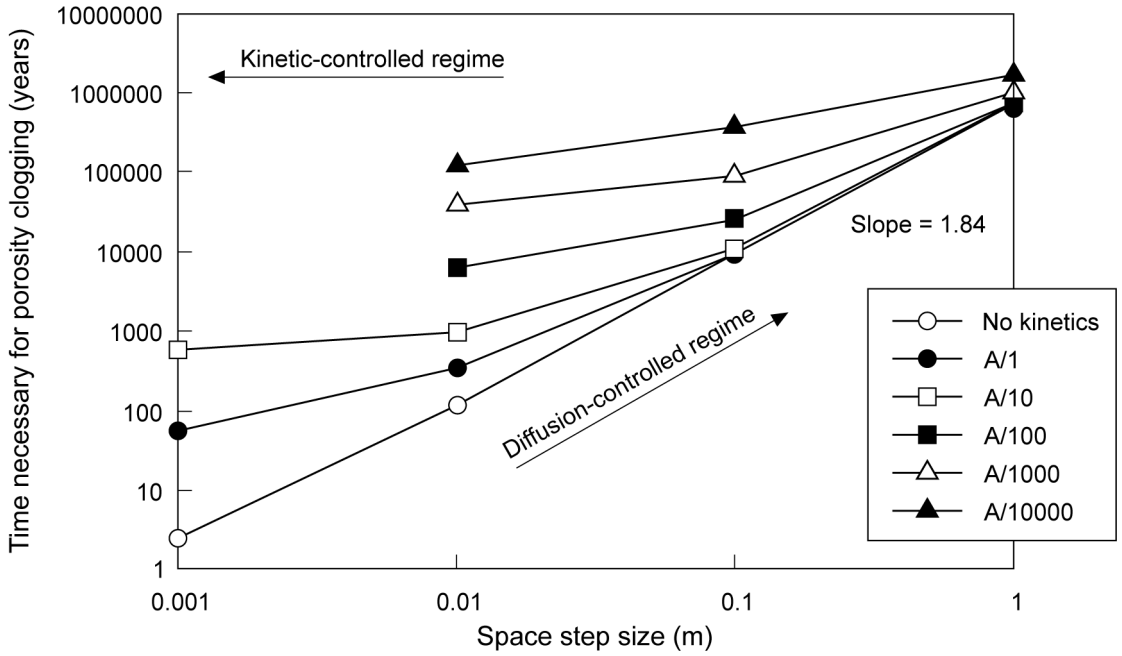

Fig. 4-1: Time necessary for porosity clogging as a function of spatial discretization and reaction rate

The reaction rate of all mineral reactions are scaled by changing the reactive surface area A. Reprinted from Marty et al. (2009) with permission from Elsevier.

4.1.4 Continuum scale parameterization of transport and other material parameters in evolving media: representative elementary volume (REV)

In macroscopic continuum-scale models, the simulation domain is divided into grid cells that are equal to or larger than the "Representative Elementary Volume" (REV), defined as the minimum volume in which the physical parameters (pressure, density, porosity, etc.) are representative of the whole domain (Bear 1972, Hill 1963). Inside this REV, each phase is treated as a single continuum exhibiting properties that represent the statistical average of each macroscopic property within this volume. This averaging concept of the macroscopic scale models has advantages and disadvantages. While it allows modelling on large spatial scales with reasonable computational resources, it is insensitive to any changes at the micro scale that occur due to geochemical reactions, within the averaged grid cell.

Examples of these micro-scale changes due to geochemical reactions are the evolution of the pore network structure because of mineral precipitation and dissolution (Patel et al. 2021, 2018, Prasianakis et al. 2018). The Darcy-scale models try to account for these reaction driven micro-scale changes by empirical relationships (Steefel et al. 2015) or coupling with lower scales models (Panga et al. 2005). For example, changes in the rock petrophysical properties such as permeability, reactive surface area, and diffusivity are a function of total porosity using empirical relationships such as Kozeny-Carman, power laws, and Archie's law.

4.1.5 Diffusive transport

Overview/general description

The reactive diffusive transport of solutes is described in its simplest form by

$$\frac{\partial \phi C}{\partial t} = \nabla D_e \nabla C + R \tag{4.2}$$

where C [mol/m^3] is the concentration of a particular species, R [mol/m^3/s] a (chemical) source/sink term representing the change in solute mass of the species due to chemical reactions, and D_e [m^2/s] are the components of the effective diffusion tensor, which depends on the porosity ϕ [-]. The diffusive flux j_D is included in Eq. 4.2 as

$$\mathrm{j}_D = D_e \nabla C \tag{4.3}$$

which is a form of Archie's law. For Diffusion in a non-Fickian sense in heterogeneous media see (Tartakovsky & Dentz 2019).

The effective diffusivity of dissolved species is temperature dependent and influenced by the properties of the pore space. Numerous definitions of the relation between the effective diffusion coefficient and the properties of the porous medium are available and definitions of parameters like tortuosity, constrictivity, formation factor or geometry factor might vary considerably between authors.

The temperature dependence of the water viscosity η_w is approximated in Appelo and Postma (2005) as

$$\eta_w = 10^{\frac{-1.37023(t_C-20.0)+8.36\cdot10^{-4}(t_C-20.0)^{2.0}}{109.0+t_C}} \tag{4.4}$$

with t_c the temperature in Celsius.

In addition, a material dependent geometry factor g_{eo} can be defined, which includes a tortuosity τ and constrictivity δ in the porous medium and a temperature correction to temperature t_K Kelvin.

$$g_{eo} = \tau/\delta \tag{4.5}$$

Often it is assumed that the size of transported molecules is much smaller than the (minimal) pore diameter which allows to set the constrictivity to one.

the geometry factor then gives

$$g_{eo} = \tau \cdot \frac{t_K \cdot 0.891}{298.0 \cdot \eta_w} \tag{4.6}$$

Often Archie's equation is used to relate the effective diffusion coefficient with the diffusion coefficient in water via the porosity ϕ and a material-dependent exponent m, the so-called cementation factor:

$$D_e = \phi^m D_w \tag{4.7}$$

m can vary for different kinds of porous media (rock types) from 1.3 (unconsolidated sediments, e.g. sand) up to 2 in well cemented (clay-free) sediments, and even higher values in clays. The diffusion coefficient of ions in electrolyte solutions at infinite dilution varies between 1.1×10^{-9} m^2s^{-1} and 2.1×10^{-9} m^2s^{-1} at 25 °C (Flury & Gimmi, 2002). In cement pastes and mortars the exponent *m* was estimated to be between 1.5 and 2.5 (Tumidajski et al. 1996). In the benchmarking calculations of Xie et al. (2015) on influence of the total porosity change on reactive transport an exponent of m-1=1/3 was used, consistent with the formulation by Millington & Quirk (1961) with m = 4/3 for "saturated unconsolidated systems".

For clay rocks, van Loon (2015) estimated a mean value of *m* = 2.4 and the following modified relation:

$$D_e = 2 \times 10^{-9}\phi^{2.4} + 1 \times 10^{-11}\phi^{1.0} \quad (4.8)$$

The effective "large scale" diffusion coefficient in the vicinity of a borehole in Opalinus Clay for several dissolved gases was determined by Damiani et al. (2021). They inversely fitted gas fluxes across a borehole/Opalinus Clay interface and fitted effective diffusion coefficients for gases in Opalinus Clay rock by combining Eqs. 4.5 and 4.6 and varying the geometry factor via the power low exponent *m* in Eq. 4.7. The manual fit of the geometry factor in terms of the exponent *m* = 2.2 results in a large-scale effective diffusion coefficient for H_2O (HTO) of 3.1×10^{-11} m/s ($D_w = 2.24 \times 10^{-9}$, $\phi = 0.16$, *m* = 2.2, T = 15.6 ºC). This value is slightly lower than those obtained in previous studies: temperature corrected values of $(4.2 \pm 0.4) \times 10^{-11}$ m/s ($\phi = 0.17$, T = 14 ºC) was measured for HTO in samples from the Mont Terri URL in the laboratory (Van Loon et al. 2004a) and the value of 4.0×10^{-11} m/s ($\phi = 0.15$, T = 14 ºC) estimated within an in situ migration experiment (Van Loon et al. 2004b).

Finally, the effective diffusion coefficient for dissolved species at the desired temperature can be calculated based on the species diffusion coefficient in water (at reference temperature), the porosity, and the geometry factor, which includes the temperature correction, constrictivity and the tortuosity.

Please note, that the pore diffusion coefficient D_p in this definition is the quotient $\frac{D_w}{g_{eo}}$

$$D_e = \phi \cdot D_w/g_{eo} = \phi \cdot D_p \quad (4.9)$$

This or a similar definition of the effective diffusion coefficient is implemented in many common reactive transport codes (e.g. Xie et al. 2015). The porosity in this definition is not part of the geometry factor, as it accounts for the reduction of cross sectional area in a porous medium compared to a water/gas filled volume.

Comparison of Eqs. 4.7 and 4.9, ignoring the temperature dependence and setting the constrictivity to one gives then for the tortuosity:

$$\tau = \phi^{1-m} \quad (4.10)$$

The main unknown parameter in this definition of the effective diffusion coefficient is the tortuosity respectively the cementation factor *m*.

Due to the negative surface charge in clays, the application of the simplest form of the reactive transport Eq. 4.2 is not always straightforward. Anions are partly excluded from regions near the surface, while cations are enriched in this region. As a result, anion fluxes are typically smaller than those of a neutral tracer (for a unit gradient and unit diffusion coefficient), while those of cations are larger (Tachi & Yotsuji 2014). As long as single ion transport is considered, it is still

possible to use Eq. 4.2, but with ion specific parameters, such as a reduced anion accessible porosity (Van Loon et al. 2007), or an increased cation diffusion coefficient (Gimmi & Kosakowski 2011). If coupled, reactive transport of anions and cations is of interest, this approach has, however, limits.

Various attempts exist to include the effect of the charged surfaces in the transport equations. In principle, the ion distribution near the charged surface can be modelled by applying the Poisson-Boltzmann (PB) equation. However, solving the PB equation is computationally demanding and would require knowledge of the detailed pore structure, which is hardly feasible. As an alternative, a Donnan approach or a mean electrostatic potential approach can be used, which treats concentrations in the pore space influenced by the charged surfaces as uniform (e.g., Tournassat & Steefel 2015). In this case, the flux Eq. 4.3 applies for the so-called free porosity (i.e., the porosity unaffected by surface charges), while the flux in the surface-affected pores (e.g., in the Donnan region), is governed by an additional equation analogous to Eq. 4.3. Moreover, it is generally assumed that the concentration of solute *i* in the Donnan region, C_{Di}, is in equilibrium with that in the free pore water, C_{fi}, according to

$$C_{Di} = C_{fi} \exp - \left(\frac{z_i F \psi_D}{RT}\right) \tag{4.11}$$

where $z_i$is the charge of the solute, F the Faraday constant, ψ_D the Donnan potential, R the universal gas constant and T the temperature. The mean electrostatic or Donnan potential has to be calculated from the surface charge and the solution composition. As anions and cations can be transported at different rates, it is needed to consider also the Nernst-Planck equations to keep the charge balanced.

Only a limited number of codes have the capability to consider transport in the two pore regions explicitly, such as Phreeqc and CrunchFlow. Gimmi & Alt-Epping (2018) presented a slightly different approach to consider a Donnan region without explicitly solving Eq. 4.11. They considered charged surfaces as immobile solutes and demonstrated with the code Flotran that by solving the Nernst-Planck equation, a Donnan region can be equally simulated. Jenni et al. (2017) used this approach to simulate transport across cement-clay interfaces. Concerning the transport part, Jenni et al. (2017) proposed a new cement/clay interface modelling framework that uses dual porosity. The porosity in the model is split into a free porosity and a Donnan porosity. The Donnan porosity is the anion depleted porosity made from the clay interlayer and the surface diffuse double layer that contains an excess of cations for balancing the negatively charged clay surfaces. This allows the transport at the interface to continue after the obstruction of the free porosity in contrast to models where the transport takes place only in the free porosity.

4.1.6 Tortuosity-porosity relationships

In general, tortuosity is the lengthening of an average flow/transport path between two observation points, compared to the shortest distance between the points. In terms of pressure or concentration gradients, it is the relative difference between the microscopic pressure/ concentration gradient along the transport pathway and the macroscopic pressure/concentration gradient. A critical review on tortuosity in porous media was conducted by Ghanbarian (2013). They stress in their review that "*proposed tortuosity models are distinct and thus may not be used interchangeably*."

Often the leading porosity in Eq. 4.9 is combined with the tortuosity definition in Eq. 4.10 to give

$$D_e = \phi/\tau \, D_w = \phi \cdot \phi^{m-1} \cdot D_w = \phi^m \cdot D_w \tag{4.12}$$

In Eq. 4.10 the tortuosity τ is related to the total porosity and is used to describe the influence of the porous medium on the effective diffusion coefficient. In addition, to the simple definition of tortuosity in Eqs. 4.6 and 4.12, more complex tortuosity models were developed for use in cementitious media. They relate for example pore size distributions and cement compositions to predict diffusivities and other transport properties (Bejaoui & Bary 2007, Bentz et al. 2000, Courcelles et al. 2010, Garboczi 1990, Oh & Jang 2004, Tumidajski 2005). Millington and Quirk (1961) state that in porous media with *"anisotropy, cementation or incomplete dispersion of pore sizes, ... both probability for continuity of the total pore area in section and the nature of the pore-radius interactions cannot be ascertained from measurements of porosity and pore-size distribution alone".*

Following the argumentation of Ghanbarian (2013), it seems not useful to use standard laws for tortuosity (and related permeability/diffusivity) implemented in reactive transport code for scenarios with strong porosity change without checking if those relations are applicable.

Busch et al. (2018) estimated effective diffusion coefficients for Opalinus Clay and other mudrocks with help of a tortuosity function based on a fractal pore space model (Fig. 4-2). They measured pore surface properties and pore size distributions with small-angle neutron scattering (SANS) measurements. They got for the cementation factor

$$m = 1 + \frac{2(D_s-2)}{3-D_v} \tag{4.12}$$

The surface fractal dimension D_s of the pore surface was obtained from the SANS measurements and D_v, the fractal dimension of the pore solid interface, from the pore size distribution. For Opalinus Clay they estimated values for m between 2.29 and 3.13, and for Boom Clay values between 2.16 and 2.60.

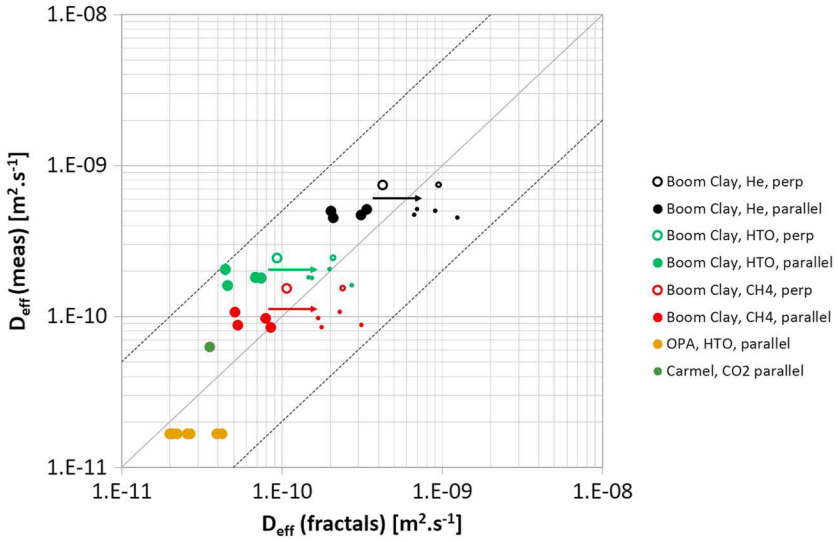

Fig. 4-2: Measured versus modelled effective diffusion coefficients for the three different sample sets used in this study

For Boom Clay, the large symbols relate to calculated diffusion coefficients based on SANS porosity, the small symbols to those using porosities from Jacops et al. (2017). Dashed lines represent factors 5 higher or lower than the 1:1 line (reprinted from Busch et al. 2018 with permission from Elsevier).

4.2 Thermodynamics, cement phases, clay precipitates, and zeolites

The main groups of alteration phases predicted to form due to the cement/clay interaction are C-S-H (calcium silicate hydrates), M-S-H (magnesium silicate hydrates), clays/ phyllosilicate minerals, zeolites, carbonates, sulphates. To be able to accurately model complex non-ideal multiphase systems we need to use a robust geochemical modelling tool that has sufficiently complex models implemented (to capture the complexity of the phases and their properties that are relevant for the investigated problem) and to use a consistent thermodynamic database containing parameters for the stability of phases and their reaction kinetics. It is well known that the reaction of different phases is controlled by disequilibrium and their evolution with time (e.g., clays dissolution/precipitation) needs to be modelled by additionally considering the underlying chemical reaction kinetics (Fritz & Noguera 2009, Marty et al. 2014). Thermodynamic modelling sits on two pillars, i.e., the thermodynamic database and the conceptual model (modelling scenario and thermodynamic methods and equations) (Meeussen et al. 2009). When modelling cement – clay interaction discrepancies arise from differences in the stability constants present in thermodynamic databases (differences in the properties of master species, stability of relevant phases and aqueous species) and data completeness, but also from differences in conceptual models used (completeness of the mineral list, methods for calculating the activity coefficient, the use of discrete phases vs. solid-solution models for C-S-H and clay phases, etc.) (Gaucher & Blanc 2006, Meeussen et al. 2009). In this section we provide an overview on the status related to geochemical modelling tools, thermodynamic models, and thermodynamic databases related to modelling cement/clay interaction with a focus on equilibrium thermodynamics.

An early cement degradation model was developed by Berner (1992) and further extended by Neall (1994) with the addition of cement hydrate phases (ettringite, hydrogarnet and hydrotalcite). The model considered the initial cement hydration stage, the incongruent dissolution of C-S-H and the degradation of cement due to interaction with natural groundwaters. The calculation used a simple mixing tank model approach, where a given amount of cement reacts to equilibrium with successive batches of pore groundwater solution (marl pore water). Such a model can provide a rough qualitative estimate of the temporal evolution of the cement in term of total porosity evolution (due to dissolution/precipitation) and helps to identify relevant mechanisms and parameters but does not account for any transport and interface related phenomena, that can have a decisive impact on the evolution (Berner 1992).

The cement degradation model was largely improved with the development of cement oriented thermodynamic databases such as cemdata07 and cemdata18 (Lothenbach et al. 2019) and the coupling of thermodynamic equilibrium/kinetics with transport into a reactive transport model (Kosakowski & Berner 2013). Such a model allows for detailed simulation of the evolution of the interfaces between concrete and other repository materials such as the Opalinus Clay host rock.

4.2.1 Geochemical modelling tools

There are two main groups of tools that calculate chemical equilibrium ((geo)chemical solvers), ones that are based on Gibbs energy minimization (GEM) method (e.g. GEMS (Kulik et al. 2012); Reaktoro (Leal et al. 2016); GIBBS/Hch (Shvarov 2008), etc.) or on solving the system of law of mass-action equations (LMA) (e.g. PHREEQC (Parkhurst & Appelo 2013), Orchestra , EQ3/6 (Wolery 1992), Geochemist's Workbench (Bethke 2007), etc.). Leal et al. (2017) showed that the two methods for solving chemical equilibrium are equivalent but that their implementation can have an effect on the speed and stability of the calculation. To model reaction controlled by kinetics these codes have implementations of kinetic models which depending on the complexity contain parameters such as rate constant, activation energy, reactive surface area and possibly their dependence on different conditions such as temperature, pH, composition (Leal et al. 2017). Nevertheless, if the models input parameters and thermodynamic properties of the species making

up the phases in the chemical system are the same, both class of codes produce the same results (Águila et al. 2021, Idiart et al. 2020, Marty et al. 2015a). For doing reactive transport calculations (geo)chemical solvers, can be coupled to T(hermo)-H(ydro)-M(echanical)-C(hemical) transport codes, e.g. OpeGeoSys-GEM (Kosakowski & Watanabe 2014), iCP (COMSOL-PHREEQ) (Idiart et al. 2020). In this case the (geo)chemical code solves the chemical equilibrium and the transport code solves the equations related to flow and transport in a sequential iterative or non-iterative approach (Shao 2009). Some codes come with combined implementations of chemical and transport solvers e.g., TOUGHREACT, PHREEQC (internal transport module), CRUNCH, HYTEC, ORCHESTRA, etc.

Extensive benchmarking exercises done on multiple reactive transport codes (including the ones exemplified above) have shown that independent from their implementation for the same chemical and transport setup the different simulators produce very similar and consistent results (Águila et al. 2021, Idiart et al. 2020, Marty et al. 2015a). The main discrepancies arise from differences in transport, thermodynamic, and kinetic parameters, and model coupling (how the feedback between changes in chemistry like mineral precipitation, and transport, like porosity update, are coded) and not from using different modelling tools (Idiart et al. 2020). A list of fifteen different computer codes used for modelling cement/clay-interactions can be found in Tab. 2-1 of Savage & Cloet (2018). Such benchmark exercises mainly cover problems that can be solved with methods and thermodynamic models available in all codes. Solid-solution-based models are useful to accurately model processes such as those related to the retention of various elements by phases that form at the cement-clay interface (e.g., uptake of radionuclides by C-S-H, carbonates, sulphates and Fe(II)/Fe(III) oxyhydroxides) (Bruno et al. 2007). Many "law of mass action" (LMA) based codes model solubility of pure solid phases other codes such as PHREEQC have the possibility to use multicomponent ideal or binary non-ideal solid solution models (Rodríguez-Galían and Prieto, 2018). GEM-Selektor is well suited for modelling systems that involve many nonideal multicomponent phase solutions and can deal with ideal and non-ideal binary, ternary and multicomponent solid-solutions (Kulik et al. 2012, Wagner et al. 2012).

GEM-Selektor (and GEMS3K standalone equilibrium solver) has been extensively used for modelling long-term evolution of engineered barriers for nuclear waste as it provides a more realistic description of complex geochemical systems (geochemical evolution of the near field, spent fuel dissolution, gas generation, and chemical stability of engineered bariers: Berner et al. 2013, Ochs et al. 2016, Kosakowski et al. 2014, Kosakowski & Smith 2014, Wieland et al. 2020). GEM-Selektor is mostly open-source software developed at PSI LES (laboratory for waste management) tightly connected to the PSI/Nagra database and projects related to modelling safety-relevant scenario for geological waste disposal. GEM-Selektor is also used in connection to the development extension and improvement of data for cement phases (Lothenbach et al. 2019, Matschei et al. 2007) as well as modelling various aspects related to cementitious materials (Dilnesa et al. 2014, Kulik et al. 2021, Lothenbach et al. 2019, Lothenbach & Winnefeld 2006, Ma & Lothenbach 2020a, Matschei et al. 2007). Some of the clay-cement interaction relevant modelling applications that used GEM-Selektor are: modelling bentonite and cement pore water chemistry and solubility limits of relevant radionuclides (Berner 2014a, 2014b, 2009, Berner et al. 2013, Kosakowski & Berner 2011) and immobilization of actinides and fission products by sulfate, carbonate solid solution (Vinograd et al. 2018).

The two methods for calculating chemical equilibrium, GEM and LMA, require two different forms of thermodynamic data. The LMA codes use reaction-based databases. These databases contain master and product species reactions and the LMA codes require only the logK of formation of the product species at the temperature and pressure of interest (and parameters to extrapolate these values at different temperatures and pressures). The GEM codes use standard molar thermodynamic property-based databases. These databases contain standard molar (or partial molal) properties, and to calculate equilibrium the GEM codes require the Gibbs energy corrected for the temperature and pressure of interests for all species forming the phases of the

chemical system. The GEM style databases are more suited for thermodynamic rigor, completeness and extrapolation capabilities as they contain all thermodynamic properties (if available) of species and are therefore used in all state-of-the-art thermodynamic data reviews and compilations (e.g., OECD-NEA TDB project (Guillaumont et al. 2003), PSI/Nagra database (Hummel et al. 2002, Thoenen et al. 2004, Thoenen & Hummel, 2021), etc.). On the other hand, LMA style databases make it easier to maintain consistency between thermodynamic data of species, by having them fixed to reaction constants derived from experimental data. An LMA database can only be converted to a GEM database after assigning thermodynamic properties to master species taken from existing databases such as OECD-NEA TDB or the PSI/Nagra database. A GEM database can be converted into an LMA database by generating all independent reactions for products species based on a selection of master species. An important issue when modelling reactions in the presence of an aqueous phase is the availability of water. Chemical reactions related to corrosion, cement hydration or formation of secondary hydrate phases consume water from the system. In solid dominated and partially saturated system changes with limited amount of water this will have an impact on the dissolved elemental concentrations and the exhaustion of water will hinder the reactions. This process can be modelled if water is included in the mass balance calculation and not considered in excess.

4.2.2 Thermodynamic data for cement phases

Thermodynamic data for relevant cement phases are available in different databases such as Thermoddem (Blanc et al. 2012) and Thermochimie (Blanc et al. 2010, Giffaut et al. 2014). Thermoddem is developed by the French geological survey (https://thermoddem.brgm.fr) for geochemical and environmental applications (e.g., geological waste storage). Thermochimie is developed by ANDRA (French National Agency for radioactive waste management), ONDRAF and RWM for the performance assessment of geologic radioactive waste (Giffaut et al. 2014, https://www.thermochimie-tdb.com). Both databases contain data on zeolites, cementitious and clay phases as well as other minerals (e.g. carbonates, sulphates, hydroxides) relevant for cement/clay interaction. The C-S-H and M-S-H phases are treated as discrete components. The databases can be used by several modelling codes such as CRUNCHFLOW, HYTEC, PHREEQC or THOUGHREACT. Thermoddem and Thermochimie are in principle compatible and comparable because they share many components. Thermoddem has a smaller data collection (Bok et al. 2019) but contains more data on the temperature dependence of the thermodynamic properties (e.g., uses the Helgeson-Kirkham-Flowers equation of state for aqueous species (Helgeson et al. 1981)), while Thermochimie uses simple temperature extrapolation such as Van't Hoff or constant heat capacity.

The cemdata18 (Lothenbach et al. 2019) is a widely used source for thermodynamic data related to cementitious systems. The database contains thermodynamic data for common cement hydrates relevant for modelling cement/clay interactions such as C-S-H, AFm and AFt phases, hydrogarnet, hydrotalcite, zeolites, and M-S-H that are valid over temperatures ranging from 0 to at least 100 °C. Compared to previous published data (cemdata07, 14) (Lothenbach et al. 2012, 2008a) cemdata18 contains improvements to the thermodynamic properties of aluminium and iron containing phases (ferric iron bearing AFm and AFt phases, hydrogarnet, and Mg-Al layered double hydroxide (LDH) type phase, as well as changes in the C-S-H models concerning volume and the alkali uptake. Depending on the input composition these changes lead to significant differences when modelling with a different database version (Lothenbach et al. 2019). cemdata18 was developed using PSI/Nagra 12/07 (Hummel et al. 2002, Thoenen et al. 2014) as source for the aqueous species, gas and other solid components. Data for solid phases, e.g., carbonates, aluminium hydroxides, iron oxides, hydroxides, sulfides, relevant for cementitious systems, distributed with cemdata18, are also from the PSI/Nagra 12/07. (Al, Fe)-ettringite, (Al, Fe)-monosulfate, (SO_4, OH)-monosulfate, and (SO_4, OH)-ettringite phases are treated as

non-ideal binary Redlich-Kister (Guggenheim) (Glynn 2019). (Al, Fe)-siliceous hydrogarnet, C-S-H, M-S-H, hydrotalcite-pyroaurite, (Mg, Al)-hydrotalcite, straetlingite and ettringite (for different water content) are treated as ideal solid solutions. The newly added (Al, Fe)-siliceous hydrogarnet solid-solution phase is highly relevant for the uptake and mobility of iron as it is the most stable iron bearing cement hydrate phase from ambient to elevated temperatures. With decreasing pH at the cement/clay interface the hydrogarnet can be replaced by ferrihydrite, which depends on the pH and Eh, can further transform into goethite, hematite and magnetite (De Windt et al. 2020, Dilnesa et al. 2014). The iron bearing silicious hydrogarnet formed within days in the experiments at 20 °C of Dilnesa et al. (2014), its stability increased with temperature, was identified in different cement compositions like ordinary Portland cement (OPC), sulphate resistant cement (HS) (Dilnesa et al. 2014) ferrite-rich cement (Elakneswaran et al. 2019), and in cement paste hydrated for 10 and 50 years (Dilnesa et al. 2014, Vespa et al. 2015). However, the stability of the Al rich hydrogarnet is close to other Al bearing cement hydrates (Dilnesa et al. 2014), its formation during cement hydration is kinetically hindered and may play a role in aged cementitious materials influencing the aluminium concentration.

Calcium silicate hydrate (C-S-H) phases of various composition are ubiquitous in cementitious materials and can form at the interface of clay and cementitious materials (Gaucher & Blanc 2006, Raúl Fernández et al. 2016). C-S-H phases have a major influence on the composition of the pore solution, pH, the stability of other cementitious phases, and the retention of radionuclides making them relevant for application of cementitious materials as waste matrices or engineering barriers. C-S-H incorporate alkali metals, alkaline earth metals and also aluminium and iron that are components of and interact with clay minerals. Interacting fluids from the clay side (more silica rich) with fluids from the cement side (more calcium rich) will lead to the formation of variable Ca/Si C-S-H phases.

One main difference in the available databases is the use of different C-S-H models. Thermoddem and ThermoChimie contain data for discrete phases of calcium silicate hydrate (C-S-H), calcium aluminate silicate hydrate (C-A-S-H) and magnesium silicate hydrate (M-S-H). The properties of these discrete phases are based on calorimetric and solubility measurements of Roosz et al. (2018). In cemdata18 database C-S-H phases are treated as solid-solution models (i.e., CSHQ and CNASH models). The CSHQ model (Kulik 2011) provisionally extended with Na and K endmembers is used for modelling ordinary Portland cements. The CNASH solid-solution model (Myers et al. 2014) is optimized for systems with more aluminium at lower Ca/Si ratios (modelling alkali activated) (Lothenbach et al. 2019).

C-S-H can incorporate Na, K, Al, Fe cations (Bach et al. 2013, L'Hôpital et al. 2015, Mancini et al. 2020, Myers et al. 2014), cations relevant for (radioactive) waste disposal such as actinides: Th(IV), U(VI), Np(IV), Np(V), Np(VI) (Gaona et al. 2011, Jan Tits et al. 2014), lanthanides: Cm(III), Am(III), Eu(III) (Tits et al. 2003, Wolter et al. 2019), fission products: Sr (Tits et al. 2006b), Ba (Missana et al. 2017), Ra (Kittnerová et al. 2020, Lange et al. 2018, Olmeda et al. 2019, Tits et al. 2006a) and base metal cations: Zn (Kulik & Kersten 2002), Pb (Zak & Deja 2015), Cs (Missana et al. 2018). Hence, it is important to be able to capture the complexity of C-S-H in the geochemical models and have an accurate prediction of its stability, density, solubility, and composition. Such predictions are possible using thermodynamic solid solution models of C-S-H phases. Many alternative thermodynamic models of C-S-H have been proposed and applied to C-S-H solubility data with various degrees of success (Kulik 2011, Kulik et al. 2022, Walker et al. 2016). Previous attempts to extend C-S-H solid solution models with such cations were only partially successful because they did not account properly for cations binding onto specific structural sites; the resulting models were not incremental and did not accurately predict the uptake isotherms measured at different Ca/Si ratios.

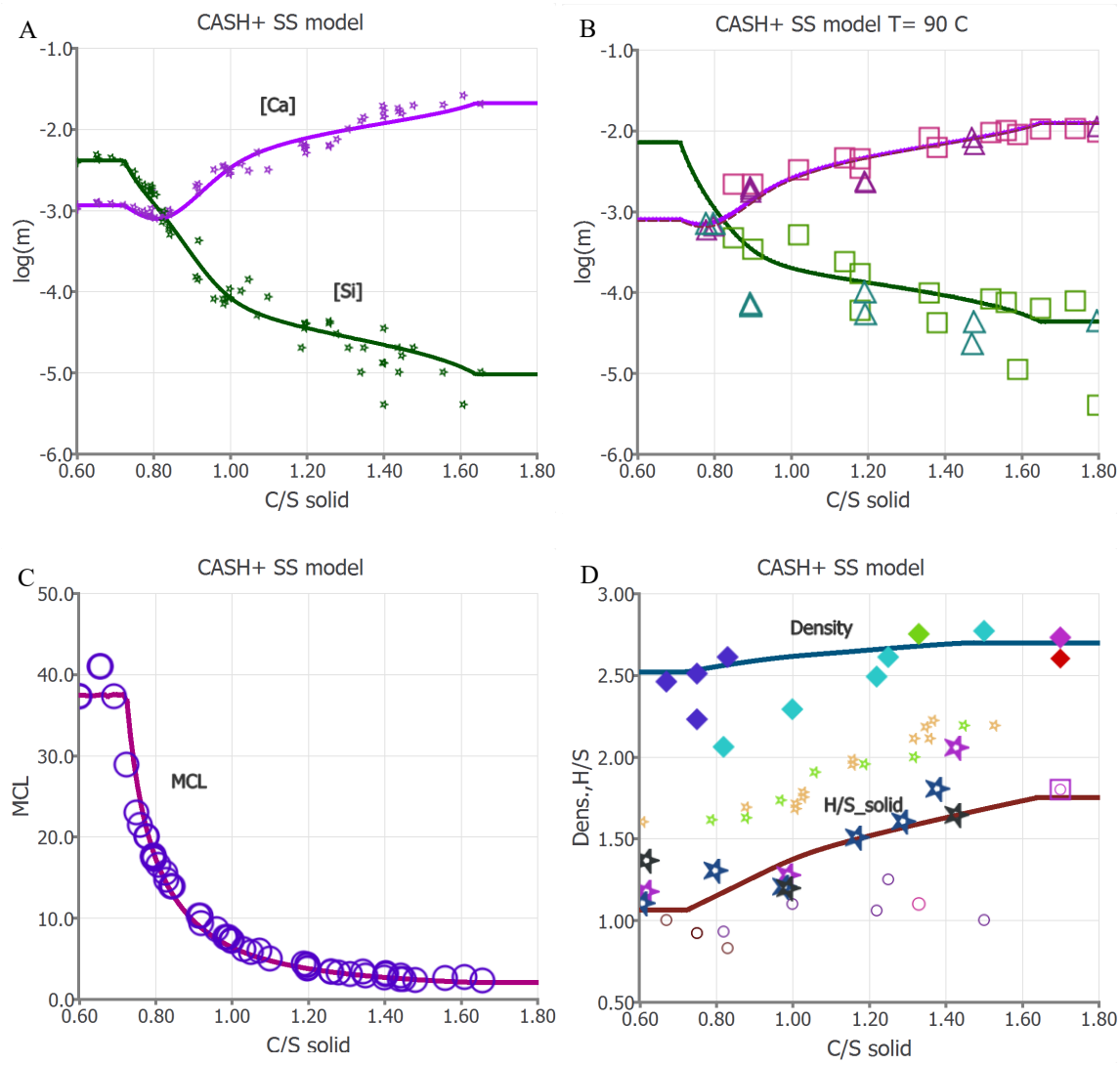

Fig. 4-3: Model predictions (curves) compared with measured data (symbols) on C-S-H (A) solubility at 25 °C. (B) solubility at 90 °C. (C) mean silicate chain length (MCL). (D) density and non-gel water content.

A new rigorous structurally consistent sublattice solid solution model CASH+ has been developed (Kulik et al. 2022, Miron et al. 2021) consistent with the cemdata18 and PSI/Nagra 14/07 databases. The model is being extended incrementally and can accurately describe the solubility, cation uptake, the non-gel water content, and the mean silicate chain length (MCL, refers to the number connected silicon tetrahedra in the C-S-H phase) of C-S-H (Fig. 4-3) from ambient to elevated temperatures (90 °C). The use of complex non-ideal multisite models is possible through the TSolMod library of solution models (Wagner et al. 2012) available with the GEM-Selektor and GEMS3K codes (Kulik et al. 2012).

Most chemical solvers and reactive transport simulations do not incorporate such models. A crude solution is the use of a discretized (solid) solution model, having the C-S-H model discretized into several pseudo-compounds, treated as pure phases. The discrete phases with their dissolution reactions can then be easily incorporated into modelling codes such as LMA solvers. Compared to the full solid-solution models that produce a C-S-H with a continuously variable composition, the discrete models have a stepwise appearance (the number of discrete phases determines how

accurate they are). Using discrete phases make calculations less computationally expensive which can be relevant in large reactive transport models. The extension of a discrete model can become impractical and the number of discrete phases will dramatically increase when having a small compositional step size or adding the uptake of various elements (De Windt et al. 2020). Usually there is a trade-off between speed and model detail. This gives GEM-Selektor, and the coupled reactive transport codes that use GEMS, a clear advantage compared to other chemical solvers that lack such models. Calculations using the CASH+ model (Kulik et al. 2022) showed that the solid solution model is consistent with the discrete phases data in Roosz et al. (2018) that are used in the Thermochimie database.

4.2.3 Thermodynamic data for clay minerals

The conceptual models for complex clay materials can be based on discrete phases or using solid-solutions constructed using cationic clay endmembers (e.g., Na-Smectite, Mg-Smectite, etc.) or using cation exchange sites. Both types can be then combined with a sorption model considering possible sorption sites. For example, (Kosakowski & Berner 2011) used an ideal solid solution with seven end members to account for the Na^+, K^+, Mg^{2+}, Ca^{2+}, Fe^{2+}, and Sr^{2+} composition and extended it for cation sorption with amphoteric ≡SOH sites based on data from Bradbury and Baeyens (2002). These models relate to the properties of the bulk phases and do not take into account the complex surface effects on the adjacent solution properties. For example, to account for the surface effect on the ion diffusion a clay surface diffusion model needs to be considered Due to the complexity of clay minerals observed in experiments and natural samples the attainment of equilibrium is ambiguous (Aja & Rosenberg 1992). This makes the solubility experiments not representative for thermodynamic equilibrium and introduce large uncertainties in the derived data (more details in NTB 19-03 (Jenni et al. 2019)). However, using a combination of thermodynamic equilibrium with metastability constraints and kinetic data can be used to roughly model the dissolution/precipitation of specific clay mineral compositions and get a qualitative information on the system evolution.

Extensive thermodynamic data on clay minerals is available in the Thermochimie database (Blanc et al. 2015). This includes data for smectites, illites (10 Å), chlorites (14 Å), and kaolinite (7 Å) type of clay minerals. Because clay minerals have a complex composition and crystallographic structure, it is difficult to acquire thermodynamic data covering the full range of compositions. Experimental measurements are available for a few selected minerals that are then used to construct predictive models for intermediate and fictive clay compositions (Blanc et al. 2021, 2015). The predictive methods are split into two main parts: first predicting the thermodynamic properties for the anhydrous clay composition (polyhedral approach, additivity method, based on differences in electronegativity) (Roosz et al. 2018) and second assigning the correction for the properties of hydration (Blanc et al. 2015, Vieillard 2000). These methods have been implemented in two computer tools ClayTherm and ISTherm (Blanc et al. 2021) that can be used to estimate properties of clay minerals and ilite/smectite mixed minerals, respectively.

The PSI/Nagra 2020 (Thoenen & Hummel 2021) thermodynamic database contains thermodynamic data for clay minerals taken from the Thermochimie database.

In GEM-Selektor each complex clay mineral phases with cation sorption can be modelled in two parts using an ion exchange phase and another separate adsorption phase (Kulik et al. 2018). The ion exchange phase can be described using non-ideal models of mixing while the adsorption phase is based on the 2SPNE SC/CE model (Bradbury & Baeyens 2002). These phases are then easy to combine with other aqueous (SIT, Debye-Huckel, Pitzer, etc.), gaseous, and solid-solution models available in GEM-Selektor and used in performance assessment, reactive transport simulations.

4.2.4 Thermodynamic data for zeolites

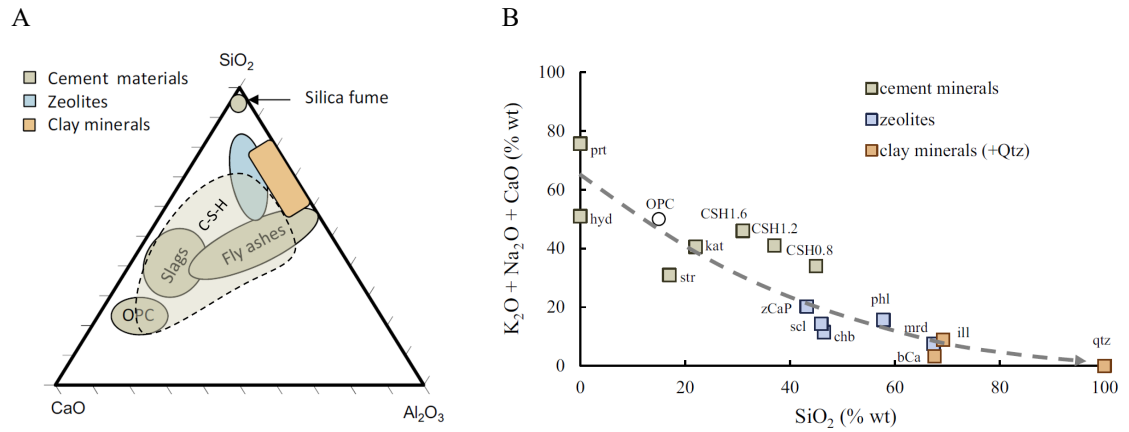

Fig. 4-4: Schematic ternary diagram

(A) Adapted from Blanc et al. (2015) with permission from Elsevier, showing the approximate compositional domains of cementitious materials, zeolites, and clay minerals. (B) composition of relevant minerals in the clay-cement system, the arrow follows a decrease in alkalinity (Reprinted from Blanc et al. 2015 with permission from Elsevier).

prt: portlandite; hyd: hydrogarnet; OPC: Ordinary Portland Cement; kat: katoite; str: straetlingite; zCaP: zeolite P(Ca); scl: scolecite; chb: chabazite; phl: phillipsite; mrd: mordenite; bCa: beidellite(Ca); ill: illite; qtz: quartz

Zeolites are secondary minerals that could form due to the interactions of clay minerals with the alkaline cementitious environment surrounding the cement-clay interface (Bildstein et al. 2019, Blanc et al. 2015, Gaucher et al. 2004, Gaucher & Blanc 2006, Lothenbach et al. 2017, Ma & Lothenbach 2020b, 2020a). Compositionally they sit in between the cementitious materials and clays (Fig. 4-4). Because of kinetic hindrance they are not observed in cement/clay interaction experiments, but they may form at later stages of evolution beyond the time scales of existing experiments.

The alkaline cementitious pore water leads to the dissolution of aluminosilicate minerals and the precipitation of secondary zeolite minerals. These influence the physico-chemical properties at the cement/clay interface. Given the chemical variability which leads to many zeolites that can form in different conditions, several studies were focused on better understanding the condition of their formation and on providing data on their thermodynamic stability (Aradóttir et al. 2012, Blanc et al. 2015, Chipera & Apps 2001, Fridriksson et al. 2001, Gaucher & Blanc 2006, Hemingway & Robie 1984, Holland & Powell 1998, Ma & Lothenbach 2020a, Zhen-Wu et al. 2020). Thermodynamic data on zeolites is based on critical selection of solubility and calorimetric measurements. The reported solubility products and thermodynamic functions are only available for a limited number of zeolites and can show large discrepancies and diverging temperature trends (Lothenbach et al. 2017, Ma & Lothenbach 2020a). This is due to the variable composition (variable Al/Si ratio, cation composition, and water content), order/disorder, crystallinity, slow reaction kinetics and presence of impurities (Bish & Carey 2001, Fialips et al. 2005, Lothenbach et al. 2017). The formation of thermodynamically stable zeolites is kinetically hindered as seen in cement/rock experiments that did not reach equilibrium after 6 years of interaction (Ma & Lothenbach 2020a). Some of the existing gaps in the thermodynamic data for zeolites are filled with estimation methods such as the oxide summation and polymer (polyhedral decomposition) method (Arthur et al. 2011, Mattigod & McGrail 1999, Myers et al. 2015, Vieillard 2010,

Vieillard & Mathieu 2009, Voskov et al. 2019). These methods are based on the contributions of elementary building blocks (e.g., oxides, hydroxides) to the overall thermodynamic properties of a zeolite mineral and can provide thermodynamic data that are in reasonable agreement with calorimetric measurements (Arthur et al. 2011, Mattigod & McGrail 1999, Voskov et al. 2019). Recent experimental work of Ma and Lothenbach (2020a, 2020b) has provided high quality thermodynamic data for several Na, Ca, and K zeolites. The thermodynamic data such as solubility constants and entropy were extracted from dissolution experiments of pure zeolite powders of different compositions measured between 20 and 80 °C. Remaining properties such as volume and heat capacity were determined from literature structure data and calorimetric data or from the additivity methods, respectively. The thermodynamic data for zeolites was derived consistently with other properties for aqueous species, gaseous species minerals and cement hydrates from PSI/Nagra (Thoenen et al. 2014) and cemdata18 databases. These data are available in cemdata18 and replace the previous zeolites in the database (Chabazite, ZeoliteP, Natrolite, ZeoliteX and ZeoliteY) (Lothenbach et al. 2017). Due to differences in the properties of master species used to represent the dissolution reactions between thermodynamic databases (e.g., PSI/Nagra, Thermochmie), different standard Gibbs free energy of formation can result. To keep consistency, the solubility constants of minerals should be used as reference data.

The zeolites dataset of the work of Ma & Lothenbach (2021, 2020b, 2020a) present in cemdata18, is compatible with the data for Na and Ca clays from Blanc et al. (2015) and can be used to model the interaction between cement and clay rocks. The calculated predominance diagrams using the updated zeolites dataset and the complementary clay data show similarities with the work of Blanc et al. (2015), but there are also noticeable differences in the predicted stable zeolite phases (Ma & Lothenbach 2020b), with mordenite, chabazite, and gismondine (LS-P(Ca) being more stable when compared to (Blanc et al. 2015) (Fig. 4-5). In the predominance diagrams all the investigated zeolites were allowed to precipitate. Therefore, the predominance results only obeyed the extent of oversaturation but might not agree exactly with the natural abundance due to various metastability and kinetic processes.

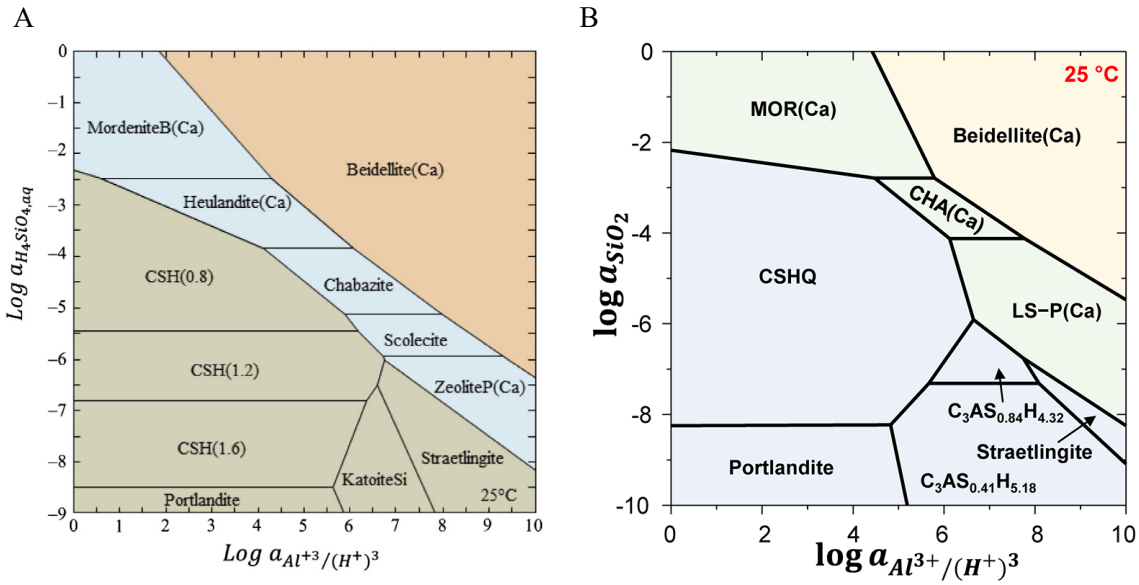

Fig. 4-5: Predominance diagrams reprinted from Blanc et al. (2015) with permission from Elsevier (A) and from Ma & Lothenbach (2020a) showing some differences between Thermochimie and cemdata18 databases

C-S-H phases is modelled as discrete phases (A) and as a solid-solution (B).

4.3 CI- Modelling with OpenGeoSys-GEM: extended summary of CI-report (Kosakowski, 2018)

4.3.1 Overview/general description

The modelling work for the Mont Terri CI project was conducted to test, if a state-of-the-art reactive transport model can reproduce all the experimental observations for a 10-year long interaction of two different cement/clay interfaces: Ordinary Portland Cement (OPC)/Opalinus Clay (OPA) and low pH concrete (ESDRED)/OPA. The study aimed at improving earlier models (Berner et al. 2013, Bradbury et al. 2014, Ochs et al. 2016, Kosakowski et al. 2014, Kosakowski & Berner 2013, Kosakowski & Smith 2014) by using an updated thermodynamic database for cement phases CEMDATA V14.01, more clay and zeolites minerals imported from Thermoddem TDB, improved handling of reaction kinetics and an alternative approach to consider cation exchange processes. A quasi 1D-radial symmetric model representation of the CI-Experiment was implemented (Fig. 4-6). As a secondary objective, the overall reactive transport modelling approach was investigated in terms of applicability and robustness.

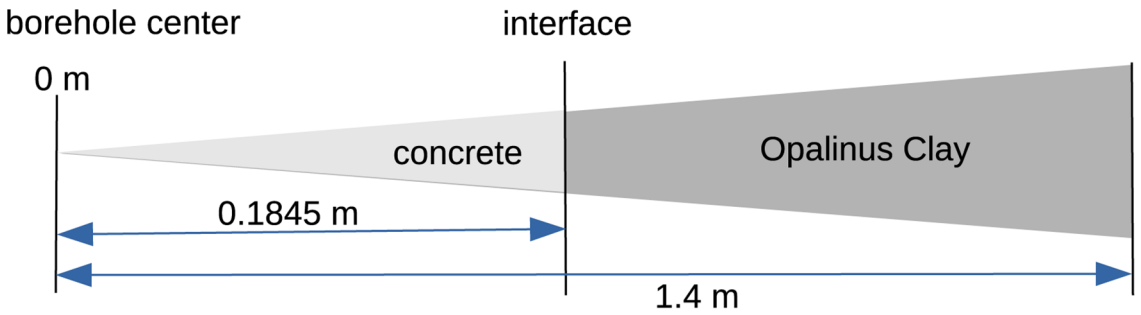

Fig. 4-6: Conceptual quasi 1D radial symmetric representation of CI Experiment
The grid and symmetry is aligned parallel to bedding of the Opalinus Clay formation. (from Kosakowski 2018).

Model results were compared to experimental data on cement hydration kinetics and mineralogical changes from extracted cement/clay interfaces after 5 years of interaction (Lothenbach 2011a, 2011b, Mäder et al. 2017). The sensitivity of the results on changes in reaction kinetics, on spatial discretization and on effective diffusivity was investigated.

4.3.2 Information from modelling with OpenGeoSys-GEM

The model calculations in Kosakowski (2018) described successfully the evolution of cement/Opalinus Clay interfaces investigated in the framework of the Mont Terri CI experiment. The models reproduce most of the experimental findings in the CI-experiment as reported in (Lothenbach 2011a, 2011b, Mäder et al.2017). The experimental observations are believed to be related to the following main processes that are listed by Cloet et al. (2014) for the influence of a high salinity Opalinus Clay pore water on cement stability. These features are:

- The Mg content of Opalinus Clay pore water and from Opalinus Clay cation exchanger will promote the formation of brucite ($Mg(OH)_2$) and to a lesser degree the formation of hydrotalcite ($MgCO_3 \cdot Fe/Al_2O_3 \cdot 5MgO$) and the formation of M-S-H (see Figs. 4-7 – 4-9).
- The ingress of sulphate SO_4^- causes the formation of ettringite and at very high sulfate concentrations, gypsum. AFm phases will be dissolved, as a source of aluminium is required for ettringite formation (see Figs 4-7 and 4-8).

- Furthermore elevated Cl concentration will result in the formation of Friedel's salt ($3CaO \cdot Al_2O_3 \cdot CaCl_2 \cdot 10H_2O$) from C-S-H and other AFm phases.
- High alkali concentration in general and specifically high sodium concentrations will influence the calcium concentrations in the cement pore water. There is a significant uptake of alkali ions in C-S-H with lower C/S ratio where they replace structural calcium ions.

All of the above more general processes are reproduced within the modelling study. The mineralogical changes and the connected transport processes for OPC/OPA and ESDRED/OPA interfaces observed in the model are shown in interfaces observed in the model (Fig. 4-7).

The formation of M-S-H from C-S-H near the interface is common for both, ESDRED and OPC. In ESDRED only M-C-H is stable due to a strongly reduced pH after a few years. Brucite is stable in OPC, but hydrotalcite is observed only in the Opalinus Clay.

The ingress of sulphate causes the formation of ettringite for both concretes, ESDRED and OPC. For ESDRED, after cement hydration is complete and most silica fume has reacted with the portlandite, the pH drops and ettringite becomes unstable. Sulphate concentrations increase strongly in ESDRED pore water and sulphate fluxes are then actually from ESDRED towards Opalinus Clay. This coincides with experimental findings from CI experiment where leaching of sulphur from ESDRED is observed after 5 years of interaction. Gypsum formation was predicted by Lothenbach (2011a) but not found experimentally; therefore gypsum was removed from the reference setup. Inclusion of kinetically controlled gypsum in the thermodynamic setup caused numerical instabilities in the reactive transport setup.

Ingress of chloride from Opalinus Clay results in the formation of Friedel's salt in OPC. Friedel's salt formation is absent in ESDRED, as all the aluminium necessary to build Friedel's salt is bound in strätlingite. The high dissolved chloride concentrations are partly responsible to the probably to low pH in ESDRED.

Uptake of alkali ions (Na^+, K^+, Sr^{2+}) is implemented in the C-S-H model and helps to limit the otherwise to high alkali concentrations in the cement compartment. The measurements of Lothenbach (2011b) show a significant reduction of the alkali concentrations with time which indicates a kinetically controlled uptake of alkali independent from the actual C-S-H formation process. The non-consideration of such kinetic effects might influence alkali concentrations in the cement pore waters and indirectly also effects the pH.

Carbonation is of minor importance in both cement/OPA systems. Calcite is precipitated in the cement site of the borehole only at early times in minor amounts due to the in-diffusion of carbonate. At later times a pH front moves into the Opalinus Clay and calcite precipitates at the front, where calcite solubility is lowered. The movement of precipitation front can be traced by the movement of the concentration drop of total dissolved carbon in relation to the pH front. The amount of calcite which is precipitated is very low and does not increase calcite content in the Opalinus Clay significantly.

The modelled precipitation/dissolution processes caused long-term changes in porosity, but no distinct clogging of the interface (Fig. 4-8). Investigations of samples from CI experiments indicate some kind of porosity changes (Jenni et al. 2014, Mäder et al. 2017), but quantitative evaluations which can be compared to model results were not available at the time this Mont Terri technical note was written.

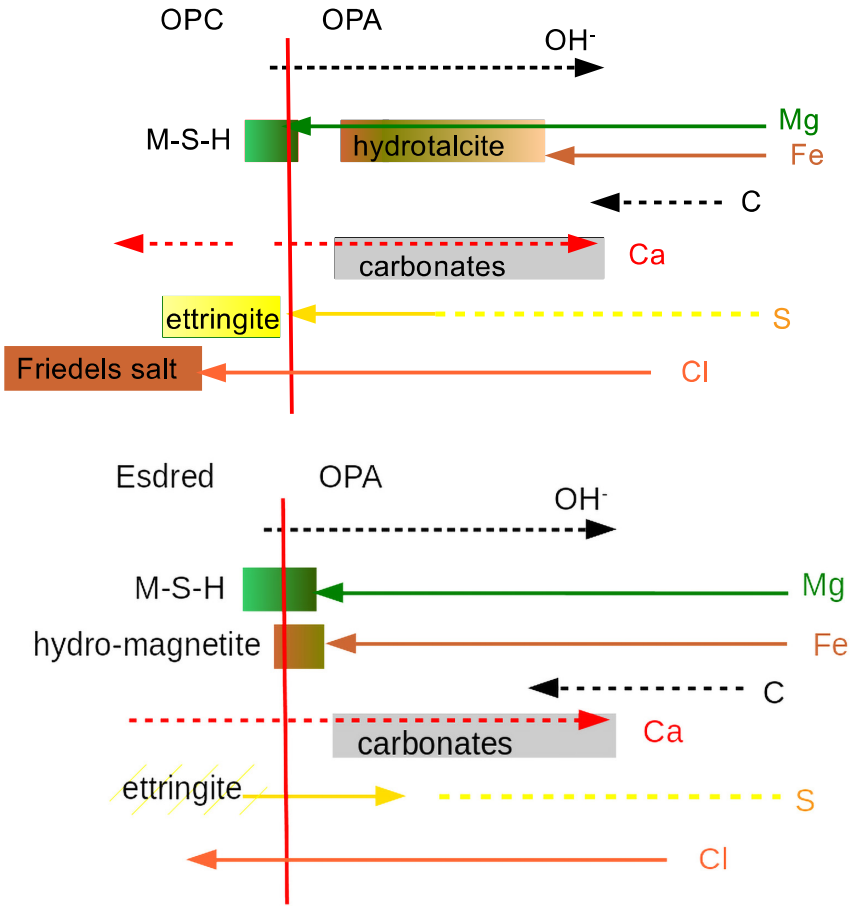

Fig. 4-7: Evolution of cement/OPA interfaces according to the model

The models show some kind of porosity decrease at the cement/OPA interface (Fig. 4-8), but in no model variant complete porosity clogging was observed. Model variants for OPC/OPA with faster dissolution rates for clays in Opalinus Clay show enhanced precipitation of Mg bearing minerals in Opalinus Clay adjacent to the interface which halves the porosity at cm scale.

There is some disagreement between modelled and measured cation exchanger occupancy in the Opalinus Clay, for both ESDRED and OPC interaction. The model calculates the cation exchanger population based on the exchange constants defined in Pearson et al. (2011) and calculated for the early experimental phase a strong increase in potassium occupancy up to several cm from the interface which goes in line with a repulsion of magnesium from the exchanger (Fig. 4-9). After some years, the exchanger populations approach the original state again due to diffusive equilibration of local pore water concentrations with surrounding Opalinus Clay. The experimental measurements in Mäder et al. (2017) show a similar, but not as pronounced trend as the model: small increase of potassium and some reduction of magnesium up to a distance of a few mm from the interface.

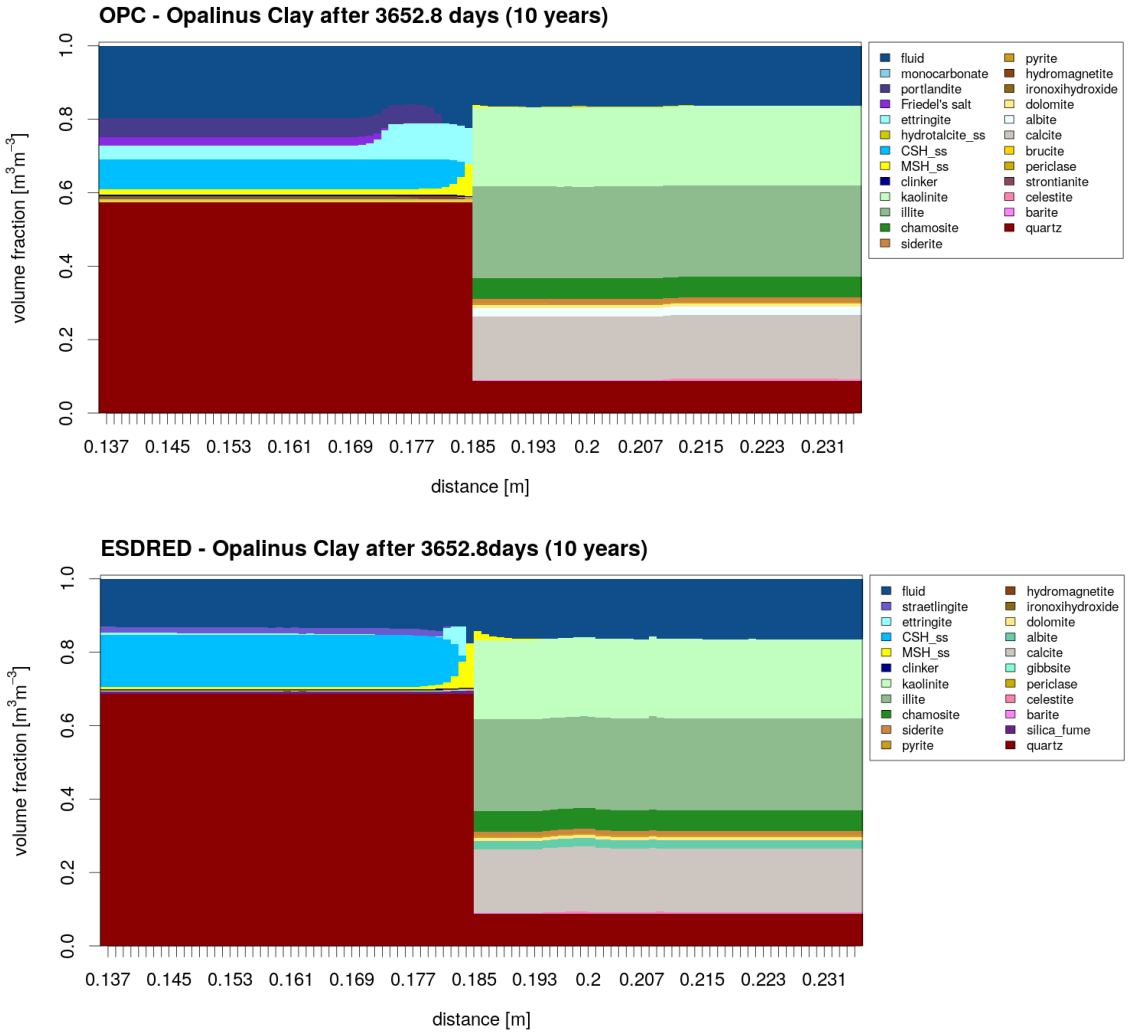

Fig. 4-8: Mineralogical profiles across the OPA/OPC interface (top) and OPA/ESDRED interface (bottom) after 10 years

The interface between concrete and OPA is positioned at x = 0.1845 m.

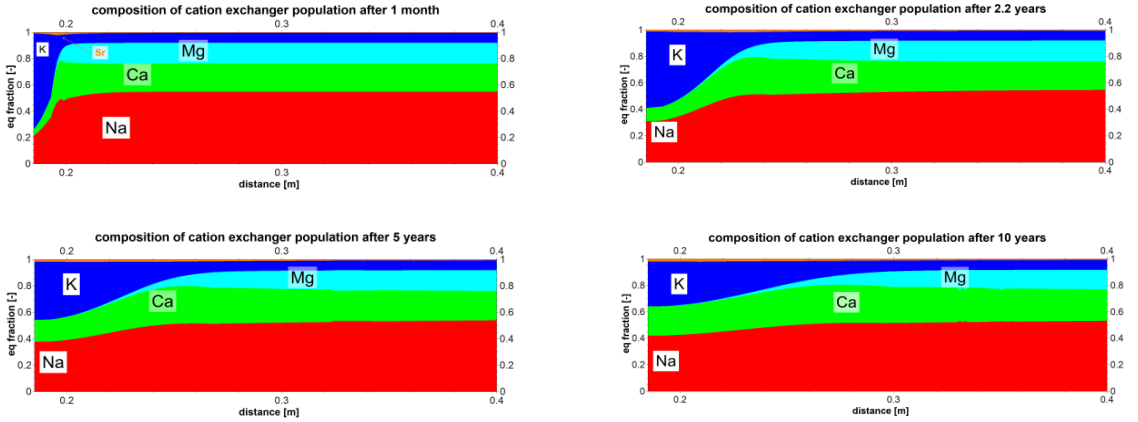

Fig. 4-9: Composition of cation exchanger composition after 1 month, 2.2, 5 and 10 years in Opalinus Clay

The interface to OPC concrete is positioned at x = 0.1845 m.

For the OPC/OPA interface a magnesium anomaly, i.e. a small increase of total amount of magnesium, was observed in OPA a few mm from the interface. The model shows a similar feature, where pyroaurite, the Fe rich endmember of the hydrotalcite-pyroaurite solid solution is found about 10 mm from the interface. Pyroaurite formation is linked to the progress of a high pH front into OPA in combination with diffusion of potassium which expels Mg from the cation exchanger (c.f. Fig. 4-9). Its formation is limited to a relatively small zone, in which Mg from exchanger is available and pH conditions from the moving pH front are favourable. One should note that the precipitation of Mg bearing minerals stops once expulsion of Mg from cation exchanger stops. The pH front is further advancing into the OPA, while the Mg anomaly stays in place. The position of the pH front coincides with a calcite precipitation front and a, not very pronounced, dolomite dissolution front. Small fractions of dolomite are converted to calcite; the magnesium released is transported towards the interface. Comparison with concentration profiles for dissolved carbon and calcium show that dissolved calcium diffuses from the OPC/OPA interface towards the pH front, whereas dissolved carbon arrives from the opposite direction. Dissolved carbon is partly supplied by dissolution of calcite ahead of the pH front. Compared to the amount of calcite initially present in the Opalinus Clay (~ 4700 mol/m^3) the additional precipitation (~ + 6 mol/m^3) at elevated pH is negligible and does not change the porosity significantly.

Hydrotalcite formation explains the experimentally observed magnesium anomaly for OPC/OPA interaction. By adjusting kinetic control and diffusivity in OPA, the type of precipitate can be changed, i.e. it is possible to suppress the formation of hydrotalcite (pyroaurite) in favour of brucite and vice versa.

In order to achieve a good agreement between modelled and observed material evolution it was necessary to include the cement hydration process in the model. This proved to be very successful for the OPC case, as the kinetic model of Lothenbach (2011a) in combination with the CEMDATA V14 DB proved to be very successful to describe the hydration of the OPC. The same kinetic model was less successful in reproducing the hydration of ESDRED concrete, because either the kinetic parameters need to be adapted or some relevant intermediately formed cement phases were missing in the thermodynamic setup.

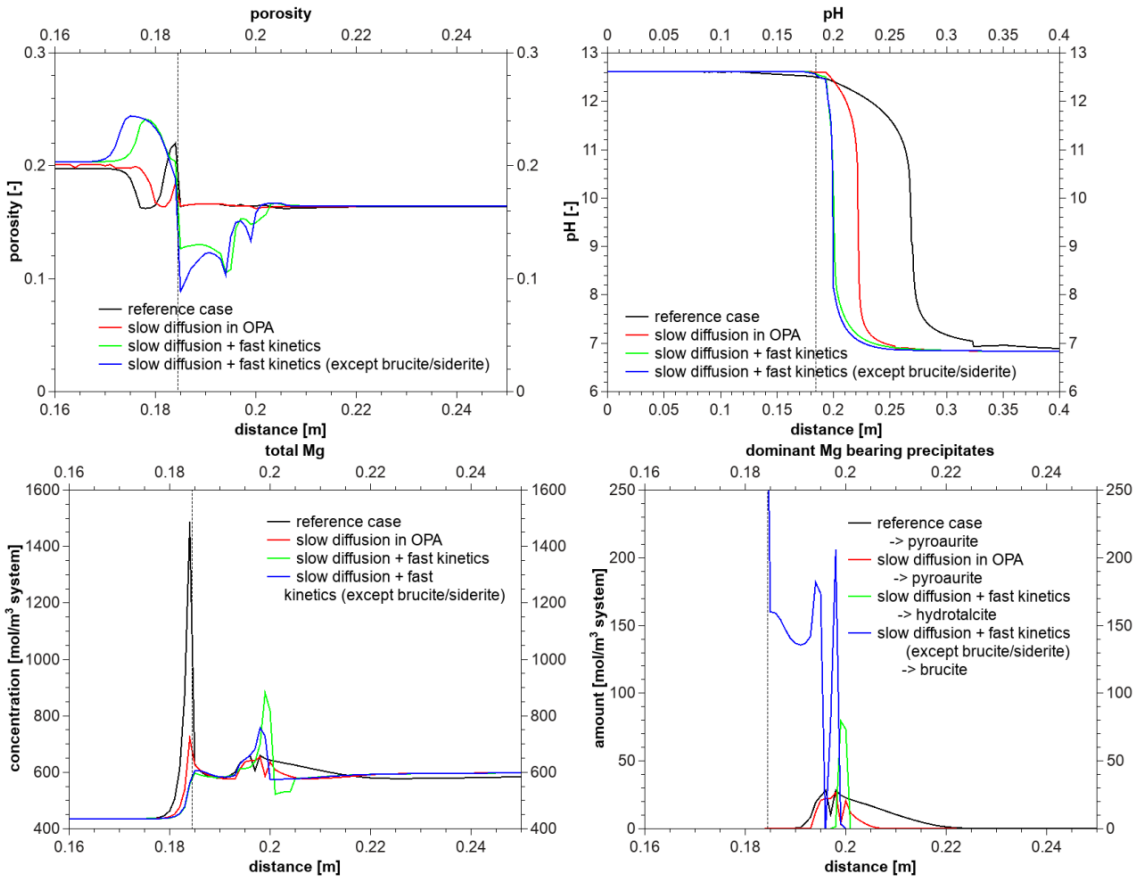

Fig. 4-10: OPC/OPA cases after 5 years: profiles for porosity, pH, total amount of magnesium and amount of the dominant mineral phase responsible for magnesium anomaly in Opalinus Clay

In each plot the black line is for the reference case, red line for the case with slow diffusion in Opalinus Clay, green lines denote the case for fast kinetics, and blue lines for fast kinetics in combination with equilibrium assumptions for brucite/siderite.

4.3.3 Time perspective/scales

In the study the 1D-model domain was about a few decimetre and the modelled time scale was limited to 10 years. The small model domain was related to the need to resolve reaction fronts of less than 0.1 mm width. The fine spatial discretization increased the computational effort in OGS-GEM and limited the modelled time scale.

4.3.4 Uncertainties

It should be noted that many details of the evolution of cement/clay interfaces are well represented in current state-of-the-art reactive transport models. Some processes, for example kinetics of dissolution reactions and specifically the kinetic control of precipitation are not well known. Marty et al. (2015b) state that the use of mean or rate-limiting values describing the reaction rates in continuum scale models appear to be questionable from a process and sub-continuum scale viewpoint.

The simulations show that models without kinetic control of slow reacting phases do not explain the evolution in the period of 5 years for which experimental results are published. Reaction of cement phases, cation exchange processes in Opalinus Clay and sorption of alkalis on C-S-H can be normally treated with an equilibrium approach. The dissolution of clays and other minerals like zeolites needs to be restricted by kinetics. There exist some measurements on the kinetic rate constants, but only indirect evidence on the "reactive surface area" in dense clay rocks. Model variants in this work show unrealistic results for models with too high reactivity of clay minerals, which allowed to constrain speed of overall dissolution reactions.

Less is known on the kinetic control of mineral precipitation. It is known that precipitation is influenced by several sub-grid processes like pore sizes distributions (Putnis 2015), but working approaches for up-scaled (and parameterized) dissolution/precipitation rates in complex media are not yet available. Currently the "reactive surface area" is used as fudge parameter and adjusted for each kinetically controlled mineral phase in order to reach desired mineral assemblies in space and time.

Obviously, these kinetic processes in combination with transport, control porosity changes on the long-term. Transport parameters are connected to porosity via empirical relations with parameters estimated in experiments. A process based modelling for such relations is not possible on continuum scale, as only the porosity change as a results of volume balance from mineral phases can be calculated, but no information on the exact geometric characteristics of an evolving pore space is available.

Therefore, uncertainties in porosity evolution and in the relation between porosity changes and transport parameters influence the predictability of the long-term and large scale evolution of effective transport parameters like permeability or diffusivity for such interfaces.

It was found in the CI-experiment, that interface evolution slowed down with time (Bernard et al. 2020a, Yokoyama et al. 2021). This observation in combination with model results from this study indicate some kind of transport control on observed mineral reactions. Three main processes might contribute to the slowdown of evolution: (1) decrease of reactivity of cement after hydration, (2) the diffusive transport regime and (3) decease of porosity near the interface.

At the beginning of the experiment, very strong chemical gradients between un-hydrated cement and Opalinus Clay exists. These gradients are partly lowered after the first few months once cement is fully hydrated. In the model hydration of cement is kinetically controlled by empirical rate laws.

In parallel, diffusion of solutes is driven by concentration gradients between the materials. Typically diffusive fluxes decrease with time due to the spatial movement of solute and reaction fronts (Square root dependence). Slow-down of diffusive fluxes with time is even stronger for systems where one compartment, in this case the cement filled borehole, is much smaller than the other compartment, in this case the Opalinus Clay. Diffusive fluxes are also strongly dependent on changes in pore space due to precipitation or dissolution of minerals. The modelled porosity change in this study is not strong enough to stop evolution of the system. In the study a simple relation between porosity and diffusivity in form of an Archie law was used (c.f. Section 4.1.6).

Jenni et al. (2017) and Jenni & Mäder (2021) modelled the evolution of the same interfaces with a dual-porosity approach where the porosity is split into two parts. One part is influenced by the negative charged clay mineral surfaces and contains excess cations to compensate for the surface charge. This part of the pore space is not freely accessible for anions or negatively charged species. The other part contains the remaining charge neutral solution and is freely accessible for all ions and solutes. For undisturbed Opalinus Clay the total porosity is approx. split in half between both pore spaces. Donnan equilibrium can be used to calculate the composition in each part of the pore space (Jenni et al. 2017). The model will only precipitate minerals in the freely accessible pore space. In addition, for a fully consistent description, the Nernst-Planck equations

were used to for calculation of diffusive fluxes in such a system. Furthermore, it should be noted, that in their approach not all cation exchange reactions are part of the geochemical system. Cation exchange reactions have to be split between specific sorption sites, where the surface is considerd to be charge balanced, and between the Donnan region, where the remaining surface charges are responsible for an EDL (electric double layer) type behaviour, such as anion exclusion and cation enrichment.

For both systems, OPC/OPA and ESDRED/OPA the calculated mineralogical evolution between our simulations and those of Jenni et al. (2017) are very similar. In both studies Mg bearing minerals are precipitated near the cement/OPA interface. The amount, place and type of precipitate, as well as the associated change in porosity is similar in the modelling studies. In both studies higher porosity changes are associated with kinetic changes[2].

The important difference between the two model studies is the effect on diffusive fluxes caused by incomplete clogging of the total pore space. In our model fluxes are decreased significantly if total porosity is halved in Opalinus Clay, but all species can still diffuse freely. In the model used by Jenni et al. (2017) the same porosity decrease in Opalinus Clay will completely clog the freely accessible porosity part. The remaining porosity is influenced by negative surface charges and not fully accessible for anions, therefore only (mainly) cations, positively charged complexes and neutral solutes can freely diffuse (with reduced rates). Transport of negatively charged complexes and anions is blocked. Therefore, in these models partial clogging of the interface occurs faster, and mineral reactions that require the flux of specific negatively charged reactants between both materials (e.g. OH, sulfate, carbonate complexes) will become strongly limited.

4.4 Modelling of pore-size dependent precipitation

Reactive transport within porous media is governed by several mechanisms which are also dependent on the porosity, connectivity and the degree of confinement. The mineral dissolution and precipitation reactions can alter the transport pathways and affect the microstructural evolution either promoting or reducing the mass transport rates. Depending on the size of the pores different mechanisms compete during mass transport and phase change. For example, at small scales (few nm), the electrostatic forces have a very strong influence in transport and in some cases may totally restrict the transport of specific ions depending on the surface charge. Reaction kinetics and crystallization paths are also dependent on the pore sizes. Very often for the initiation of precipitation, a threshold supersaturation must be achieved, before which, the solution remains in a metastable state. The classical nucleation theory or its extended variants may be used to model such processes. The model developed by Prieto (2014) can be used to calculate the Supersaturation-Nucleation-Time (SNT) dynamics for homogeneous (HON) nucleation in a pore solution and heterogeneous (HET) nucleation where the nucleus grows on a surface. The nucleation rate, J [m^3/s] varies exponentially with the free energy change ΔG_c associated with the formation of a nucleus of critical size:

$$J = \Gamma \exp\left(-\frac{\Delta G_c}{kT}\right) \tag{4.14}$$

[2] Jenni & Mäder (2021) found strong porosity decrease for the ESDRED/OPA system, while we calculated a similar effect for he OPC/OPA system for a variant with high dissolution rates of clay minerals in Opalinus Clay. We expect similar changes also for ESDRED/OPA with similar high dissolution rates. In Jenni et al. (2017) and Jenni & Mäder (2021) not all required information on kinetic rates can be found, which hampers a more quantitative comparison.

where k is the Boltzmann constant, T is the absolute temperature and Γ a pre-exponential factor. The nucleation energy barrier is highly dependent upon the interfacial tension σ and saturation index SI. This barrier is higher for HON compared to HET. In Fig. 4-11 a schematic plot of the total Gibbs free energy (ΔG) for HON and HET is shown as a function of the radius of spherical nuclei. As soon as a critical nucleus is formed and the energetic barrier is exceeded (at the maximum of the ΔG curve) further growth of the nucleus is more favourable than its disaggregation and precipitation starts. For HON nucleation to occur a higher activation barrier compared to HET has to be exceeded thus explaining why homogeneous nucleation requires higher levels of supersaturation to occur. The exact relation reads:

$$\Delta G_c = \frac{\beta v^2 \sigma^3}{\left(kT \ln(\mathrm{SI})\right)^2} \tag{4.15}$$

where β is a geometry factor, σ is the interfacial tension, v is the volume of a single spherical monomer of the mineral. The pre-exponential factor Γ represents the rate of attachment of monomers controlled by diffusion and is a function of the diffusion coefficient of the monomers, the number of nucleation sites, the number of monomers that form a critical nuclei and the degree of supersaturation. The appearance of many nuclei and their growth are responsible for the breakdown of the solution metastability. This process can be quantified with the induction time t_i which is the time that the system remains in a metastable state, before the onset of precipitation.

$$t_i = \left(\frac{1}{JV_p}\right) \tag{4.16}$$

where V_p is the volume of the local pore under consideration.

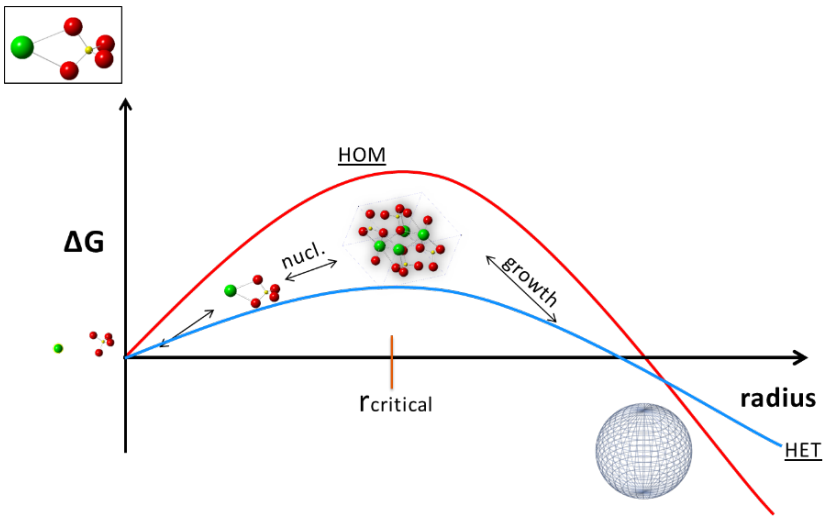

Fig. 4-11: Schematic of the Gibbs free energy (ΔG) for homogeneous (HON) and heterogeneous (HET) nucleation as a function of the radius of spherical nuclei

As soon as a critical nucleus is formed ($r_{critical}$) and the energetic barrier is exceeded (at the maximum of the ΔG curve) further growth of the nucleus is more favourable than its disaggregation and precipitation starts (Prasianakis et al. 2017).

The dependence of induction time on saturation index (SI), for pore sizes of 1 µm and 10 µm and for the HON and HET crystallization paths is shown for the case of Baryte ($BaSO_4$) in Fig. 4-12 (left). The effect of poresize in this case, favours precipitation in large pores compared to the small pores. SI is defined as the decimal logarithm of the ratio of ionic activity product in solution, in this case $IAP = \alpha_{Ba2+} \cdot \alpha_{SO4}^{2-}$, to the thermodynamic solubility product of baryte, K_{0sp}, i.e. $SI = \log_{10}(IAP/K_{0sp})$. Different crystallization paths are possible depending on the local supersaturation conditions. The time-frame during which the system remains in a metastable condition depends both on the mechanism and the respective poresize. The heterogeneous nucleation, while it is more likely to occur in low supersaturations, it is greatly facilitated when a compatible crystallographic template is available, meaning that the heterogeneous nucleation kinetics depend both on the mineral that precipitates as well as on the surface characteristics of the specific pore where precipitation takes place. Once the mineral precipitates are formed, the local mass transport properties of the material change accordingly in a way that is reflected to the diffusivity and permeability of the material. Modelling results, based on multiscale lattice Boltzmann modelling, which are able to reproduce the characteristic features of the respective experiments are shown in Fig. 4-12 (right), for the case of competitive Celestine ($SrSO_4$) dissolution/Baryte ($BaSO_4$) precipitation, for four different solution supersaturations highlighting the effect of chemical conditions on the pore-space evolution (Prasianakis et al. 2017).

For the geochemical evolution of the cement-clay interface, and from the mineral nucleation perspective, it essentially means that the precipitation products will first appear at locations of large pores with high-supersaturation (close to the interface). For lower supersaturation the heterogeneous nucleation mechanism will be more favoured, again at the larger pores. For the same supersaturation, the smaller the pore the longer it takes for precipitation to occur.

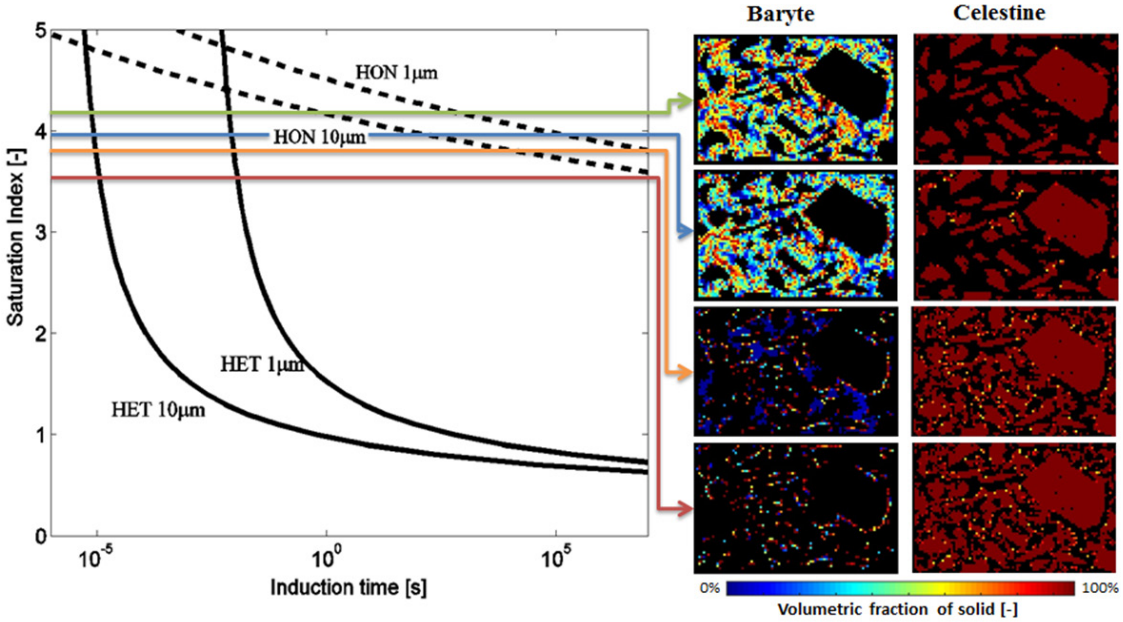

Fig. 4-12: Left: Supersaturation – nucleation time diagram for the case of Baryte precipitation ($BaSO_4$)

Different crystallization paths are possible depending on the local supersaturation conditions. Timeframe during which the system remains in a metastable condition depends both on the mechanism and the respective pore size. Right: Interplay of Baryte precipitation mechanisms and simultaneous Celestine dissolution at different chemical conditions. The volumetric fraction after 140 hours of reaction at SI = 4.08, 3.96, 3.8 and 3.6 (top to bottom) is shown (Prasianakis et al. 2017).

4.5 Pore-scale modelling of clay porosity reduction and effect on transport

The microstructural alterations occurring at the thin zone around the cement-clay interface is the result of geochemical dissolution and precipitation reactions. As discussed in the previous sections, at the first stages of interaction, on the OPC side, the capillary porosity increases mainly due to dissolution of portlandite, and on the clay (Na-Montmorillonite) side, one of the main solids which precipitate are the C-S-H phases which result in a decrease in the interaggregate porosity. A complete blockage of the transport pathways has not been observed in any of the experiments and this could be attributed to the microstructural properties of the materials involved: a) the clay itself which contains a percentage of interlayer and diffuse double layer porosity (expected to remain open) b) the C-S-H phases which precipitate, contain the C-S-H gel porosity (which is comparable to the interlayer porosity). Since anions are not efficiently transported through the interlayers and through the lower range of gel pores, due to electrostatic interactions, in combination with the very long induction times and high saturation index needed to start the precipitation in very small pores, it is unlikely that a complete blocking of the multiscale porosity (or of the continuity of pores) will ever occur. To illustrate the effect of C-S-H precipitation processes and the effect of the microstructure evolution on the transport properties, a simplified pore-level model has been constructed and simulations have been conducted. The model focuses on the conditions which result in CSH precipitation, as well as on the expected transport properties of the new precipitates by modelling also their respective microporosity.

4.5.1 Description of the pore level model, the computational domain and the boundary conditions

The contact zone between cement (OPC) and clay (Na-Montmorillonite) is considered, focusing on the clay side. A simplified schematic of such an interface is shown in Fig. 3-12. Cement-clay interaction is usually modelled using macroscopic codes. However, the lack of information regarding the microstructure evolution does not allow to fully understand and predict the evolution of the system and its transport properties. To investigate the microscopic processes a pore-level modelling approach is implemented, where generic microstructures can be used to illustrate to certain accuracy the underlying processes. The microstructures are designed in a way to represent a clay region where large pores exist, and where mixing and precipitation is more likely to occur first. The microstructural evolution of the relatively large pores is expected to have a stronger overall effect on transport.

The physical mechanisms considered for the simulations involve mass diffusion and detailed chemical reactions which are relevant and result in C-S-H precipitation. For simplification the clay particles are considered impermeable and non-reacting. Therefore the diffusion through the interlayers of the clay particles is neglected and the effect of electrostatic forces is not considered. After the formation of precipitates a diffusion test is conducted to measure the change of the effective diffusivity of the evolved structures (resembling to the diffusion of neutral species e.g. HTO through the evolved structure). The resulting microporosity of the CSH precipitates is below the resolution of the simulation and a subgrid model emulating a subgrid porous medium is used to describe the transport through the computational voxels which are filled with CSH, during the diffusion test. For the measurement of the effective diffusivity the transport through the interlayers of the clay particles is also in this case neglected. We note that this simplified setup allows to visualize and investigate the main participating mechanisms and can be the starting point for more complex future investigations, where refined models and more realistic microstructures may be used. A complete clogging at a microstructural level of the new formed phases, in this system, is not foreseen mainly due to the CSH microstructural properties.

For the modelling presented here, the major transport and reaction mechanisms are illustrated in Fig. 4-13. Focus is on the mass transport and precipitation processes that occur at the clay side of cement-clay interfaces. A geometry with relatively high porosity, composed of clay particles is considered to represent a clay region where major mass diffusion and chemical reactions will take place. From the left boundary of the computational domain, cementitious pore water enters the domain. A solution rich in $Ca(OH)_2$ enters from the left side resembling the cementitious solution which is in equilibrium with the dissolving portlandite similar to the experimental observations. For the investigations, the concentration of this solution is varied to represent regions next to the interface (strong geochemical contrast), as well as regions deeper in the clay side, where the cementitious solution attenuates (weak geochemical contrast), but still drives certain geochemical reactions. At the clay side, SiO_2 is in equilibrium with amorphous silica in the clay pore-water. For the model, it is considered that from the unaltered clay side, which corresponds to the right boundary condition, a solution containing SiO_2 in equilibrium with clay pore water diffuses towards the cement side. The concentration on the right boundary remains constant throughout the simulation. At the location where the two solutions meet, the geochemical contrast leads to the precipitation of C-S-H phases. The computational domain is describing a region of 1.6 µm × 1 µm such that several clay particles may be included.

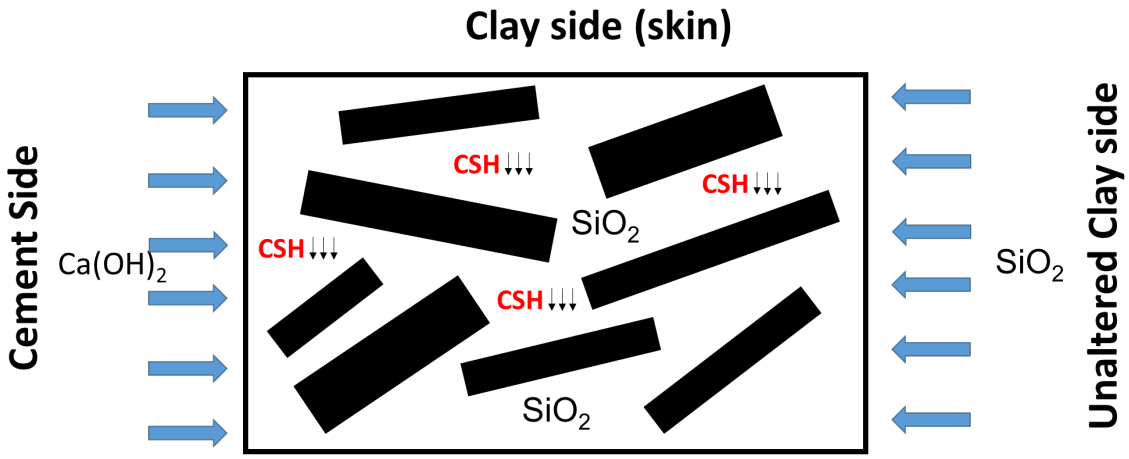

Fig. 4-13: Example of the computational setup for the simulation of precipitation at the clay side of cement-clay interfaces

Solution rich in $Ca(OH)_2$ enters from the left boundary resembling the cementitious solution which is in equilibrium with the dissolving portlandite. On the clay side, SiO_2 exists in solution and in equilibrium with amorphous silica. From the unaltered clay side (right boundary) dissolved SiO_2 in equilibrium with clay pore water diffuses towards the cement side. The resulting geochemical contrast (which can be adjusted to represent regions close/far to the interface) leads to the precipitation of C-S-H phases. The size of the considered domain is 1.6µm x 1µm and can be arbitrary filled with clay particles (black color).

The reactive transport simulations at the pore-level are based on a multicomponent lattice Boltzmann model (Prasianakis et al. 2017) which is equipped with machine learning capabilities for accelerating the geochemical calculations (Prasianakis et al. 2020). The thermodynamic modelling is conducted within GEMS and several geochemical realisations are exported in order to create a training basis for the neural network based machine learning algorithm. After training, the neural network replaces the GEMS geochemical software during runtime. The whole workflow results in geochemical calculations four orders of magnitude faster, without loss in accuracy, allowing to simulate with very high geochemical details the evolution of the clay system.

4.5.2 Lattice Boltzmann method

The lattice Boltzmann method (LB) is a special discretization of the Boltzmann equation and originates from the gas kinetic theory. The elementary variables are the so-called populations or distribution functions f_i which represent the probability of finding in space a particle with a given velocity. To every distribution function corresponds a discrete velocity vector (Succi 2001). Depending on the dimensions and number of discrete velocities, there exist different lattice models. For two-dimensional simulations the standard D2Q9 square lattice with 9 discrete velocities is implemented. The projection of this lattice in 3D results in the D3Q27 cubic lattice with 27 discrete velocities (see Fig. 4-14).

These lattices require communication and exchange of information only within the next neighbouring nodes. This has the advantage of (a) simple implementation of complex geometry boundary conditions, and (b) efficient parallelization of the algorithm for use in high performance computing facilities.

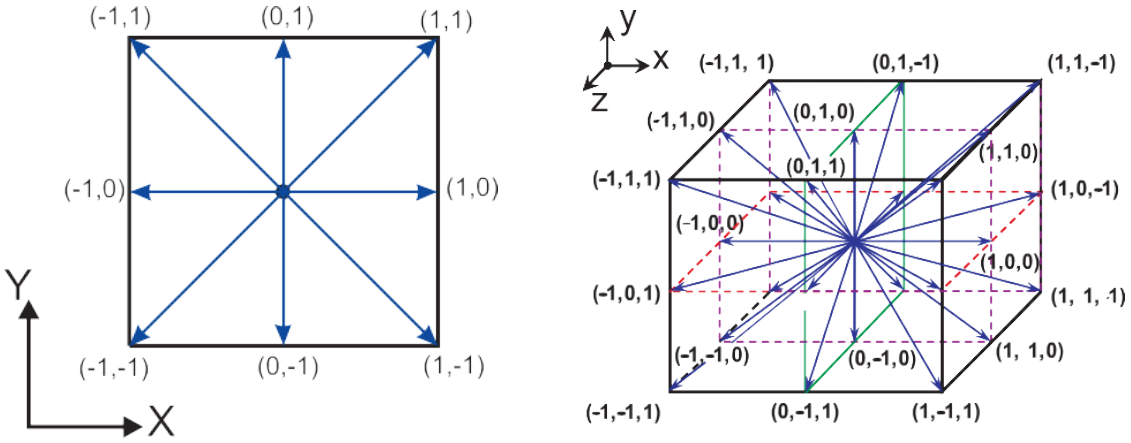

(a) D2Q9-lattice (b) D3Q27-lattice

Fig. 4-14: Lattice models

(a) Two dimensional 9-velocity lattice (D2Q9). (b) Three dimensional 27-velocity lattice (D3Q27). Only next-neighbours communication is required for these space-filling lattices.

The lattice BGK equation is a discrete variant of the Boltzmann equation and can be written as:

$$f_i(x + c_i\delta t, t + \delta t) = f_i(x,t) + \frac{1}{\tau'}\left[f_i^{eq} - f_i(x,t)\right] \tag{4.17}$$

where i is the index of the lattice velocity vectors, i = 0...8 for D2Q9 lattice and i = 0...26 for D3Q27 lattice, $\boldsymbol{c}_{i\alpha} = c_i\boldsymbol{e}_\alpha$ are the discrete lattice velocities, the direction vector of velocity $\mathbf{e}_\alpha$ is given as,

$$\boldsymbol{e}_\alpha = \begin{cases} (0,0)\ \alpha = 0 \\ (cos\theta_\alpha, cos\theta_\alpha)\ c_i\ \alpha = 1,3,5,7 \\ (cos\theta_\alpha, cos\theta_\alpha)\sqrt{2}\ c_i\ \alpha = 2,4,6,8 \end{cases} \tag{4.18}$$

where α is the coordinate index ($\alpha = x, y, z$), and $c_i = \delta x/\delta t$ is the lattice discrete velocity speed. Here, δx and δt are the lattice spatial step (spacing between consecutive nodes) and lattice time step, respectively. For a single component LB model δx=1 and δt=1 in lattice units. Parameter τ is the relaxation time which controls the viscosity of the fluid and the diffusivity of the solutes in a passive scalar approach; f^{eq} is the equilibrium distribution function and the most commonly used form is:

$$f_i^{eq}(\rho, u) = \omega_i \rho \left[1 + 3\left(\frac{c_i.u}{c^2}\right) + \frac{9}{2}\left(\frac{c_i.u}{c^2}\right)^2 - \frac{3}{2}\left(\frac{u}{c}\right)^2\right] \quad (4.19)$$

where the weight factors ω_i for D2Q9 lattice model are $\omega_0 = 4/9$, $\omega_{1,2,3,4} = 1/9$, $\omega_{5,6,7,8} = 1/36$. Every species has each own population set. The local density ρ and the local velocity **u** are calculated as the first moments of the distribution functions:

$$\rho = \sum_{i=0}^{8} f_i \, , u_\alpha = \frac{\sum_{i=0}^{8} c_{i\alpha} f_i}{\rho} \quad (4.20)$$

The multicomponent model is implemented following a passive scalar approach (Molins et al. 2020, Prasianakis et al. 2018, 2017). During precipitation, the alteration and the properties of the evolving microstructure can be followed. A permeability and a diffusivity test can be conducted by applying a differential pressure and a differential concentration along the sides of the evolved geometries using the same lattice Boltzmann solver.

4.5.3 Thermodynamic modelling of the involved geochemical reactions

For the simplified modelling of the geochemical reactions that occur at the clay side of the cement-clay interface, solutions of $Ca(OH)_2$ and SiO_2 have been considered. Depending on their relative concentrations the reactants may lead to precipitation or not of C-S-H phases. In Fig. 4-15 calculations were done via jupyter notebook using the xGEMS python interface (commit 96c06cf) for the GEM3K numerical kernel (commit b15f40a). A simplified cement chemical system was created in GEM-Selektor (v3.8.0) containing only Ca-Si-O-H elements.

Thermodynamic data for the considered solids (portlandite, C-S-H, and amorphous silica) and aqueous ions and complexes stem from PSI/Nagra 12/07 (Thoenen et al. 2014) and the cemdata18 (Lothenbach et al. 2019) thermodynamic databases. The C-S-H phase is modelled as an ideal quaternary solid solution model of tobermorite–jennite-like structure (Kulik 2011).

Mixing two aqueous solutions, one in equilibrium with portlandite and another in equilibrium with amorphous silica is shown. From left to right going from 100% amorphous silica solution to 100% portlandite solution, the aqueous speciation, the pH, the composition of the solid C-S-H phases and the volume of precipitates is shown. The lattice Boltzmann solver is equipped with the thermodynamic data encoded in a neural network.

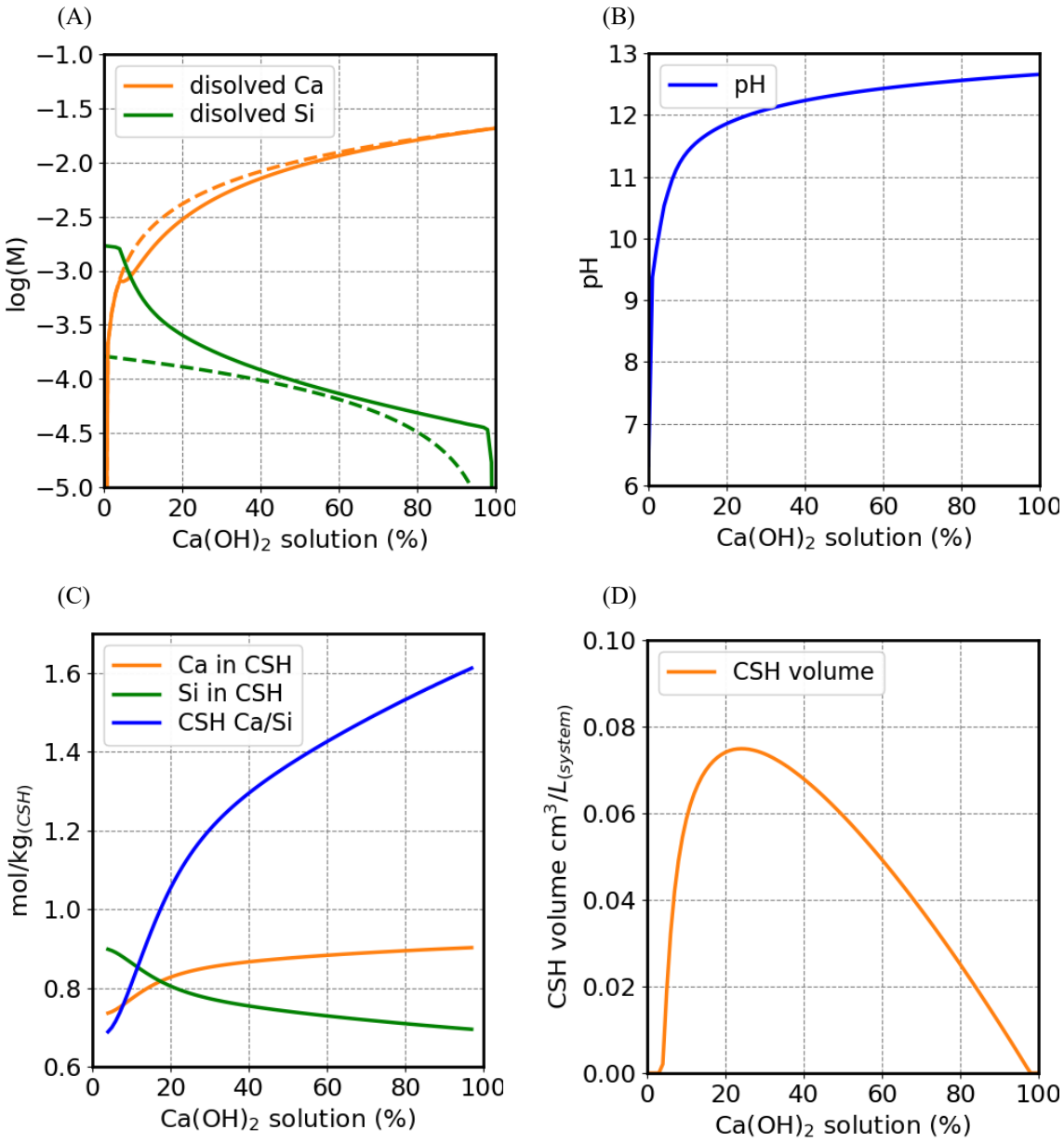

Fig. 4-15: Thermodynamic modelling

(A) aqueous concentration of dissolved Ca and Si, dotted lines are the aqueous concentrations if the amorphous silica solution is replaced with a solution in equilibrium with quartz (note that in this case the Si concentration is ~ 10× lower, and there is no C-S-H precipitation because the dissolved Si is always bellow the Si concentration in equilibrium with C-S-H, dotted green line is below the continuous line). (B) pH of the mixed solution. (C) C-S-H composition. (D) precipitated C-S-H volume, per 1 L of the chemical system. The horizontal axis of the graphs corresponds to the percentage of $Ca(OH)_2$ in the solution which is composed solely by $Ca(OH)_2$ and SiO_2.

4.5.4 Machine learning for thermodynamic coupling

Major computational efforts in reactive transport simulations are related to the calculations of thermodynamic equilibrium and the geochemical speciation. The reason for that is the large number of involved species, and the need to perform chemical calculations at each mesh point and every time step. Geochemical speciation calculations are used to find the quantities of chemical species in the system under the assumption of local equilibrium. This type of calculations can be done using the Law of Mass Action (LMA) (as in PhreeqC (Parkhurst 1995)) or Gibbs Energy Minimization (GEM) (as in GEMS-Selektor (Kulik et al. 2012)). In a reactive transport code, reactions and mass transport are usually coupled in one of three main ways: by directly implementing the chemical speciation routines within the code (Xu et al. 2012), by using a pre-calculated look-up table that contains speciation calculations (Huang et al. 2018, Poonoosamy et al. 2019), or for more complex chemical systems by coupling the mass transport code to an external geochemical software (Kosakowski & Watanabe, 2014). The look-up table approach is in general faster but requires the pre-calculation of the full geochemical system, and the accuracy depends on the resolution of the lookup-table. On the other hand a direct calculation solving the chemical system will give an exact result, but it will be slower due to the involved calculations. In a reactive transport calculation the number of geochemical calculations scales linearly with the number of computational grid points and the involved time steps.

Artificial neural networks (NN) are computational models that can represent complex relationships between input and output data in multidimensional spaces (Jain et al. 1996). Different NN's types are assembled to exhibit specific behaviour depending on their architecture, and the type of the problem to be solved. The main challenge of machine learning algorithms is to sufficiently train a NN using an existing training set of input and output data, such that the NN can be used to forecast accurate output values for data that do not belong to the training dataset. At the same time, it should be noted that there is no optimum predefined number of neurons or an a-priori guarantee that a trained NN with a specific number of neurons can predict the output with the desired accuracy.

The feedforward type of neural networks are used for the pore-level simulations. This is one of the simplest but most efficient network type, suitable for solving complex regression problems. The neural networks used in this study were obtained by a supervised learning approach in order to encode the thermodynamic equilibrium depending on the composition of the solution, with the data that GEMS provides. The mean squared error loss function is used.

The NN training is using the backpropagation technique introduced by (Rumelhart et al. 1986). The right balance between the size of the network and its resulting accuracy was pursued. For that, several networks were tested, by varying the number of neurons per hidden layer, the number of hidden layers and the activation functions of the neurons. Moreover, several training algorithms were tested. It is noted, that a common issue in this type of networks is the element mass conservation between input and output of the networks, which cannot be fully preserved and which at the moment is source of uncertainty (Guérillot & Bruyelle 2020, Jatnieks et al. 2016). However, the resulting networks trained in this work achieve excellent accuracy which is not affecting the simulation results similar to (Prasianakis et al. 2020). The resulting neural network is shown in Fig. 4-16.

The network has been trained using a sample of 90'000 pre-calculated geochemical calculations that spanned the space of possible solutions. The metrics of the efficiency of the neural network are shown in Fig. 4-17. The mean square error (MSE) error after 17'000 epoques of training reached the value of MSE = 2.8×10^{-5} which is adequate for this application. A regression plot (in log-units) shows some small deviation only at very low values of concentrations ($< 10^{-8}$) which have practically no effect in the simulation.

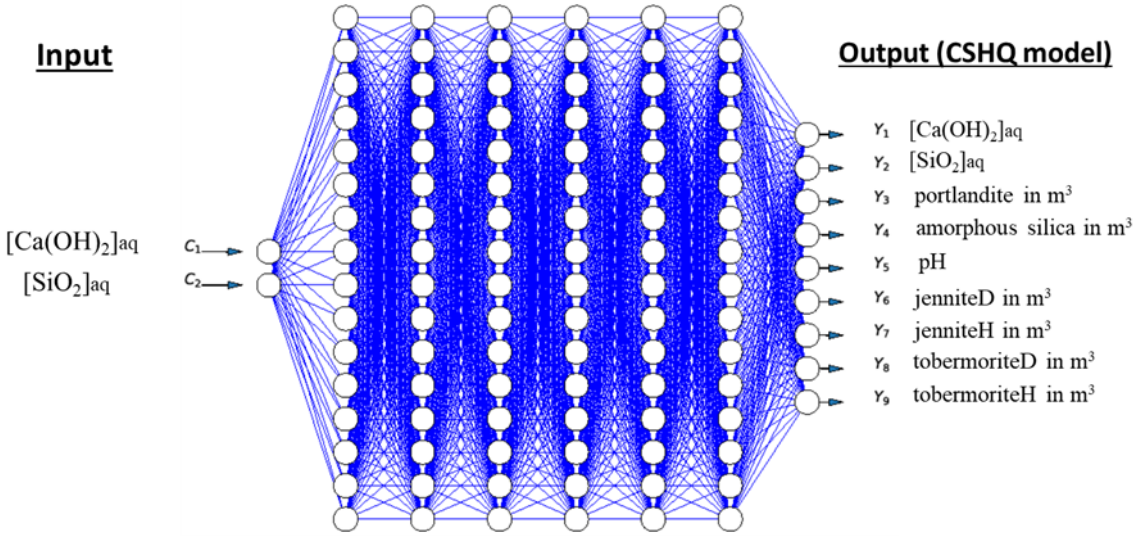

Fig. 4-16: Visualization of the feedforward neural network which is coupled with the lattice Boltzmann solver and is used for the geochemical reactions

This NN has six hidden layers composed by sixteen neurons per layer. This NN accepts two variables as input, the two master species concentrations $C_1 = [Ca(OH)_2]_{aq}$ and $C_2 = [SiO_2]_{aq}$ and predicts nine variables $Y_1 = [Ca(OH)_2]_{aq}$, $Y_2 = [SiO_2]_{aq}$, $Y_3 =$ portlandite in m^3, $Y_4 =$ amorphous silica in m^3, $Y_5 =$ pH, $Y_6 =$ jenniteD in m^3, $Y_7 =$ jenniteH in m^3, $Y_8 =$ tobermoriteD in m^3, $Y_9 =$ tobermoriteH in m^3, following the CSHQ model of an ideal quaternary solid solution model (Kulik 2011).

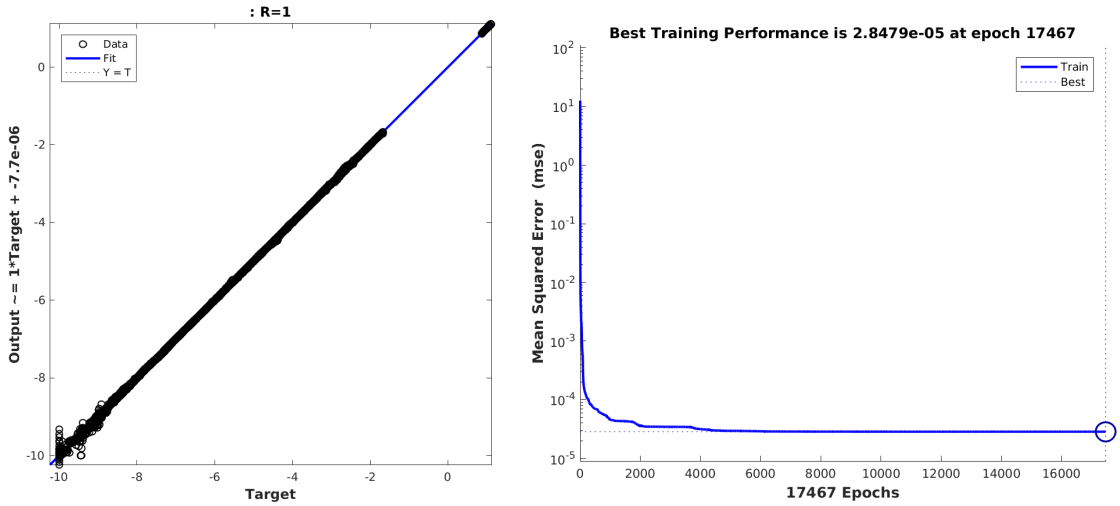

Fig. 4-17: The mean square error is maintained at low levels for the 6 layer × 16 neuron /layer network

A regression analysis shows a small mismatch at very low concentrations which has practically no influence in the simulations.

In Fig. 4-18, characteristic manifolds of input variables versus the predicted ones are plotted. Blue circles correspond to the data produced by GEMS. Red symbols correspond to the neural network predictions. Results are plotted in a logarithmic scale.

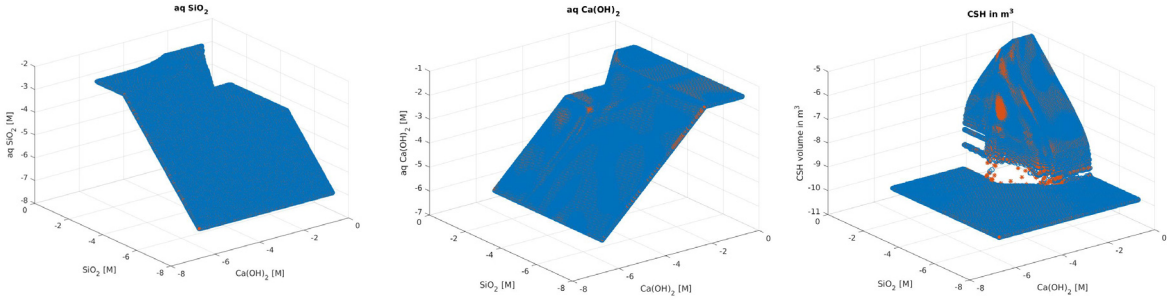

Fig. 4-18: The manifolds of input variables (C_1 = $[Ca(OH)_2]$ and C_2= $[SiO_2]$) versus the calculated and neural network predicted fields at thermodynamic equilibrium Y_1 = $[Ca(OH)_2]_{aq}$, Y_2 = $[SiO_2]_{aq}$, $Y_6 + Y_7 + Y_8 + Y_9$ = [CSH] volume in m^3 are plotted

Blue circles correspond to the data produced by GEMS. Red symbols correspond to the neural network predictions. Results are plotted in a logarithmic scale. Manifolds are almost indistinguishable showing a very good match.

4.5.5 C-S-H precipitation in clays and subsequent microstructural changes

The simulations have been conducted using the geometry of Fig. 4-20 by considering several clay particles within the computational domain. The system evolution was followed, subject to two different boundary conditions which represent typical in situ conditions as shown in Tab. 4-1. The boundary conditions for the strong and weak geochemical contrast are relevant to the conditions very close to the interface, and within the alteration zone. In Fig. 4-20 an example of the strong geochemical contrast is illustrated. The concentration of $Ca(OH)_2$ in equilibrium with dissolving portlandite from the cement side is fixed at $C_{Ca(OH)2}$ = 0.02065 M, and the concentration of SiO_2 in equilibrium with amorphous silica from clay side is fixed at C_{SiO2} = 0.0017 M. The $C_{Ca(OH)2}$_aq is plotted on Fig. 4-19 right side, while the pH is in the middle of the same figure, for a snapshot of the transient simulation where the $Ca(OH)_2$ front is advancing via diffusion within the clay structure. As discussed, for simplification, the transport through the interlayer porosity of the clay particles as well as through the interlayer porosity of the C-S-H precipitates is not considered during the reactive transport simulations. Also, mechanical deformation and electrical effects are neglected. The different scenarios assume that the heterogeneous nucleation mechanism is mostly favoured. This assumption is based on the low degree of supersaturations which makes the precipitation close to a surface more favourable, rather than in the bulk aqueous solution.

Tab. 4-1: Two cases are considered in a counter diffusion setup with fixed boundary concentrations, which correspond to strong and weak geochemical contrast in situ conditions

Concentrations	Strong	Weak
$C_{Ca(OH)2}$	0.02065M	0.001M
C_{SiO2}	0.0017M	0.0017M

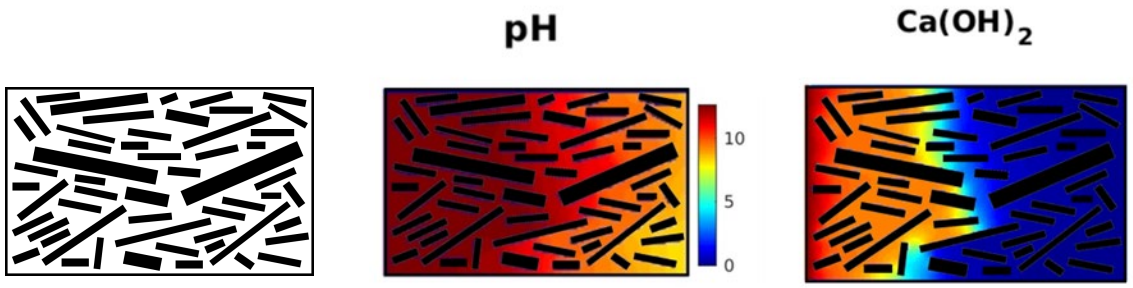

Fig. 4-19: Left: the clay geometry used in this analysis. Middle: the pH map during the transient mixing of the two solutions. Right: the concentration $C_{Ca(OH)2}$ at the same snapshot in time

Red means high, blue means low concentration

Due to the different geochemical conditions, the microstructure evolution follows distinct paths. The locations of the precipitates depend on the major preferential mass transport pathways. The chemical composition of the precipitates and their porosity, depends on the local composition of the aqueous solution at the time of precipitation. The reactions are assumed to bring the local system in equilibrium instantaneously and therefore, the evolution of the system is transport limited. When the precipitates form in the open porosity, the microstructure is evolving. Given the fixed boundary conditions, the concentration field reaches a steady state, which is changing only after significant solid precipitation takes places. This allows to advance the simulations at considerably larger timesteps between successive significant changes in the microstructure and allow to accelerate the overall numerical simulations.

In the first case described by a strong geochemical contrast, the conditions adjacent to the interface are simulated. The $C_{Ca(OH)2}$ receives its maximum value $C_{Ca(OH)2}$ = 0.02065 M on the left boundary and remains constant throughout the simulation. The C_{SiO2} is initialised with C_{SiO2} = 0.0017 M on the right boundary, while it is allowed to be depleted from the left boundary. This emulates the conditions under which the initial precipitates appear near the interface, which are the product of the first mixing phase of the solutions.

In the second case a weak geochemical contrast with fixed concentrations of C_{SiO2} = 0.0017 M on the right boundary, and $C_{Ca(OH)2}$ = 0.0010 M on the left boundary is studied. The second case evolves at a much slower pace and represents in situ conditions within the clay

The two cases lead to significantly different microstructural evolution paths as shown in Fig. 4-20. In the strong geochemical contrast the precipitation zone is concentrated on the right side of the domain (note that for this simulation the C_{SiO2} = 0.0017 M is held constant at the right boundary), while for the weak geochemical contrast case, the precipitation zone is more uniform. This may partially explain the experimental observations of Chapter 3, where the low porosity zone in Na-montmorillonite did not appear right at the material interface, but some distance behind the interface (~ 0.5 – 1 mm), and that in some samples, no distinct low porosity zone did form, but the reactions appeared to happen in a wider zone. The latter may be related to the specific diffusion properties of each sample.

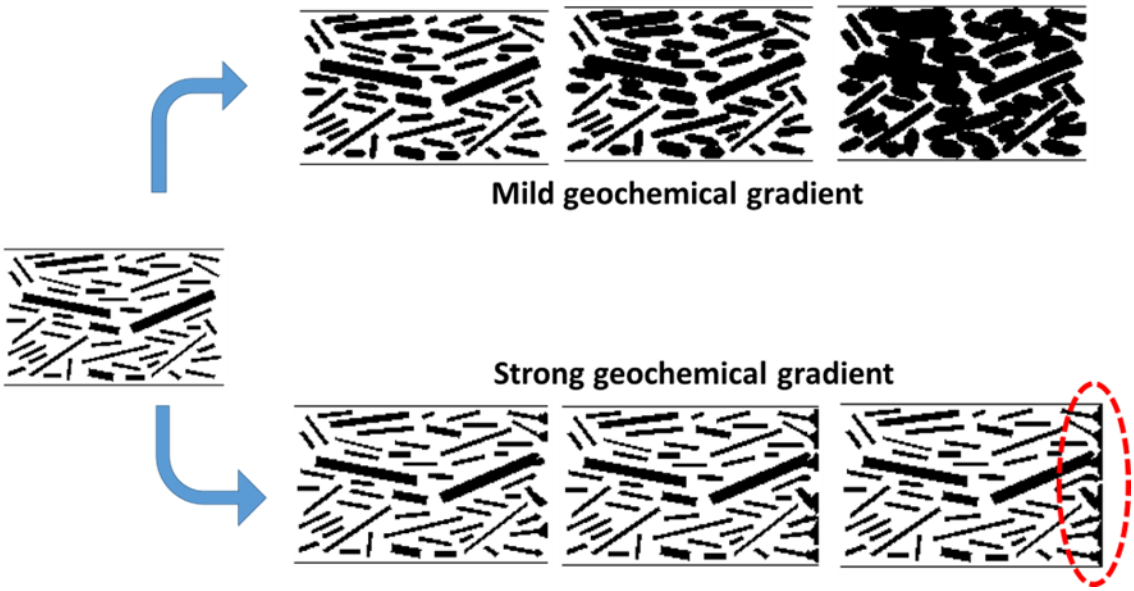

Fig. 4-20: Two significantly different microstructural evolution paths, which occur for the same microstructure, but at different geochemical conditions

The top series of pictures corresponds to the evolution subject to mild geochemical contrast (evolving at a slower pace), while the lower series of pictures corresponds to the evolution under strong geochemical gradients. Diffusion can still take place through the C-S-H precipitates.

4.5.6 Microstructural properties of C-S-H precipitates

The implemented geochemical reaction model allows to trace the properties of the precipitated C-S-H phases. The C/S ratio, the total weight% of water within the C-S-H phases, the interlayer porosity as well as the C-S-H gel porosity for the two different scenarios are plotted in Fig. 4-21. The histogram of the phases predicted by the ideal quaternary solid solution model of tobermorite-jennite-like structure (Kulik 2011) are also plotted. By knowing the distribution of CSH phases, the interlayer water which exists within the C-S-H precipitates (IL), the gel pore water (in the space between C-S-H precipitates) and the bulk water may be calculated using Eqs. 4.21 to 4.23. It is noted that the interlayer- and gel- pore sizes are below the resolution of the simulation. However, diffusion through this kind of porosity can be incorporated via sub-grid modelling as is show in the next section. For the two extreme cases, the gel porosity varies from a minimum of 12% for the weak gradient to 33% for the strong gradient. It is noted that the C-S-H properties are not uniform within the same domain and simulation case due to the evolving microstructure. The reduction in total porosity due to precipitation has an effect on the diffusive fluxes and in turn this affects the resulting local reactant concentrations. The local concentrations at the fluid-solid reactive zone define the composition of the C-S-H solid solution.

In order to calculate the gel and interlayer porosity the water fraction (H/S) within the CSH interlayer may be calculated as:

$$(H/S)_{H2O,IL} = 7/6\left(x_{TobH} + x_{JenH}\right) + 8/6\left(x_{TobD} + x_{JenD}\right) \quad (4.21)$$

Within the bulk water may be calculated as:

$$(H/S)_{H2O,bulk} = \frac{9}{6}x_{TobH} + \frac{13}{6}x_{JenH} + \frac{11}{4}x_{TobD} + \frac{15}{4}x_{JenD} \tag{4.22}$$

And finally within the gel porosity:

$$(H/S)_{H2O,gel}=(H/S)_{H2O,bulk} - (H/S)_{H2O,IL} \tag{4.23}$$

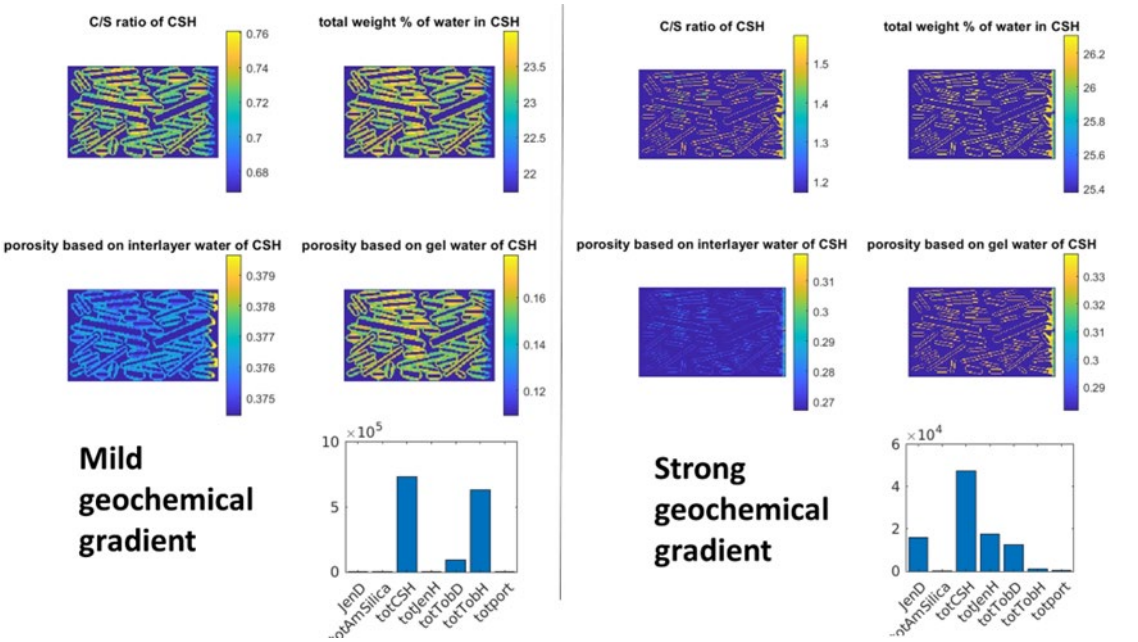

Fig. 4-21: C-S-H composition for the two different cases

Left: the mild geochemical contrast. Right: the strong geochemical contrast. The properties of the CSH precipitates are very different. For both cases, transport pathways through the gel porosity and the interlayers continue to exist even after the micrometer size porosity seems to be filled with precipitates. The histogram of the phases predicted by the ideal quaternary solid solution model of tobermorite–jennite-like structure are also shown (Kulik 2011)

4.5.7 Evolution of diffusivity versus porosity reduction due to geochemical reactions

The porosity and microstructure within the considered domain has evolved in the previous section due to the precipitation of C-S-H phases. Along with the changes in porosity, the transport properties are also changing in a non-linear way, a process which strongly depends on the local chemical conditions during which the precipitants were formed. It is clear that a global Kozeny-Carman or Archie law (power-law dependence on porosity) typical type of correlation is not possible to describe this dependency, since such correlations are not dependent on the local geochemical conditions, rather dependent on porosity changes only. As also can be inferred from Fig. 4-20, the exact same geometry will evolve differently when subject to different geochemical conditions. For the same amount of precipitates, a different effect on the resulting diffusivity is expected similar to (Churakov & Prasianakis 2018).

For the measurement of the alteration of the diffusivity, the diffusion in the open porosity as well as the diffusion through the gel porosity is considered. The diffusion through the interlayer porosity of the clay particles and of the interlayers of the C-S-H phases is not considered. The gel pore sizes are below the resolution of the computational domain; thus the local diffusion coefficient in the gel porosity is modelled using Archies law. Therefore, the diffusion coefficient assigned to the open pore space is $D = D_w$ while that assigned to the sub-grid gel porosity $D_{gel} = \phi^2 D_w$, with the cementation factor set to m=2, and porosity being the local C-S-H porosity at every computational grid point depending on the local solid solution composition. As illustrated in Fig. 4-21 (left), the gel porosity of the C-S-H phases which are formed under the weak geochemical contrast conditions is of the order of 0.15. The computationally determined diffusivity corresponds to that of a cation or a neutral species, since the transport of anions might be hindered via the small gel pores by surface charge, which is ignored in the present simulations.

In Fig. 4-22, the derived diffusivities for the evolved geometry under weak geochemical contrast are presented at different instances of the microstructural evolution. We note that as the CSH phases precipitate there is always open interlayer and gel porosity. Due to the C-S-H microstructure, the C-S-H precipitation cannot completely clog the porosity. On the contrary the presence of C-S-H phases guarantees the existence of connected interlayer and gel porosity which in principle should be always open for cations and neutral species. This mechanism may partially explain the experimental observations that neither porosity nor diffusion coefficients for a water tracer tend to zero in clay (Na-Montmorillonite) contacting OPC, at least for a duration of up to 6 years (Luraschi et al. 2020, Shafizadeh et al. 2020). For the setup in consideration setup, a 25% percent reduction in the porosity results in diffusivity drop of one order of magnitude. It should be noted that the simulation results are sensitive to the cementation factor *m* used for the diffusion through the gel porosity. The reduction in diffusivity may be also understood with a back of the envelope calculation by considering that the diffusion through a C-S-H volume characterised by a 0.15 gel porosity, compared to the same water volume would be $D_{CSH} = 0.15^2 D_w = 0.025 D_w$. The pore-level modelling presented here may be expanded to study arbitrary initial clay microstructures, to include the Nernst-Planck equations for charge balance (Yang et al. 2019) as well as to include a larger number of reactants and possible precipitation products.

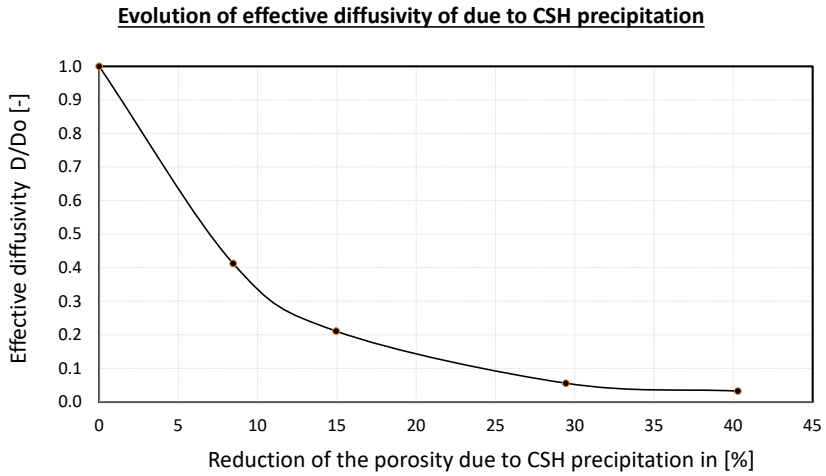

Fig. 4-22: Evolution of effective diffusivity versus total porosity reduction for the weak geochemical gradient

The interlayer and gel porosity of the CSH phases is considered as remaining open porosity. On the x-axis, the reduction in% of the original porosity is plotted.

5 Summary and conclusions

In the previous chapters a detailed analysis of experimental data and modelling relevant to the geochemical evolution of porous media with focus on cement-clay interfaces was presented. The main processes and interactions influencing the change of porosity at different scales have been identified. Pore sizes range from nm to cm as shown in Fig. 2-4 and 2-7. Starting from the lower end, the nanometer scale pores may be found both in cement and clay (< 2 nm e.g. interlayers), next are the meso-pores of size 2 – 50 nm (e.g. gel pores in cement and inter-granular pores in clays), followed by the micrometer capillary pores mainly in cement (~ 1 μm) and finally the macro-pores (~ 1 mm).

Several competing processes will affect the post-closure evolution of the repository for a long period of time. Of major importance are the dissolution precipitation reactions and material fluxes which impact the mass transport pathways and permeability/diffusivity across the cement/clay interface. It is expected that after the closure, the repository will slowly re-saturate. At the same time, gas will be produced due to the degradation of materials and will be transported through seals, tunnels and galleries under partially saturated conditions. The partially saturated conditions are particularly favourable for the escape of gas phase. Under certain conditions the capillary porosity evolution due to geochemical reactions and mechanical processes are expected to affect the (i) ingress of water into the repository; (ii) the escape of gases from the repository, and (iii) the escape of ions from the repository.

Some major conclusions about the geochemical evolution of the cement/clay interface and system can be summarised as follow:

a) The expected extent of the long-term cement-clay interaction may be estimated based on the experimental evidence and on numerical models. Both methods indicate, that cement-clay interaction may alter the material structural and transport properties of cements and clays near the interface.

    a. Cement materials are degraded faster and to a larger (spatial) extend. It seems, that for most scenarios porosity will be increased in cement compartment.

    b. Clay materials have much slower reactivity, and the precipitation of minerals causing porosity decrease is observed only in a very thin zone (mm to cm) adjacent to the interface.

b) For most of the realistic scenarios that describe the evolution of a repository (Leupin et al. 2016a, 2016b), it seems that at least at larger scale, it is unlikely to completely clog the cement/clay interface. At fully saturated conditions, the large amount of nano- and meso-pores which are difficult or impossible to fill with precipitates, prevent complete blockage of transport pathways. In addition, large parts of the L/ILW repository are expected to be only partially saturated for several 10'000 to 100'000 years (Papafotiou & Senger 2016). At such conditions gas is expected to fill the macro-porosity and keep partially saturated cement/clay interfaces open for gas transport.

c) Quantitative temporal and spatial predictions of porosity reduction remains difficult due to the hierarchical pore structure. For fully fluid saturated conditions the cementation of capillary pores and macropores due to mineral precipitation will partially reduce the mass transport in the affected domains. It is unlikely that precipitates can uniformly block the diffusion of liquids, dissolved gases and charged species through the smaller meso- or nano-pores e.g. gel pores, interlayers.

d) At partially liquid saturated conditions, the largest pores are expected to be gas-filled and would not contain precipitates, while smaller liquid filled pores could be blocked by precipitates. Formation of precipitates due to evaporation in large gas filled pores is possible, but will probably not cause complete clogging of gas pathways.

5.1 Porosity reduction due to precipitation in fully liquid saturated media and consequences for transport

Most of the engineered technical barriers are composed of hierarchical materials that span a large range of pore-sizes. Different mechanisms act at each scale, and for different local boundary conditions it is possible that precipitation occurs only in small size pores or in large size pores. In principle, within the nanopores (e.g. interlayers of clay and cement minerals) and mesopores (e.g. cement gel pores and capillary pores), the probability of precipitation reactions is very low or requires very high oversaturation (Meldrum & O'Shaughnessy 2020). According to the classical nucleation theory, which provides a framework of explaining precipitation phenomena, precipitation in small meso- and nanopores requires a very long induction time compared to larger pores, especially when the supersaturation of the liquid phase is not very high. Accordingly, this class of pores remains water filled and maintain the percolation of aqueous phase, where cations and neutral species can be still mobile.

Under saturated conditions, precipitation is expected to occur mainly in larger pores (according to nucleation theory and experimental observations). Smaller pores are then expected to remain open for transport of solutes. In clayey media with charged surfaces, however, this concerns only transport of cations and uncharged species (e.g., dissolved gases), whereas transport of anions may be severely hampered by precipitations in larger pores, because of the anion exclusion effects that manifest at nano-pores and at the lower end of the mesopores (experimental evidence, see e.g. Wigger et al. 2018). Through charge coupling, partial blocking of anion transport may also affect transport of cations, for instance when salinity gradients are present, even though transport of neutral species (e.g., dissolved gases) or equimolar counter-diffusion of cations may still persist. Partial blocking of anion transport may also be relevant with respect to the observed slow-down of the propagation of the reaction front on the clay side of cement-clay interfaces, while at the same time HTO (and water) continues to diffuse. As an example, for a solution with 0.5 M ionic strength, due to existence of electric double layers the anion exclusion may occur for nanopores and even small meso pores (< 10nm).

5.2 Porosity reduction at partial liquid saturated conditions and consequences for transport

The reduction in aqueous transport properties at partially saturated conditions can be considered by analogy to the effect of drastic reduction in transport properties of a fully saturated medium due to precipitation. At partially saturated repository conditions the nano and meso-pores are expected to be mainly filled with liquid. Larger pores, capillary pores and macro-pores like inter-grain spaces and micro-cracks, will be gas/air filled according to the suction pressure.

At partially saturated conditions diffusion shall continue through smaller, still water-filled pores, but at a significantly lower pace, since the tortuosity of the aqueous phase will be increasing, especially in the case where precipitates will be deposited to the next level of pore sizes, e.g. the inter-grain space. If large pores are filled with gas, it is unlikely that precipitation will take place in these pores and therefore the clogging of big pores will not occur. According to the description of processes in Nachshon et al. (2011) in unsaturated media, crystals are limited to growing where liquid is present. In case a medium dries, growth is restricted to the lower range of smaller pores

whose water content is more difficult to be depleted. According to nucleation theory, precipitation is increasingly inhibited with decreasing pore size and therefore the precipitation in nano-pores and meso-pores is highly unlikely.

Under partially saturated conditions, diffusive solute transport is generally much slower than under saturated conditions (Section 2.6), which is expected to delay the development of alteration zones and precipitations. But desaturation leads at the same time to increased solute concentrations, which favours precipitations. As mostly small pores tend to be water-filled under partially saturated conditions, precipitation may then start predominantly in small pores. In this case, transport of all types of solutes (charged and uncharged) will be even more strongly restricted, beyond the restriction by partial saturation.

Desaturation of initially fully saturated interface with blocked large pores might be still possible although this is not predicted by the most repository scale models (Papafotiou & Senger 2016a, 2016b). For a scenario in which the meso-pores above a few nm size still exist, the capillary adhesive forces between pore wall and liquid become more important in the small pores compared to the large pores, and this increases the resistance of water flow and may lead to longer times of local partial saturation.

For a scenario in bentonite systems in which the large pores are filled with precipitates, the advective gas transport via the gas phase or as dissolved gas via the liquid phase, will be slowed down and the dilation mechanism will be the major transport mechanism. The diffusion of dissolved gases will also be slowed down because of the increase of the aqueous phase tortuosity. Lower partial saturation (due to precipitates or gas filling the pores) results in higher suction. Precipitates might also block the preferential gas flow paths in bentonite, but new flow paths are expected to be generated thus bypassing the newly formed precipitates.

It is noted that the time needed to fill a volume with precipitates is proportional to the transport rate and size of the volume. It is possible to interpret this description as an analogy for filling of large pores in granular media. For the same transport rate of reactants, it will need more time to fill larger pores with precipitates. For a given filling rate, it will need 10^{12} times longer to fill a pore with a volume of 1 cm^3 than a pore with a volume of 1 μm^3.

5.3 Extent of zones with porosity change and associated change of material properties

As discussed, for hierarchical porous media, it is likely that precipitation does not reduce the porosity at all scales. In addition, the extent of the total porosity change will be limited by the interplay between chemical reactions and the transport of reactants. A reduction of the capillary porosity will lead to a reduction of (diffusive) mass transport (evidence from experiments and modelling), which then slows down any further development of the reaction zones, including further precipitations. So this is a self-limiting process.

Chemical and mineralogical alterations reported for cement-clay interfaces will affect various local material properties. Of special interest are the changes in porosities and diffusion properties (or generally transport properties) of clay and cement, swelling characteristics of the clay, or also the mechanical properties of the cement in a restricted area in the vicinity of the interface.

Many indirect evidences based on measured element maps and phase distributions exist for an increase of porosity in cement (for instance, dissolution of portlandite; e.g. Bartier et al. (2013), Read et al. (2001) or for a decrease of porosity in cement and clay (for instance, carbonation, precipitation of C-S-H, C-S-A-H, M-S-H or other, partly not well characterised phases; e.g., Dauzeres et al. (2016a), Lerouge et al. (2017). However, a direct quantification of the net porosity change based on such observations is rarely possible; it would require an exact volume balance of dissolution and precipitation reactions, which is often impossible because neither the exact

amounts nor the exact structure of the phases can be derived. Measurements of specific surface areas (e.g., Bartier et al. 2013) also point to increased porosity in cement and decreased porosity in clay, but again, such data do not directly allow to infer porosity values.

Change of porosity

Direct measurements of porosities of altered regions exist in some cases. For instance, Gaboreau et al. (2011) determined a clearly increased porosity in the first ~ 3 cm of a cement that has been in contact with Tournemire argillite for 15 years, with values of porosity of ~ 0.4 in cement far away from the interface to ~ 0.56 at < 2 cm from the interface, as well as a decreased porosity in the clay in the first ~ 1 cm from the interface (~ 0.02, vs ~ 0.07 at larger distances). Jenni et al. (2014) determined 2D porosity maps of OPC concrete-Opalinus Clay samples from the Mont Terri CI experiment after 2.2 years of interaction. Heterogeneities in the samples (e.g., aggregates) made the determination difficult, but they reported a smaller porosity (~ 0.2) in the carbonated zone of the OPC near the interface with a thickness of ~ 1.2 mm compared to more distant regions (porosity > ~ 0.27), and no significant porosity changes in Opalinus Clay. The porosity values determined in the cement material were however all larger than expected (~ 0.1) from the used water to binder ratio, which may be related to the heterogeneities. Shafizadeh et al. (2020) finally could quantify time-dependent porosity changes in 1-cm sized model systems composed of ~ 0.5 cm OPC and ~ 0.5 cm Na-montmorillonite. They found first increasing, later again decreasing porosities in OPC (from ~ 0.63 to ~ 0.69 at most, about corresponding to portlandite dissolution, later locally decreasing values again, probably corresponding to precipitation of new mineral phases), as well as decreasing porosities in Na-montmorillonite, from 0.4 to ~ 0.26 in one sample. They noted, however, that different extents for different samples were observed (partly smaller changes).

Overall, it appears that porosity tends first to increase in OPC due to portlandite dissolution but may locally decrease again due to carbonation or precipitation of other new phases, while porosity tends to decrease in the clay, but does not approach values of zero. The exact spatial extents and porosity changes depend on the type of materials used, the internal material structure (e.g. bedding as possible for shotcrete material) and the interaction time.

Change of transport properties measured

Diffusion coefficients are related to porosities, but the exact relations for a specific materials is not known. The data base with regard to directly measured diffusion coefficients of altered zones is very sparse. Luraschi et al. (2020) reported that effective diffusion coefficients of a neutral tracer (HTO) in the 1-cm samples composed of ~ 0.5 cm OPC and ~ 0.5 cm Na-montmorillonite investigated also by Shafizadeh et al. (2020), and where a low-porosity zone developed in the clay, decreased by a factor of ~ 2 within 6 years of interaction; the decrease was most pronounced in first 1.5 years. Considering only the 5-mm clay part including the low porosity zone, or only the low porosity zone with a thickness of ~ 1 mm, the HTO effective diffusion coefficients reduced by a factor of ~ 3 – 4 or ~ 15 – 20, respectively. The corresponding diffusivity-porosity relationship did follow an exponential law (Archie's law). For the measured anion (Cl), the effects were much more pronounced (reduction of the effective diffusion coefficient by ~ 2 orders of magnitude for the clay part only, or by ~ 3 orders of magnitude for the low-porosity zone only). As in many cases no flux could be measured anymore, the reduction was partly even larger. The stronger effect of precipitations on anions is related to anion exclusion effects.

In conclusion, the diffusion coefficients across or along the material interfaces are certainly related to porosity changes in the relevant materials. Mass transfer across cement-clay interfaces or in clay along interfaces will tend to be reduced due to reduced porosity in the clay, while they tend to be increased in the cement along the cement-clay interfaces. The reduction within or across the clay is much more pronounced for anions compared to neutral tracers.

Cation exchange

Cation exchange capacity (CEC) and exchanger compositions of the clay material were also partly measured, typically with large uncertainty. While Gaboreau et al. (2011) reported an increased CEC close to the cement interface and explained it by newly precipitated phases with increased surface charge, most newer studies find the contrary. Jenni et al. (2014) reported a slight decrease of the CEC towards the interface in Opalinus Clay in contact with OPC concrete, and that the cation exchanger was reduced in Mg and enriched in Na and K. Such modifications may decrease the swelling capacity of the OPA; however, the changes were relatively small and in a narrow zone. In systems of OPC in contact with Na-montmorillonite or Na-bentonite (Luraschi et al. 2020), Ca enrichment of the cation exchanger will certainly happen. So far, it appears that changes are limited in terms of amount and spatial extent, but as the cations on the exchanger represent a significant pool of ions readily available for reactions, studies extending over larger times as well as addressing directly the swelling capacity would we very valuable.

5.4 Extent of the cement/clay alteration zone

Experimental observations indicate that the extent of the altered zones in cement and clay remains relatively limited, that is, within the order of millimetres to a few centimetres. The extent depends, however, on time, on type of materials involved, and on type of alteration considered. For instance, in the Mont Terri CI experiment, alterations in terms of increased or decreased element concentrations and dissolution or precipitation of new phases did extend mostly up to ~ 1 mm or less in OPC and Opalinus Clay that were in contact, with the exception of a slight Mg enrichment in OPA about 7 mm from the interface, and up to ~ 2 mm in ESDRED in contact with Opalinus Clay after 5 years (Mäder et al. 2017). For samples from the same experiment but including bentonite instead of Opalinus Clay, a larger extent of ~ 10 mm of mineral perturbations was seen in the clay (Yokoyama et al. 2021) after 5 to 10 years. Shafizadeh et al. (2020) found altered zones in terms of total porosity changes in Na-montmorillonite in contact with OPC cement up to ~ 1 – 2 mm after 6 years of interaction, while the porosity in the OPC was altered up to ~ 3 – 4 mm. Alteration distances of ~ 2 – 4 mm as well as the maximum 30 mm were reported from the FEBEX experiment (Turrero & Cloet 2017), while somewhat larger distances of 1 – 3 cm were inferred from samples from the Tournemire site that reacted for 15 years (Bartier et al. 2013; Gaboreau et al. 2011). The front of increased pH may propagate further into the clay, as indicated for instance by zones of Mg precipitates located at a distance of about 1.5 cm from the interface (Yokoyama et al. 2021). In a recent review, (Wilson et al. 2021) conclude that the extent of clearly altered zones is typically on the mm to cm-scale, but that the actual extent will very likely be site-specific, that is, depend on type of materials and geometries.

The relatively small extents found in experiments are broadly consistent with modelling results, and appear generally also consistent with observations of decreasing diffusion coefficients in Na-montmorillonite due to a zone of reduced porosity. The decrease of diffusion coefficients essentially means that the reactants which are required to continue the precipitation reactions are transported at an ever reducing pace. At the same time nano and meso porosity appear to remain open which allows the transport of mainly neutral or positively charged solutes through and along the interfaces, at least during the time of the experiments (several years). Finally, relevant to the gas transport across these material alteration zones, it is noted that even if under specific

circumstances, locally the porosity may be greatly reduced, due to the heterogeneity of the cement and host rock, it is unlikely that such a continuous and uniform zone will be formed. Moreover, under compressive strength (e.g. tunnel system) small cracks which will disrupt such a zone are likely to appear. Gas transport will be promoted by the existence of cracks, voids and the zone of higher porosity on the cement side.

6 References

Abubaker, F., Lynsdale, C. & Cripps, J. (2014): Investigation of concrete-clay interaction with regards to the thaumasite form of sulfate attack. Construction and Building Materials 67, 88-94. https://doi.org/10.1016/J.CONBUILDMAT.2013.10.033

Adler, M., Mäder, U. & Waber, N.H. (1999): High-pH alteration of argillaceous rocks : an experimental study. SCHWEIZ. MINERAL. PETROGR. MITT 79, 445-454. https://doi.org/10.5169/seals-60219

Águila, J.F., Montoya, V., Samper, J., Montenegro, L., Kosakowski, G., Krejci, P. & Pfingsten, W. (2021): Modeling cesium migration through Opalinus Clay: a benchmark for single- and multi-species sorption-diffusion models. Computational Geosciences 25, 1405-1436. https://doi.org/10.1007/s10596-021-10050-5

Aja, S.U. & Rosenberg, P.E. (1992): The Thermodynamic Status of Compositionally-Variable Clay Minerals: A Discussion. Clays and Clay Minerals 1992 40:3 40, 292-299. https://doi.org/10.1346/CCMN.1992.0400307

Al-Amoudi, O.S.B. (2002): Attack on plain and blended cements exposed to aggressive sulfate environments. Cement and Concrete Composites 24, 305-316. https://doi.org/10.1016/S0958-9465(01)00082-8

Alexander, W.R., Arcilla, C.A., McKinley, I.G., Kawamura, H., Takahashi, Y., Aoki, K. & Miyoshi, S. (2008): A New Natural Analogue Study of the Interaction of Low-Alkali Cement Leachates and the Bentonite Buffer of a Radioactive Waste Repository. MRS Online Proceedings Library (OPL) 1107, 493-500. https://doi.org/10.1557/PROC-1107-493

Alexander, W.R., Milodowski, A.E., Pitty, A.F., Hardie, S.M.L., Kemp, S.J., Rushton, J.C., Siathas, Andreas, Siathas, Avrim, Mackenzie, A.B., Korkeakoski, P., Norris, S., Sellin, P. & Rigas, M. (2013): Bentonite reactivity in alkaline solutions: interim results of the Cyprus Natural Analogue Project (CNAP). Clay Minerals 48, 235-249. https://doi.org/10.1180/CLAYMIN.2013.048.2.06

Andrade, C., Sarría, J. & Alonso, C. (1999): Relative humidity in the interior of concrete exposed to natural and artificial weathering. Cement and Concrete Research 29, 1249-1259. https://doi.org/10.1016/S0008-8846(99)00123-4

Andreola, F., Leonelli, C., Romagnoli, M. & Miselli, P. (2000): Techniques used to determine porosity. Americal Ceramic Scociety Bulletin 79, 49-52

Appelo, C.A.J. & Postma, D. (2005): Geochemistry, Groundwater and Pollution. A.A.Balkema Publishers, Amsterdam, Netherlands

Aradóttir, E.S.P., Sonnenthal, E.L. & Jónsson, H. (2012): Development and evaluation of a thermodynamic dataset for phases of interest in CO2 mineral sequestration in basaltic rocks. Chemical Geology 304-305, 26-38. https://doi.org/10.1016/j.chemgeo.2012.01.031

Arthur, R., Sasamoto, H., Walker, C. & Yui, M. (2011): Polymer model of zeolite thermochemical stability. Clays and Clay Minerals 59, 626-639. https://doi.org/10.1346/CCMN.2011.0590608

Ashraf, W. (2016): Carbonation of cement-based materials: Challenges and opportunities. Construction and Building Materials 120, 558-570. https://doi.org/10.1016/j.conbuildmat.2016.05.080

Atkins, M. & Glasser, F.P. (1992): Application of portland cement-based materials to radioactive waste immobilization. Waste Management 12, 105-131. https://doi.org/10.1016/0956-053X(92)90044-J

Atkinson, A., Goult, D.J. & Hearne, J.A. (1985): An assessment of the long-term durability of concrete in radioactive waste repositories. MRS Proceedings 50, 239-246. https://doi.org/10.1557/PROC-50-239

Bach, T.T.H., Chabas, E., Pochard, I., Cau Dit Coumes, C., Haas, J., Frizon, F. & Nonat, A. (2013): Retention of alkali ions by hydrated low-pH cements: Mechanism and Na$^+$/K$^+$ selectivity. Cement and Concrete Research 51, 14-21. https://doi.org/10.1016/J.CEMCONRES.2013.04.010

Bartier, D., Techer, I., Dauzères, A., Boulvais, P., Blanc-Valleron, M.-M. & Cabrera, J. (2013): In situ investigations and reactive transport modelling of cement paste/argillite interactions in a saturated context and outside an excavated disturbed zone. Applied Geochemistry 31, 94-108. https://doi.org/10.1016/j.apgeochem.2012.12.009

Bear, J. (1972): Dynamics of Fluids in Porous Media. Elsevier

Beckingham, L.E., Steefel, C.I., Swift, A.M., Voltolini, M., Yang, L., Anovitz, L.M., Sheets, J.M., Cole, D.R., Kneafsey, T.J., Mitnick, E.H., Zhang, S., Landrot, G., Ajo-Franklin, J.B., DePaolo, D.J., Mito, S. & Xue, Z. (2017): Evaluation of accessible mineral surface areas for improved prediction of mineral reaction rates in porous media. Geochimica et Cosmochimica Acta 205, 31-49. https://doi.org/10.1016/j.gca.2017.02.006

Bejaoui, S. & Bary, B. (2007): Modeling of the link between microstructure and effective diffusivity of cement pastes using a simplified composite model. Cement and Concrete Research 37, 469-480. https://doi.org/10.1016/j.cemconres.2006.06.004

Bentz, D., Jensen, O., Coats, A. & Glasser, F. (2000): Influence of silica fume on diffusivity in cement-based materials. Cement and Concrete Research 30, 953-962. https://doi.org/10.1016/S0008-8846(00)00264-7

Bernard, E., Jenni, A., Fisch, M., Grolimund, D. & Mäder, U. (2020a): Micro-X-ray diffraction and chemical mapping of aged interfaces between cement pastes and Opalinus Clay. Applied Geochemistry 115, 104538. https://doi.org/10.1016/j.apgeochem.2020.104538

Bernard, E., Jenni, A., Fisch, M., Grolimund, D. & Mäder, U. (2020b): Micro-X-ray diffraction and chemical mapping of aged interfaces between cement pastes and Opalinus Clay. Applied Geochemistry 115. https://doi.org/10.1016/j.apgeochem.2020.104538

Berner, U. (2014a): Solubility of radionuclides in a bentonite environment for provisional safety analyses for SGT-E2. Nagra Technical Report NTB 14-06)

Berner, U. (2014b): Solubility of Radionuclides in a Concrete Environment for Provisional Safety Analyses for SGT-E2. Nagra Technical Report NTB 14-07

Berner, U. (2009): Modelling hydrated HTS cement and its pore water (Internal Report AN-44-09-10). Paul Scherrer Institut, Villigen, Switzerland

Berner, U., Kulik, D.A. & Kosakowski, G. (2013): Geochemical impact of a low-pH cement liner on the near field of a repository for spent fuel and high-level radioactive waste. Physics and Chemistry of the Earth, Parts A/B/C 64, 46-56. https://doi.org/10.1016/j.pce.2013.03.007

Berner, U.R. (1992): Evolution of pore water chemistry during degradation of cement in a radioactive waste repository environment. Waste Management 12, 201-219. https://doi.org/10.1016/0956-053X(92)90049-O

Bethke, C.M. (2007): Geochemical and Biogeochemical Reaction Modeling. Cambridge University Press, Cambridge. https://doi.org/10.1017/CBO9780511619670

Bildstein, O., Claret, F. & Frugier, P. (2019): RTM for waste repositories. Reviews in Mineralogy and Geochemistry 85, 419-457. https://doi.org/10.2138/rmg.2019.85.14

Bish, D.L. & Carey, J.W. (2001): Thermal behaviour of natural zeolites. Reviews in Mineralogy and Geochemistry 45, 403-452. https://doi.org/10.2138/rmg.2001.45.13

Blanc, P., Bourbon, X., Lassin, A. & Gaucher, E.C. (2010): Chemical model for cement-based materials: Temperature dependence of thermodynamic functions for nanocrystalline and crystalline C-S-H phases. Cement and Concrete Research 40, 851-866. https://doi.org/10.1016/j.cemconres.2009.12.004

Blanc, P., Gherardi, F., Vieillard, P., Marty, N.C.M., Gailhanou, H., Gaboreau, S., Letat, B., Geloni, C., Gaucher, E.C. & Madé, B. (2021): Thermodynamics for clay minerals: Calculation tools and application to the case of illite/smectite interstratified minerals. Applied Geochemistry 130. https://doi.org/10.1016/j.apgeochem.2021.104986

Blanc, P., Lassin, A., Piantone, P., Azaroual, M., Jacquemet, N., Fabbri, A. & Gaucher, E.C. (2012): Thermoddem: A geochemical database focused on low temperature water/rock interactions and waste materials. Applied Geochemistry 27, 2107-2116. https://doi.org/10.1016/j.apgeochem.2012.06.002

Blanc, P., Vieillard, P., Gailhanou, H., Gaboreau, S., Gaucher, É., Fialips, C.I., Madé, B. & Giffaut, E. (2015): A generalized model for predicting the thermodynamic properties of clay minerals. American Journal of Science 315, 734-780. https://doi.org/10.2475/08.2015.02

Blanc, P., Vieillard, P., Gailhanou, H., Gaboreau, S., Marty, N.C.M., Claret, F., Madé, B. & Giffaut, E. (2015): ThermoChimie database developments in the framework of cement/clay interactions. Applied Geochemistry 55, 95-107. https://doi.org/10.1016/j.apgeochem.2014.12.006

Bok, F., Salah, S., Heath, T., De Windt, L., Spahiu, K. & Reed, D. (2019): ThermoChimie Benchmarking Workshop Report (Report TCIII-2019-09E). Thermochimie

Bonen, D. (1992): Composition and appearance of magnesium silicate hydrate and its Relation to deterioration of cement-based materials. Journal of the American Ceramic Society 75, 2904-2906. https://doi.org/10.1111/j.1151-2916.1992.tb05530.x

Bossart, P. & Nussbaum, C. (2007): Mont Terri Project - Heater experiment, engineered barrier emplacement and ventilation experiment (Reports of the Swiss Geological Survey/Berichte der Landesgeologie 1). Wabern, Switzerland

Botes, A., James, C. & Sheridan, C.M. (2018): Assessing the clogging and permeability of degrading packed bed reactors. Water SA 44, 20-26. https://doi.org/10.4314/wsa.v44i1.03

Bowers, M.C., Ehrlich, R., Howard, J.J. & Kenyon, W.E. (1995): Determination of porosity types from NMR data and their relationship to porosity types derived from thin section. Journal of Petroleum Science and Engineering 13, 1-14. https://doi.org/10.1016/0920-4105(94)00056-A

Bradbury, M.H. & Baeyens, B. (2002): Porewater chemistry in compacted re-saturated MX-80 bentonite: Physico-chemical characterisation and geochemical modelling (PSI Report 02-10). Paul Scherrer Institut, Villigen, Switzerland

Bradbury, M.H., Berner, UrsCurti, E., Hummel, W., Kosakowski, G. & Thoenen, T. (2014): Geochemical near-field evolution of a deep geological repository for spent fuel and high-level radioactive waste. Nagra Technical Report NTB 12-01

Bradbury, M.H. & Van Loon, L.R. (1996): Cementitious near-field sorption data bases for performance assessment of a L/ILW repository in a Palfris marl host rock. Nagra Technical Report NTB 96-04

Brantley, S.L. (2008): Kinetics of Mineral Dissolution, in: Kinetics of Water-Rock Interaction. Springer New York, New York, NY, pp. 151-210. https://doi.org/10.1007/978-0-387-73563-4_5

Brovelli, A., Malaguerra, F. & Barry, D.A. (2009): Bioclogging in porous media: Model development and sensitivity to initial conditions. Environmental Modelling & Software 24, 611-626. https://doi.org/10.1016/j.envsoft.2008.10.001

Brueckner, R., Williamson, S.J. & Clark, L.A. (2012): The effects of the thaumasite form of sulfate attack on skin friction at the concrete/clay interface. Cement and Concrete Research 42, 424-430. https://doi.org/10.1016/j.cemconres.2011.11.009

Bruno, J., Bosbach, D., Kulik, D. & Navrotsky, A. (2007): Chemical Thermodynamics of Solid Solutions of Interest in Radioactive Waste Management, OECD Nuclear Energy Agency, Chemical Thermodynamics. OECD. https://doi.org/10.1787/9789264033191-en

Busch, A., Kampman, N., Bertier, P., Pipich, V., Feoktystov, A., Rother, G., Harrington, J., Leu, L., Aertens, M. & Jacops, E. (2018): Predicting Effective Diffusion Coefficients in Mudrocks Using a Fractal Model and Small-Angle Neutron Scattering Measurements. Water Resources Research 54, 7076-7091. https://doi.org/10.1029/2018WR023425

Chagneau, A., Claret, F., Enzmann, F., Kersten, M., Heck, S., Madé, B. & Schäfer, T. (2015): Mineral precipitation-induced porosity reduction and its effect on transport parameters in diffusion-controlled porous media. Geochemical Transactions 16, 13. https://doi.org/10.1186/s12932-015-0027-z

Chipera, S.J. & Apps, J.A. (2001): Geochemical stability of natural zeolites. Reviews in Mineralogy and Geochemistry 45, 117-161. https://doi.org/10.2138/rmg.2001.45.3

Churakov, S.V. & Prasianakis, N.I. (2018): Review of the current status and challenges for a holistic process-based description of mass transport and mineral reactivity in porous media. American Journal of Science 318, 921-948. https://doi.org/10.2475/09.2018.03

Churakov, S.V. (2013): Mobility of Na and Cs on Montmorillonite Surface under Partially Saturated Conditions. Environmental Science and Technology 47, 9816-9823

Claveau-Mallet, D. & Comeau, Y. (2020): Chemical clogging and evolution of head losses in steel slag filters used for phosphorus removal. Water (Switzerland) 12. https://doi.org/10.3390/W12061517

Cloet, V., Schwyn, B., Baeyens, B., Curti, E., Diomidis, N., Johnson, L.H., Leupin, O.X., Mibus, J., Van Loon, L.R. & Wieland, E. (2014): Einfluss der Salinität des Porenwassers der Wirtgesteine auf die Langzeitsicherheit der Tiefenlager. Nagra Arbeitsbericht NAB 14-09

Courcelles, B., Modaressi-Farahmand-Razavi, A., Gouvenot, D. & Esnault-filet, A. (2010): Influence of Precipitates on Hydraulic Performance of Permeable Reactive Barrier Filters. International Journal of Geomechanics 1, 56. https://doi.org/10.1061/(ASCE)GM.1943-5622.0000098

Damiani, L.H., Kosakowski, G., Vinsot, A. & Churakov, S. V. (2021): Hydrogen gas transfer between a Bbrehole and claystone: experiment and geochemical model. Environmental Geotechnics 1-11. https://doi.org/10.1680/jenge.21.00061

Dauzeres, A., Achiedo, G., Nied, D., Bernard, E., Alahrache, S. & Lothenbach, B. (2016a): Magnesium perturbation in low-pH concretes placed in clayey environment – Solid characterizations and modeling. Cement and Concrete Research 79, 137-150. https://doi.org/10.1016/j.cemconres.2015.09.002

Dauzeres, A., Achiedo, G., Nied, D., Bernard, E., Alahrache, S. & Lothenbach, B. (2016b): Magnesium perturbation in low-pH concretes placed in clayey environment – Solid characterizations and modeling. Cement and Concrete Research 79, 137-150. https://doi.org/10.1016/j.cemconres.2015.09.002

Dauzeres, A., Le Bescop, P., Sardini, P. & Cau Dit Coumes, C. (2010): Physico-chemical investigation of clayey/cement-based materials interaction in the context of geological waste disposal: Experimental approach and results. Cement and Concrete Research 40, 1327-1340. https://doi.org/10.1016/J.CEMCONRES.2010.03.015

De Windt, L., Miron, G.D., Fabian, M., Goethals, J. & Wittebroodt, C. (2020): First results on the thermodynamic databases and reactive transport models for steel-cement interfaces at high temperature. European Commission

Deissmann, G., Ait Mouheb, N., Martin, C., Turrero, M.J., Torres, E., Kursten, B., Weetjens, E., Jacques, D., Cuevas, J., Samper, J., Montenegro, L., Leivo, M., Somervuori, M. & Carpen, L. (2021): Experiments and numerical model studies on interfaces. Final version as of 12.05.2021 of deliverable D2.5 of the HORIZON 2020 project EURAD. EC Grant agreement no: 847593

Despotou, E., Shtiza, A., Schlegel, T. & Verhelst, F. (2016): Literature study on the rate and mechanism of carbonation of lime in mortars/Literaturstudie über Mechanismus und Grad der Karbonatisierung von Kalkhydrat im Mörtel. Mauerwerk 20, 124-137. https://doi.org/10.1002/dama.201500674

Dilnesa, B.Z., Wieland, E., Lothenbach, B., Dähn, R. & Scrivener, K.L. (2014): Fe-containing phases in hydrated cements. Cement and Concrete Research 58, 45-55. https://doi.org/10.1016/j.cemconres.2013.12.012

Diomidis, N., Cloet, V., Leupin, O.X., Marschall, P., Poller, A. & Stein, M. (2016): Production, consumption and transport of gases in deep geological repositories according to the Swiss disposal concept. Nagra Technical Report NTB 16-03

Dippenaar, M.A. (2014): Porosity reviewed: Quantitative multi-disciplinary understanding, recent advances and applications in vadose zone hydrology. Geotechnical and Geological Engineering 32, 1-19. https://doi.org/10.1007/s10706-013-9704-9

Dolder, F., Mäder, U., Jenni, A. & Münch, B. (2017): Alteration of MX-80 bentonite backfill material by high-pH cementitious fluids under lithostatic conditions – an experimental approach using core infiltration techniques. Geological Society, London, Special Publications 443, 281 LP - 305. https://doi.org/10.1144/SP443.10

Dolder, F., Mäder, U., Jenni, A. & Schwendener, N. (2014): Experimental characterization of cement-bentonite interaction using core infiltration techniques and 4D computed tomography. Physics and Chemistry of the Earth 70-71, 104-113. https://doi.org/10.1016/j.pce.2013.11.002

Duro, L., Altmaier, M., Holt, E., Mäder, U., Claret, F., Grambow, B., Idiart, A., Valls, A. & Montoya, V. (2020): Contribution of the results of the CEBAMA project to decrease uncertainties in the Safety Case and Performance Assessment of radioactive waste repositories. Applied Geochemistry 112, 104479. https://doi.org/10.1016/J.APGEOCHEM.2019.104479

Dutzer, V., Dridi, W., Poyet, S., Le Bescop, P. & Bourbon, X. (2019): The link between gas diffusion and carbonation in hardened cement pastes. Cement and Concrete Research 123, 105795. https://doi.org/10.1016/j.cemconres.2019.105795

Elakneswaran, Y., Noguchi, N., Matumoto, K., Morinaga, Y., Chabayashi, T., Kato, H. & Nawa, T. (2019): Characteristics of ferrite-rich portland cement: Comparison with ordinary portland cement. Frontiers in Materials 6, 97. https://doi.org/10.3389/fmats.2019.00097

Fahim, A., Carufel, S. De, Ghods, P., Alizadeh, A.R. & Salehi, M. (2019): Practical Model for Predicting Internal Relative Humidity of Concrete Exposed to Drying. Journal of Materials in Civil Engineering 31, 04019143. https://doi.org/10.1061/(ASCE)MT.1943-5533.0002785

Farzam, H. (ACI C. 116 chairman) (2000): 116R-90: Cement and Concrete Terminology (Report ACI 116R-00). American Concrete Institute

Feldman, R.F. & Sereda, P.J. (1968): A model for hydrated Portland cement paste as deduced from sorption-length change and mechanical properties. Matériaux et Constructions 1, 509-520. https://doi.org/10.1007/BF02473639

Fernández, R., Ruiz, A.I. & Cuevas, J. (2016): Formation of C-A-S-H phases from the interaction between concrete or cement and bentonite. Clay Minerals 51, 223-235. https://doi.org/10.1180/claymin.2016.051.2.09

Fernández, R., Torres, E., Ruiz, A.I., Cuevas, J., Alonso, M.C., García Calvo, J.L., Rodríguez, E. & Turrero, M.J. (2017): Interaction processes at the concrete-bentonite interface after 13 years of FEBEX-Plug operation. Part II: Bentonite contact. Physics and Chemistry of the Earth, Parts A/B/C 99, 49-63. https://doi.org/10.1016/J.PCE.2017.01.009

Fernández, R.M., Rodríguez, M., Virgildela Villa, R. & Cuevas, J. (2009): Alteration of compacted bentonite by diffusion of highly alkaline solutions. European Journal of Mineralogy 21, 725-735. https://doi.org/10.1127/0935-1221/2009/0021-1947

Fialips, C.I., Carey, J.W. & Bish, D.L. (2005): Hydration-dehydration behaviour and thermodynamics of chabazite. Geochimica et Cosmochimica Acta 69, 2293-2308. https://doi.org/10.1016/j.gca.2004.11.007

Fischer, C., Kurganskaya, I., Schäfer, T. & Lüttge, A. (2014): Variability of crystal surface reactivity: What do we know? Applied Geochemistry. https://doi.org/10.1016/j.apgeochem.2014.02.002

Flury, M. & Gimmi, T.F. (2002): Solute diffusion, in: Dane, J.H., & Topp, G.C. (Eds.), Methods of Soil Analysis, Part 4: Physical Methods. Soil Science Society of America, Madison, Wisconsin, USA, pp. 1323-1351

Fridriksson, T., Neuhoff, P.S., Arnórsson, S. & Bird, D.K. (2001): Geological constraints on the thermodynamic properties of the stilbite-stellerite solid solution in low-grade metabasalts. Geochimica et Cosmochimica Acta 65, 3993-4008. https://doi.org/10.1016/S0016-7037(01)00629-9

Fritz, B. & Noguera, C. (2009): Mineral precipitation kinetics. Reviews in Mineralogy and Geochemistry 70, 371-410. https://doi.org/10.2138/rmg.2009.70.8

Fukatsu, Y., Van Loon, L.R., Shafizadeh, A., Grolimund, D., Ikeda, Y. & Tsukahara, T. (2017): Effect of celestite precipitation in compacted illite on the Diffusion of HTO, 36 Cl^-, and 22 Na^+. Energy Procedia 131, 133-139. https://doi.org/10.1016/j.egypro.2017.09.450

Gaboreau, S., Prêt, D., Tinseau, E., Claret, F., Pellegrini, D. & Stammose, D. (2011): 15 years of in situ cement-argillite interaction from Tournemire URL: Characterisation of the multi-scale spatial heterogeneities of pore space evolution. Applied Geochemistry 26, 2159-2171. https://doi.org/10.1016/j.apgeochem.2011.07.013

Gaboreau, S., Rodríguez-Cañas, E., Maeder, U., Jenni, A., Turrero, M.J. & Cuevas, J. (2020): Concrete perturbation in a 13-year in situ concrete/bentonite interaction from FEBEX experiments. New insight of 2:1 Mg phyllosilicate precipitation at the interface. Applied Geochemistry 118, 104624. https://doi.org/10.1016/j.apgeochem.2020.104624

Gaona, X., Dähn, R., Tits, J., Scheinost, A.C. & Wieland, E. (2011): Uptake of Np(IV) by C-S-H phases and cement paste: An EXAFS study. Environmental Science and Technology 45, 8765-8771. https://doi.org/10.1021/es2012897

Garboczi, E. (1990): Permeability, diffusivity, and microstructural parameters: A critical review. Cement and Concrete Research 20, 591-601. https://doi.org/10.1016/0008-8846(90)90101-3

Gaucher, E.C. & Blanc, P. (2006): Cement/clay interactions - a review: experiments, natural analogues, and modeling. Waste Management 26, 776-788. https://doi.org/10.1016/j.wasman.2006.01.027

Gaucher, E.C., Blanc, P., Matray, J.M. & Michau, N. (2004): Modeling diffusion of an alkaline plume in a clay barrier. Applied Geochemistry 19, 1505-1515. https://doi.org/10.1016/j.apgeochem.2004.03.007

Gautschi, A. (2015): Deep geological disposal of radioactive waste - An international perspective. Bulletin fuer Angewandte Geologie. https://doi.org/10.5169/seals-632523

Ghanbarian, B., Hunt, A.G., Ewing, R.P. & Sahimi, M. (2013): Tortuosity in Porous Media: A Critical Review. Soil Science Society of America Journal 77, 1461-1477. https://doi.org/10.2136/sssaj2012.0435

Giffaut, E., Grivé, M., Blanc, P., Vieillard, P., Colàs, E., Gailhanou, H., Gaboreau, S., Marty, N.C.M., Madé, B. & Duro, L. (2014): Andra thermodynamic database for performance assessment: ThermoChimie. Applied Geochemistry 49, 225-236. https://doi.org/10.1016/J.APGEOCHEM.2014.05.007

Gimmi, T. & Alt-Epping, P. (2018): Simulating Donnan equilibria based on the Nernst-Planck equation. Geochimica et Cosmochimica Acta 232, 1-13. https://doi.org/10.1016/J.GCA.2018.04.003

Gimmi, T. & Churakov, S.V. (2019): Water retention and diffusion in unsaturated clays: Connecting atomistic and pore scale simulations. Applied Clay Science 175, 169-183. https://doi.org/10.1016/J.CLAY.2019.03.035

Gimmi, T. & Kosakowski, G. (2011): How mobile are sorbed cations in clays and clay rocks? Environmental Science and Technology 45, 1443-1449. https://doi.org/10.1021/ES1027794/SUPPL_FILE/ES1027794_SI_001.PDF

Gimmi, T., Leupin, O.X., Eikenberg, J., Glaus, M.A., Van Loon, L.R., Waber, H.N., Wersin, P., Wang, H.A.O., Grolimund, D., Borca, C.N., Dewonck, S. & Wittebroodt, C. (2014): Anisotropic diffusion at the field scale in a 4-year multi-tracer diffusion and retention experiment – I: Insights from the experimental data. Geochimica et Cosmochimica Acta 125, 373-393. https://doi.org/10.1016/j.gca.2013.10.014

Glasser, F.P. (2013): Cements in Radioactive Waste Disposal (IAEA-TECDOC-CD-1701(Companion CD)). International Atomic Energy Agency (IAEA)

Glasser, F.P., Marchand, J. & Samson, E. (2008): Durability of concrete – Degradation phenomena involving detrimental chemical reactions. Cement and Concrete Research 38, 226-246. https://doi.org/10.1016/j.cemconres.2007.09.015

Glynn, P. (2019): Solid-solution solubilities and thermodynamics: Sulfates, carbonates and halides, in: Sulfate Minerals: Crystallography, Geochemistry, and Environmental Significance. Walter de Gruyter GmbH, pp. 481-511. https://doi.org/10.2138/rmg.2000.40.10

Gollop, R.S. & Taylor, H.F.W. (1996): Microstructural and microanalytical studies of sulfate attack. V. Comparison of different slag blends. Cement and Concrete Research 26, 1029-1044. https://doi.org/10.1016/0008-8846(96)00090-7

Gong, F., Zhang, D., Sicat, E. & Ueda, T. (2013): Empirical Estimation of Pore Size Distribution in Cement, Mortar, and Concrete. Journal of Materials in Civil Engineering 26, 04014023. https://doi.org/10.1061/(ASCE)MT.1943-5533.0000945

González-Santamaría, D.E., Fernández, R., Ruiz, A.I., Ortega, A. & Cuevas, J. (2020a): High-pH/low pH ordinary Portland cement mortars impacts on compacted bentonite surfaces: Application to clay barriers performance. Applied Clay Science 193. https://doi.org/10.1016/j.clay.2020.105672

González-Santamaría, D.E., Fernández, R., Ruiz, A.I., Ortega, A. & Cuevas, J. (2020b): Bentonite/CEM-II cement mortar interface experiments: A proxy to in situ deep geological repository engineered barrier system surface reactivity. Applied Geochemistry 117. https://doi.org/10.1016/j.apgeochem.2020.104599

Guérillot, D. & Bruyelle, J. (2020): Geochemical equilibrium determination using an artificial neural network in compositional reservoir flow simulation. Computational Geosciences 24, 697-707. https://doi.org/10.1007/s10596-019-09861-4

Guillaumont, R., Fanghänel, T., Neck, V., Fuger, J., Palmer, D.A., Grenthe, I. & Rand, M.H. (2003): Update on the chemical thermodynamics of uranium, neptunium, plutonium, americium and technetium. Chemical Thermodynamics 5, 919

Hayek, M., Kosakowski, G. & Churakov, S. (2011): Exact analytical solutions for a diffusion problem coupled with a precipitation-dissolution reaction and feedback of porosity change. Water Resources Research 47, W07545. https://doi.org/10.1029/2010WR010321

Hayek, M., Kosakowski, G., Jakob, A. & Churakov, S. V. (2012): A class of analytical solutions for multidimensional multispecies diffusive transport coupled with precipitation-dissolution reactions and porosity changes. Water Resources Research 48, W03525. https://doi.org/10.1029/2011WR011663

Helgeson, H.C., Kirkham, D.H. & Flowers, G.C. (1981): Theoretical prediction of the thermodynamic behaviour of aqueous electrolytes by high pressures and temperatures; IV, Calculation of activity coefficients, osmotic coefficients, and apparent molal and standard and relative partial molal properties to 600 d. American Journal of Science 281, 1249-1516. https://doi.org/10.2475/ajs.281.10.1249

Hemingway, B.S. & Robie, R.A. (1984): Thermodynamic properties of zeolites: low-temperature heat capacities and thermodynamic functions for phillipsite and clinoptilolite. Estimates of the thermochemical properties of zeolitic water at low temperature. American Mineralogist 69, 692-700

Hewlett, P.C. (1998): Lea's Chemistry of Cement and Concrete, Lea's Chemistry of Cement and Concrete. Elsevier Ltd. https://doi.org/10.1016/B978-0-7506-6256-7.X5007-3

Hill, R. (1963): Elastic properties of reinforced solids: Some theoretical principles. Journal of the Mechanics and Physics of Solids 11, 357-372. https://doi.org/10.1016/0022-5096(63)90036-X

Hoch, A.R., Baston, G.M.N., Glasser, F.P., Hunter, F.M.I. & Smith, V. (2012): Modelling evolution in the near field of a cementitious repository. Mineralogical Magazine 76, 3055-3069. https://doi.org/10.1180/minmag.2012.076.8.21

Holland, T.J.B. & Powell, R. (1998): An internally consistent thermodynamic data set for phases of petrological interest. Journal of Metamorphic Geology 16, 309-343. https://doi.org/10.1111/j.1525-1314.1998.00140.x

Hommel, J., Coltman, E. & Class, H. (2018): Porosity-Permeability Relations for Evolving Pore Space: A Review with a Focus on (Bio-)geochemically Altered Porous Media. Transport in Porous Media 124, 589-629. https://doi.org/10.1007/s11242-018-1086-2

Huang, Y., Shao, H., Wieland, E., Kolditz, O. & Kosakowski, G. (2021): Two-phase transport in a cemented waste package considering spatio-temporal evolution of chemical conditions. npj Materials Degradation 5, 4. https://doi.org/10.1038/s41529-021-00150-z

Huang, Y., Shao, H., Wieland, E., Kolditz, O. & Kosakowski, G. (2018): A new approach to coupled two-phase reactive transport simulation for long-term degradation of concrete. Construction and Building Materials 190, 805-829. https://doi.org/10.1016/j.conbuildmat.2018.09.114

Hummel, W., Berner, U., Curti, E., Pearson, F.J. & Thoenen, T. (2002): Nagra/PSI Chemical Thermodynamic Data Base 01/01. Radiochimica Acta 90, 805-813. https://doi.org/10.1524/ract.2002.90.9-11_2002.805

Idiart, A., Laviña, M., Kosakowski, G., Cochepin, B., Meeussen, J.C.L., Samper, J., Mon, A., Montoya, V., Munier, I., Poonoosamy, J., Montenegro, L., Deissmann, G., Rohmen, S., Damiani, L.H., Coene, E. & Naves, A. (2020): Reactive transport modelling of a low-pH concrete/clay interface. Applied Geochemistry 115, 104562. https://doi.org/10.1016/j.apgeochem.2020.104562

Indraratna, B., Medawela, S., Rowe, R.K., Thamwattana, N. & Heitor, A. (2020): Biogeochemical Clogging of Permeable Reactive Barriers in Acid-Sulfate Soil Floodplain. Journal of Geotechnical and Geoenvironmental Engineering 146, 04020015. https://doi.org/10.1061/(asce)gt.1943-5606.0002231

IUPAC (2019): The IUPAC Compendium of Chemical Terminology. International Union of Pure and Applied Chemistry (IUPAC), Research Triangle Park, NC. https://doi.org/10.1351/goldbook

Jacops, E., Aertsens, M., Maes, N., Bruggeman, C., Krooss, B.M., Amann-Hildenbrand, A., Swennen, R. & Littke, R. (2017): Interplay of molecular size and pore network geometry on the diffusion of dissolved gases and HTO in Boom Clay. Applied Geochemistry 76, 182-195. https://doi.org/10.1016/j.apgeochem.2016.11.022

Jacques, D., Wang, L., Martens, E. & Mallants, D. (2010): Modelling chemical degradation of concrete during leaching with rain and soil water types. Cement and Concrete Research 40, 1306-1313. https://doi.org/10.1016/j.cemconres.2010.02.008

Jain, A.K., Mao, J. & Mohiuddin, K.M. (1996): Artificial neural networks: A tutorial. Computer. https://doi.org/10.1109/2.485891

Jatnieks, J., De Lucia, M., Dransch, D. & Sips, M. (2016): Data-driven surrogate model approach for improving the performance of reactive transport simulations. European Geosciences Union General Assembly 2016 97, 447-453. https://doi.org/10.1016/j.egypro.2016.10.047

Jenni, A., Gimmi, T., Alt-Epping, P., Mäder, U. & Cloet, V. (2017): Interaction of ordinary Portland cement and Opalinus Clay: Dual porosity modelling compared to experimental data. Physics and Chemistry of the Earth, Parts A/B/C 99, 22-37. https://doi.org/10.1016/j.pce.2017.01.004

Jenni, A. & Mäder, U. (2021): Reactive Transport Simulation of Low-pH Cement Interacting with Opalinus Clay Using a Dual Porosity Electrostatic Model. Minerals 11, 664. https://doi.org/10.3390/min11070664

Jenni, A. & Mäder, U. (2018): Coupling of chemical and hydromechanical properties in bentonite. Applied Geochemistry 97, 147-156. https://doi.org/10.1016/ J.APGEOCHEM.2018.08.013

Jenni, A., Mäder, U., Lerouge, C., Gaboreau, S. & Schwyn, B. (2014): In situ interaction between different concretes and Opalinus Clay. Physics and Chemistry of the Earth 70-71, 71-83. https://doi.org/10.1016/j.pce.2013.11.004

Jenni, A., Wersin, P., Thoenen, T., Baeyens, B., Ferrari, A., Gimmi, T., Mäder, U.K., Marschall, P., Hummel, W. & Leupin, O.X. (2019): Benotnite backfill performance in a high-level waste repository: a geochemical perspective. Nagra Technical Report NTB 19-03

Jennings, H.M., Bullard, J.W., Thomas, J.J., Andrade, J.E., Chen, J.J. & Scherer, G.W. (2008): Characterization and Modeling of Pores and Surfaces in Cement Paste. Journal of Advanced Concrete Technology 6, 5-29. https://doi.org/10.3151/jact.6.5

Jennings, H.M., Thomas, J.J., Rothstein, D. & Chen, J.J. (2002): Cements as Porous Materials, in: Handbook of Porous Solids. Wiley-VCH Verlag GmbH, Weinheim, Germany, pp. 2971-3028. https://doi.org/10.1002/9783527618286.ch40

Kia, A., Wong, H.S. & Cheeseman, C.R. (2017): Clogging in permeable concrete: A review. Journal of Environmental Management 193, 221-233. https://doi.org/10.1016/j.jenvman.2017.02.018

Kittnerová, J., Drtinová, B., Štamberg, K., Vopálka, D., Evans, N., Deissmann, G. & Lange, S. (2020): Comparative study of radium and strontium behaviour in contact with cementitious materials. Applied Geochemistry 104713. https://doi.org/10.1016/j.apgeochem.2020.104713

Kosakowski, G. (2018): CI experiment: Reactive transport modeling of interface evolution with OpenGeoSys-GEM (Internal Report TM-44-18-5). Paul Scherrer Institut, Villigen, Switzerland

Kosakowski, G. (2013): Reactive transport calculations on porosity changes in the Engineered Gas Transport System. Paul Scherrer Institut, Internal Report, Villigen, Switzerland

Kosakowski, G. (2004): Anomalous transport of colloids and solutes in a shear zone. Journal of Contaminant Hydrology 72, 23-46. https://doi.org/10.1016/j.jconhyd.2003.10.005

Kosakowski, G. & Berner, U. (2013): The evolution of clay rock/cement interfaces in a cementitious repository for low- and intermediate level radioactive waste. Physics and Chemistry of the Earth, Parts A/B/C 64, 65-86. https://doi.org/10.1016/j.pce.2013.01.003

Kosakowski, G. & Berner, U. (2011): Base data set and concepts for reactive transport calculations. Villigen, Switzerland

Kosakowski, G., Berner, U., Wieland, E., Glaus, M.A. & Degueldre, C. (2014): Geochemical evolution of the L/ILW near-field. Naga Technical Report NTB 14-11

Kosakowski, G. & Smith, P. (2014): Long-term evolution of the Engineered Gas Transport System. Nagra Arbeitsbericht NAB 14-16

Kosakowski, G. & Watanabe, N. (2014): OpenGeoSys-Gem: A numerical tool for calculating geochemical and porosity changes in saturated and partially saturated media. Physics and Chemistry of the Earth, Parts A/B/C 70-71, 138-149. https://doi.org/10.1016/j.pce.2013.11.008

Kuila, U. & Prasad, M. (2013): Specific surface area and pore-size distribution in clays and shales. Geophysical Prospecting 61, 341-362. https://doi.org/10.1111/1365-2478.12028

Kulik, D.A. (2011): Improving the structural consistency of C-S-H solid solution thermodynamic models. Cement and Concrete Research 41, 477-495. https://doi.org/10.1016/j.cemconres.2011.01.012

Kulik, D.A., Fernandes, M.M. & Baeyens, B. (2018): The 2SPNE SC/CE sorption model in GEM-Selektor v.3.4 code package (ClaySor): Implementation, tests, and user guide

Kulik, D.A. & Kersten, M. (2002): Aqueous solubility diagrams for cementitious waste stabilization systems. 4. A carbonation model for Zn-Doped calcium silicate hydrate by Gibbs energy minimization. Environmental Science and Technology 36, 2926-2931. https://doi.org/10.1021/es010250v

Kulik, D.A., Miron, G.D. & Lothenbach, B. (2022): A structurally-consistent CASH+ sublattice solid solution model for fully hydrated C-S-H phases: Thermodynamic basis, methods, and Ca-Si-H2O core sub-model. Cement and Concrete Research 151. https://doi.org/10.1016/j.cemconres.2021.106585

Kulik, D.A., Wagner, T., Dmytrieva, S.V., Kosakowski, G., Hingerl, F.F., Chudnenko, K.V. & Berner, U.R. (2012): GEM-Selektor geochemical modeling package: revised algorithm and GEMS3K numerical kernel for coupled simulation codes. Computational Geosciences 17, 1-24. https://doi.org/10.1007/s10596-012-9310-6

Kulik, D.A., Winnefeld, F., Kulik, A., Miron, G.D. & Lothenbach, B. (2021): CemGEMS – an easy-to-use web application for thermodynamic modeling of cementitious materials. RILEM Technical Letters 6, 36-52. https://doi.org/10.21809/rilemtechlett.2021.140

Kunther, W., Lothenbach, B. & Scrivener, K.L. (2013): Deterioration of mortar bars immersed in magnesium containing sulfate solutions. Materials and Structures/Materiaux et Constructions 46, 2003-2011. https://doi.org/10.1617/s11527-013-0032-6

Kurganskaya, I. & Rohlfs, R.D. (2020): Atomistic to meso-scale modeling of mineral dissolution: Methods, challenges and prospects. American Journal of Science 320, 1-26. https://doi.org/10.2475/01.2020.02

L'Hôpital, E., Lothenbach, B., Le Saout, G., Kulik, D. & Scrivener, K. (2015): Incorporation of aluminium in calcium-silicate-hydrates. Cement and Concrete Research 75, 91-103. https://doi.org/10.1016/j.cemconres.2015.04.007

Lalan, P., Dauzères, A., De Windt, L., Bartier, D., Sammaljärvi, J., Barnichon, J.-D., Techer, I. & Detilleux, V. (2016): Impact of a 70 °C temperature on an ordinary Portland cement paste/claystone interface: An in situ experiment. Cement and Concrete Research 83, 164-178. https://doi.org/10.1016/j.cemconres.2016.02.001

Landolt, D., Davenport, A., Payer, J. & Shoesmith, D.W. (2009): No TitleA review of materials and corrosion issues regarding canisters for disposal of spent fuel and high-level waste in Opalinus Clay. Nagra Technical Report NTB 09-02

Lange, S., Kowalski, P.M., Pšenička, M., Klinkenberg, M., Rohmen, S., Bosbach, D. & Deissmann, G. (2018): Uptake of 226Ra in cementitious systems: A complementary solution chemistry and atomistic simulation study. Applied Geochemistry 96, 204-216. https://doi.org/10.1016/j.apgeochem.2018.06.015

Lasaga, A.C. (1981a): Kinetics of geochemical processes, Kinetics of Geochemical Processes, Reviews in Mineralogy Vol. 8. De Gruyter, Berlin, Boston. https://doi.org/10.1515/9781501508233

Lasaga, A.C. (1981b): Transition state theory, in: Lasaga, Anthonio C., & Kirkpatrick, J. (Eds.), Kinetics of Geochemical Processes. De Gruyter, Berlin, Boston, pp. 135-170. https://doi.org/10.1515/9781501508233-008

Leal, A.M.M., Kulik, D.A., Kosakowski, G. & Saar, M.O. (2016): Computational methods for reactive transport modeling: An extended law of mass-action, xLMA, method for multiphase equilibrium calculations. Advances in Water Resources 96, 405-422. https://doi.org/10.1016/j.advwatres.2016.08.008

Leal, A.M.M., Kulik, D.A., Smith, W.R. & Saar, M.O. (2017): An overview of computational methods for chemical equilibrium and kinetic calculations for geochemical and reactive transport modeling. Pure and Applied Chemistry 89, 597-643. https://doi.org/10.1515/pac-2016-1107

Lee, L.I.N. (2001): Soil-pile interaction of bored and cast in situ piles. University of Birmingham

Leemann, A. & Moro, F. (2017): Carbonation of concrete: the role of CO_2 concentration, relative humidity and CO_2 buffer capacity. Materials and Structures 50, 30. https://doi.org/10.1617/s11527-016-0917-2

Lerouge, C., Gaboreau, S., Grangeon, S., Claret, F., Warmont, F., Jenni, A., Cloet, V. & Mäder, U. (2017): In situ interactions between Opalinus Clay and Low Alkali Concrete. Physics and Chemistry of the Earth 99, 3-21. https://doi.org/10.1016/j.pce.2017.01.005

Leupin, O.X., Smith, P., Marschall, P., Johnson, L., Savage, D., Cloet, V., Schneider, J. & Senger, R. (2016a): High-level waste repository-induced effects. Nagra Technical Report NTB 14-13

Leupin, O.X., Smith, P., Marschall, P., Johnson, L., Savage, D., Cloet, V., Schneider, J. & Senger, R. (2016b): Low- and intermediate-level waste repository-induced effects. Nagra Technical Report NTB 14-14

Leupin, O.X., Zeyer, J., Cloet, V., Smith, P., Marschall, P., Papafotiou, A. & Schwyn, B. (2016c): An assessment of the possible fate of gas generated on a repository for low- and intermediate-level waste. Nagra Technical Report NTB 16-05

Liu, M., Starchenko, V., Anovitz, L.M. & Stack, A.G. (2020): Grain detachment and transport clogging during mineral dissolution in carbonate rocks with permeable grain boundaries. Geochimica et Cosmochimica Acta 280, 202-220. https://doi.org/10.1016/j.gca.2020.04.022

Lothenbach, B. (2011a): CI Experiment: Thermodynamic modelling of the hydration of ordinary Portland cement and low-pH cements (Technical note TN 2009-33). Empa, Dübendorf, Switzerland

Lothenbach, B. (2011b): CI experiment: Hydration experiments of OPC, LAC and ESDRED cements: 1h to 3.5 years (Technical Note 2010-75). Mont Terri Project

Lothenbach, B., Bernard, E. & Mäder, U. (2017): Zeolite formation in the presence of cement hydrates and albite. Physics and Chemistry of the Earth 99, 77-94. https://doi.org/10.1016/j.pce.2017.02.006

Lothenbach, B., Kulik, D.A., Matschei, T., Balonis, M., Baquerizo, L., Dilnesa, B., Miron, G.D. & Myers, R.J. (2019): Cemdata18: A chemical thermodynamic database for hydrated Portland cements and alkali-activated materials. Cement and Concrete Research 115, 472-506. https://doi.org/10.1016/j.cemconres.2018.04.018

Lothenbach, B., Le Saout, G., Gallucci, E. & Scrivener, K. (2008a): Influence of limestone on the hydration of Portland cements. Cement and Concrete Research 38, 848-860. https://doi.org/10.1016/J.CEMCONRES.2008.01.002

Lothenbach, B., Matschei, T., Möschner, G. & Glasser, F.P. (2008b): Thermodynamic modelling of the effect of temperature on the hydration and porosity of Portland cement. Cement and Concrete Research 38, 1-18. https://doi.org/10.1016/j.cemconres.2007.08.017

Lothenbach, B., Pelletier-Chaignat, L. & Winnefeld, F. (2012): Stability in the system CaO-Al2O3-H2O. Cement and Concrete Research 42, 1621-1634. https://doi.org/10.1016/j.cemconres.2012.09.002

Lothenbach, B. & Winnefeld, F. (2006): Thermodynamic modelling of the hydration of Portland cement. Cement and Concrete Research 36, 209-226. https://doi.org/10.1016/j.cemconres.2005.03.001

Luraschi, P. et al. (n.d.): In preparation for publication.

Luraschi, P. (2022): Interactions of cement and clay components studied experimentally at small scale. PhD thesis, Universität Bern, in preparation.

Luraschi, P., Gimmi, T., Van Loon, L.R., Shafizadeh, A. & Churakov, S.V. (2020): Evolution of HTO and 36Cl− diffusion through a reacting cement-clay interface (OPC paste-Na montmorillonite) over a time of six years. Applied Geochemistry 119, 104581. https://doi.org/10.1016/j.apgeochem.2020.104581

Lüttge, A., Arvidson, R.S. & Fischer, C. (2013): A stochastic treatment of crystal dissolution kinetics. Elements 9, 183-188. https://doi.org/10.2113/gselements.9.3.183

Ma, B. & Lothenbach, B. (2021): Synthesis, characterization, and thermodynamic study of selected K-based zeolites. Cement and Concrete Research 148, 106537. https://doi.org/https://doi.org/10.1016/j.cemconres.2021.106537

Ma, B. & Lothenbach, B. (2020a): Thermodynamic study of cement/rock interactions using experimentally generated solubility data of zeolites. Cement and Concrete Research 135, 106149. https://doi.org/10.1016/j.cemconres.2020.106149

Ma, B. & Lothenbach, B. (2020b): Synthesis, characterization, and thermodynamic study of selected Na-based zeolites. Cement and Concrete Research 135, 106111. https://doi.org/10.1016/j.cemconres.2020.106111

MacQuarrie, K.T.B. & Mayer, K.U. (2005): Reactive transport modeling in fractured rock: A state-of-the-science review. Earth-Science Reviews 72, 189-227. https://doi.org/10.1016/j.earscirev.2005.07.003

Mäder, U., Jenni, A., Lerouge, C., Gaboreau, S., Miyoshi, S., Kimura, Y., Cloet, V., Fukaya, M., Claret, F., Otake, T., Shibata, M. & Lothenbach, B. (2017): 5-year chemico-physical evolution of concrete-claystone interfaces, Mont Terri rock laboratory (Switzerland). Swiss Journal of Geosciences 110, 307-327. https://doi.org/10.1007/s00015-016-0240-5

Mancini, A., Wieland, E., Geng, G., Dähn, R., Skibsted, J., Wehrli, B. & Lothenbach, B. (2020): Fe(III) uptake by calcium silicate hydrates. Applied Geochemistry 113. https://doi.org/10.1016/j.apgeochem.2019.104460

Martin, L.H.J., Leemann, A., Milodowski, A.E., Mäder, U.K., Münch, B. & Giroud, N. (2016): A natural cement analogue study to understand the long-term behaviour of cements in nuclear waste repositories: Maqarin (Jordan). Applied Geochemistry 71, 20-34. https://doi.org/10.1016/j.apgeochem.2016.05.009

Marty, N.C.M., Bildstein, O., Blanc, P., Claret, F., Cochepin, B., Gaucher, E.C., Jacques, D., Lartigue, J.-E., Liu, S., Mayer, K.U., Meeussen, J.C.L., Munier, I., Pointeau, I., Su, D. & Steefel, C.I. (2015a): Benchmarks for multicomponent reactive transport across a cement/clay interface. Computational Geosciences 19, 635-653. https://doi.org/10.1007/s10596-014-9463-6

Marty, N.C.M., Claret, F., Lassin, A., Tremosa, J., Blanc, P., Madé, B., Giffaut, E., Cochepin, B. & Tournassat, C. (2015b): A database of dissolution and precipitation rates for clay-rocks minerals. Applied Geochemistry 55, 108-118. https://doi.org/10.1016/j.apgeochem.2014.10.012

Marty, N.C.M., Munier, I., Gaucher, E.C., Tournassat, C., Gaboreau, S., Vong, C.Q., Giffaut, E., Cochepin, B. & Claret, F. (2014): Simulation of cement/clay interactions: Feedback on the increasing complexity of modelling strategies. Transport in Porous Media 104, 385-405. https://doi.org/10.1007/s11242-014-0340-5

Marty, N.C.M., Tournassat, C., Burnol, A., Giffaut, E. & Gaucher, E.C. (2009): Influence of reaction kinetics and mesh refinement on the numerical modelling of concrete/clay interactions. Journal of Hydrology 364, 58-72. https://doi.org/10.1016/j.jhydrol.2008.10.013

Massazza, F. (1998): Pozzolana and Pozzolanic Cements, in: Lea's Chemistry of Cement and Concrete. Elsevier, pp. 471-635. https://doi.org/10.1016/B978-075066256-7/50022-9

Matschei, T., Lothenbach, B. & Glasser, F.P. (2007): Thermodynamic properties of Portland cement hydrates in the system CaO-AlO-SiO-CaSO-CaCO-HO. Cement and Concrete Research 37, 1379-1410. https://doi.org/10.1016/j.cemconres.2007.06.002

Mattigod, S.V. & McGrail, B.P. (1999): Estimating the standard free energy of formation of zeolites using the polymer model. Microporous and Mesoporous Materials 27, 41-47. https://doi.org/10.1016/S1387-1811(98)00228-5

Mayer, K.U., Blowes, D.W. & Frind, E.O. (2001): Reactive transport modeling of an in situ reactive barrier for the treatment of hexavalent chromium and trichloroethylene in groundwater. Water Resources Research 37, 3091-3103. https://doi.org/10.1029/2001WR000234

Meeussen, J.C.L., van der Sloot, H.A., Dijkstra, J.J. & Kosson, D.S. (2009): Review of Thermodynamic and Adsorption Databases. International Atomic Energy Agency

Meldrum, F.C. & O'Shaughnessy, C. (2020): Crystallization in Confinement. Advanced Materials. https://doi.org/10.1002/adma.202001068

Metcalfe, R. & Walker, C. (2004): Proceedings of the International Workshop on Bentonite-Cement Interaction in Repository Environments, 14 – 16 April 2004, Tokyo, Japan (Technical Report NUMO-TR-04-05), October. Nuclear Waste Management Organization of Japan (NUMO), Olkiluoto, Finnland

Millington, R.J. & Quirk, J.P. (1961): Permeability of porous solids. Transactions of the Faraday Society 57, 1200-1207. https://doi.org/10.1039/TF9615701200

Miron, G.D., Kulik, D.A. & Lothenbach, B. (2021): Incremental parameterisation of cash+ sublattice solid solution model against recent data for Na, K, and Al uptake in C-S-H. ERICA CASH II final conference. https://www.dora.lib4ri.ch/psi/islandora/object/psi%3A36243

Missana, T., García-Gutiérrez, M., Mingarro, M. & Alonso, U. (2018): Comparison between cesium and sodium retention on calcium silicate hydrate (C-S-H) phases. Applied Geochemistry 98, 36-44. https://doi.org/10.1016/j.apgeochem.2018.09.007

Missana, T., García-Gutiérrez, M., Mingarro, M. & Alonso, U. (2017): Analysis of barium retention mechanisms on calcium silicate hydrate phases. Cement and Concrete Research 93, 8-16. https://doi.org/10.1016/j.cemconres.2016.12.004

Molins, S., Soulaine, C., Prasianakis, N.I., Abbasi, A., Poncet, P., Ladd, A.J.C., Starchenko, V., Roman, S., Trebotich, D., Tchelepi, H.A. & Steefel, C.I. (2020): Simulation of mineral dissolution at the pore scale with evolving fluid-solid interfaces: review of approaches and benchmark problem set. Computational Geosciences. https://doi.org/10.1007/s10596-019-09903-x

Morandeau, A., Thiéry, M. & Dangla, P. (2014): Investigation of the carbonation mechanism of CH and C-S-H in terms of kinetics, microstructure changes and moisture properties. Cement and Concrete Research 56, 153-170. https://doi.org/10.1016/j.cemconres.2013.11.015

Münch, B., Martin, L.H.J. & Leemann, A. (2015): Segmentation of elemental EDS maps by means of multiple clustering combined with phase identification. Journal of Microscopy 260, 411-426. https://doi.org/10.1111/jmi.12309

Muntean, A. & Böhm, M. (2009): Interface conditions for fast-reaction fronts in wet porous mineral materials: The case of concrete carbonation. Journal of Engineering Mathematics 65, 89-100. https://doi.org/10.1007/s10665-009-9295-x

Muntean, A., Böhm, M. & Kropp, J. (2011): Moving carbonation fronts in concrete: A moving-sharp-interface approach. Chemical Engineering Science 66, 538-547. https://doi.org/10.1016/j.ces.2010.11.011

Myers, R.J., Bernal, S.A. & Provis, J.L. (2014): A thermodynamic model for C-(N-)A-S-H gel: CNASH_ss. Derivation and validation. Cement and Concrete Research 66, 27-47. https://doi.org/10.1016/j.cemconres.2014.07.005

Myers, R.J., Lothenbach, B., Bernal, S.A. & Provis, J.L. (2015): Thermodynamic modelling of alkali-activated slag cements. Applied Geochemistry 61, 233-247. https://doi.org/10.1016/j.apgeochem.2015.06.006

Nachshon, U., Weisbrod, N., Dragila, M.I. & Grader, A. (2011): Combined evaporation and salt precipitation in homogeneous and heterogeneous porous media. Water Resources Research 47. https://doi.org/10.1029/2010WR009677

Nagra (2022a): Entsorgungsprogramm 2021 der Entsorgungspflichtigen. Nagra Technischer Bericht NTB 21-01

Nagra (2022b): The Nagra Research, Development and Demonstration (RD&D) Plan for the Disposal of Radioactive Waste in Switzerland. Nagra Technical Report NTB 21-02

Nagra (2002a): Project Opalinus Clay: Safety Report. Nagra Technical Report NTB 02-05

Nagra (2002b): Projekt Opalinuston: Synthese der geowissenschaftlichen Untersuchungs-ergebnisse. Nagra Technischer Bericht NTB 02-03

Nagra (1994): Bericht zur Langzeitsicherheit des Endlagers SMA am Standort Wellenberg (Gemeinde Wolfenschiessen, NW). Nagra Technischer Bericht NTB 94-06

Nakarai, K., Shibata, M., Sakamoto, H., Owada, H. & Kosakowski, G. (2021a): Calcite precipitation at cement-bentonite interface. Part 1: Effect of carbonate admixture in bentonite. Journal of Advanced Concrete Technology 19, 433-446. https://doi.org/10.3151/jact.19.433

Nakarai, K., Watanabe, M., Koibuchi, K. & Kosakowski, G. (2021b): Calcite precipitation at cement-bentonite interface. Part 2: Acceleration of transport by an electrical gradient. Journal of Advanced Concrete Technology 19, 447-461. https://doi.org/10.3151/jact.19.447

Neall, F. (1994): Modelling of the Near-Field Chemistry of the SMA Repository at the Wellenberg Site: Application of the Extended Cement Degradation Model. Nagra Technical Report NTB 94-03

Noiriel, C. & Daval, D. (2017): Pore-Scale Geochemical Reactivity Associated with CO2 Storage: New Frontiers at the Fluid-Solid Interface. Accounts of Chemical Research 50, 759-768. https://doi.org/10.1021/acs.accounts.7b00019

Ochs, M., Mallants, D. & Wang, L. (2016): Radionuclide and Metal Sorption on Cement and Concrete, Topics in Safety, Risk, Reliability and Quality. Springer International Publishing, Cham. https://doi.org/10.1007/978-3-319-23651-3

Oh, B.H. & Jang, S.Y. (2004): Prediction of diffusivity of concrete based on simple analytic equations. Cement and Concrete Research 34, 463-480. https://doi.org/10.1016/j.cemconres.2003.08.026

Olmeda, J., Missana, T., Grandia, F., Grivé, M., García-Gutiérrez, M., Mingarro, M., Alonso, U., Colàs, E., Henocq, P., Munier, I. & Robinet, J.C. (2019): Radium retention by blended cement pastes and pure phases (C-S-H and C-A-S-H gels): Experimental assessment and modelling exercises. Applied Geochemistry 105, 45-54. https://doi.org/10.1016/j.apgeochem.2019.04.004

Palandri, J.L. & Kharaka, Y.K. (2004): A compilation of rate parameters of water-mineral interaction kinetics for application to geochemical modeling (Open File Report 2004-1068). U.S. Geological Survey, Menlo Park, California

Panga, M.K.R., Ziauddin, M. & Balakotaiah, V. (2005): Two-scale continuum model for simulation of wormholes in carbonate acidization. Aiche Journal 51, 3231-3248

Papadakis, V.G., Vayenas, C.G. & Fardis, M.N. (1991): Fundamental Modeling and Experimental Investigation of Concrete Carbonation. Materials Journal 88, 363-373. https://doi.org/10.14359/1863

Papafotiou, A. & Senger, R. (2016a): Sensitivity analyses of gas releases from a L/ILW repository in the Opalinus Clay including the microbial consumption of hydrogen. Nagra Arbeitsbericht NAB 16-07

Papafotiou, A. & Senger, R.K. (2016b): Sensitivity analyses of gas release from a SF/HLW repository in the Opalinus Clay. Nagra Arbeitsbericht NAB 16-08

Pape, H., Clauser, C. & Iffland, J. (2000): Variation of Permeability with Porosity in Sandstone Diagenesis Interpreted with a Fractal Pore Space Model. Pure and Applied Geophysics 157, 603-619. https://doi.org/10.1007/PL00001110

Parkhurst, D.L. (1995): User's guide to PHREEQC: A computer program for speciation, reaction-path, advective-transport, and inverse geochemical calculations. US Department of the Interior, US Geological Survey

Parkhurst, D.L. & Appelo, C. a. J. (2013): Description of Input and Examples for PHREEQC Version 3 – A Computer Program for Speciation , Batch-Reaction , One-Dimensional Transport , and Inverse Geochemical Calculations. U.S. Geological Survey Techniques and Methods, book 6, chapter A43, 497 p., Techniques and Methods, book 6, chapter A43. U.S. Geological Survey

Parrott, L.J. & Killoh, D.C. (1989): Carbonation in a 36 year old, in situ concrete. Cement and Concrete Research 19, 649-656. https://doi.org/10.1016/0008-8846(89)90017-3

Patel, R.A., Churakov, S.V. & Prasianakis, N.I. (2021): A multi-level pore scale reactive transport model for the investigation of combined leaching and carbonation of cement paste. Cement and Concrete Composites 115, 103831. https://doi.org/10.1016/J.CEMCONCOMP.2020.103831

Patel, R.A., Perko, J., Jacques, D., De Schutter, G., Ye, G. & Van Breugel, K. (2018): A three-dimensional lattice Boltzmann method based reactive transport model to simulate changes in cement paste microstructure due to calcium leaching. ConstructionBuilding Materials 166, 158-170

Pearson, F., Tournassat, C. & Gaucher, E.C. (2011): Biogeochemical processes in a clay formation in situ experiment: Part E - Equilibrium controls on chemistry of pore water from the Opalinus Clay, Mont Terri Underground Research Laboratory, Switzerland. Applied Geochemistry 26, 990-1008. https://doi.org/10.1016/j.apgeochem.2011.03.008

Pearson, F.J. (1998): Geochemical and other porosity types in clay-rich rocks, in: Arehart, GB and Hulston, J. (Ed.), Water-Rock Interaction. A Balkema Publishers, Schipholweg 107C, PO BOX 447, 2316 XC Leiden, Netherlands, pp. 259-262

Phung, Q.T., Maes, N. & Jacques, D. (2018): Current Concerns on Durability of Concrete Used in Nuclear Power Plants and Radioactive Waste Repositories, in: Conference: Congrès International de Géotechnique – Ouvrages – Structures. springer, pp. 1107-1121. https://doi.org/10.1007/978-981-10-6713-6_111

Pinson, M.B., Masoero, E., Bonnaud, P.A., Manzano, H., Ji, Q., Yip, S., Thomas, J.J., Bazant, M.Z., Van Vliet, K.J. & Jennings, H.M. (2015): Hysteresis from Multiscale Porosity: Modeling Water Sorption and Shrinkage in Cement Paste. Physical Review Applied 3, 064009. https://doi.org/10.1103/PhysRevApplied.3.064009

Pitty, A.F. & Alexander, W.R. (2014): A natural analogue study of cement buffered , hyperalkaline groundwaters and their interaction with a repository host rock IV : an examination of the Khushaym Matruk (central Jordan) and Maqarin (norhtern Jordan) sites (Technical Report BG-TR-11-02). Bedrock Geosciences, Auenstein, Switzerland

Plecis, A., Schoch, R.B. & Renaud, P. (2005): Ionic transport phenomena in nanofluidics: Experimental and theoretical study of the exclusion-enrichment effect on a chip. Nano Letters 5, 1147-1155. https://doi.org/10.1021/NL050265H

Poller, A., Mayer, G., Darcis, M. & Smith, P. (2016): Modelling of Gas Generation in Deep Geological Repositories after Closure. Nagra Technical Report NTB 16-04

Poller, A., Smith, P., Mayer, G. & Hayek, M. (2014): Modelling of radionuclide transport along the underground access structures of deep geological repositories. Nagra Technical Report NTB 14-10

Poonoosamy, J., Klinkenberg, M., Deissmann, G., Brandt, F., Bosbach, D., Mäder, U. & Kosakowski, G. (2020): Effects of solution supersaturation on barite precipitation in porous media and consequences on permeability: Experiments and modelling. Geochimica et Cosmochimica Acta 270, 43-60. https://doi.org/10.1016/j.gca.2019.11.018

Poonoosamy, J., Kosakowski, G., Van Loon, L.R. & Mäder, U. (2015): Dissolution-precipitation processes in tank experiments for testing numerical models for reactive transport calculations: Experiments and modelling. Journal of Contaminant Hydrology 177-178, 1-17. https://doi.org/10.1016/j.jconhyd.2015.02.007

Poonoosamy, J., Westerwalbesloh, C., Deissmann, G., Mahrous, M., Curti, E., Churakov, S.V., Klinkenberg, M., Kohlheyer, D., von Lieres, E., Bosbach, D. & Prasianakis, N.I. (2019): A microfluidic experiment and pore scale modelling diagnostics for assessing mineral precipitation and dissolution in confined spaces. Chemical Geology 528. https://doi.org/10.1016/j.chemgeo.2019.07.039.

Prasianakis, N.I., Curti, E., Kosakowski, G., Poonoosamy, J. & Churakov, S.V. (2017): Deciphering pore-level precipitation mechanisms. Scientific Reports 7, 13765. https://doi.org/10.1038/s41598-017-14142-0

Prasianakis, N.I., Gatschet, M., Abbasi, A. & Churakov, S.V. (2018): Upscaling strategies of porosity-permeability correlations in reacting environments from pore-scale simulations. Geofluids 2018. https://doi.org/10.1155/2018/9260603

Prasianakis, N.I., Haller, R., Mahrous, M., Poonoosamy, J., Pfingsten, W. & Churakov, S.V. (2020): Neural network based process coupling and parameter upscaling in reactive transport simulations. Geochimica et Cosmochimica Acta 291, 126-143

Prieto, M. (2014): Nucleation and supersaturation in porous media (revisited). Mineralogical Magazine 78, 1437-1447. https://doi.org/10.1180/minmag.2014.078.6.11

Putnis, A. (2015): Transient porosity resulting from fluid-mineral interaction and its consequences. Reviews in Mineralogy and Geochemistry 80, 1-23. https://doi.org/10.2138/rmg.2015.80.01

Rasheeduzzafar; Al-Amoudi, O.S.B., Abduljauwad, S.N. & Maslehuddin, M. (1994): Magnesium-sodium sulfate attack in plain and blended cements. Journal of Materials in Civil Engineering 6, 201-222. https://doi.org/10.1061/(asce)0899-1561(1994)6:2(201)

Read, D., Glasser, F.P., Ayora, C., Guardiola, M.T. & Sneyers, A. (2001): Mineralogical and microstructural changes accompanying the interaction of Boom Clay with ordinary Portland cement. Advances in Cement Research 13, 175-183. https://doi.org/10.1680/adcr.2001.13.4.175

Reijonen, H.M. & Alexander, W.R. (2015): Bentonite analogue research related to geological disposal of radioactive waste: current status and future outlook. Swiss Journal of Geosciences 108, 101-110. https://doi.org/10.1007/S00015-015-0185-0/FIGURES/6

Rodríguez-Galían, R.M. & Prieto, M. (2018): Interaction of nonideal, multicomponent solid solutions with water: A simple algorithm to estimate final equilibrium states. Geochemistry, Geophysics, Geosystems 19, 1348-1359. https://doi.org/10.1029/2017GC007261

Roosz, C., Vieillard, P., Blanc, P., Gaboreau, S., Gailhanou, H., Braithwaite, D., Montouillout, V., Denoyel, R., Henocq, P. & Madé, B. (2018): Thermodynamic properties of C-S-H, C-A-S-H and M-S-H phases: Results from direct measurements and predictive modelling. Applied Geochemistry 92, 140-156. https://doi.org/10.1016/J.APGEOCHEM.2018.03.004

Rumelhart, D.E., Hinton, G.E. & Williams, R.J. (1986): Learning representations by back-propagating errors. Nature 323, 533-536. https://doi.org/10.1038/323533a0

Russell, D., Basheer, P.A.M., Rankin, G.I.B. & Long, A.E. (2001): Effect of relative humidity and air permeability on prediction of the rate of carbonation of concrete. Proceedings of the Institution of Civil Engineers – Structures and Buildings 146, 319-326. https://doi.org/10.1680/stbu.2001.146.3.319

Saripalli, K.P., Meyer, P.D., Bacon, D.H. & Freedman, V.L. (2001): Changes in hydrologic properties of aquifer media due to chemical reactions: A review. Critical Reviews in Environmental Science and Technology 31, 311-349. https://doi.org/10.1080/20016491089244

Savage, D. (2013): Constraints on Cement-Clay Interaction. Procedia Earth and Planetary Science 7, 770-773. https://doi.org/10.1016/j.proeps.2013.03.005

Savage, D. (2011): A review of analogues of alkaline alteration with regard to long-term barrier performance. Mineralogical Magazine 75, 2401-2418. https://doi.org/10.1180/minmag.2011.075.4.2401

Savage, D. & Cloet, V. (2018): A review of Cement-Clay Modelling. Nagra Arbeitsbericht NAB 18-24

Savage, D., Walker, C., Arthur, R., Rochelle, C.A., Oda, C. & Takase, H. (2007): Alteration of bentonite by hyperalkaline fluids: A review of the role of secondary minerals. Physics and Chemistry of the Earth, Parts A/B/C 32, 287-297. https://doi.org/10.1016/j.pce.2005.08.048

Savage, D., Wilson, J., Benbow, S., Sasamoto, H., Oda, C., Walker, C., Kawama, D. & Tachi, Y. (2020): Using natural systems evidence to test models of transformation of montmorillonite. Applied Clay Science 195, 105741. https://doi.org/10.1016/j.clay.2020.105741

Savoye, S., Beaucaire, C., Fayette, A., Herbette, M. & Coelho, D. (2012): Mobility of cesium through the callovo-oxfordian claystones under partially saturated conditions. Environmental Science and Technology 46, 2633-2641. https://doi.org/10.1021/ES2037433/SUPPL_FILE/ES2037433_SI_001.PDF

Savoye, S., Page, J., Puente, C., Imbert, C. & Coelho, D. (2010): New experimental approach for studying diffusion through an intact and unsaturated medium: A case study with callovo-oxfordian argillite. Environmental Science and Technology 44, 3698-3704. https://doi.org/10.1021/ES903738T/SUPPL_FILE/ES903738T_SI_001.PDF

Schmidt, T. (2007): Sulfate attack and the role of internal carbonate on the formation of thaumasite. EPF Lausanne

Schmidt, T., Lothenbach, B., Romer, M., Neuenschwander, J. & Scrivener, K. (2009): Physical and microstructural aspects of sulfate attack on ordinary and limestone blended Portland cements. Cement and Concrete Research 39, 1111-1121. https://doi.org/10.1016/j.cemconres.2009.08.005

Scott, S.W. & Driesner, T. (2018): Permeability changes resulting from quartz precipitation and dissolution around upper crustal intrusions. Geofluids 2018, 1-19. https://doi.org/10.1155/2018/6957306

Seigneur, N., Mayer, K.U. & Steefel, C.I. (2019): Reactive transport in evolving porous media. Reviews in Mineralogy and Geochemistry 85, 197-238. https://doi.org/10.2138/rmg.2019.85.7

Seiphoori, A. (2015): Thermo-hydro-mechanical characterisation and modelling of Wyoming granular bentonite. Nagra Technical Report NTB 15-05

Senger, R., Papafotiou, A. & Marschall, P. (2013): Gas related property distributions in the proposed host rock formations of the candidate siting regions in Northern Switzerland and in the Helvetic Zone. Nagra Arbeitsbericht NAB 13-83

SFOE (2008): Sectoral Plan for Deep Geological Repositories – Conceptual Part

Shafizadeh, A. (2019): Neutron Imaging Study of Evolution of Structural and Transport Properties of Cement-Clay Interfaces, PhD Thesis. Universität Bern

Shafizadeh, A., Gimmi, T., Van Loon, L.R., Kaestner, A., Lehmann, E., Mäder, U.K. & Churakov, S.V. (2015): Quantification of water content across a cement-clay interface using high resolution neutron radiography. Physics Procedia 69, 516-523. https://doi.org/10.1016/j.phpro.2015.07.073

Shafizadeh, A., Gimmi, T., Van Loon, L.R., Kaestner, A.P., Mäder, U.K. & Churakov, S. V. (2020): Time-resolved porosity changes at cement-clay interfaces derived from neutron imaging. Cement and Concrete Research 127, 105924. https://doi.org/10.1016/j.cemconres.2019.105924

Shao, H. (2009): Modelling reactive transport processes in porous med. Technische Universität Dresden PhD, 76

Shvarov, Y.V. (2008): HCh: New potentialities for the thermodynamic simulation of geochemical systems offered by windows. Geochemistry International 46, 834-839. https://doi.org/10.1134/S0016702908080089

Soler, J.M. (2013): Reactive transport modeling of concrete-clay interaction during 15 years at the Tournemire Underground Rock Laboratory. European Journal of Mineralogy 25, 639-654. https://doi.org/10.1127/0935-1221/2013/0025-2324

Steefel, C.I., Appelo, C.A.J., Arora, B., Jacques, D., Kalbacher, T., Kolditz, O., Lagneau, V., Lichtner, P.C., Mayer, K.U., Meeussen, J.C.L., Molins, S., Moulton, D., Shao, H., Šimůnek, J., Spycher, N., Yabusaki, S.B. & Yeh, G.T. (2015): Reactive transport codes for subsurface environmental simulation. Computational Geosciences 19, 445-478. https://doi.org/10.1007/s10596-014-9443-x

Stefanoni, M., Angst, U.M. & Elsener, B. (2018): Electrochemistry and capillary condensation theory reveal the mechanism of corrosion in dense porous media. Scientific Reports 2018 8:1 8, 1-10. https://doi.org/10.1038/s41598-018-25794-x

Steiner, S., Lothenbach, B., Proske, T., Borgschulte, A. & Winnefeld, F. (2020): Effect of relative humidity on the carbonation rate of portlandite, calcium silicate hydrates and ettringite. Cement and Concrete Research 135, 106116. https://doi.org/10.1016/j.cemconres.2020.106116

Succi, S. (2001): The lattice Boltzmann equation: for fluid dynamics and beyond. Oxford university press

Ta, V.-L., Bonnet, S., Senga Kiesse, T. & Ventura, A. (2016): A new meta-model to calculate carbonation front depth within concrete structures. Construction and Building Materials 129, 172-181. https://doi.org/10.1016/j.conbuildmat.2016.10.103

Tachi, Y. & Yotsuji, K. (2014): Diffusion and sorption of Cs+, Na+, I- and HTO in compacted sodium montmorillonite as a function of porewater salinity: Integrated sorption and diffusion model. Geochimica et Cosmochimica Acta 132, 75-93. https://doi.org/10.1016/J.GCA.2014.02.004

Tang, Y., Yao, X., Chen, Y., Zhou, Y., Zhu, D.Z., Zhang, Y., Zhang, T. & Peng, Y. (2020): Experiment research on physical clogging mechanism in the porous media and its impact on permeability. Granular Matter 22, 37. https://doi.org/10.1007/s10035-020-1001-8

Tartakovsky, D.M. & Dentz, M. (2019): Diffusion in Porous Media: Phenomena and Mechanisms. Transport in Porous Media 130, 105-127. https://doi.org/10.1007/s11242-019-01262-6

Thiery, M., Villain, G., Dangla, P. & Platret, G. (2007): Investigation of the carbonation front shape on cementitious materials: Effects of the chemical kinetics. Cement and Concrete Research 37, 1047-1058. https://doi.org/10.1016/j.cemconres.2007.04.002

Thoenen, T., Berner, U., Curti, E., Hummel, W. & Pearson, F.J. (2004): Development and application of the Nagra/PSI Chemical Thermodynamic Data Base 01/01. Geological Society, London, Special Publications. https://doi.org/10.1144/GSL.SP.2004.236.01.31

Thoenen, T. & Hummel, W. (2021): The PSI Chemical Thermodynamic Database 2020. Nagra Technical Report NTB 21-03

Thoenen, T., Hummel, W., Berner, U.R. & Curti, E. (2014): The PSI/Nagra Chemical Thermodynamic Database 12/07. Villigen, Switzerland

Thomas, M. (2013): Supplementary cementing materials in concrete, Supplementary Cementing Materials in Concrete. CRC Press. https://doi.org/10.1201/b14493

Thouvenot, P., Bildstein, O., Munier, I., Cochepin, B., Poyet, S., Bourbon, X. & Treille, E. (2013): Modeling of concrete carbonation in deep geological disposal of intermediate level waste. EPJ Web of Conferences 56, 05004. https://doi.org/10.1051/epjconf/20135605004

Tinseau, E., Bartier, D., Hassouta, L., Devol-Brown, I. & Stammose, D. (2006): Mineralogical characterization of the Tournemire argillite after in situ interaction with concretes. Waste Management 26, 789-800. https://doi.org/10.1016/j.wasman.2006.01.024

Tits, J., Fujita, T., Harfouche, M., Dähn, R., Tsukamoto, M. & Wieland, E. (2014): Radionuclide uptake by calcium silicate hydrates: Case studies with Th(IV) and U(VI). Villigen, Switzerland

Tits, J., Fujita, T., Harfouche, M., Dähn, R., Tsukamoto, M. & Wieland, E. (2014): Radionuclide uptake by calcium silicate hydrates: Case studies with Th (IV) and U (VI). Nuclear Energy and Safety Research Department Laboratory for Waste Management (LES)

Tits, J., Iijima, K., Wieland, E. & Kamei, G. (2006a): The uptake of radium by calcium silicate hydrates and hardened cement paste, in: Radiochimica Acta. De Gruyter, pp. 637-643. https://doi.org/10.1524/ract.2006.94.9-11.637

Tits, J., Stumpf, T., Rabung, T., Wieland, E. & Fanghänels, T. (2003): Uptake of Cm(III) and Eu(III) by calcium silicate hydrates: A solution chemistry and time-resolved laser fluorescence spectroscopy study. Environmental Science and Technology 37, 3568-3573. https://doi.org/10.1021/es030020b

Tits, J., Wieland, E., Müller, C.J., Landesman, C. & Bradbury, M.H. (2006b): Strontium binding by calcium silicate hydrates. Journal of Colloid and Interface Science 300, 78-87. https://doi.org/10.1016/j.jcis.2006.03.043

Torkzaban, S., Bradford, S.A., Vanderzalm, J.L., Patterson, B.M., Harris, B. & Prommer, H. (2015a): Colloid release and clogging in porous media: Effects of solution ionic strength and flow velocity. Journal of Contaminant Hydrology 181, 161-171. https://doi.org/10.1016/j.jconhyd.2015.06.005

Torkzaban, S., Vanderzalm, J., Treumann, S. & Amirianshoja, T. (2015b): Understanding and quantifying clogging and its management during re-injection of CSG water permeates, brines and blends (Final Rep). CSIRO, Australia

Tournassat, C. & Steefel, C.I. (2015): Ionic Transport in Nano-Porous Clays with Consideration of Electrostatic Effects. Reviews in Mineralogy and Geochemistry 80, 287-329. https://doi.org/10.2138/RMG.2015.80.09

Trotignon, L., Thouvenot, P., Munier, I., Cochepin, B., Piault, E., Treille, E., Bourbon, X. & Mimid, S. (2011): Numerical simulation of atmospheric carbonation of concrete components in a deep geological radwaste disposal site during operating period. Nuclear Technology 174, 424-437

Trotignon, L., Thouvenot, P., Munier, I., Cochepin, B., Piault, E., Treille, E., Bourbon, X. & Mimid, S. (2009): Numerical simulation of atmospheric carbonation of concrete components in a deep geological radwaste disposal site during operating period, in: TOUGH Symposium 2009

Tumidajski, P. (2005): Relationship between resistivity, diffusivity and microstructural descriptors for mortars with silica fume. Cement and Concrete Research 35, 1262-1268. https://doi.org/10.1016/j.cemconres.2004.10.007

Tumidajski, P., Schumacher, A., Perron, S., Gu, P. & Beaudoin, J. (1996): On the relationship between porosity and electrical resistivity in cementitious systems. Cement and Concrete Research 26, 539-544. https://doi.org/10.1016/0008-8846(96)00017-8

Turrero, M.J. & Cloet, V. (2017): FEBEX-DP Concrete ageing, concrete/bentonite and concrete/rock interaction analysis. Nagra Arbeitsbericht NAB 16-18

van Brakel, J. & Heertjes, P.M. (1974): Analysis of diffusion in macroporous media in terms of a porosity, a tortuosity and a constrictivity factor. International Journal of Heat and Mass Transfer 17, 1093-1103. https://doi.org/10.1016/0017-9310(74)90190-2

Van Loon, L.R., Glaus, M.A. & Müller, W. (2007): Anion exclusion effects in compacted bentonites: Towards a better understanding of anion diffusion. Applied Geochemistry 22, 2536-2552. https://doi.org/10.1016/J.APGEOCHEM.2007.07.008

Van Loon, L.R. & Jakob, A. (2005): Evidence for a second transport porosity for the diffusion of tritiated water (HTO) in a sedimentary rock (Opalinus clay - OPA): Application of through- and out-diffusion techniques. Transport in Porous Media 61, 193-214. https://doi.org/10.1007/s11242-004-7464-y

Van Loon, L.R., Soler, J.M., Müller, W. & Bradbury, M.H. (2004a): Anisotropic Diffusion in Layered Argillaceous Rocks: A Case Study with Opalinus Clay. Environmental Science & Technology 38, 5721-5728. https://doi.org/10.1021/es049937g.

Van Loon, L.R., Wersin, P., Soler, J.M., Eikenberg, J., Gimmi, T., Hernán, P., Dewonck, S. & Savoye, S. (2004b): In situ diffusion of HTO, 22Na^+, Cs^+ and I^- in Opalinus Clay at the Mont Terri underground rock laboratory. Radiochimica Acta 92, 757-763. https://doi.org/10.1524/ract.92.9.757.54988

Velbel, M.A. (1990): Influence of Temperature and Mineral Surface Characteristics on Feldspar Weathering Rates in Natural and Artificial Systems: A First Approximation. Water Resources Research 26, 3049-3053. https://doi.org/10.1029/WR026i012p03049

Vespa, M., Wieland, E., Dähn, R. & Lothenbach, B. (2015): Identification of the Thermodynamically Stable Fe-Containing Phase in Aged Cement Pastes. Journal of the American Ceramic Society 98, 2286-2294. https://doi.org/10.1111/jace.13542

Vieillard, P. (2010): A predictive model for the entropies and heat capacities of zeolites. European Journal of Mineralogy 22, 823-836. https://doi.org/10.1127/0935-1221/2010/0022-2026

Vieillard, P. (2000): A new method for the prediction of Gibbs free energies of formation of hydrated clay minerals based on the electronegativity scale. Clays and Clay Minerals 48, 459-473. https://doi.org/10.1346/CCMN.2000.0480406

Vieillard, P. & Mathieu, R. (2009): A predictive model for the enthalpies of hydration of zeolites. American Mineralogist 94, 565-577. https://doi.org/10.2138/am.2009.3028

Vinograd, V.L., Kulik, D.A., Brandt, F., Klinkenberg, M., Weber, J., Winkler, B. & Bosbach, D. (2018): Thermodynamics of the solid solution – Aqueous solution system (Ba,Sr,Ra)SO + HO: I. The effect of strontium content on radium uptake by barite. Applied Geochemistry 89, 59-74. https://doi.org/10.1016/j.apgeochem.2017.11.009.

Voskov, A.L., Voronin, G.F., Kutsenok, I.B. & Kozin, N.Y. (2019): Thermodynamic database of zeolites and new method of their thermodynamic properties evaluation for a wide temperature range. Calphad: Computer Coupling of Phase Diagrams and Thermochemistry 66, 101623. https://doi.org/10.1016/j.calphad.2019.04.008

Wagner, T., Kulik, D.A., Hingerl, F.F. & Dmytrievava, S. V. (2012): GEM-Selektor geochemical modeling package: TSolMod library and data interface for multicomponent phase models. Canadian Mineralogist 50, 1173-1195. https://doi.org/10.3749/canmin.50.5.1173

Walker, C.S., Sutou, S., Oda, C., Mihara, M. & Honda, A. (2016): Calcium silicate hydrate (C-S-H) gel solubility data and a discrete solid phase model at 25 °C based on two binary non-ideal solid solutions. Cement and Concrete Research 79, 1-30. https://doi.org/10.1016/j.cemconres.2015.07.006

Wantanaphong, J., Mooney, S.J. & Bailey, E.H. (2006): Quantification of pore clogging characteristics in potential permeable reactive barrier (PRB) substrates using image analysis. Journal of contaminant hydrology 86, 299-320. https://doi.org/10.1016/j.jconhyd.2006.04.003

Watkinson, D. & Lewis, M. (2004): ss Great Britain iron hull: modelling corrosion to define storage relative humidity. researchgate.net 592, 967

Wersin, P., Mazurek, M., Waber, H.N., Mäder, U., Gimmi, T., Rufer, D. & de Haller, A. (2013): Rock and porewater characterisation on drillcores from the Schlattingen borehole. Nagra Arbeitsbericht NAB 12-54.

White, A.F. & Brantley, S.L. (2003): The effect of time on the weathering of silicate minerals: why do weathering rates differ in the laboratory and field? Chemical Geology 202, 479-506. https://doi.org/10.1016/j.chemgeo.2003.03.001

Whittaker, M. & Black, L. (2015): Current knowledge of external sulfate attack. Advances in Cement Research 27, 532-545. https://doi.org/10.1680/adcr.14.00089

Wieland, E. (2014): Sorption data base for the cementitious near field of L/ILW and ILW repositories for provisional safety analyses for SGT-E2. Nagra Technical Report NTB 14-08

Wieland, E. & Kosakowski, G. (2020): Review of the compositions of hydrated cements and cement-type pore water at different stages of the cement degradation. Nagra Arbeitsbericht NAB 20-12.

Wieland, E., Kosakowski, G., Lothenbach, B. & Kulik, D.A. (2020): Geochemical modelling of the effect of waste degradation processes on the long-term performance of waste forms. Applied Geochemistry 115, 104539. https://doi.org/10.1016/j.apgeochem.2020.104539

Wieland, E., Tits, J., Dobler, J.-P. & Spieler, P. (1998): Interaction of Eu (III) and Th (IV) with Sulphate-resisting Portland cement. Mater. Res. Soc. Symp. Proc. 506, 573-578. https://doi.org/doi.org/10.1557/PROC-506-573

Wieland, E. & Van Loon, L.R. (2003): Cementitious Near-Field Sorption Data Base for Perfomance Assessment of an ILW Repository in Opalinus Clay (PSI Report 03-06). Villigen, Switzerland

Wigger, C., Plötze, M. & van Loon, L.R. (2018): Pore geometry as a limiting factor for anion diffusion in argillaceous rocks. Clays and Clay Minerals 66, 329-338. https://doi.org/10.1346/CCMN.2018.064101

Wilson, J., Bateman, K. & Tachi, Y. (2021): The impact of cement on argillaceous rocks in radioactive waste disposal systems: A review focusing on key processes and remaining issues. Applied Geochemistry 130, 104979. https://doi.org/10.1016/j.apgeochem.2021.104979

Winter, N.B. (2009): Understanding Cement: An introduction to cement production, cement hydration and deleterious processes in concrete. WHD Microanalysis Consultants, Woodbridge, UK

Wolery, T.J. (1992): EQ3/6, a software package for geochemical modeling of aqueous systems: Package overview and installation guide (Version 7.0). Lawrence Livermore National Lab., CA, United States

Wolter, J.M., Schmeide, K., Huittinen, N. & Stumpf, T. (2019): Cm(III) retention by calcium silicate hydrate (C-S-H) gel and secondary alteration phases in carbonate solutions with high ionic strength: A site-selective TRLFS study. Scientific Reports 9, 1-12. https://doi.org/10.1038/s41598-019-50402-x

Xie, M., Mayer, K.U., Claret, F., Alt-Epping, P., Jacques, D., Steefel, C., Chiaberge, C. & Simunek, J. (2015): Implementation and evaluation of permeability-porosity and tortuosity-porosity relationships linked to mineral dissolution-precipitation. Computational Geosciences 19, 655-671. https://doi.org/10.1007/s10596-014-9458-3

Xu, T., Sonnenthal, E., Spycher, N., Zhang, G., Zheng, L. & Pruess, K. (2012): Toughreact: A simulation program for subsurface reactive chemical transport under non-isothermal multiphase flow conditions, in: Groundwater Reactive Transport Models. pp. 74-95. https://doi.org/10.2174/978160805306311201010074

Yang, Y., Patel, R.A., Churakov, S.V., Prasianakis, N.I., Kosakowski, G. & Wang, M. (2019): Multiscale modeling of ion diffusion in cement paste: electrical double layer effects. Cement and Concrete Composites 96, 55-65. https://doi.org/10.1016/j.cemconcomp.2018.11.008

Yokoyama, S., Shimbashi, M., Minato, D., Watanabe, Y., Jenni, A. & Mäder, U. (2021): Alteration of bentonite reacted with cementitious materials for 5 and 10 years in the mont terri rock laboratory (Ci experiment). Minerals 11, 1-17. https://doi.org/10.3390/min11030251

Yuan, Y. & Rezaee, R. (2019): Comparative porosity and pore structure assessment in ahales: Measurement techniques, influencing factors and implications for reservoir characterization. Energies 12, 2094. https://doi.org/10.3390/en12112094

Zak, R. & Deja, J. (2015): Spectroscopy study of Zn, Cd, Pb and Cr ions immobilization on C-S-H phase. Spectrochimica Acta - Part A: Molecular and Biomolecular Spectroscopy 134, 614-s620. https://doi.org/10.1016/j.saa.2014.06.069s

Zhen-Wu, B.Y., Prentice, D.P., Ryan, J. V., Ellison, K., Bauchy, M. & Sant, G. (2020): zeo19: A thermodynamic database for assessing zeolite stability during the corrosion of nuclear waste immobilization glasses. npj Materials Degradation 4, 1-12. https://doi.org/10.1038/s41529-019-0106-1

Zhu, C. (2005): In situ feldspar dissolution rates in an aquifer. Geochimica et Cosmochimica Acta 69, 1435-1453. https://doi.org/10.1016/j.gca.2004.09.005